博士論文

Experimental investigation of mechanism at ultimate drift capacity in reinforced concrete beams subjected to reversed cyclic loading

（繰り返し載荷を受ける鉄筋コンクリート梁の終局変形限界機構に関する実験的研究）

トリベディ　シュバーン

(TRIVEDI Shubham)

Shubham TRIVEDI

Experimental investigation of mechanism at ultimate drift capacity in reinforced concrete beams subjected to reversed cyclic loading

2018

Ph.D. Thesis
The University of Tokyo

This thesis was typeset using LaTeX with the `tufte-latex` book class. All illustrations were generated using the `tikz` package and graphs were plotted using the `pgfplots` package. The bibliography was processed in BibLaTeX using `biber` backend. Palatino and Helvetica are used as main text and sans serif fonts respectively.

Abstract

Reinforced concrete beams subjected to reverse cyclic loading to simulate earthquake response exhibit much lower deformation capacities as compared to beams in monotonic loading. In the strength-based design procedures, this phenomenon was not important as ultimate strength is not significantly affected by cyclic loading. With the advent of performance-based design, accurate and reliable assessment of deformation capacity has become increasingly important for economic and efficient design. This study was aimed at identifying the mechanism responsible for loss of strength at ultimate state which can be used for accurately determining deformation capacity through experimental testing.

Chapter 2, Background: Experimental studies conducted over the past 50 years were reviewed to identify key characteristics of ultimate state response and the parameters that influence response. Various drift capacity estimation models proposed in the past were and grouped with the respect to the definition of limit state: concrete compression, shear strength degradation, bar buckling, and empirical. Key characteristics of each of these models and their limitations are discussed.

Chapter 3, Experiment: Experimental program was designed with nineteen number one-third scale specimens encompassing parameters such as concrete strength (30 MPa to 60 MPa), longitudinal reinforcement content (1.29 % to 1.94 %), transverse reinforcement content (0.26 % to 2.04 %), shear-span ratio (2.91 to 5.41), transverse reinforcement strength (341 MPa to 824 MPa) and bar-diameter (9.5 mm to 15.9 mm). Beams were tested in cantilever configuration and increasingly large target displacements with three repetitions each were applied. Detailed surface deformation patterns were measured by implementing synthetic targets and pattern-matching based photogrammetric analysis algorithm.

Chapter 4, Results: Observed response is presented in terms of moment-drift relationships, moment-hinge rotation relationships, and hinge zone axial strain-drift relationships using conventional sensor data and lateral strain profile, axial strain profile, rotation profile and grid deformed shape using photogrammetry data. Validity of photogrammetric measurements is established by comparing against similar quantities recorded with conventional displacement sensors.

Chapter 5, Discussion: Comparative evaluation of equivalent specimen pair response revealed that more than 100 % variation in shear

strength related parameters, concrete strength and transverse reinforcement strength, did not result in any improvement in drift capacity. While transverse reinforcement content, shear-span ratio, and bar diameter consistently affected the ultimate drift capacity. Based on this observation and the hinge zone lateral expansion patterns observed from photogrammetry, a new mechanism based on lateral inclination of inelastic rebars on the compressive side was proposed to explain the phenomenon of loss of strength at ultimate state. Validity of the proposed mechanism was qualitatively established by relating photogrammetric estimations of rebar inclinations to the initiation of loss of strength.

Chapter 6, Conclusion: Concluding remarks are expressed on the contents of all chapters and significant sections followed by a brief discussion highlighting scope for possible experimental and analytical future research work stemming from the findings of this study.

Appendices A to E: All the relevant specimen and material specification and details are included for reference. Photographs expressing specimen states at peak loading stages over each cycle and the corresponding surface deformation measured from photogrammetry, expressed as grid deformed shapes are provided for all specimens.

Acknowledgements

Contents

Dedicated to all my friends and family.

1
Introduction

Extreme earthquake events induce severe actions in building components. Seismic design aims to provide sufficient strength and ductility in structural members to survive the imposed earthquake forces without causing collapse of the building.

Conventional strength-based design procedures popular in the past stipulated provision of a minimum design strength and good detailing practices to ensure ductile response beyond yield. Accurate assessment of deformation capacity was not required as long as required detailing guidelines were adhered. Consequently, large volume of earthquake engineering research over the years has enabled vastly improved estimation of strength. Deformation capacity estimation, however, has not attracted similar research attention. With the growing emphasis on rational design of structures through the principles of performance-based design, accurate and reliable estimation of deformation capacity is not only increasingly important but also essential for successful realization of performance-based design.

In the context of reinforced concrete frames, both columns and beams are expected to undergo inelastic response. In the strong column-weak beam design philosophy, plastic response of columns plays a crucial role in controlling overall collapse of the structure. Accordingly, significant research on drift capacity of columns has already been conducted and a wide array of numerical models have been proposed. Ultimate state response of beams has not attracted research interest of the same order.

This research gap was addressed in this study. Ultimate state response was investigated to determine the drift capacity defining mechanism in beams which is a less complicated response case as compared to columns and therefore allows easier comprehension of the mechanism involved.

1.1 *Objectives*

This study was conducted primarily to investigate response at ultimate state in RC beams subjected to reverse cyclic loading. Main objective of this investigation was to determine the mechanism governing response at the ultimate state. Accurate and reliable estimation of drift capacity and other response quantities is possible only after the

defining mechanism has been comprehended. Secondary objectives
of this study may be stated as:

· identifying ways to accurately determine ultimate moment strength
  and post-yielding stiffness, two quantities required in addition to
  ultimate drift capacity to comprehensively define ultimate state
  response;

· testing qualitatively the validity of existing approaches on drift
  capacity determination;

· improving the comprehension of standard defined performance
  states through experiment data;

· determining ways to efficiently improve plastic response of beams;
  and

· finding appropriate ways to implement photogrammetry in mea-
  surement of deformations in reinforced concrete experiments.

1.2   *Outline*

EXISTING literature on the subject including experiment reports and
analytical models was first reviewed to gain insight on key characte-
ristics of ultimate state response and possible explanations of defining
mechanism. Significant findings from this review study are reported
in Chapter 2[1] along with references to the original research.

   A large experimental program was undertaken to investigate the
ultimate state response of beams. Details on the specimen design and
all relevant experiment procedures are expressed in Chapter 3[2].

   All measurements and deduced response quantities obtained from
the experiment are presented in Chapter 4[3]. Detailed description
of the photogrammetric analysis scheme is also expressed in this
chapter before presenting the resulting data and photogrammetric
deformation plots.

   Experiment results were systematically analyzed and various re-
sponse quantities were closely studied to understand the mechanism
at ultimate state of response. Resulting findings are discussed in
Chapter 5[4]. Based on the observations, a new mechanism explaining
the phenomenon of loss of strength at drift capacity is proposed and
detailed in this chapter.

   Finally, a summary of the findings on ultimate state response
and design implications of the proposed mechanism are included in
Chapter 6[5].

   Large quantities of details and data regarding the experiment are
not included in the main chapters listed above but provided as appen-
dix instead. Construction drawings according to which the specimens
were manufactured are expressed in Appendix A[6]. Results of material
testing including data for each test piece are detailed in Appendix B[7].
A note on the data processing methodology used to reduce the ex-
periment data is included for reference in Appendix C[8]. Large set of

digital images expressing specimen response states at various loading stages are provided in Appendix D[9]. Photogrammetric analysis results expressed as specimen grid deformation states at peak loading stages are expressed for all specimens in Appendix E[10]. Other miscellaneous experiment data not discussed elsewhere is included in Appendix F[11].

All chapters of this report have a self explanatory title. While the chapters are intended to represent a sequence starting from background study to final conclusion, it may be reasonable to skip some details without loss of continuity. All major findings of the study are reasoned and concluded in Chapter 5. While references are frequently made to literature and results reported in previous chapters, it is possible to jump straight to Discussion and return to previous chapters for specific details when necessary.

[9] See page 177.

[10] See page 205.

[11] See page 223.

2
Background

Previous investigations on ultimate response of reinforced concrete beams were first reviewed to establish a better understanding of the expected response. Experimental investigation reports from the past were studied to comprehend failure patterns and the effect of various specimen properties on drift capacity. Following which models proposed to estimate deformation capacities were reviewed.

2.1   *Experiment reports*

Early attempts to quantify ultimate deformation capacity of reinforced concrete members in flexure typically involved monotonic loading of beams at mid-span. Mattock[1] tested thirty-seven beams in simple flexure using concrete and reinforcement strengths and span-to-depth ratio as investigation parameters. Deformations at the ultimate state, defined as the rotation at maximum applied moment, were found to be in excess of 15 times the yield deformations. Maximum concrete compressive strain was used as the key parameter to define ultimate rotation capacity.

Influence of cyclic loading was first investigated by Sinha et al..[2] Nine singly reinforced simple beams were tested in two-point loading to increasing deformation cycles. Only a minimal effect of cycling was observed on the ultimate deformation capacity and moment strength. A follow-up study considering reversed cyclic loading on a similar testing configuration but with doubly reinforced beams was conducted by Agrawal et al.[3] Although full deformation reversals were not considered, cyclic reversal was found to have a detrimental influence on response characteristics.

Effect of cyclic loading on cantilever beams representative of actual earthquake forces was comprehensively demonstrated by Brown.[4] Monotonic, unidirectional cyclic and revered cyclic loading histories were applied to similar specimens. While unidirectional cyclic loading produced little loss in ductility observed in monotonic response, reverse cyclic loading resulted in significantly different response. Non-linearity induced due to Bauschinger effect in steel and shear and slip deformations in concrete caused deterioration of stiffness and strength with cycling. All specimens were reported to fail in shear followed by buckling of compression reinforcement.

[1] A. H. Mattock. "Rotational capacity of hinging regions in reinforced concrete beams". In: *Proceedings of the International Symposium on Flexural Mechanics of Reinforced Concrete*. International Symposium on Flexural Mechanics of Reinforced Concrete. Miami, FL: American Society of Civil Engineers, 1965, pp. 143–180.

[2] B. P. Sinha et al. "Response of singly reinforced beams to cyclic loading". In: *ACI Structural Journal* 61.8 (1964), pp. 1021–1037. DOI: 10.14359/7819.

[3] G. L. Agrawal et al. "Response of doubly reinforced concrete beams to cyclic loading". In: *ACI Structural Journal* 62.7 (1965), pp. 823–834. DOI: 10.14359/7726.

[4] R. H. Brown. "Reinforced concrete cantilever beams under slow cyclic loadings". PhD thesis. Rice University, 1970.

These findings were confirmed in a similar investigation with reversed loading cycles at large deformations by Wight and Sozen.[5] Decrease in strength and stiffness was observed with continuous cycling. Formation of inclined cracks, yielding of stirrups and spalling of concrete were observe at failure. Increase in axial load and transverse reinforcement ratio were found to slow down the deterioration. Role of shear was also found significant in tests reported by Gosain.[6] Decrease in moment-shear ratio was found to consistently reduce the ability to withstand cyclic loading.

In contrast to the above tests where cyclic loads were applied at a large constant deformation, Popov et al.[7] and Bertero et al.[8] reported test conducted in University of California at Berkeley where cyclic loading was applied at increasingly large amplitudes. Beams in cantilever configuration with a rigidly clamped joint were studied. Behavior in post-yielding range and ultimate deformation capacities were reported to be influenced by shear deformations and deterioration of shear resistance under load reversals. Special reinforcement web reinforcement arrangement consisting of inclined bars to control the formation of shear cracks were found to be effective in improving deformation capacity and energy dissipation characteristics under large deformation reversals.

Celebi and Penzien[9] tested twelve beam specimens to study the effects of shear stress and loading rate on ultimate state response. Specimens with larger nominal shear stress were found to exhibit increasingly pinched hysteresis loops. Rate of dynamic loading was not observed to significantly affect any inelastic response parameter but yield load was found to increase with rapid loading rates. Role of shear stress in inelastic cyclic loading was also emphasized by Nmai and Darwin[10] in a report on tests of lightly reinforced RC Beams. Reduction of maximum shear in beams by using low longitudinal reinforcement ratio was found to successfully reduce the rate of degradation at large loading cycles.

Unlike previous findings, Scribner and Wight[11] reported buckling of longitudinal reinforcement to be a significant factor in determining ultimate state of beams. Twelve beams with an anchored column stub were loaded to multiple reversed loading cycles at two levels of large deformation. Buckling of reinforcement at ultimate state was observed in most of the specimens. Size and strength of stirrups were found to be more important than stirrup spacing in preventing buckling.

EFFECT of applied loading history on inelastic response of beams was comprehensively investigated by Ingham et al.[12] Similar cantilever beam specimens were subjected to various loading histories including monotonic, unidirectional cyclic, reverse cyclic at constant amplitude, reverse cyclic with various cycles at each increasing amplitude level and loading histories directly simulating recorded earthquake ground motions. Ultimate deformation capacity was found to vary significantly with the applied loading history. Moreover, lab fabrica-

[5] J. K. Wight and M. A. Sozen. *Shear strength decay in reinforced concrete columns subjected to large deflection reversals*. SRS 403. Urbana-Champaign, IL: University of Illinois, 1973.

[6] N. K. Gosain. "Effect of cyclic loads on beams with high-strength reinforcement". PhD thesis. Houston, TX: Rice University, 1973.

[7] E. P. Popov et al. *Cyclic behavior of three R.C. flexural members with high shear*. EERC 72-5. Berkeley, CA: Earthquake Engineering Research Center, University of California, 1972.

[8] V. V. Bertero et al. *Hysteretic behavior of reinforced concrete flexural members with special web reinforcement*. EERC 74-9. Berkeley, CA: Earthquake Engineering Research Center, University of California, 1974.

[9] M. Celebi and J. Penzien. *Experimental investigation into the seismic behavior of critical regions of reinforced concrete components as influenced by moment and shear*. EERC 73-4. Berkeley, CA: Earthquake Engineering Research Center, University of California, 1973.

[10] C. K. Nmai and D. Darwin. *Cyclic behavior of lightly reinforced concrete beams*. SM Report 12. Lawrence, KS: University of Kansas, 1984.

[11] C. F. Scribner and J. K. Wight. *Delaying shear strength decay in reinforced concrete flexural members under large load reversals*. UMEE 78R2. Ann Arbor, MI: University of Michigan, 1978.

[12] J. M. Ingham et al. "Influence of loading history on the response of a reinforced concrete beam". In: *Bulletin of the New Zealand Society for Earthquake Engineering* 34.2 (2001), pp. 107–124.

ted symmetric loading histories gave an inaccurate approximation of demands induced by real earthquake simulations. Failure was not reported in any of the applied earthquake loading history.

In more recent investigations of beam response, response of high-strength concrete has also been reported. Fang et al.[13] tested fifteen cantilever beam specimens constructed from high-strength concrete. Better displacement ductility and smaller strength degradation than normal-strength concrete beams was reported. Failure was governed by deterioration of shear resistance mechanism in concrete.

Tests on high-strength concrete beams in double-curvature configuration were reported by Xiao and Ma.[14] Stable flexural response was observed with more closely spaced cracks in high-strength beams. Higher transverse reinforcement content was found improve deformation capacity. Moment strength at capacity was found to exceed the strength calculated using to 0.3 % ultimate concrete strain. It was suggested to include the effects of reinforcement strain hardening and concrete confinement to accurately determine ultimate strength in high-strength concrete members. In another report on the same series of tests, Xiao et al.[15] reported test results of six beams with varying shear-span ratio and reinforcement content. Highly reinforced beams resulted in smaller ultimate drift capacities due to increased shear demand. Distribution of longitudinal reinforcement vertically along the depth was found to be an effective way to improve drift capacity in highly reinforced beams.

MORE recently, Panagiotou et al.[16] have reported tests on large scale cantilever beams with different transverse reinforcement spacing. Code defined minimum stirrup spacing was found to be insufficient to ensure ductile response at large deformations. Smaller stirrups spacing was suggested to deter buckling of rebars.

To and Moehle[17] tested two beams to investigate the performance of high strength reinforcement with different tensile to yield strength ratios (T/Y). Beam with higher T/Y was found to result in larger ultimate drift capacity due to larger spread of plasticity at the yielding section. Failure in both the cases was reported to be caused by buckling of rebars over several stirrup spacings.

Marder et al.[18] reported tests on seventeen similar beams subjected to various loading protocols. In additional conventional monotonic and cyclic loading protocols used to characterize beam response, prior dynamic loading cycles were implemented to simulate a damaged specimen state before application of quasi-static loading cycles. Response states were noted in terms of the first appearance of buckling of rebar and delamination of concrete cover. Degradation of concrete core and opening of hoops accompanied by large shear deformations were observed at failure.

This background survey was limited to beam specimens only. While large amounts of literature have also been reported on column response, study of beam sections only was deemed sufficient in the scope of this study.

[13] I.-K. Fang et al. "Cyclic behavior of high-strength concrete short beams with lower amount of flexural reinforcement". In: *ACI Structural Journal* 91.1 (1994), pp. 10–18. DOI: 10.14359/4477.

[14] Y. Xiao and R. Ma. "Seismic behavior of high strength concrete beams". In: *The Structural Design of Tall Buildings* 7.1 (1998), pp. 73–90. DOI: 10.1002/(SICI)1099-1794(199803)7:1<73::AID-TAL92>3.0.CO;2-A.

[15] Y. Xiao et al. "High-strength concrete short beams subjected to cyclic shear". In: *ACI Structural Journal* 96.3 (1999), pp. 392–399. DOI: 10.14359/673.

[16] M. Panagiotou et al. *Effect of hoop reinforcement spacing on the cyclic response of large reinforced concrete special moment frame beams*. PEER 2013/16. Pacific Earthquake Engineering Research Center, 2013.

[17] D. V. To and J. P. Moehle. "Seismic performance of beams with high-strength reinforcement". In: *Proceedings of the 16th World Conference on Earthquake Engineering*. 16th World Conference on Earthquake Engineering. Santiago, Chile, 2017.

[18] K. Marder et al. "Testing of seventeen identical ductile reinforced concrete beams with various loading protocols and boundary conditions". In: *Earthquake Spectra* 34.2 (2018). DOI: 10.1193/101717EQS215DP.

2.2   *Capacity models*

ESTIMATION of drift capacity in reinforced concrete members based on experimental observations is discussed in terms of the limit state considered. All existing estimation models may be divided into three categories based on the limit state considered and one additional group of models that empirically estimate capacity without any consideration of actual limit state. Unlike, the background study on experimental investigations, review on capacity models was expanded to include research on columns due lack of beam-only models.

2.2.1   *Concrete compression*

EARLIEST methods of estimating ultimate deformation capacity of reinforced concrete were based on crushing of concrete as the ultimate state. This was largely based on the observations of monotonic loading test. Mattock[19] proposed simple expression for ultimate compressive concrete strain in terms of span-to-depth ratio only based on the findings a testing program of thirty seven half scale beam specimens. Corley[20] further expanded this data set and suggested refined expressions on maximum compressive concrete strain in terms of span-to-depth ratio and concrete confinement. Confinement was expressed in terms transverse and compressive reinforcement content and yield strength.

Papia and Russo[21] proposed an interesting new estimation for maximum concrete compressive strain not based on experimental evidence but on theoretical limit state considering buckling of longitudinal reinforcement. Constitutive model or steel in inelastic compression was used in conjunction with lateral stiffness of hoops and to determine limiting strain in concrete. A calculation procedure was formulated in terms of rebar slenderness and hoop lateral stiffness to determine concrete strain. Proposed expressions were found to predict rotation capacity observed in monotonic tests of beams with reasonable accuracy.

Similar approach to quantify drift capacity limited by concrete compressive strain in flexure dominated columns was developed Inai and Hiraishi.[22] Cyclic response characteristics of concrete were also incorporated in the determination of ultimate curvatures possible for the maximum concrete compressive strain. Design equations were proposed to determine the lower bound drift capacity.

In more recent past, Grammatikou et al.[23] have proposed new estimates of maximum compressive concrete strain to evaluate ultimate state response characteristics using a large database of monotonic and cyclic tests. Experimentally observed drift capacities were related to analytical moment-curvature relationships of the specimen section to generate estimates of ultimate strain. Different strain estimates were given for cyclic and monotonic loading using parameters such as volumetric confinement ratio, concrete strength, number of longitudinal bars in compression zone and ratio of bar size to stirrup spacing.

[19] Mattock, op. cit.

[20] W. G. Corley. "Rotational capacity of reinforced concrete beams". In: *Journal of the Structural Division, ASCE* 92.5 (1966), pp. 121–146.

[21] M. Papia and G. Russo. "Compressive concrete strain at buckling of longitudinal reinforcement". In: *Journal of Structural Engineering, ASCE* 115.2 (1989), pp. 382–397.

[22] E. Inai and H. Hiraishi. "Design equations for deformation capacity of reinforced concrete columns failing in flexure". In: *AIJ Journal of Technology and Design* 9.18 (2003), pp. 109–114. DOI: `10.3130/aijt.9.109`.

[23] S. Grammatikou et al. "Ultimate strain criteria for RC members in monotonic or cyclic flexure". In: *Journal of Structural Engineering, ASCE* 142.9 (2016). DOI: `10.1061/(ASCE)ST.1943-541X.0001501`.

While application of concrete compression limit state to estimate drift capacity is relatively simple and has therefore attracted interest from the research community, lack of consideration to cyclic loading effect is one major drawback of this approach. It may be possible to accurately estimate monotonic drift capacity with this approach but since the detrimental effect of cyclic loading on ultimate state response has been shown through numerous experimental investigations, it would not be reasonable to apply this approach in seismic design.

2.2.2 *Shear strength deterioration*

ONE of the commonly reported observation in early experiments on reversed cyclic loading was formation of large inclined cracks and deterioration of core concrete at large deformations. Based on these observations, first model to define a new ultimate state for seismic design was introduced by the ATC 6 report.[24] A shear strength enve- lope was defined with an initial static shear strength that decreased linearly with increasing deformation. Ultimate state was determi- ned as the point where shear strength drops the level of shear force corresponding to flexural strength.

Following this approach, several researchers have proposed simi- lar relations assisted by experimental databases. Priestley et al.[25] used a database of columns failing in shear to suggest a relation for degrading concrete contribution to shear strength with increasing dis- placement ductility. No effect of any other design parameter such as transverse reinforcement content or shear span ratio was considered. Aschheim and Moehle[26] conducted a similar investigation using a database of bridge columns failing in shear. Again, shear resistance contributed by concrete was expressed as a function of displacement ductility. Transverse reinforcement content and strength were used as parameter in the proposed expressions. Later, Sezen and Moehle[27] used a large database of column experiments to investigate shear strength degradation at large deformations. Degradation coefficient was proposed to apply equally to both concrete and transverse reinfor- cement contributions to shear resistance. Aspect ratio and transverse reinforcement were used as determining parameters.

Ichinose[28] proposed another relation expressing the reduction of effective shear strength of concrete with increasing inelastic rotations in hinge region. Unlike purely empirical estimations reported above, degradation in shear strength at large deformations was expressed through change of inclinations of strut and tie components in an assumed strut-tie mode of shear resistance. Proposed shear strength expressions were validated through experimental data of columns failing in shear.

Another approach to theoretical determination of shear strength degradation characteristics was poposed by Martín-Pérez and Pan- tazopoulou[29] using modified compression field theory (MCFT) of shear deformation in two-dimensional cracked concrete. Influence of various cyclic loading parameters on concrete shear strength was

[24] See Section 8.4.1 on page 43 of Applied Technology Council. *Seismic design guidelines for highway bridges (ATC-6)*. Berkeley, CA, 1981.

[25] M. J. N. Priestley et al. "Sesimic shear strength of reinforced concrete co- lumns". In: *Journal of Structural Engineer- ing, ASCE* 120.8 (1994), pp. 2310–2329.

[26] M. Aschheim and J. P. Moehle. *Shear strength and deformability of RC bridge co- lumns subjected to inelastic cyclic displa- cements*. EERC 92/04. Berkeley, CA: Earthquake Engineering Research Cen- ter, University of California, 1992.

[27] H. Sezen and J. P. Moehle. "Shear strength model for lightly reinforced concrete columns". In: *Journal of Struc- tural Engineering, ASCE* 130.11 (2004), pp. 1692–1703. DOI: 10.1061/(ASCE) 0733-9445(2004)130:11(1692).

[28] T. Ichinose. "A shear design equation for ductile RC members". In: *Earthquake Engineering & Structural Dynamics* 21.3 (1992), pp. 197–214. DOI: 10.1002/eqe. 4290210302.

[29] B. Martín-Pérez and S. J. Pantazopou- lou. "Mechanics of concrete participa- tion in cyclic shear resistance of RC". in: *Journal of Structural Engineering, ASCE* 124.6 (1998), pp. 633–641. DOI: 10.1061/ (ASCE)0733-9445(1998)124:6(633).

demonstrated through analytical simulations of the model. A design expression for concrete shear strength in terms of using only transverse reinforcement content as a parameter was derived using the model. Comparison with other models resulted in the conclusion that the proposed analytical model yields estimates very similar to Aschheim and Moehle's model.

While the aforementioned degradation models were developed with the objective of determining strength at given deformation demand, it was common to use them the other way round and estimate the deformation capacity at which sufficient degradation in strength was observed. Elwood and Moehle[30] demonstrated for the first time the inherent inaccuracies associated with such applications due to the variability present in approximate empirical expressions. Consequently, they proposed a specific drift capacity model was propsed using a database of columns failing in shear. Transverse reinforcement ratio and concrete strength were used as parameters in model definition. The model was stated to be particularly applicable to columns with low transverse reinforcement ratios due to the nature of the database considered.

UNLIKE previous approaches where cyclic loading was considered in only a general sense, Pujol et al.[31] proposed a numerical model to directly estimate drift capacity as function of the number of applied loading cycles. Increase in shear deformations with cycling was related to loss of stiffness and strength. Approximate expressions based on experimental data were determined to estimate number of cycles before loss of strength at given drift level.

Lee and Watanabe[32] discussed a different approach to shear deterioration determined drift capacity by representing concrete deformations using compatibility aided truss models. Shear force in the model was corresponded to development of axial strain in hinge region of beams and strength was deteriorated with the accumulation of axial strains. Experiments conducted on beams in double curvature showed reasonable agreement with the proposed model.

Park et al.[33] suggested another model for shear strength degradation by representing shear resistance of concrete to be limited to the compression zone of concrete. Degradation in strength was expressed as a function of increasing curvature and subsequntly decreasing compression zone. Deformation capacity thus determined was verified against an extensive dataset of column subjected to cyclic loadings. While columns failing in shear were predicted with reasonable accuracy, other failure modes such as bar nuckling or bar fracture were not adequately captured by the model.

Another approach to shear strength degradation was proposed by Colajanni et al.[34] using a static interaction of axial force, bending moment and shear force. Numerical analyses were conducted to evaluate the inclination of stress fields and corrsponding internal forces to the applied external deformation. Simplified curves were generated relating ratio of transverse reinforcement to the rate of

[30] K. J. Elwood and J. P. Moehle. "Drift capacity of reinforced concrete columns with light transverse reinforcement". In: *Earthquake Spectra* 21.1 (2005), pp. 71–89. DOI: 10.1193/1.1849774.

[31] S. Pujol et al. "Displacement history effects on drift capacity of reinforced concrete columns". In: *ACI Structural Journal* 103.2 (2006), pp. 253–262. DOI: 10.14359/15183.

[32] J.-Y. Lee and F. Watanabe. "Shear deterioration of reinforced concrete beams subjected to reversed cyclic loading". In: *ACI Structural Journal* 100.4 (2003), pp. 480–489. DOI: 10.14359/12657.

[33] H.-G. Park et al. "Shear-strength degradation model for RC columns subjected to cyclic loading". In: *Engineering Structures* 34 (2012), pp. 187–197. DOI: 10.1016/j.engstruct.2011.08.041.

[34] P. Colajanni et al. "Shear strength degradation due to flexural ductility demand in circular RC columns". In: *Bulletin of Earthquake Engineering* 13.6 (2015), pp. 1795–1807. DOI: 10.1007/s10518-014-9691-0.

degradation of ductility demand. However, no verfications were performed with experimental data and neither was the effect of cyclic loading appropriately incorporated.

Estimation based on shear degradation models represents a definite upgrade over the monotonic capacity estimation. General effect of cyclic loading is appropriately accounted for and primary parameters observed to influence response in experiments are also explained through the model. Accurate capacity estimation through such models, however, remains due to problems related with accurate estimation of shear strength itself.

2.2.3 *Reinforcement buckling*

INSTABILITY of laongitudinal reinforcement at ultimate state was often reported in experimental investigations on reversed cyclic loading. Inspired by such observations, Scribner[35] first discussed the rebar buckling in limiting the deformation capacity. Simple relations using the lateral stiffness provided by the ties were formulated to determine the critical bar diameter and stirrup spacing ratio for which buckling might occur. Experimental findings were reported to show evidence of the proposed mechanism with some limitations.

More comprehensive consideration of bar buckling was discussed by Pantazopoulou.[36] Mechanical model of buckled bar over variable tie spacings was considered to evaluate all possible defelcted shapes. Relations between limiting strain in ties and rebars were established by enforcing equilibrium requirements and material strength limits. Vast database of column experiemnts was then utilized to develop empirical requirements for stability of reinforcement. Finally, approximate expressions for ductility at bar buckling in terms of stirrup spacing to rebar diameter ratio and shear-span ratio were also suggested.

Moyer and Kowalsky[37] further discussed the buckling phenomenon in the context of reverse cyclic loading. Mechanism of buckling was described in terms of alternate tension and compression loading cycles and cyclic hysteretic behavior of steel. Development of tension strain was illustrated to be significant in causing ultimate buckling of rebars. Two columns were tested different loading histories to demonstrate the proposed mechanism. Growth and subsequent accumulation of tension strain longitudinal reinforcements was identified as the main cause of buckling. Simple expressions were proposed to determine specimen curvature at the initiation of buckling in terms of longitudinal reinforcement ratio, transverse reinforcement ratio and rebar diameter.

Berry and Eberhard[38] used a large database of column experiemnts to propose simple expressions for directly estimating drift at the initiation of bar buckling in columns dominated by flexure. Defining parameters included shear-span ration, transverse reinforcement ratio, trasnverse reinforcement strength and bar diameter. Intermediate variation of the order of 25 % was reported in the approximate expres-

[35] C. F. Scribner. "Reinforcement buckling in reinforced concrete flexural members". In: *ACI Structural Journal* 83.6 (1986), pp. 966–973. DOI: 10.14359/2648.

[36] S. J. Pantazopoulou. "Detailing for reinforcement stability in RC members". In: *Journal of Structural Engineering, ASCE* 124.6 (1998), pp. 623–632. DOI: 10.1061/(ASCE)0733-9445(1998)124:6(623).

[37] M. J. Moyer and M. J. Kowalsky. "Influence of tension strain on buckling of reinforcement in concrete columns". In: *ACI Structural Journal* 100.1 (2003), pp. 75–85. DOI: 10.14359/12441.

[38] M. P. Berry and M. O. Eberhard. "Practical performance model for bar buckling". In: *Journal of Structural Engineering, ASCE* 131.7 (2005), pp. 1060–1070. DOI: 10.1061/(asce)0733-9445(2005)131:7(1060).

sion.

Evaluation of rebar buckling in reinforced concrete elements through direct modeling of became possible with constitutive material models for steel including the effect of bar buckling. Models by Dhakal and Maekawa[39] and Bae et al.[40] represent two such recent investigations. Bae et al. established rebar model through extensive testing of rebar specimens in compression buckling. Developed model was demonstrated to improve the estimation of ultimate state response in column experiments controlled by buckling. Dhakal and Maekawa's model improved on existing constitutive models for steel reinforcement by incorporating a theoretically defined tension envelope and non-linear buckling defined compression envelope. A new parameter expressed as rebar length to size and square root of yield strength ratio was used to control compression behavior.

While estimation of buckling through refined mechanical models has proved to be promising, reflection on experiment results remains an issue. Experimental observations frequently report buckling on visual evidence only once the cover has spalled. It is therefore difficult to directly relate the initiation of mechanically defined bar buckling with loss of strength at large deformations.

2.2.4   Empirical estimation

ONE or the other limit state was assumed in the previous discussion to define the ultimate drift capacity. Final category of drift estimation models consist of purely empirical equations derived from experimental data without any consideration to limit state at failure.

Panagiotakos and Fardis[41] used a database of more than a thousand tests on various configurations of RC members to propose expressions for estimating drift at capacity defined by a drop of strength after reaching a peak. Separate expressions were proposed for monotonic and cyclic loadings using shear-span ratio, concrete strength, confinement effectiveness factor and rebar slip coefficient as parameters. While the estimations were generally around the median mark, large scatter of the order of 60 % were reported.

In a similar investigation, Brachmann et al.[42] used a smaller dataset of about two hundred column tests to predict drift capacity of columns. Confining effect of transverse reinforcements was considered as the primary parameter. Minimum transverse reinforcement content required to achieve a given drift ratio for columns in highly seismic regions were proposed. Drift ratio was expressed in a parabolic relation with transverse reinforcement content implying the decreasing effectiveness of confining with increasing transverse reinforcement. Variation of up to 50 % was reported for the proposed empirical expression.

Sasani[43] discussed another approach to estimate drift capacity using experiment data through Bayesian parameter estimation technique. Parameters influencing drift capacity were first and drift was expressed in parametric terms using a simple cantilever model. Pro-

[39] R. P. Dhakal and K. Maekawa. "Path-dependent cyclic stress–strain relationship of reinforcing bar including buckling". In: *Engineering Structures* 24.11 (2002), pp. 1383–1396. DOI: 10.1016/S0141-0296(02)00080-9.

[40] S. Bae et al. "Inelastic buckling of reinforcing bars". In: *Journal of Structural Engineering, ASCE* 131.2 (2005), pp. 314–321. DOI: 10.1061/(ASCE)0733-9445(2005)131:2(314).

[41] T. B. Panagiotakos and M. N. Fardis. "Deformations of reinforced concrete members at yielding and ultimate". In: *ACI Structural Journal* 98.2 (2001), pp. 135–148. DOI: 10.14359/10181.

[42] I. Brachmann et al. "Drift-dependent confinement requirements for reinforced concrete columns under cyclic loading". In: *ACI Structural Journal* 101.5 (2004), pp. 669–677. DOI: 10.14359/13389.

[43] M. Sasani. "Life-safety and near-collapse capacity models for seismic shear behavior of reinforced concrete columns". In: *ACI Structural Journal* 104.1 (2007), p. 30. DOI: 10.14359/18430.

babilistic distribution of each parameter was identified by examining a database of column experiments and drift capacity was thus expressed probabilistic terms. Mean drift capacities at both life safety and near collapse levels were expressed from the probabilistic model. Transverse reinforcement content and shear-span ratio were the only considered parameters. Variation of the order of 25 % were reported around the proposed mean estimates.

Haselton et al.[44] expanded this approach to uniformly estimate all parameters related with cyclic loading response of RC elements. Observed experiment response was simulated through a strength and stiffness degradation enabled hysteresis model. Respective model parameters were determined by calibrating simulated response against experimentally observed response of more than two hundred and fifty column tests. Evaluated quantities initial stiffness, yield rotation, ultimate strength, plastic rotation capacity and cyclic deterioration parameter. Rotation capacity was determined in terms of steel and concrete material strengths, a confinement effectiveness factor, a rebar buckling coefficient and rebar slip indicator. Variation of the order of 60 % was reported for the proposed drift capacity estimation. Applicability of the proposed expressions at ultimate state was noted to be limited due to lack of experimental data with post drift limit response.

While the empirical estimation schemes prove successful in capturing the general effect of parameters affecting ultimate state response and result in good mean response estimation, inaccuracies associated with empirical relations having large variability make it unsuitable for application in the modern design framework. Application is also limited by the range of considered datasets.

[44] C. B. Haselton et al. *Beam-column element model calibrated for predicting flexural response leading to global collapse of RC frame buildings*. PEER 2007/03. Pacific Earthquake Engineering Research Center, 2008.

3
Experiment

A large experimental program was conducted to observe and investigate the response at ultimate state.

3.1 *Specimen design*

Beam specimens were designed as cantilevers representing the framed end of girders in typical special moment frames at approximately one-third scale. A total of nineteen beam specimens were constructed and tested in three different phases.

3.1.1 *Parameter selection*

Since one of the primary objectives of the research was to investigate the mechanism at ultimate deformation state, specimens were designed considering numerous parametric variations to enable effective study of limit state behavior. Parameters were selected based on the observations from the review of past experimental investigations and drift prediction models models as discussed in the previous chapter.

Concrete compressive strength (f'_c) was selected as an experiment parameter to evaluate the validity of shear-strength deterioration models. Higher strength concrete is expected to have shear strength and thus delay the mechanism leading to loss of resistance at ultimate deformation capacity.

The most commonly reported parameter effecting deformation capacity in RC members is *Transverse reinforcement ratio (ρ_t)*. Transverse reinforcement is associated with drift capacity in a number of mechanism models. It contributes to the member shear strength, provides confinement to the core concrete, and ensures greater lateral stability of the longitudinal reinforcement.

Transverse reinforcement yield strength (f_{yt}), *Longitudinal reinforcement ratio (ρ)*, *Shear-span ratio (l/D)* were selected as parameters to verify the shear-strength deterioration mechanism as all these parameters contribute to the member shear strength in one way or the other.

Bar diameter (d_b) was expected to influence the buckling performance of the specimens and thus effect ultimate drift capacity as implied by the bar-buckling approach.
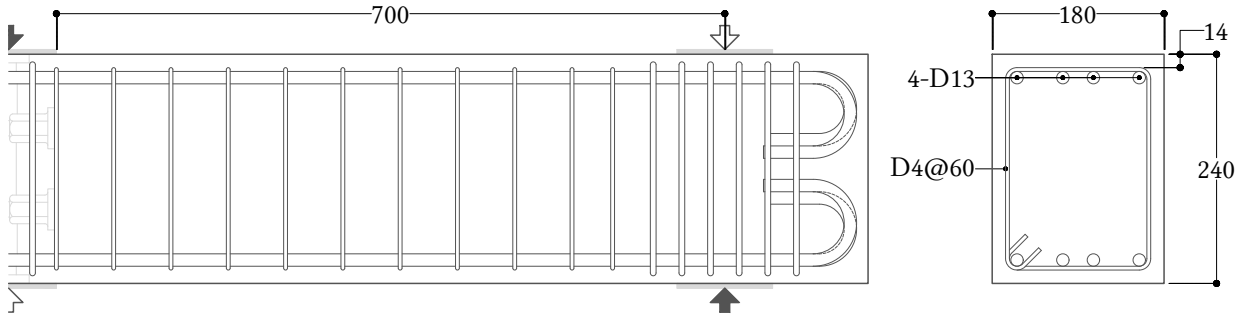
Figure 3.1: SB01 reinforcement details (all dimensions are in mm)

3.1.2 Section details

Specimens were designed in three different phases SA, SB, and SC. All sections were uniformly 180 mm × 240 mm in size. SB01 was provided with equal longitudinal reinforcement in the form of 4-D13 bars on both faces bound with equally spaced transverse reinforcement consisting of two-legged D4 bars with 135° hooks. No intermediate ties were however provided. Loading was carried out to induce cantilever response over a span of 700 mm. Reinforcement layout and section details for SB01 are illustrated in Figure 3.1.

Specimen SB01 was designated as the control specimen and all other specimens were designed as parametric variations from the base design. Distribution of parameters among various specimen designs is illustrated in the specimen matrix of Figure 3.2 and detailed specifications of respective specimens are listed in Table 3.1. Specimens of the SA series were designed with a different bar diameter (d_b). 2-D16 bars and 5-D10 bars were respectively used in specimens SA1 and SA3 resulting in very similar total reinforcement areas.

A total of twelve specimens from SB and SC series were casted in high-strength concrete with target compressive strength of about 60 MPa while all other specimens had normal strength concrete with target compressive strength of about 30 MPa. Among these, four specimens of SB series were reinforced with additional 2-D13 bars in a second layer of reinforcement.

Five specimens from SB and SC series were loaded at longer loading spans (l) to investigate the effect of span-to-depth ratio (l/D) on beam response. Two variations, 1000 mm and 1300 mm, were designed to compare response in contrast to 700 mm loading span of the control specimen.

Transverse reinforcement content (ρ_t) was the altered parameter in another ten specimens. Six specimens of SB series consisted of the same two-legged stirrups as in SB01 but were placed at half the spacing. Two specimens from SC series were designed with additional two legs of stirrups while another two specimens consisted of even greater reinforcement content in the form D6 stirrups instead of the D4 ones. Among these, three SB series specimens consisted of high strength transverse reinforcement.

Figure 3.2: Parameter distribution

f_c' : **30** | **60** MPa
  Target strength of casting batch

ρ : **1.29** | **1.94** %
  4 | **6** - D13 bars

ρ_t : **0.26** | **0.52** | **1.04** | **2.34** %
  2 | **4** - **D4** | **D6** @ **60** | **30** mm

f_{yt} : **365** | **824** MPa
  SD295 | **S45C** grade stirrups

l/D : **2.91** | **4.16** | **5.41**
  700 | **1000** | **1300** mm loading span (l)

d_b : **15.9** | **9.5** mm
  D16 | **D10** bars
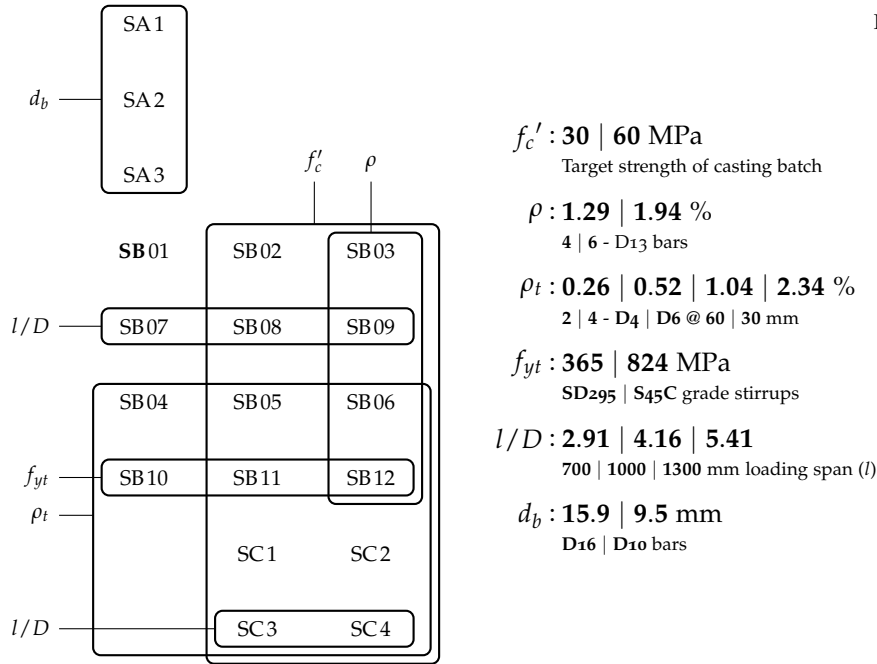
Table 3.1: Specimen specifications

	Concrete	Long. reinf.	ρ(%)	Trans. reinf.	ρ_t(%)	l(mm)	l/D
SA1	M30	2-D16	1.04	2-D6 @ 65	0.56	700	2.91
SA2	M30	2-D16	1.04	2-D6 @ 65	0.56	700	2.91
SA3	M30	5-D10	1.02	2-D6 @ 65	0.58	700	2.91
SB01	M30	4-D13	1.29	2-D4 @ 60	0.26	700	2.91
SB02	M60	4-D13	1.29	2-D4 @ 60	0.26	700	2.91
SB03	M60	6-D13	1.94	2-D4 @ 60	0.26	700	2.91
SB04	M30	4-D13	1.29	2-D4 @ 30	0.52	700	2.91
SB05	M60	4-D13	1.29	2-D4 @ 30	0.52	700	2.91
SB06	M60	6-D13	1.94	2-D4 @ 30	0.52	700	2.91
SB07	M30	4-D13	1.29	2-D4 @ 60	0.26	1000	4.16
SB08	M60	4-D13	1.29	2-D4 @ 60	0.26	1000	4.16
SB09	M60	6-D13	1.94	2-D4 @ 60	0.26	1000	4.16
SB10	M30	4-D13	1.29	2-ϕ4 @ 30	0.52	700	2.91
SB11	M60	4-D13	1.29	2-ϕ4 @ 30	0.52	700	2.91
SB12	M60	6-D13	1.94	2-ϕ4 @ 30	0.52	700	2.91
SC1	M60	4-D13	1.29	4-D4 @ 30	1.04	700	2.91
SC2	M60	4-D13	1.29	4-D6 @ 30	2.34	700	2.91
SC3	M60	4-D13	1.29	4-D4 @ 30	1.04	1300	5.41
SC4	M60	4-D13	1.29	4-D6 @ 30	2.34	1300	5.41

Reinforcement details in the section and elevation views are illustrated for few typical specimens in Figure 3.3. All other specimens follow similar details and a complete set of specimen drawings and details is attached in Appendix A[1].

[1] See page 123.

3.1.3   Construction

All specimens were assembled and casted at the specimen construction facility of Assis K.K.[2] in Ibaraki prefecture. Reinforcement bars were cut and bent in required shapes as per the detailed drawings before instrumenting with strain gauges in predetermined locations[3]. All bars were assembled according to the drawings to form a reinforcement cage and secured in position through extensive use of binding wires. Assembled reinforcement cages were placed in epoxy coated wooden formworks and held in position through spacers for concrete pouring.

[2] https://www.asiss.co.jp

[3] Strain gauge placement positions discussed in Section 3.3.3.

Concrete mix with desired proportions was obtained from ready-mix concrete supplier Kohata Building Materials K.K. located in Chiba prefecture. Pouring was carried out over four phases covering all specimens of SA, SB, and SC series. Two batches each of normal-strength concrete and high-strength concrete were poured as indicated in Table 3.2. Ten cylinders per specimen were also poured at the same time as the specimen pouring for later measurement of concrete strength. Further ten cylinders were poured at each casting phase to measure concrete properties at 28-days after casting.

	Notation	Casting date
SA normal-strength	Batch-1	2017-02-18
SB normal-strength	Batch-2	2017-08-10
SB high-strength	Batch-3	2017-08-19
SC high-strength	Batch-4	2018-02-16

Table 3.2: Concrete casting phases

After curing for a week, formwork was removed and specimens were transported to the testing facility at University of Tokyo (Engineering Building 11, B2F) where they were stored for experiments later.

3.1.4   Material properties

Reinforcement grade SD345 conforming to JIS G 3112 specifications[4] was used for all longitudinal bars D10, D13, and D16. Lower strength grade SD295A, also conforming to JIS G 3112 specifications was used for stirrup bars D4 and D6 while high-strength stirrups ϕ4 were made from S45C grade steel conforming to JIS G 4051 specifications.[5]

[4] Japanese Standards Association. *Steel bars for concrete reinforcement (JIS G 3112:2010)*. Tokyo, Japan, 2010.

[5] Japanese Standards Association. *Carbon steels for machine structural use (JIS G 4051:2016)*. Tokyo, Japan, 2016.

Material characteristics for all reinforcement bars were estimated by tensile testing of five samples of each bar. Strain gauges YFLA-2 with 2 mm gauge length and large strain measurement range were attached to longitudinal reinforcement bars while small gauge width strain gauges FLK-2 were used for strain measurement in small diameter stirrup bars. Tensile loading and load measurement was performed
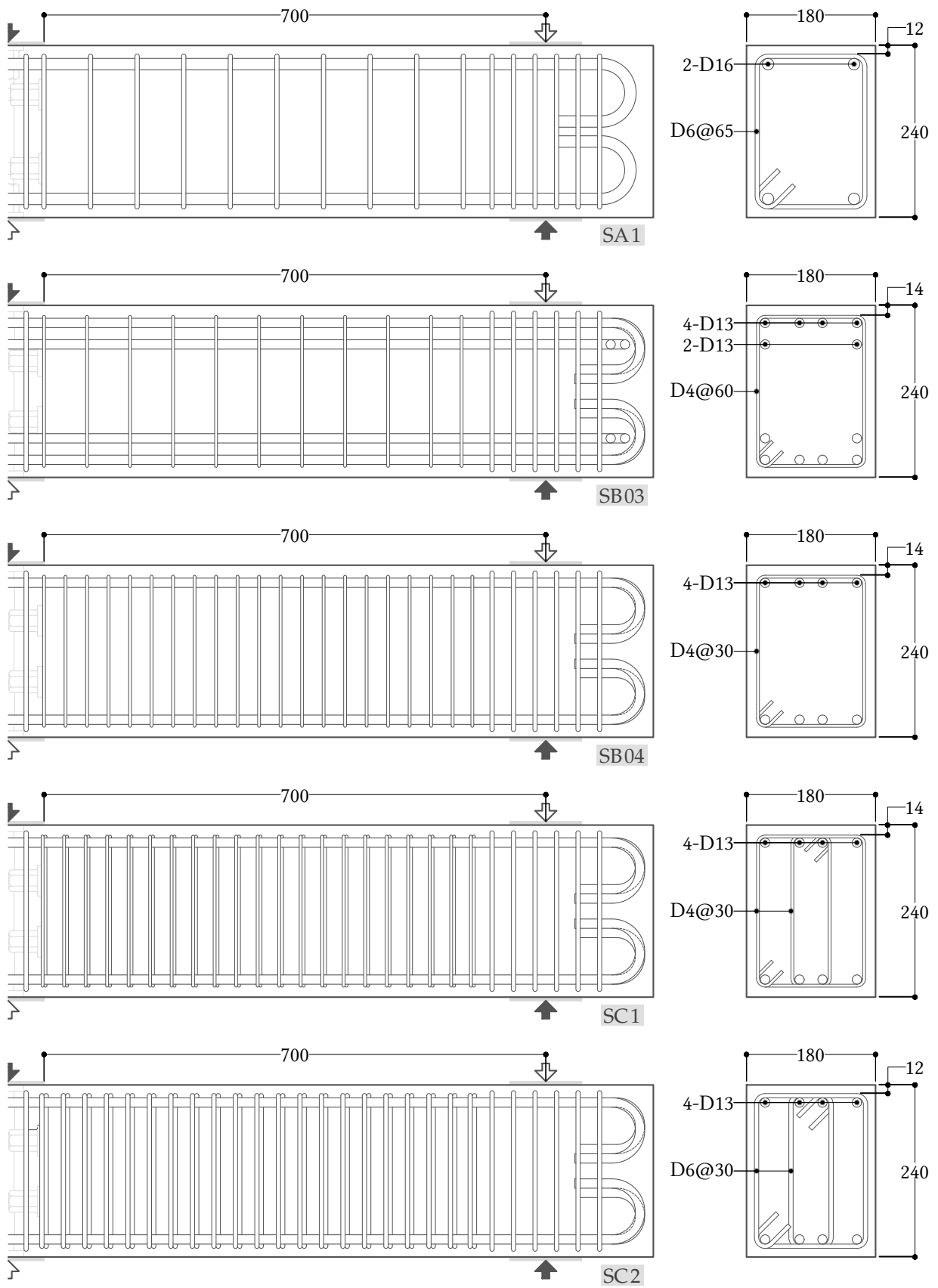
Figure 3.3: Specimen reinforcement details (all dimensions are in mm)

using Tokyo Koki K.K. manufactured UTM machine. Average stress-strain curves thus obtained for each reinforcement type are illustrated in Figure 3.4 and material characteristics thus calculated are listed in Table 3.3. Measurements for all individual bars and corresponding calculations are included in Appendix B[6] for reference.

[6] See page 165.
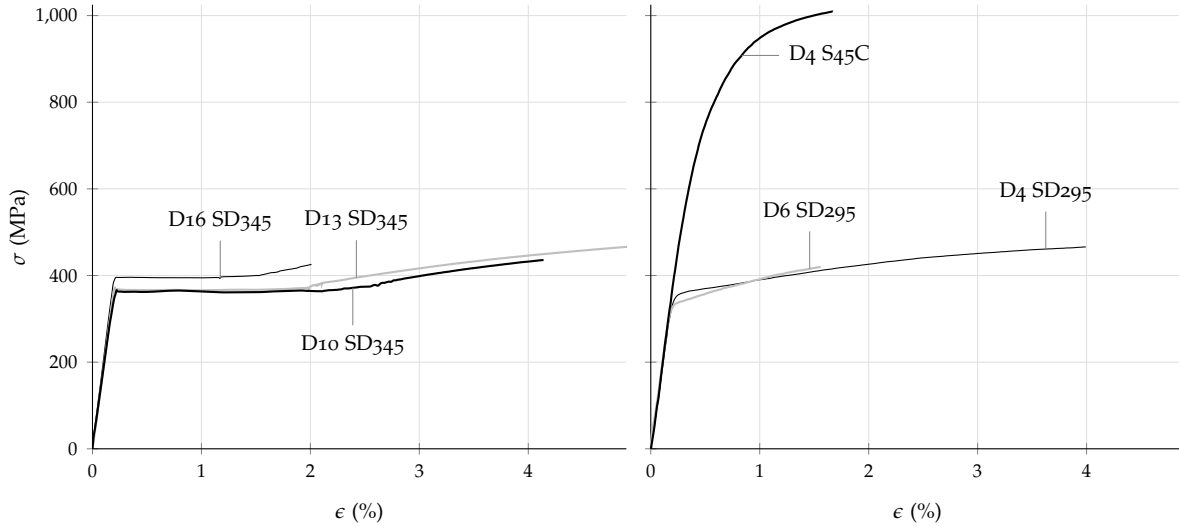
Figure 3.4: Average reinforcement bar stress-strain characteristics

Table 3.3: Average reinforcement properties

	f_y (MPa)	ϵ_y (%)	E_s (GPa)	f_u (MPa)	ϵ_u (%)
SD345 D16	396	0.21	197	578	20
SD345 D13	372	0.21	188	546	25
SD345 D10	365	0.22	181	539	23
SD295A D6	348	0.39	180	520	32
SD295A D4	365	0.40	182	503	28
S45C φ4	824	0.63	193	1061	21

Concrete mix design for all four casting batches is expressed in Table 3.4 based on the specification sheet provided by the supplier except slump and air content which are based on actual measurements taken prior to concrete pouring.

Table 3.4: Concrete mix properties

	Batch 1	Batch 2	Batch 3	Batch 4
Target strength (MPa)	19.5	24	50	50
Largest aggregate size (mm)	13	13	13	13
Slump/Flow (cm)	17.5	17	54	51
Cement (kg/m^3)	301	320	488	488
Water (kg/m^3)	193	190	185	185
Fine aggregate (kg/m^3)	876	873	791	791
Coarse aggregate (kg/m^3)	859	856	853	853
Admixtures (kg/m^3)	3.01	3.52	7.81	7.81
Air (%)	4.4	3.2	3.3	3.5
W/C ratio (%)	64.2	59.4	37.9	37.9

Concrete material characteristics were estimated through compres-

sion and tension-split testing of standard $100\,\text{mm} \times 200\,\text{mm}$ cylinders. Five test pieces were used for either tests on the day of specimen loading and at 28-days from concrete casting. Compression tests were carried out on high stiffness compression testing machine manufactured by Shimadzu K.K. and tension split tests were conducted on the same UTM used for reinforcement tension tests. Strain measurements for compression tests were taken using compressometers with $100\,\text{mm}$ gauge length while only peak strength was noted for tension split tests.

Average stress strain curves for compressive tests performed on each day are illustrated in Figure 3.5. Although average compressive strength obtained from these tests could be directly used as expected concrete strength for the beam specimen, a different procedure was used as expressed in Figure 3.6. Compressive strengths obtained from cylinder tests throughout the experiment duration were used to derive an approximate concrete strength-specimen age relation through simple linear regression. Separate strength-age relations were used for each casting batch.
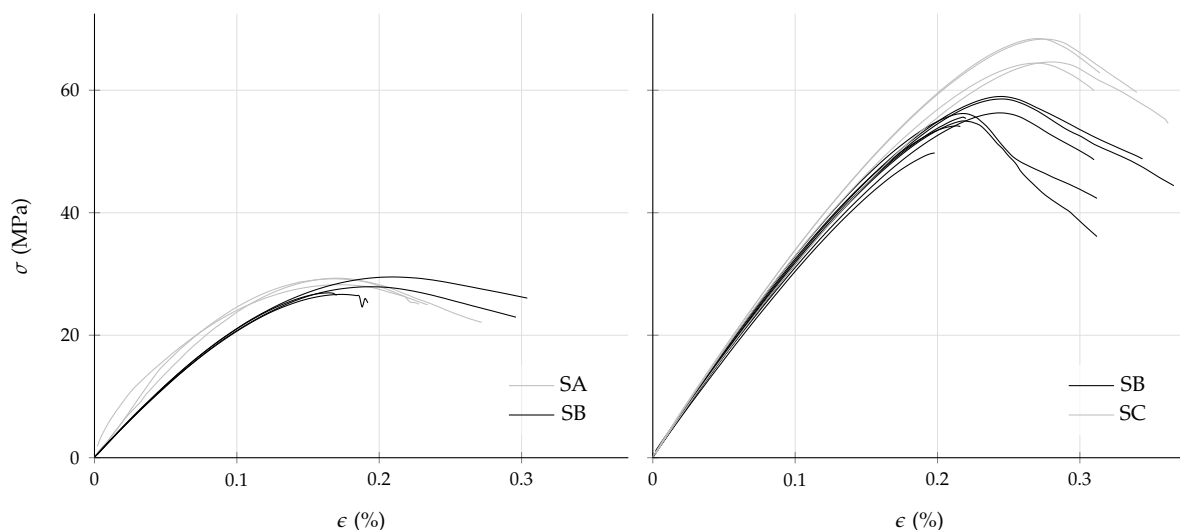
Figure 3.5: Average concrete stress-strain characteristics

Elastic modulus for concrete (E_c) was also calculated for each cylinder test as expressed in Figure 3.7 against corresponding compressive strengths (f'_c). Again, although the observed data has large scatter, relation recommended by Martinez et al.[7] for high-strength and by the ACI 318-14 code[8] for normal-strength concrete are found to be good approximations.

Tensile strength values calculated from split tension test of concrete cylinders are similarly expressed against concrete compressive strength in Figure 3.8. The relation recommended by Carrasquillo et al.[9] is used an approximation for both high-strength and normal-strength concrete.

Finally, above discussed concrete properties were calculated for each specimen based on age since casting and appropriate approximation equations and are listed in Table 3.5. Corresponding calculations and individual specimen test results are included in Appendix B[10]

[7] S. Martinez et al. "Spirally reinforced high-strength concrete columns". In: *ACI Structural Journal* 81.5 (1984), pp. 431–442. DOI: 10.14359/10693.

[8] Equation 19.2.2.1.b in American Concrete Institute. *Building code requirements for structural concrete (ACI 318-14)*. Farmington Hills, MI, 2014. ISBN: 978-1-942727-11-8.

[9] R. L. Carrasquillo et al. "Properties of high strength concrete subject to short-term loads". In: *ACI Structural Journal* 78.3 (1981), pp. 171–178. DOI: 10.14359/6914.

[10] See page 165.
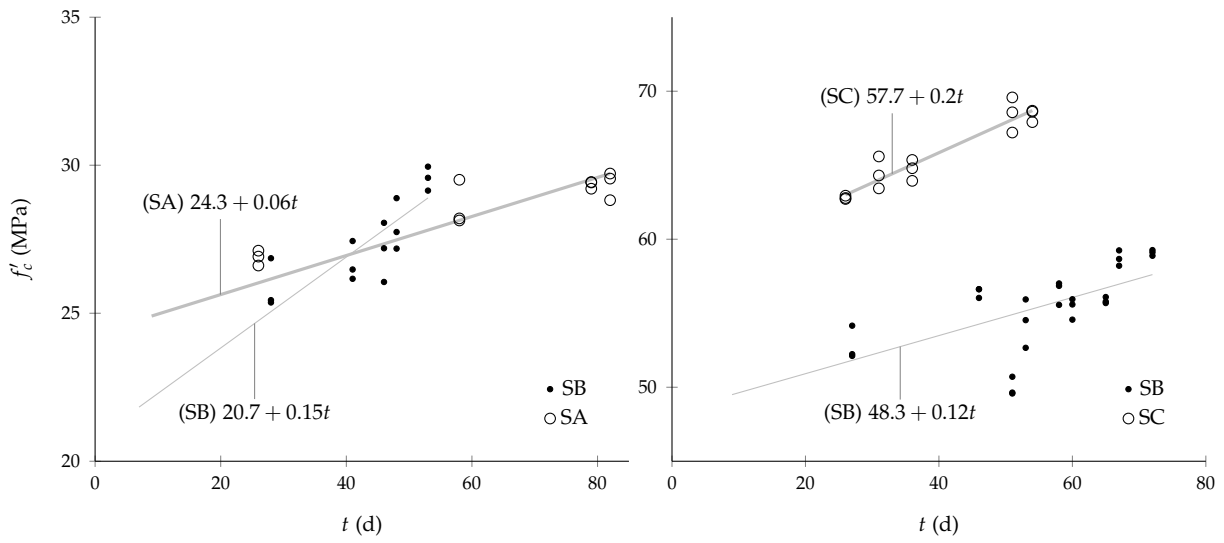
Figure 3.6: Concrete strength history over the experiment duration
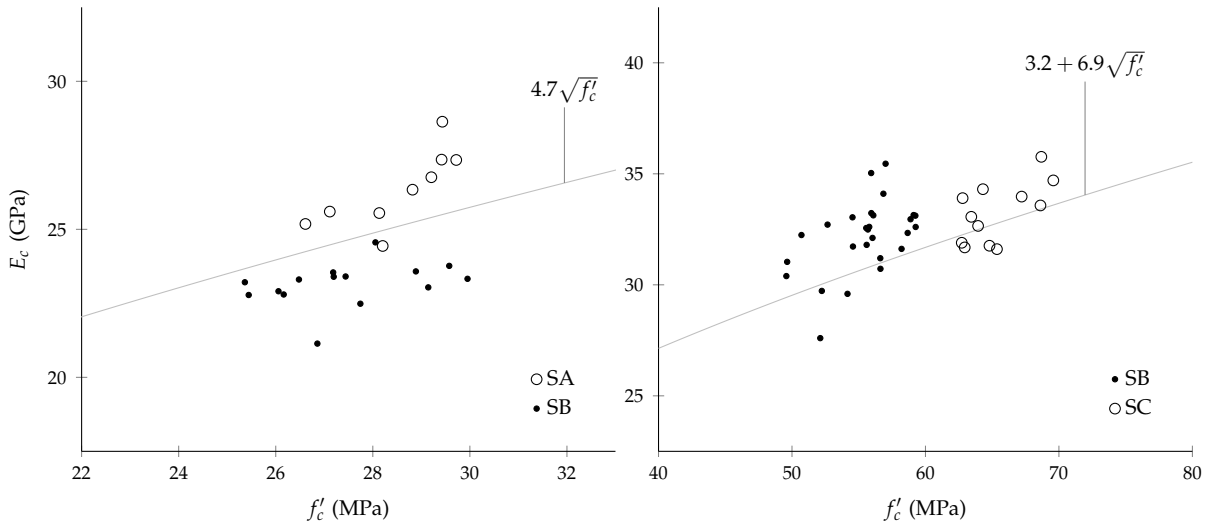
Figure 3.7: Concrete modulus of elasticity and compressive strength relation
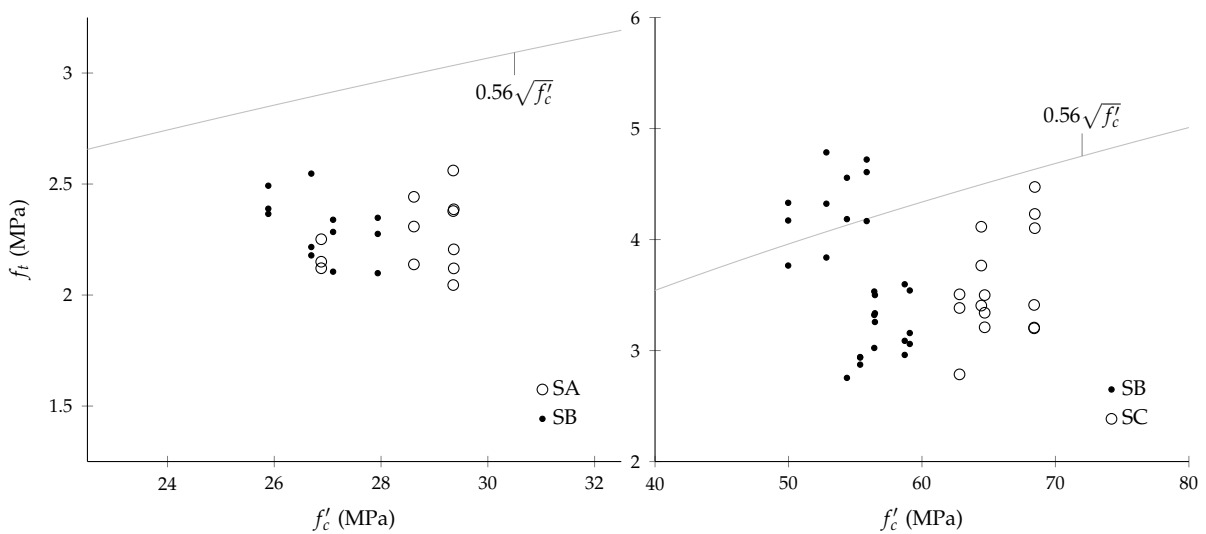
Figure 3.8: Concrete splitting tensile strength and compressive strength relation

for reference.

	Age (d)	f_c' (MPa)	E_c (GPa)	f_t (MPa)
SA1	58	28.1	24.9	3.1
SA2	79	29.5	25.5	3.2
SA3	82	29.7	25.6	3.2
SB01	41	27.1	24.4	3.1
SB02	46	54.3	30.5	4.3
SB03	51	54.9	30.6	4.4
SB04	46	27.8	24.8	3.1
SB05	53	55.2	30.7	4.4
SB06	58	55.8	30.8	4.4
SB07	48	28.1	24.9	3.1
SB08	67	57.0	31.1	4.5
SB09	72	57.6	31.2	4.5
SB10	53	28.9	25.3	3.2
SB11	60	56.1	30.9	4.4
SB12	65	56.7	31.0	4.4
SC1	31	64.0	32.5	4.7
SC2	36	65.0	32.7	4.8
SC3	51	68.1	33.3	4.9
SC4	54	68.7	33.4	4.9

Table 3.5: Estimated concrete properties at the time of specimen test

3.2   Loading setup

ALL beam specimens were tested with similar loading procedures to simulate the response of a typical building frame member during an earthquake shaking. To this end, loading setup was designed to induce alternate cycles of increasing load in a three-point loading pattern as indicated in Figure 3.9. Desired loadings were applied at the end of a four-pin pantograph frame through a hydraulic jack set against a strong reaction frame. Beam specimen was placed in vertical configuration and the bottom stub portion was locked against deformation by connecting to short reaction stubs on either side. Specimen loading tip was connected to two parallel legs of the pantograph to induce cantilevered loading in the upper portion of the specimen.

Alternate positive and negative loading cycles were applied by pushing or pulling the pantograph from the initial state. Prestressing steel rods connected to either sides of the specimen tip to transfer the applied frame deformation by alternately pulling the specimen with the frame. Steel rods were connected to specimen and loading frame through rectangular attachments to ensure uniform load transfer across the specimen width and minimize torsion. Spherical washers were used at each connection to ensure horizontal load transfer through the steel rods even when the frame and specimen are pushed to large inclinations.

Force distribution in the three point loaded specimen is illustrated

Figure 3.9: Loading setup

$b = 500\,\mathrm{mm}$ $a = l + 50\,\mathrm{mm}$

$F(a+b)/b$

Fa/b F

$V = F$

$M = Fl$
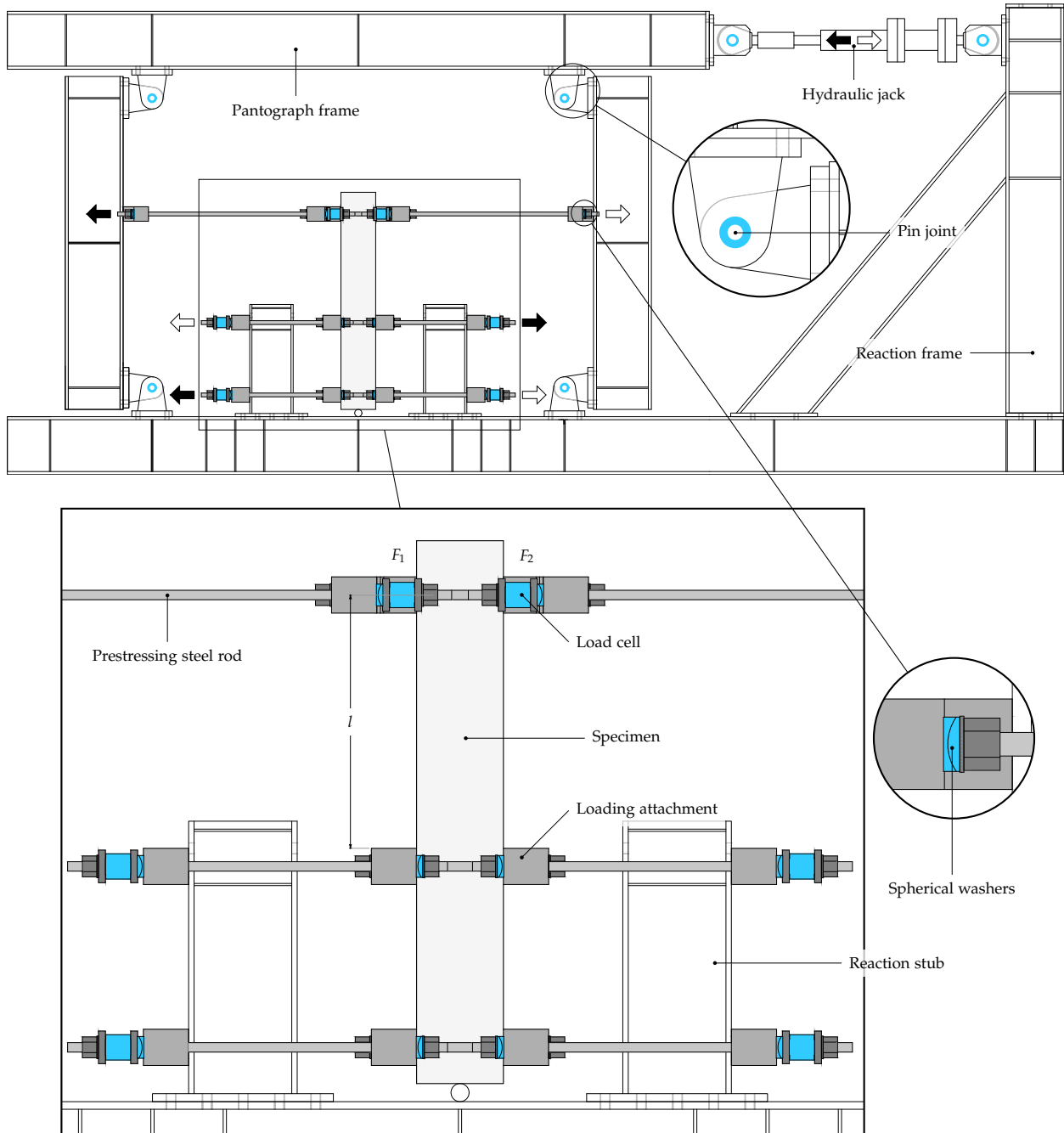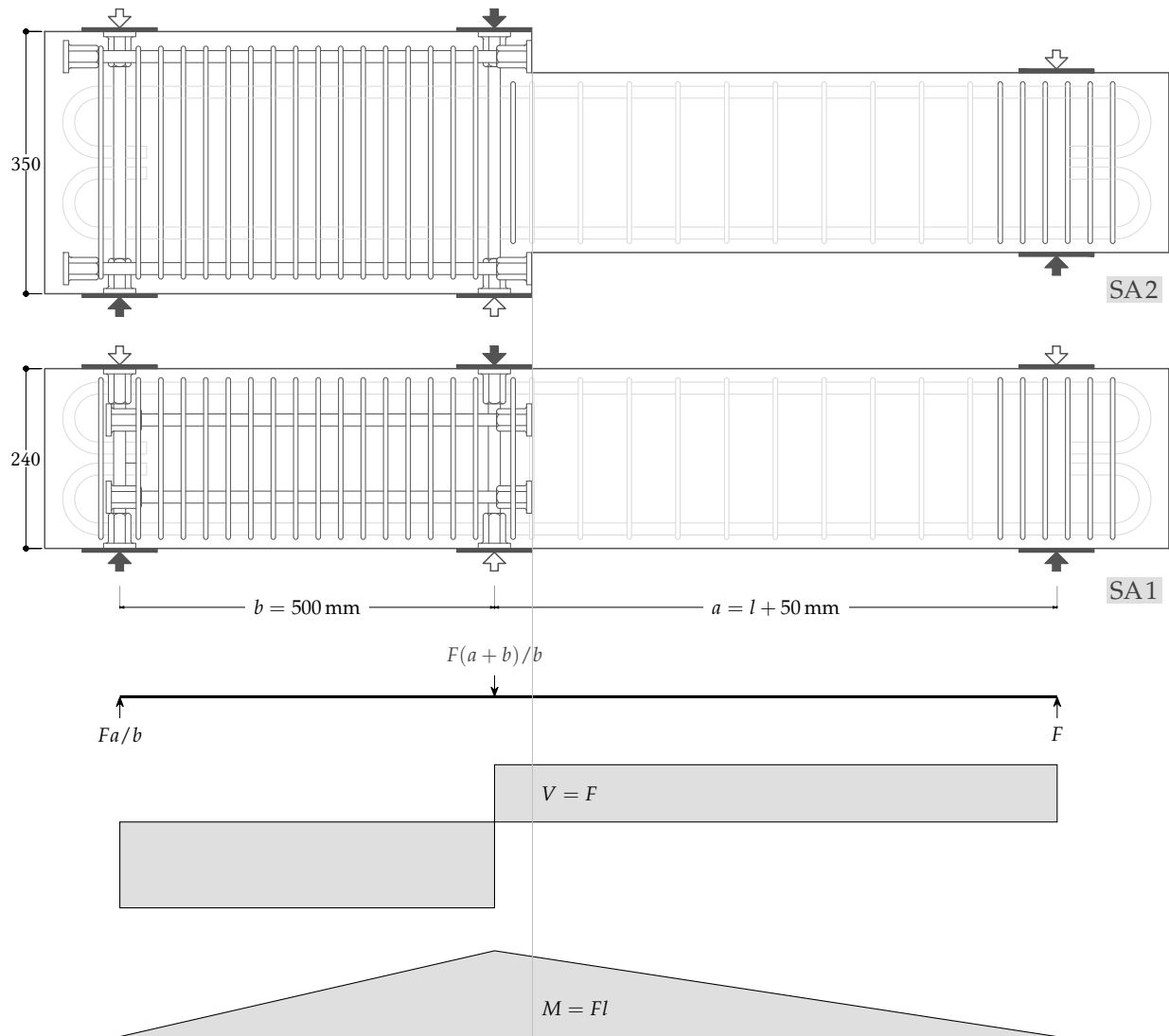
Figure 3.10: Specimen loading diagram

in Figure 3.10. Stub portion of the beam specimen was reinforced with additional longitudinal and transverse reinforcement to ensure sufficient strength such that stub portion remains elastic for the range of forces expected in the test region of the specimen. Loading point was also stiffened with extra transverse reinforcement. Critical section of the specimen was located at the tip of the loading attachment tool just above the stub portion. Loading span (*l*) is thus measured from the critical section to the center of the tip loading attachment. This loading setup was validated by comparing against the conventional cantilever testing setup through specimen SA 2. Stub portion in SA 2 was constructed wider while the section was designed identical to SA 1.

3.3   *Instrumentation*

SPECIMEN response during the tests was recorded using various sensors. Description of instruments and their role in quantification of specimen response is detailed.

3.3.1   *Loads*

Applied loads were measured using center-hole type load cells attached to one end of each prestressing steel rod as indicated in Figure 3.9. Strain gauge based load cells with 200 kN capacity, KCM200KNA manufactured by Tokyo Sokki Kenkyujo K.K., were used. Load applied (F) at the specimen tip was determined as the difference of load cell measurements on either side of the tip as follows:

$$F = F_1 - F_2 \tag{3.1}$$

3.3.2   *Deformations*

All deformation measurements were taken in reference to the stub portion of the specimen. Tip deflection, which was also the control parameter for loading cycles throughout the experiment, was measured against a stiff reference frame attached to the stub portion at 50 mm below the critical section through laser displacement sensors attached to the loading tip as illustrated in Figure 3.11. Keyence K.K. manufactured LB300 sensors with a range of ±100 mm from a reference distance of 300 mm were used. Two sensors were attached on either sides of the tip on a small frame to avoid intersection with the prestressing rods passing through the center. Specimen drift (Δ) was thus calculated from the mean of displacement sensor readings as follows:

$$\Delta(\%) = \frac{\delta_1 + \delta_2}{2} \times \frac{100}{l} \tag{3.2}$$

Beam rotation in the hinge region was measured through two laser displacement sensors attached on the critical section loading attachment tool on either sides against reflection boards attached on the specimen side faces as shown in Figure 3.11. Keyence K.K. manufactured LB080 sensors with a range of ±15 mm from a reference distance of 80 mm were used. Hinge rotation (θ_{hinge}) was thus calculated as follows:

$$\theta_{hinge}(\text{rad}) = \tan^{-1}\left(\frac{\delta_3 - \delta_4}{d_2}\right) \tag{3.3}$$

The same sensors were also used to determine axial strain (ϵ_{axial}) in the hinge region as follows:

$$\epsilon_{axial}(\%) = \frac{\delta_3 + \delta_4}{2} \times \frac{100}{d_3} \tag{3.4}$$
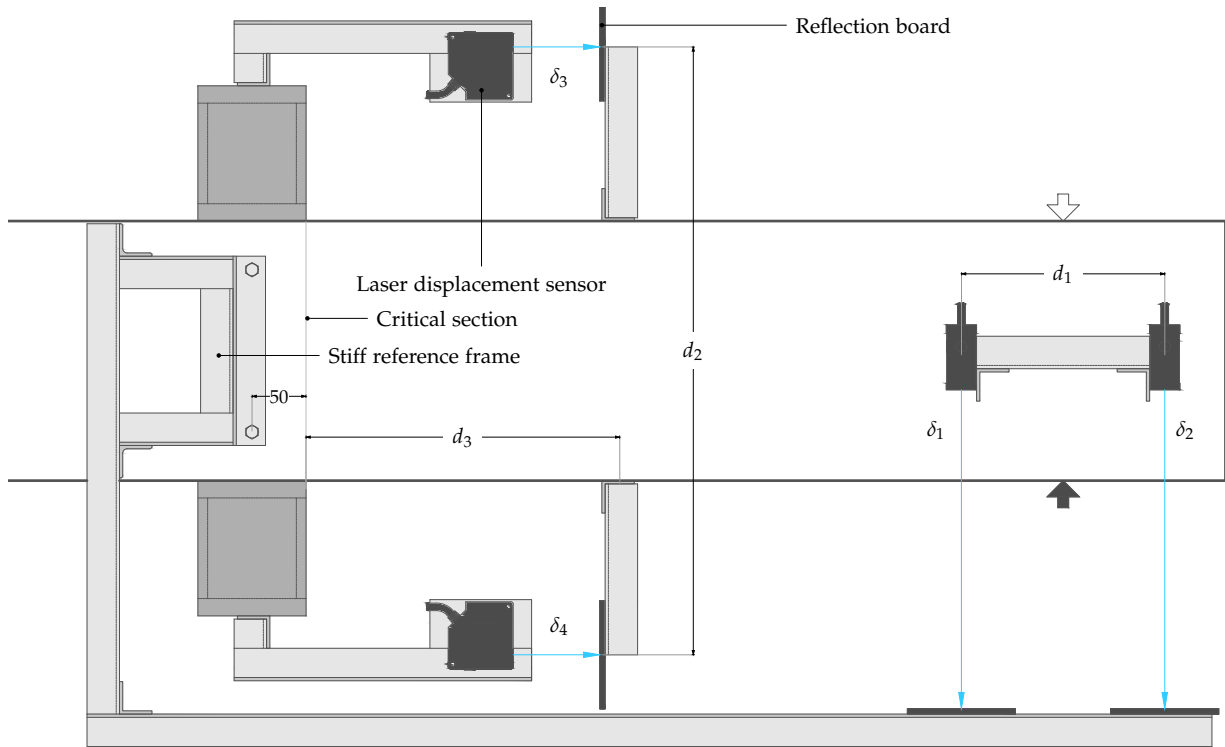
Figure 3.11: Reference frame for deformation measurements
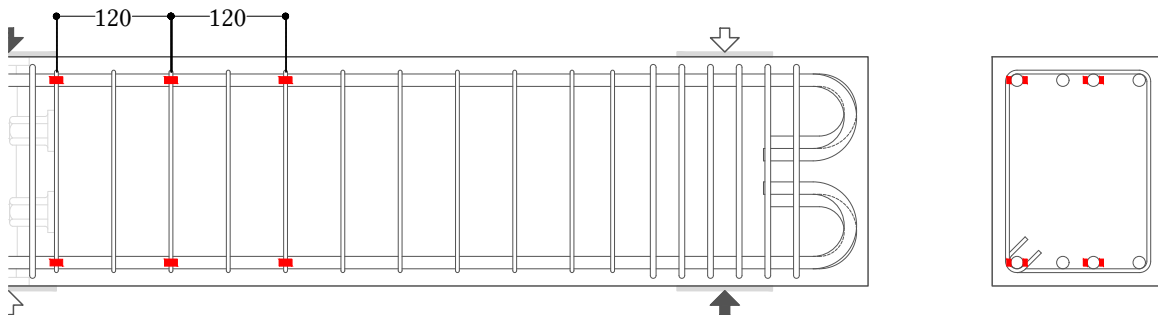
Figure 3.12: Strain gauge instrumentation on longitudinal reinforcement (all dimensions are in mm)

3.3.3   Reinforcement strains

Strains were measured in longitudinal reinforcements through strain gauges attached to the bars prior to concrete casting. Three locations in the hinge zone were monitored for reinforcement strain in all specimens as indicated in Figure 3.12. Two bars, one exterior and one interior, among the four on top and bottom sides were instrumented with strain gauges. Further, two strain gauges were attached on opposite sides on reinforcement bar resulting in a total of twenty-four strain gauges per specimen. Strain at the desired location was thus calculated as the mean of strain gauge readings from opposite sides. Tokyo Sokki Kenkyujo K.K. manufactured FLA-3 strain gauges with 3 mm gauge length were used in all cases.

For specimens SC3 and SC4, strain gauges were located at 120 mm and 240 mm instead of the typical 120 mm and 240 mm. For speci-

mens of the of SA series, strain gauges were instrumented at only the critical section.

3.3.4   *Photogrammetry*

In addition to the aforementioned conventional measurements, an innovative concrete surface deformation measurement technique using digital photogrammetry was also implemented. Two Canon EOS Kiss X8i digital single-lens reflex (DSLR) cameras were used to capture photos of both the opposite concrete surfaces. Again, all measurements were made in reference to the specimen stub portion using a stiff frame to secure the camera in position as illustrated in Figure 3.13. Camera was positioned parallel to the concrete face and at a distance of 650 mm. This arrangement ensured photographing 500 mm of the surface extent with 18 mm focal length and 22.3 mm × 14.9 mm sensor size. All photographs were taken at a resolution of 24 MP and an aspect ratio of 2 : 3, resulting in 4000 × 6000 pixel picture sizes.

Two different photogrammetry methods were implemented on opposite specimen faces. On one surface a coarse measurement technique with fast post-processing (Method-A) was used while on the other surface a technique affording measurements over much finer grid but requiring heavy post-processing (Method-B) was used.

Method-A was based on concept of pattern-matching using digital image processing and generalized fourier transform as proposed by Nair et al.[11] For this method, specimen surface was affixed with targets over a 50 mm × 50 mm grid as illustrated in Figure 3.14. Targets consisted of a circular-symmetric pattern printed on a thick sheet of paper and pasted on the concrete surface with two-sided tape as indicated in Figure 3.15. A small strip of two-side tape was used to minimize the contact of target with concrete surface and therefore reduce the possibility of interference from concrete surface cracks. Thick paper sheet was chosen to ensure sufficient stiffness in the target to remain stable and undeformed. Paper sheets of 0.335 mm thickness were obtained from Sanwa Supply K.K. and 1.1 mm thick two-sided tape applicable to concrete surfaces was obtained from 3M Japan K.K.

Method-B was based an innovative implementation of speckle metrology based digital image correlation[12] using random patterns of natural concrete surface introduced by Saito and Zhao.[13] No specific surface preparation was required in this method. However, only grid lines were marked in pencil for reference.

3.4   *Testing protocol*

SPECIMEN tests were carried out in three phases spread over a period of eleven months. Timeline of the specimen tests is listed in Table 3.6. Similar test protocols were followed for all specimens over the three phases. Minor differences are noted where applicable.

[11] D. Nair et al. "Pattern matching based on a generalized fourier transform". In: *Proceedings of SPIE Vol. 4116*. Advanced Signal Processing Algorithms, Architectures, and Implementations. 2000, pp. 472–480. DOI: 10.1117/12.406527.

[12] Earliest overview on the general methodology is available from W. H. Peters and W. F. Ranson. "Digital imaging techniques in experimental stress analysis". In: *Optical engineering* 21.3 (1982), pp. 427–431. DOI: 10.1117/12.7972925.

[13] T. Saito and Y.-G. Zhao. "Optical full field measurement of concrete deformation using digital image correlation method". In: *Proceedings of the JCI Annual Convention*. Takamatsu, Japan: Japan Concrete Institute, 2014.

Figure 3.13: Frame for camera positioning (all dimensions are in mm)
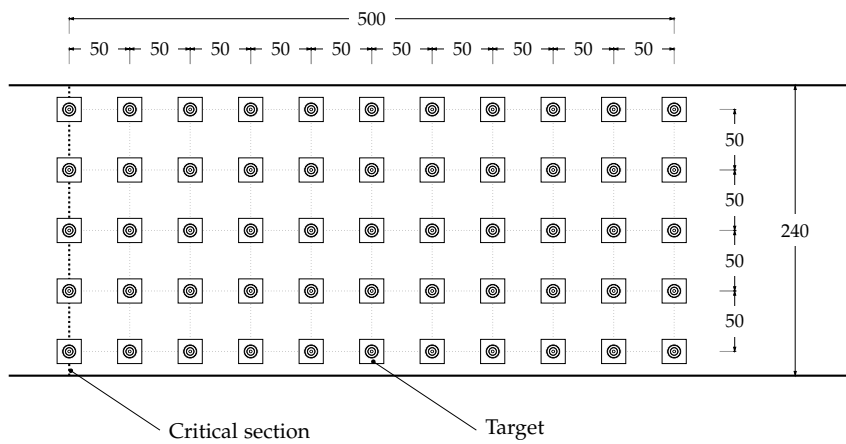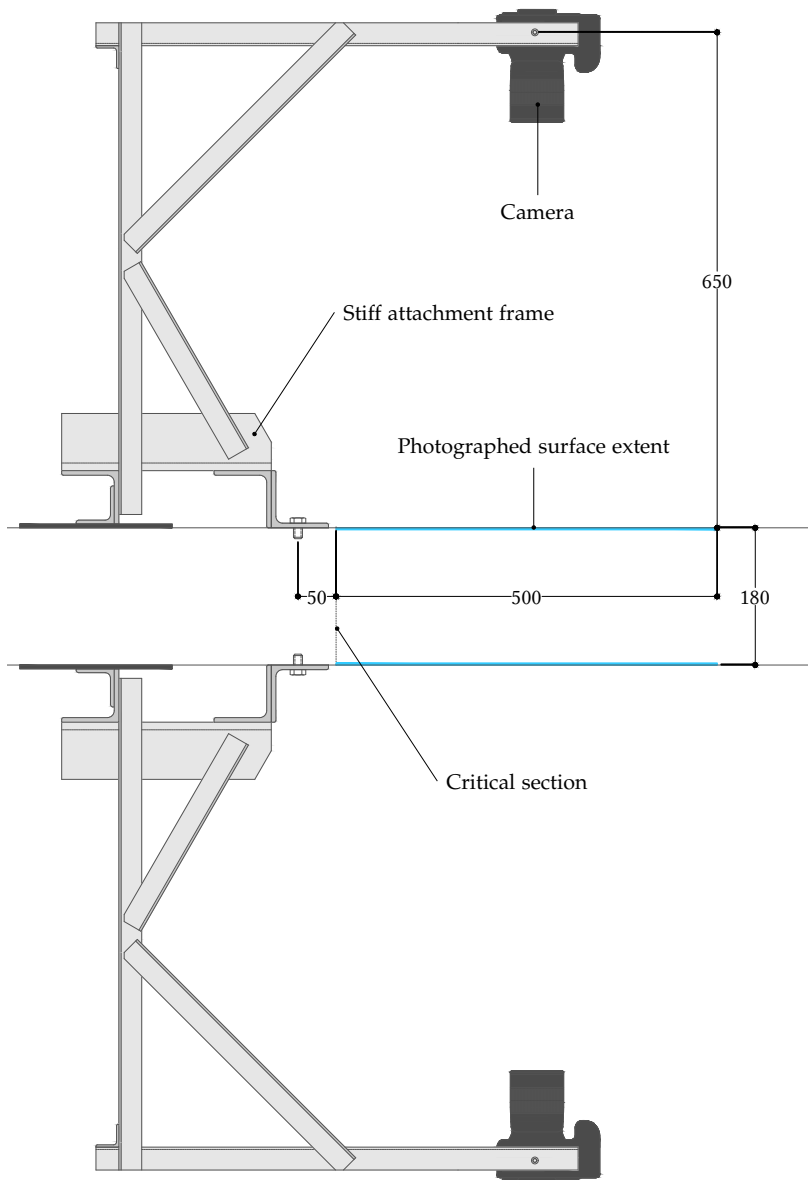
Figure 3.14: Surface preparation for photogrammetric measurements using Method-A (all dimensions are in mm)
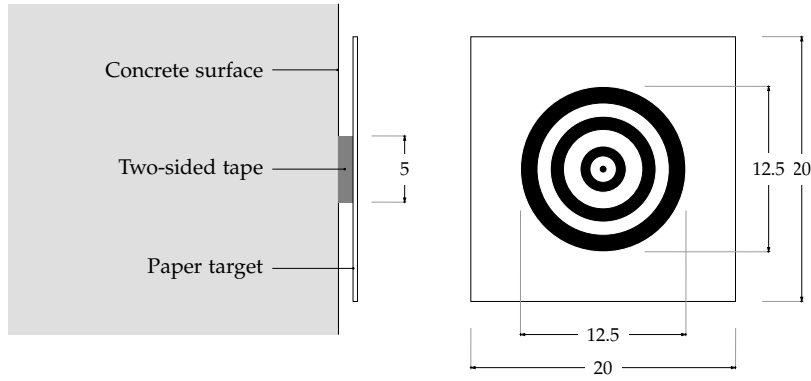
Figure 3.15: Target affixation (all dimensions are in mm)

	Test duration
SA series	April–May 2017
SB series	September–October 2017
SC series	March–April 2018

Table 3.6: Specimen testing timeline

3.4.1 Load application

Load was applied and controlled through a manual single tube oil pump. After initial elastic cycles of load-controlled deformation, deformation-controlled loading cycles were applied with increasing target drift level and three cyclic repetitions at each target drift as expressed in Figure 3.16. Loading was continued until significant reduction in the peak cycle strength was observed or clear specimen failure such as bar-fracture was noted.
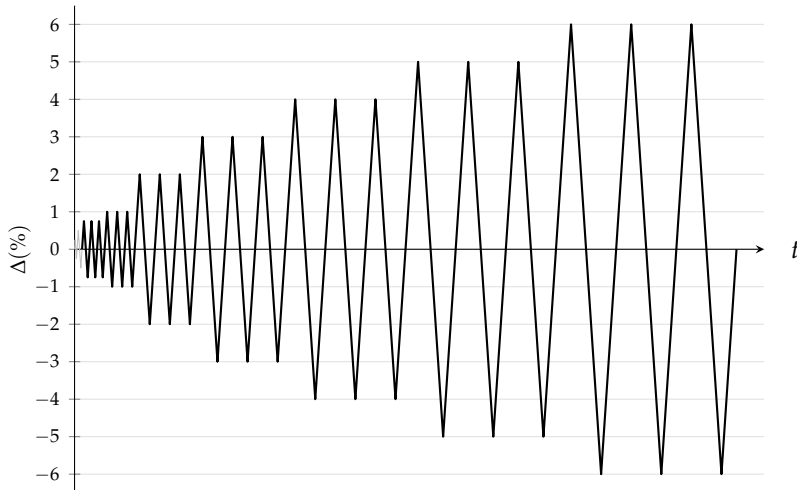
Figure 3.16: Applied loading history

3.4.2 Camera calibration

Deformation measurement using photogrammetry requires estimation of camera characteristics[14] to accurately map photograph pixel coordinates to real-world coordinates and remove undue distortions. Camera calibration was performed to measure camera parameters ba-

[14] D. C. Brown. "Close-range camera calibration". In: *Photogrammetric Engineering* 37 (1971), pp. 855–866.

sed on the technique proposed by Zhang.[15] A chequerboard pattern was prepared and shot at various orientations from both cameras prior to the experiment. This procedure was carried out with the camera in position on the attachment frame of Figure 3.13 to ensure good approximation of camera parameters in the range of in-experiment photographed extents.

3.4.3   Data acquisition

Measurement data for all sensors including load cells, laser displacement sensors, and strain gauges was recorded using Tokyo Sokki Kenkyujo K.K. manufactured data logger TDS-540. Companion static measurement software TDS-7130 was used to monitor and digitally store the recorded sensor data for the entire test duration. Data entries were recorded by the logger at typically 2 s to 3 s interval at the fastest given the large number of channels scanned.

Photographic data acquisition was performed using free and open source camera control software digiCamControl[16]. This simple camera control tool provided simultaneous manipulation of both the cameras through an easily programmable command-line interface, features not available in most commercial camera control softwares. The tool was programmed to shoot simultaneous photos from both the cameras at an interval of 10 s throughout the test duration. Additional shots were also taken at peak loading states. Photos were stored on a connected computer and were programmatically named to include loading direction, target drift, cycle number, and timestamp information.

[15] Z. Zhang. "A flexible new technique for camera calibration". In: *IEEE Transactions on Pattern Analysis and Machine Intelligence* 22.11 (2000), pp. 1330–1334. DOI: 10.1109/34.888718.

[16] http://digicamcontrol.com/

4
Results

LARGE amounts of data were recorded over the duration of phases of experiment for nineteen beam specimens. Obtained sensor and photographic data was processed and reduced to relevant physical quantities presented in this chapter. Details on data processing methodology and implementation of other definitions used in this chapter are expressed in Appendix C[1].

[1] See page 175.

4.1 General behavior

AN overview of the entire test results is expressed in Table 4.1. Experimentally observed moment strength, drift, and hinge rotation at three states namely, yield, peak resistance, and loss of resistance are expressed for either loading directions. Flexural yield point is identified as the first observance of strain exceeding rebar yield strain in any of the attached strain gauges at the critical section. State of maximum observed moment resistance is referred as the peak state. Loss of resistance is referred as the point when peak resistance observed over a loading cycle drops at least 20 % from the peak resistance state. Also indicated for comparison are yield moment (M_y) calculated using Bernoulli's assumption with actual material properties, and maximum moment strength approximated as 1.25 times nominal moment strength (M_{nm}) calculated as per ACI 318-14 code with actual material properties.

Observed specimen states at various loading stages are displayed in Figure 4.1 for SB01 as a typical example. Represented states include peak positive and negative deformations during the third and final loading cycle at each target drift level starting from 1 %. Also indicated are the states when specimen is retuned to zero deformation after completion of all loading cycles at each target drift level. Corresponding damage state for each specimen can be found in Appendix D[2].

[2] See page 177.

As a comparison between specimen responses, damage states at the peak of first cycle at -4 % target drift for all specimens are expressed in Figure 4.2. Damage states at peak resistance and loss of resistance states for all specimens are also expressed comparatively in figures 4.3 and 4.4 respectively. Target drift and loading cycle corresponding to respective states are also indicated next to the specimen number for reference.

Table 4.1: Summary of test results

	Experiment									Estimate	
	M (kN m)			Δ (%) Cycle			θ_{hinge} (mrad)			M (kN m)	
	Yield	Max.	Cap.	Yield	Max.	Cap.	Yield	Max.	Cap.	M_y	$1.25M_{nm}$
SA1	31.8	37.5	25.3	0.92[1]	4.28[1]	5.37[2]	–	–	–	30.6	39.2
	−31.2	−36.1	−17.3	−0.82[1]	−4.24[1]	−5.04[2]	–	–	–		
SA2	29.9	37.9	29.6	0.85[1]	5.29[1]	5.37[3]	6.2	40.8	35.7	30.6	39.3
	−31.7	−36.4	−29.1	−0.79[1]	−5.32[1]	−5.38[3]	−8.7	−41.1	−37.8		
SA3	26.7	31.7	24.2	0.75[1]	3.20[1]	4.31[3]	4.8	22.8	20.5	24.9	32.1
	−24.4	−29.8	−22.3	−0.48[1]	−4.22[1]	−4.15[3]	−4.5	−34.5	−31.6		
SB01	40.6	41.9	29.0	0.71[1]	2.94[1]	3.99[3]	–	–	–	36.6	47.1
	−36.7	−41.8	−32.2	−0.62[1]	−2.97[1]	−3.95[2]	–	–	–		
SB02	42.0	44.5	33.4	0.63[1]	3.99[1]	4.01[3]	5.7	29.3	23.2	37.0	48.3
	−38.8	−42.0	−29.5	−0.68[1]	−2.98[1]	−4.01[3]	−4.5	−20.6	−37.6		
SB03	53.9	57.0	45.4	0.68[1]	1.83[1]	2.98[2]	5.9	16.9	27.0	51.6	67.6
	−52.3	−54.1	−39.5	−0.78[1]	−1.99[1]	−3.00[3]	−6.1	−15.2	−11.4		
SB04	31.6	46.3	31.2	0.53[2]	3.97[1]	5.00[3]	3.4	29.8	29.0	36.6	47.1
	−38.9	−43.0	−32.9	−0.65[1]	−3.89[1]	−5.03[3]	−5.7	−35.7	−47.2		
SB05	37.7	44.6	30.5	0.64[1]	3.96[1]	4.99[3]	4.8	29.4	30.9	37.0	48.4
	−36.3	−44.5	−33.8	−0.35[1]	−3.97[1]	−4.96[2]	−3.5	−32.5	−38.9		
SB06	53.4	59.2	43.9	0.75[1]	3.95[1]	4.95[1]	5.1	30.3	36.9	51.6	67.7
	−49.2	−61.1	−47.9	−0.53[1]	−3.99[1]	−4.01[3]	−4.4	−35.9	−31.7		
SB07	38.0	42.3	31.2	0.81[1]	3.95[1]	3.96[3]	4.8	36.7	41.0	36.6	47.1
	−35.8	−43.1	−32.6	−0.72[1]	−2.97[1]	−4.03[2]	−4.6	−24.2	−16.6		
SB08	39.5	43.4	31.3	0.72[1]	2.99[1]	5.00[3]	5.3	26.7	49.0	37.0	48.4
	−35.4	−43.7	−32.5	−0.54[1]	−2.90[1]	−3.99[2]	−3.7	−24.5	−35.7		
SB09	51.4	57.2	40.3	0.85[1]	2.98[1]	3.94[3]	5.5	25.9	25.3	51.7	67.8
	−54.1	−60.6	−46.7	−0.77[1]	−3.91[1]	−3.71[2]	−5.7	−30.7	−36.1		
SB10	37.6	43.4	30.7	0.68[1]	3.97[1]	5.02[3]	5.1	32.4	44.1	36.6	47.2
	−38.6	−43.8	−34.0	−0.77[1]	−3.91[1]	−5.00[3]	−5.9	−27.9	−30.3		
SB11	37.1	43.8	33.1	0.78[1]	3.98[1]	4.95[2]	5.1	29.4	34.1	37.0	48.4
	−38.9	−45.3	−28.2	−0.59[1]	−3.98[1]	−4.89[2]	−5.3	−32.8	−33.7		
SB12	55.2	59.4	43.2	0.69[1]	3.87[1]	5.00[2]	5.6	32.0	34.8	51.7	67.8
	−54.1	−61.2	−38.2	−0.74[1]	−4.00[1]	−5.04[2]	−5.3	−34.6	−41.8		
SC1	38.9	46.7	33.6	0.64[1]	5.09[1]	6.96[2]	4.5	32.8	31.4	37.0	48.5
	−38.2	−46.5	−35.5	−0.48[1]	−4.99[1]	−6.00[3]	−4.8	−34.8	−30.7		
SC2	38.5	46.8	32.6	0.61[1]	5.03[1]	7.01[3]	4.5	33.1	29.4	37.0	48.5
	−37.3	−46.6	−34.8	−0.52[1]	−4.95[1]	−6.96[2]	−4.3	−30.6	−27.6		
SC3	38.2	49.9	38.5	0.84[1]	6.08[1]	7.17[3]	4.8	52.2	56.2	37.0	48.5
	−38.4	−52.4	−41.6	−0.73[1]	−6.09[1]	−7.10[2]	−4.8	−53.6	−59.3		
SC4	39.2	48.5	33.0	0.89[1]	7.14[1]	8.14[3]	5.2	59.7	60.6	37.0	48.5
	−37.6	−50.6	−36.2	−0.82[1]	−6.12[1]	−8.17[2]	−4.1	−45.6	−64.3		
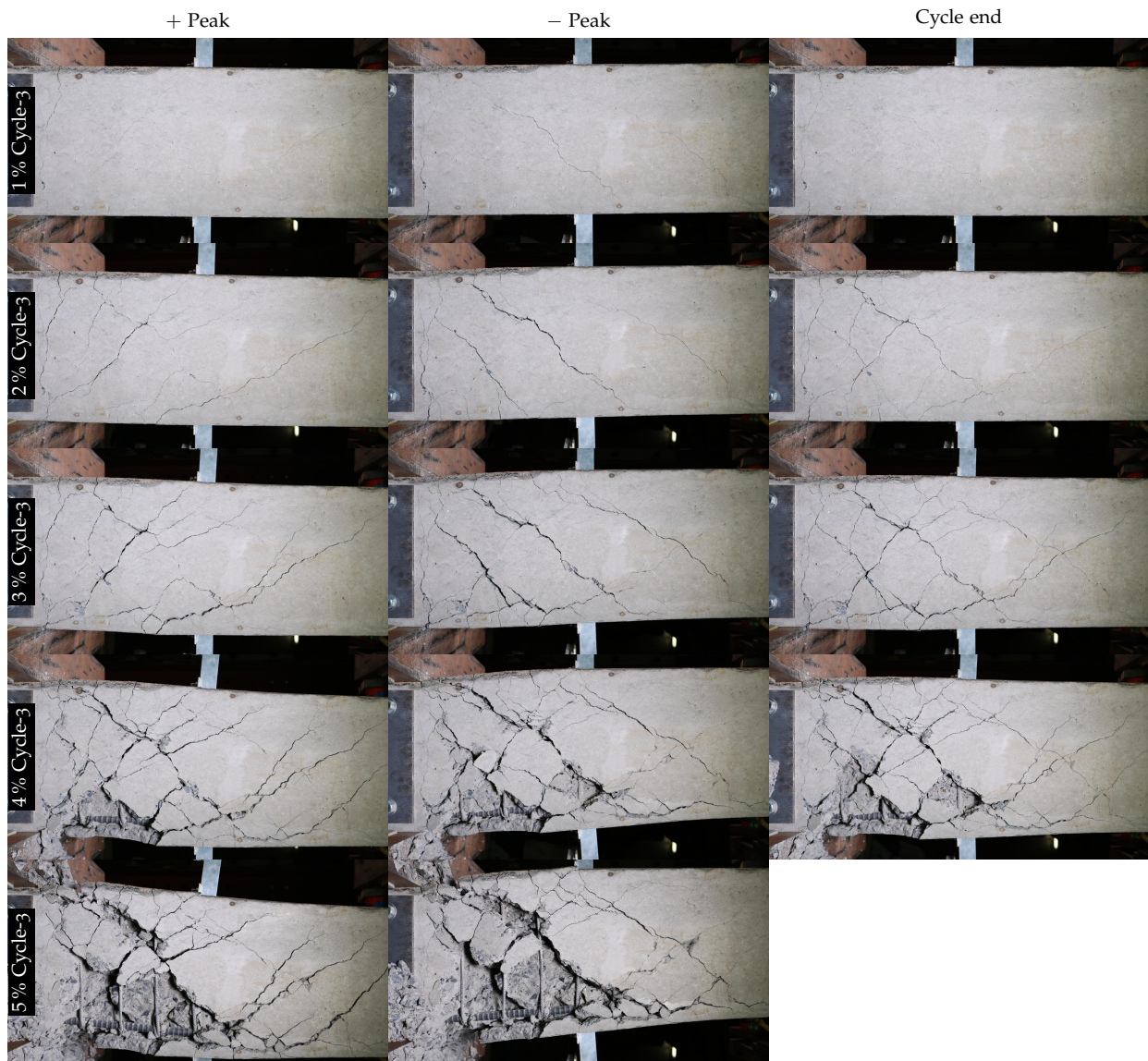
Figure 4.1: Typical damage progression through peak and cycle completion loading states (for SB01)
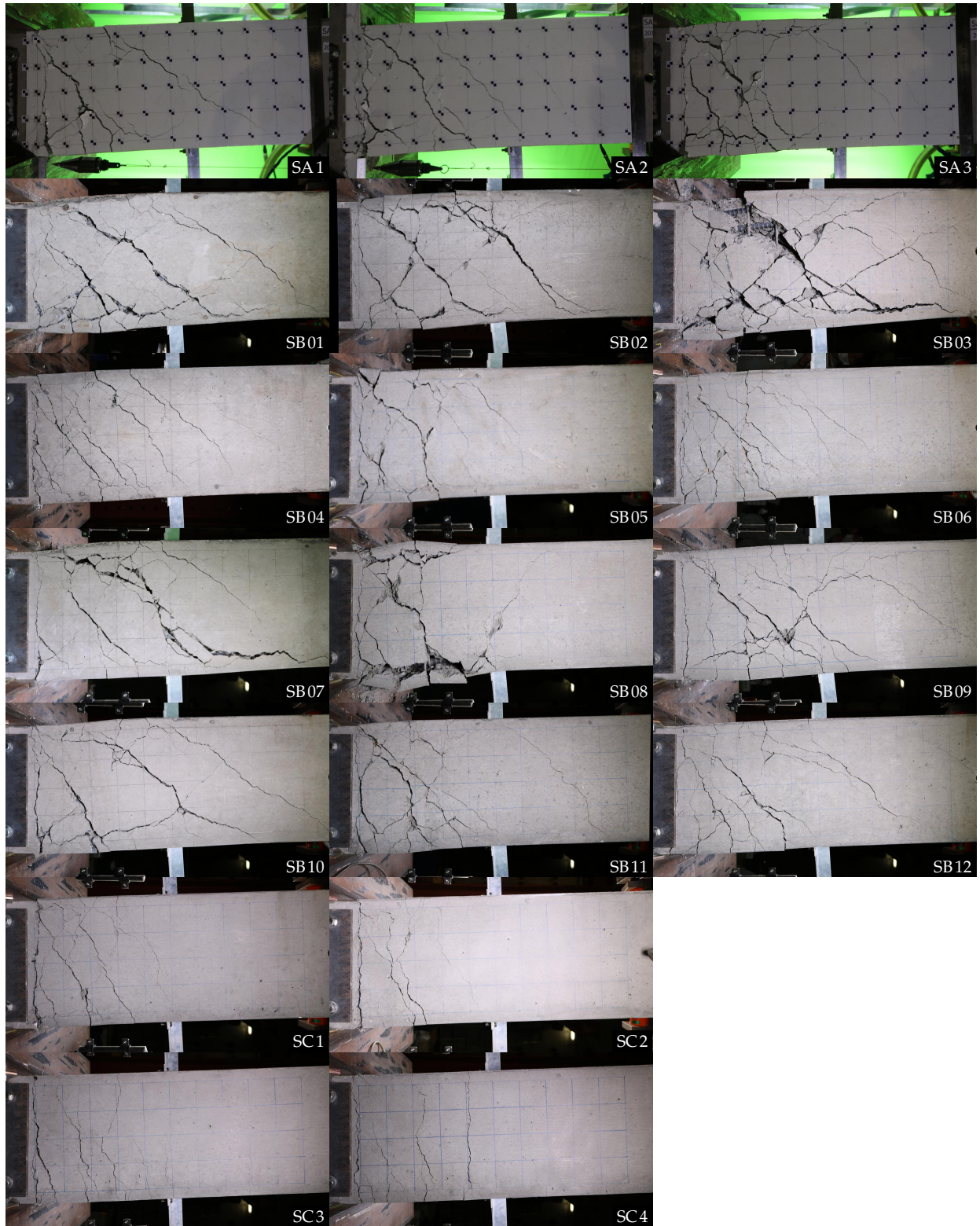
Figure 4.2: Comparison of damage states for all specimens at peak of first loading cycle at −4 % target drift
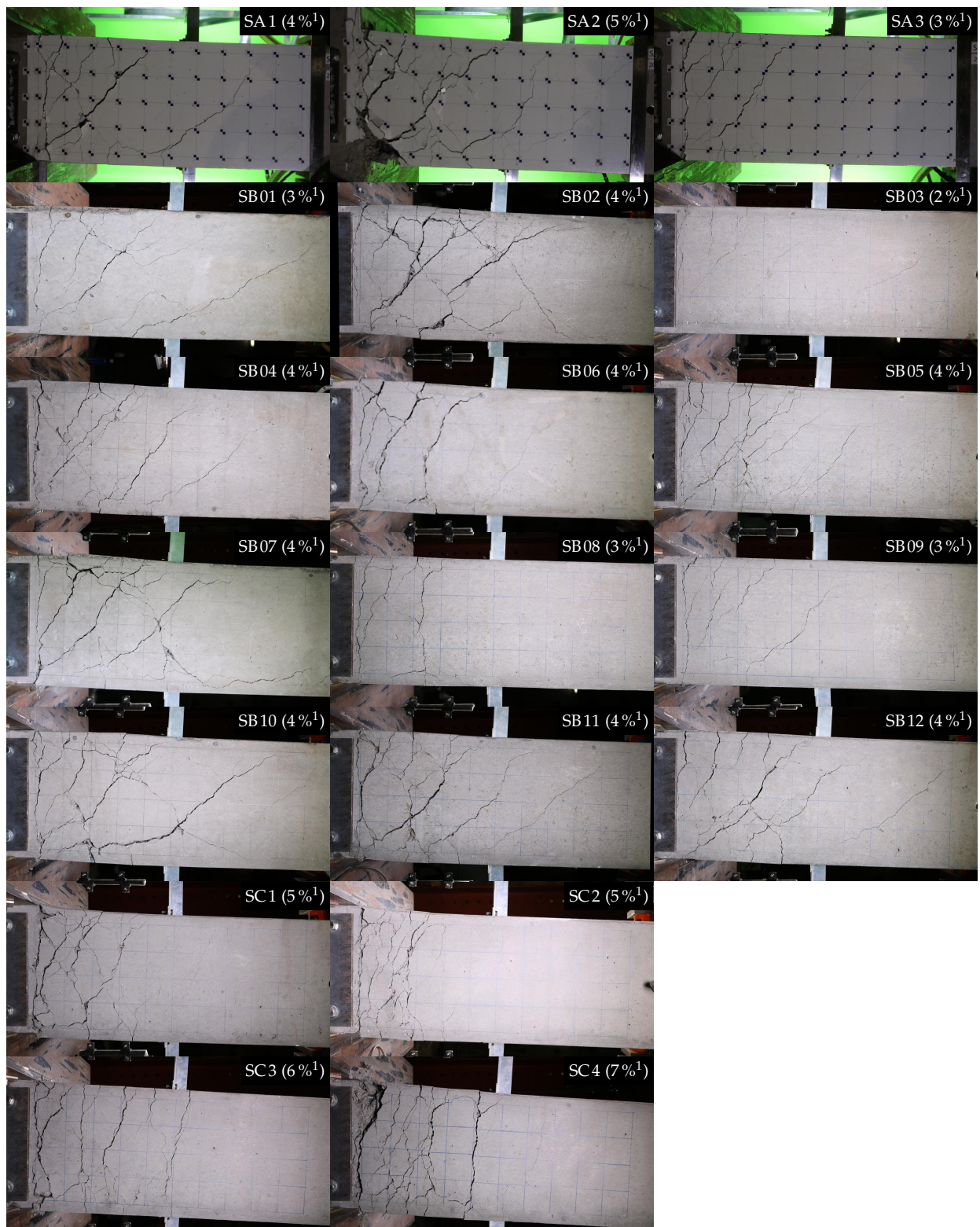
Figure 4.3: Comparison of damage states for all specimens at peak resistance state
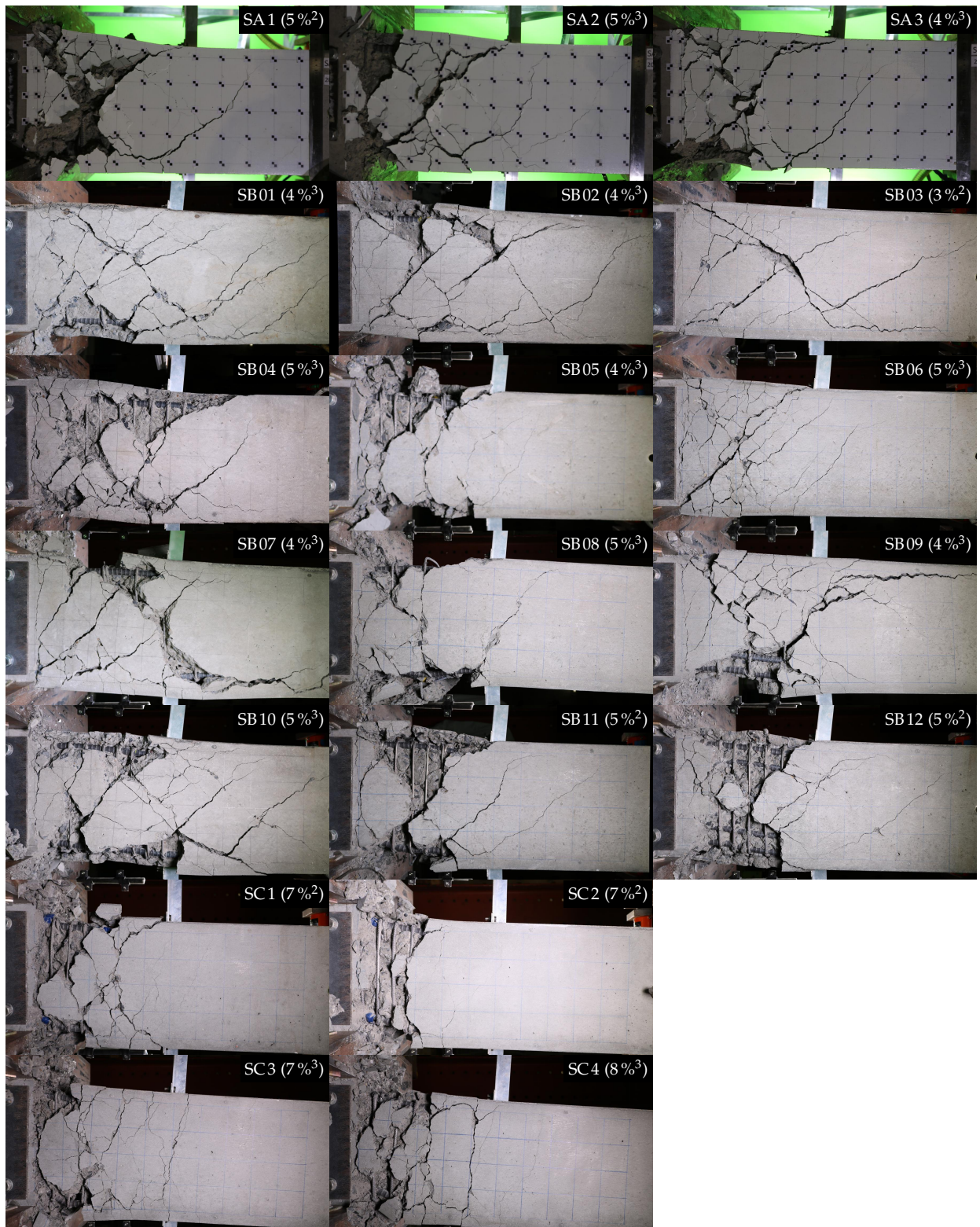
Figure 4.4: Comparison of damage states for all specimens at loss of resistance state
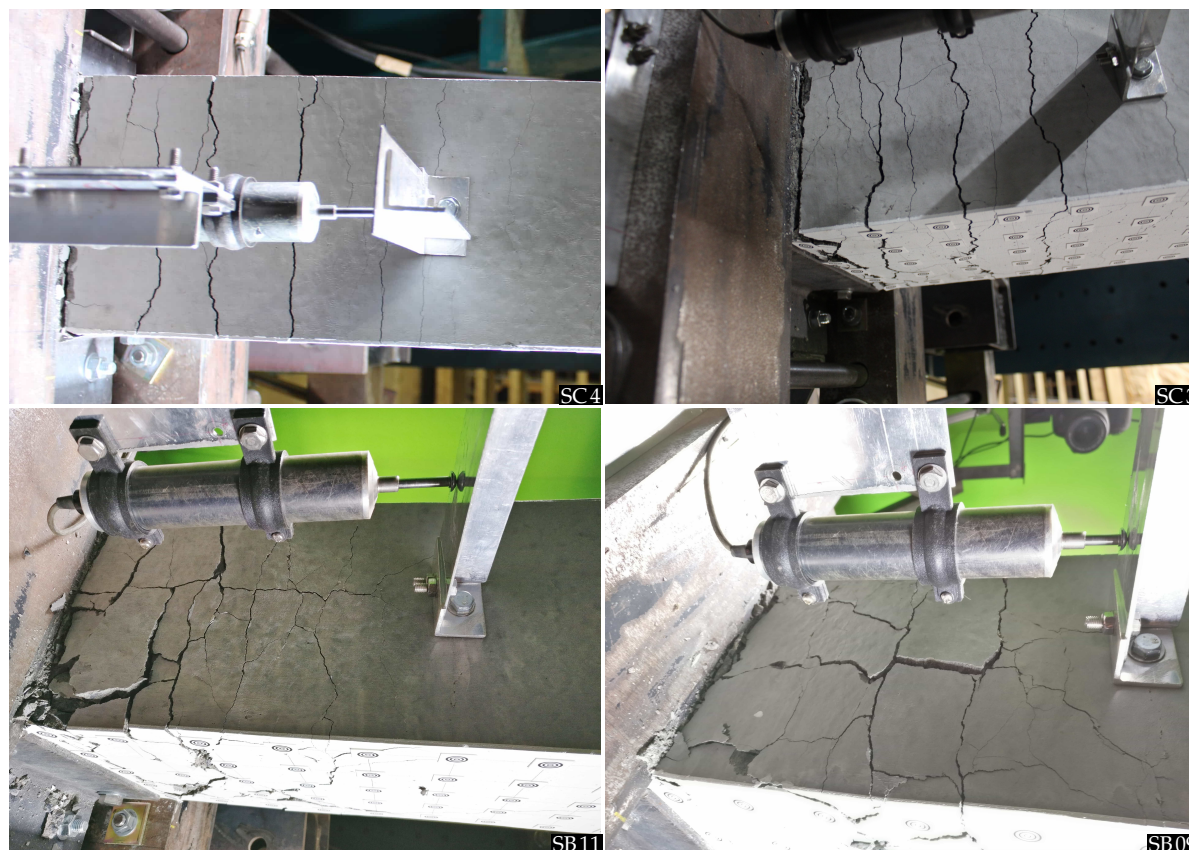
Typical crack patterns observed on the beam top and bottom faces are illustrated in Figure 4.5. Photos for only two representative specimens from SC and SB series are show since other specimens developed almost patterns.

General damage states noted at the conclusion of all scheduled loading cycles are expressed for some representative specimens in Figure 4.6.

Several observations can be made on the presented specimen behavior as follows:

· Most specimens yielded in first loading cycles at 0.75 % or 1 % target drift and exhibited stable hysteretic response over repeated loading cycles before suffering from strength deterioration in the range of 3 % to 5 % drift. SC series specimens sustained much larger deformations, exceeding 7 %, before suffering loss of strength. Yield was consistently observed at a moment larger than the calculated. Most specimens did not attain the calculated moment strength and lost strength after exhibiting only a fractional increase in resistance post yield. Small variations were observed in the positive and negative direction response with negative direction not necessarily being the worst.

· Typical damage pattern consisted to increasingly large flexural cracks close to the critical section accompanied by increasingly inclined flexure-shear cracks over some length. New cracks appeared on loading to a new target drift level while the existing
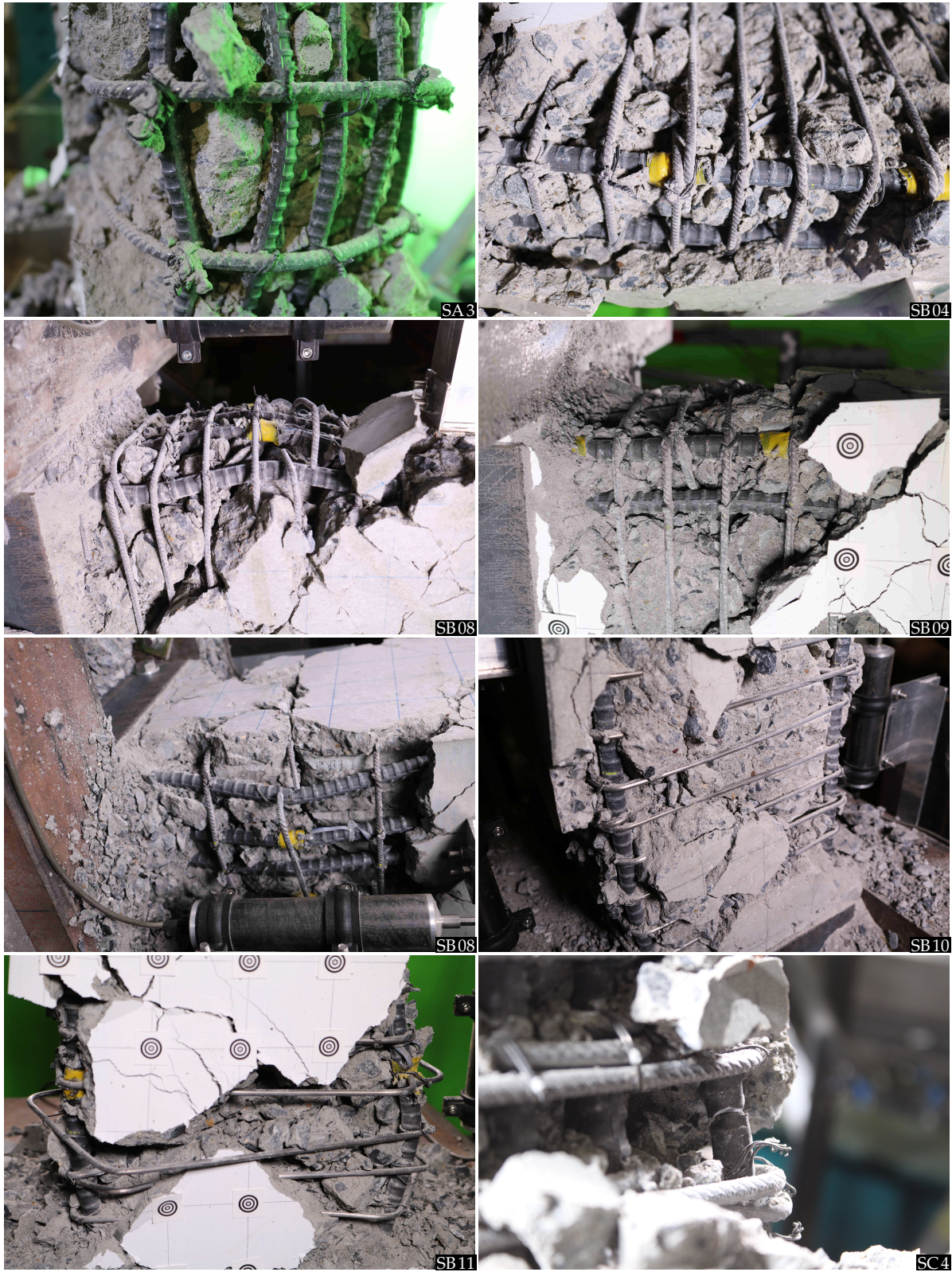
Figure 4.6: General damage patterns noted at the end of the loading regime

cracks continued to widen with cyclic repetitions. At the end of the loading cycle increasingly wider cracks still remained, leading to accumulation of permanent axial and lateral strains. Lateral bulging of the hinge region was especially prominent at large target drift levels.

· While general cracking pattern was similar in specimens, remarkable variation was observed in specimens with higher ρ_s. In the specimens with 0.52 % transverse reinforcement, more closely spaced cracks of much thinner size were observed. While in the specimens with ρ_s exceeding 1 %, inclined cracks were almost non existent and flexural cracks almost parallel to the critical section were observed. Lateral bulging was also significantly reduced in specimens with higher ρ_s.

· At the peak loading state, no spalling or severe disintegration of concrete was observed. Cracking pattern was also noted to be well distributed in most specimens. Size of the cracks at peak state also appear to be nearly similar for all specimens.

· Severe spalling and concrete crushing in some cases was observed at the loss of resistance loading state. Pronounced bulging of reinforcement and opening of hoops were also noted in some cases. Specimen state at this point presents a stark contrast to the peak loading state even though the difference between the two was only a few loading cycles. In most cases, peak state was observed at the very previous target drift cycle.

· In specimens of the SC series, cracks on the side faces of the beam were also nearly parallel, connecting front and back surfaces. While the cracking was similarly parallel the SB series specimens also, additional presence of orthogonal cracks along the length was also noted. This signifies the differential lateral bulging of longitudinal bars which were not supported by cross ties in SB series specimens.

· Lateral bulging of the longitudinal reinforcement was frequently observed in the final specimen state. Another distinct phenomenon observed in some specimens was the sideways buckling of the rebars. In the specimens with closely spaced stirrups, however, perfectly straight shape of the rebars was preserved until the end. Opening of hoops was also frequently noted in the hinge region of the specimens. Specimens with a second layer of reinforcement exhibited greater bulging in the second layer reinforcement which was not tied with any stirrups. Rebar fracture was observed in only one (SC 4) of 19 specimens tested in the experimental program.

4.2   Response plots

MOMENT at critical section against drift at tip response of all specimens is expressed in Figure 4.7 to show the hysteresis characteristics. Yield point, maximum moment resistance point, and loss of resistance point in both positive and negative loading directions are also indicated in each plot using the data previously presented in Table 4.1. Also indicated in the plots are the levels of estimated yield and ultimate

moment strengths.

Corresponding hinge rotation response for all specimens is expressed in Figure 4.9. Occurrence of yield, maximum moment, and loss of resistance are also similarly noted on the response curves.

Same sensors as hinge rotation were also used to measure the development of average axial strain in hinge region as expressed in Figure 4.11 against applied drift levels.

Degradation of moment resistance with increasing cyclic loading is illustrated through Figure 4.13. Normalized moment at peak target drift in first, second, and third loading repetitions is plotted for both negative and positive directions. Normalization against maximum moment for each specimen is performed to facilitate convenient comparison between specimens exhibiting different strengths.

Contribution of flexural deformations to the total target drift over the loading history is expressed through Figure 4.15. Observed hinge rotations and target drifts (expressed in rad) at the peak state of each loading cycle against each for both positive and negative loading directions on square axes. Unit line which signifies equal hinge rotation and total drift is also indicated for reference.

Note that due to malfunction of one of the displacement sensors at the hinge no rotations or axial strains could be measured for specimens SA1 and SB01.

Several observations can be made on the expressed specimen response plots as follows:

· Yielding the specimens was immediately followed by softening of response. Peak resistance at the cycles following yield was typically lower than the yield moment. Coupled with the fact that the observed yield moment was higher than the calculations, this observation may be attributed to the upper yield point of the reinforcements followed by soft yield plateau at the lower yield point. Peak moment resistance observed was consistently lower than the calculated maximum strength in most specimens. The difference was noted to be especially pronounced in the specimens with a second layer of reinforcement.

· At the loading cycles exceeding 2 % target drift, most specimens exhibited pinched hysteresis loops. Specimens with greater transverse reinforcements or shear-span ratios resulted in improved hysteresis loops with lesser pinching. Specimens SC3 and SC4 with both, high ρ_s and large l/D exhibited almost pinching no in the hysteresis loops.

· Although stiffness degradation was consistently observed with increasing target drifts, no deterioration in peak cycle resistance was noted over the repetitive loading cycles before reaching the overall peak resistance. Loss of strength that occurred after the peak resistance was usually steep and accompanied by large stiffness degradations. Negative loading stiffness, however, was not observed in any of the specimens even when loaded to very large displacements. Only at the occurrence of violent events such as rebar fracture or hoop opening was momentary negative stiffness
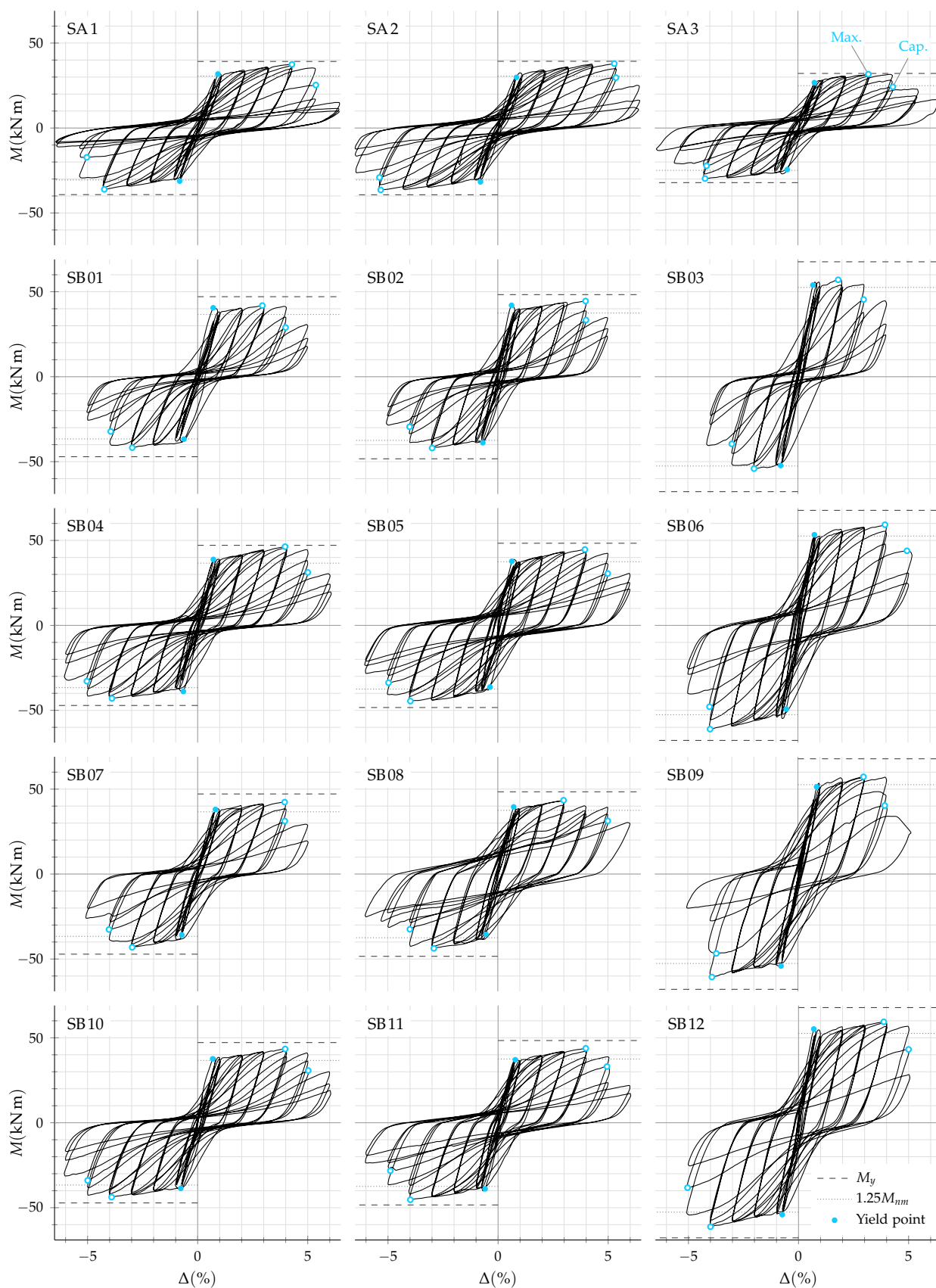
Figure 4.7: Moment-drift response (SA and SB series)
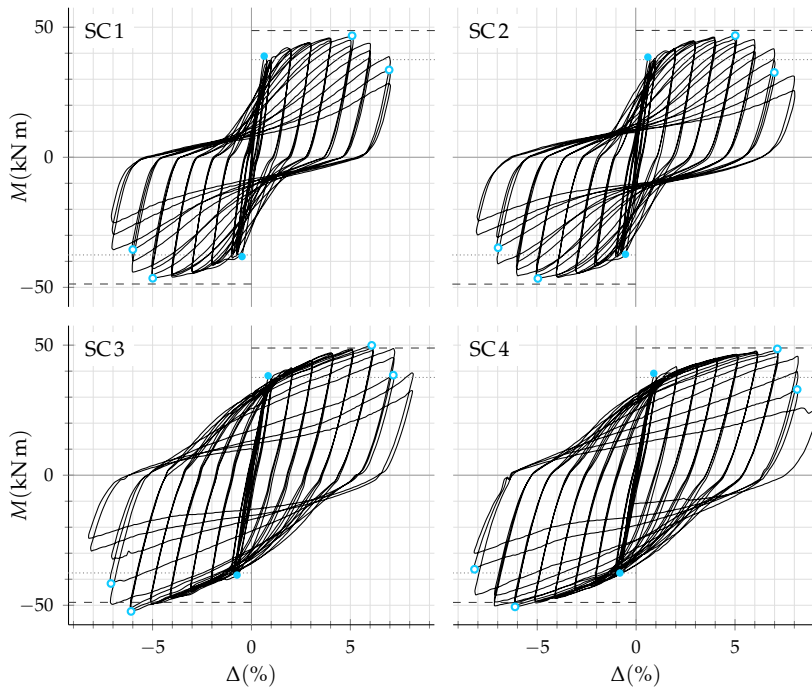
Figure 4.8: Moment-drift response (SC series)

    observed.

· Rotation response was not always symmetric like the drift response. Since, drift was the control variable of the loading scheme, the rotation response can be read as a response quantity to the imposed tip displacement. At large displacements, large rotations accumulated to one of the positive or negative loading sides. Similar pinching of the hysteresis loop as in drift response was also observed in rotation response at large rotations. Specimens with a larger l/D usually exhibited larger rotations and smaller pinching.

· Axial strain was observed to continuously accumulate each new target drift loading cycle and also with cyclic repetition at the same target drift cycle. Increase of axial strain with cyclic at the same target drift level was observed to be increasingly smaller.

· Accumulation of axial strain ceased with loss of resistance and axial shortening was observed over cycles at large drifts. The peak resistance, however, was not obtained at exactly the same time as the peak axial strain. Axial strain continued to increase with loading for some cycles even as resistance dropped.

· Smallest axial strains were recorded in SB03 which also exhibited the smallest drift capacity.

· Generally speaking, strength in the negative direction was slightly smaller than the positive direction loading. In some specimens such as SB11 and SC4, however, the opposite was the case. Rapid deterioration following the peak strength observed in specimens with a second reinforcement layer is also clearly evident from strength-degradation plots.

· Hinge rotations were fractionally smaller than total drift angles at small deformations. The contribution of hinge rotation to total drift
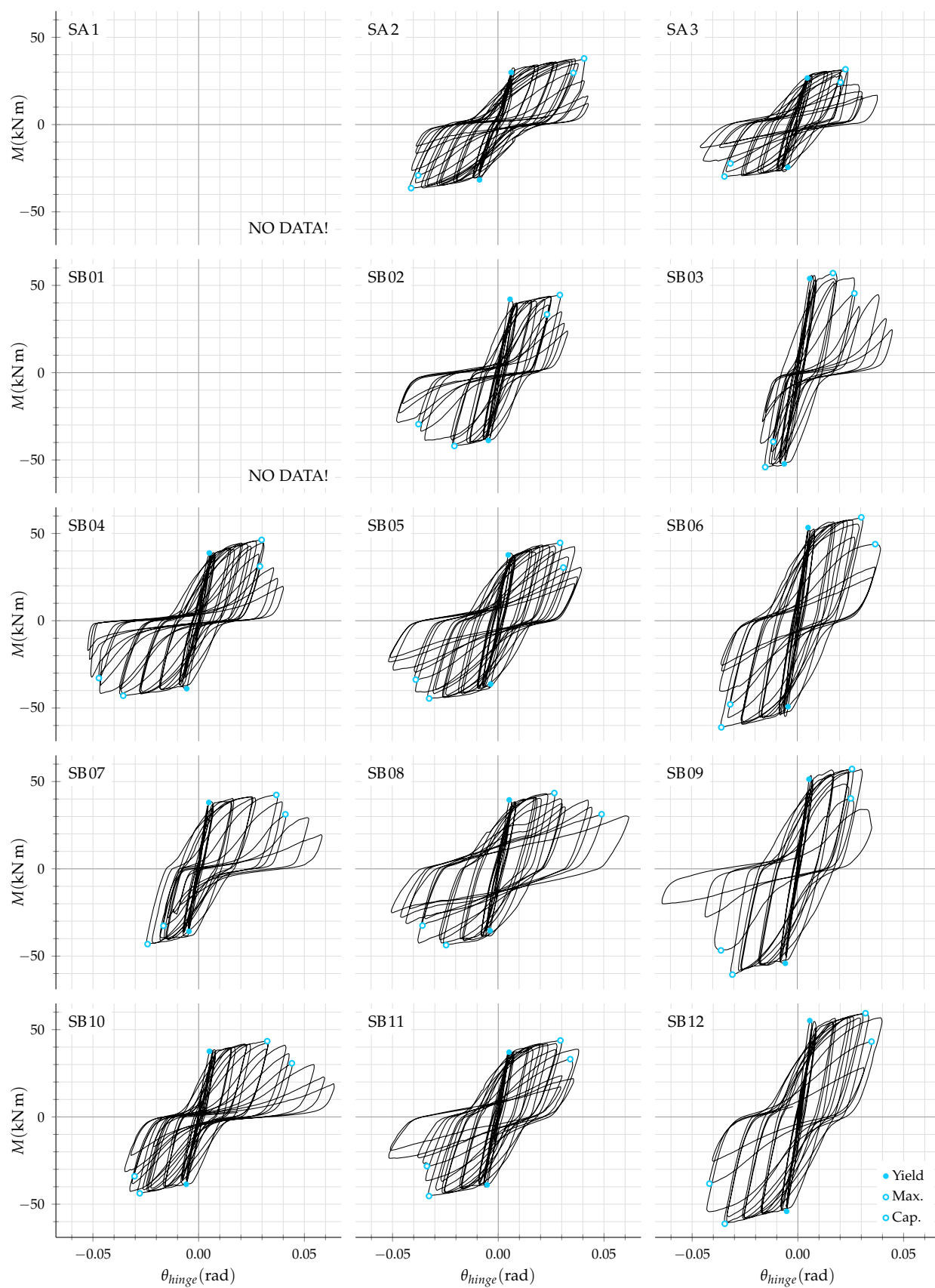
Figure 4.9: Moment-hinge response (SA and SB series)
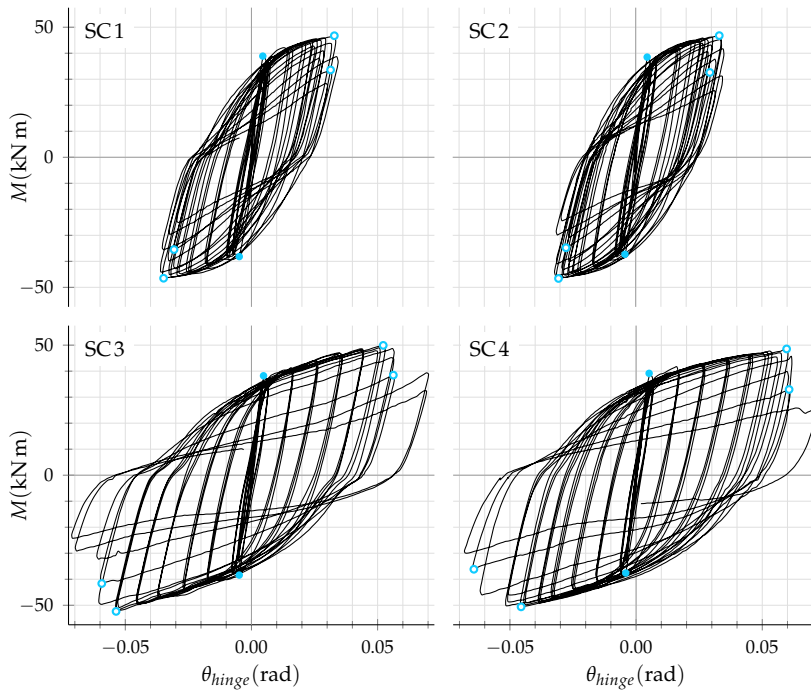
Figure 4.10: Moment-hinge rotation response (SC series)

was observed to decrease with cyclic loading repetitions at the same target drift cycles. The total contribution of hinge rotations was also observed to decrease at large deformations. In the specimens with large l/D, however, hinge rotations tended to form a greater portion of the total drift and suffered lesser loss of participation at large drifts.

4.3 *Photogrammetry*

LARGE number of digital photographs recorded during the experiment were analyzed to deduce concrete surface deformations using principles of photogrammetry. A simplified overview of the analysis procedure is represented in Figure 4.17. Camera calibration to measure camera parameters was required to be performed only once however remaining steps were performed for all sets of digital images recorded for each specimen. Image analysis was performed using OpenCV,[3] an open-source library of computer vision functions.

[3] G. Bradski. "The OpenCV Library". In: *Dr. Dobb's Journal of Software Tools* (2000).

4.3.1 *Calibration and pre-processing*

Chequerboard photographs taken before the start of the experiment were used to estimate camera *parameters* using the procedure listed in Algorithm 4.1. `OpenCV`functions used in the process are also noted where applicable. Calibration principally involves determining corners of checquerboard from images (on Line 3) and using all the identified corner locations over numerous images to determine camera parameters using OpenCV implementation of Zhang's[4] calibration algorithm (on Line 6).

[4] Zhang, op. cit.

Figure 4.11: Axial strain-drift response (SA and SB series)
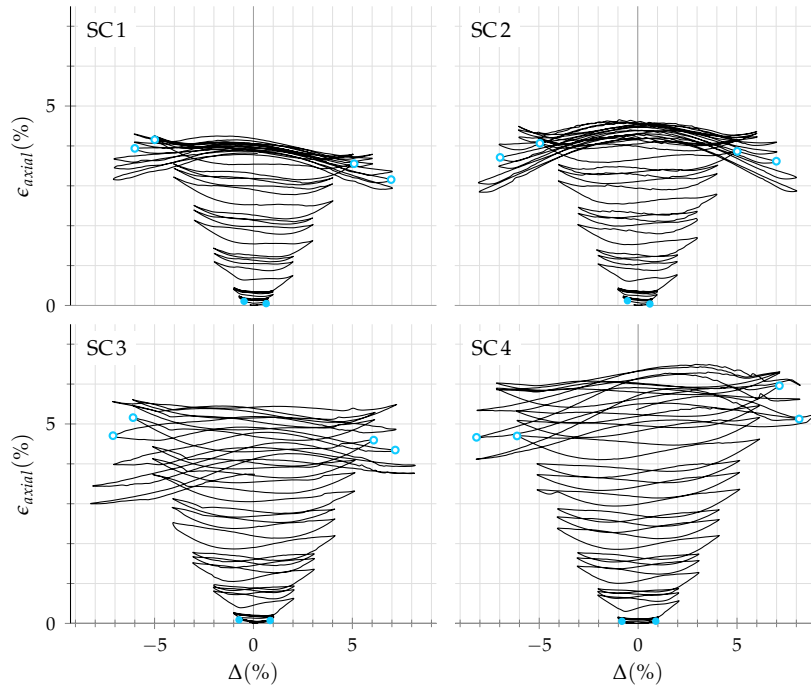
Figure 4.12: Axial strain-drift response (SC series)

Algorithm 4.1: Camera calibration using OpenCV

Require: checquerboard *images*
 1: **for all** *images* **do**
 2:     convert *images* to *grayscale* using `cvtColor`
 3:     find checquerboard *corners* using `findChessboardCorners`
 4:     refine identified *corners* using `cornerSubPix`
 5: **end for**
 6: find *parameters* using all *corners* and `calibrateCamera`
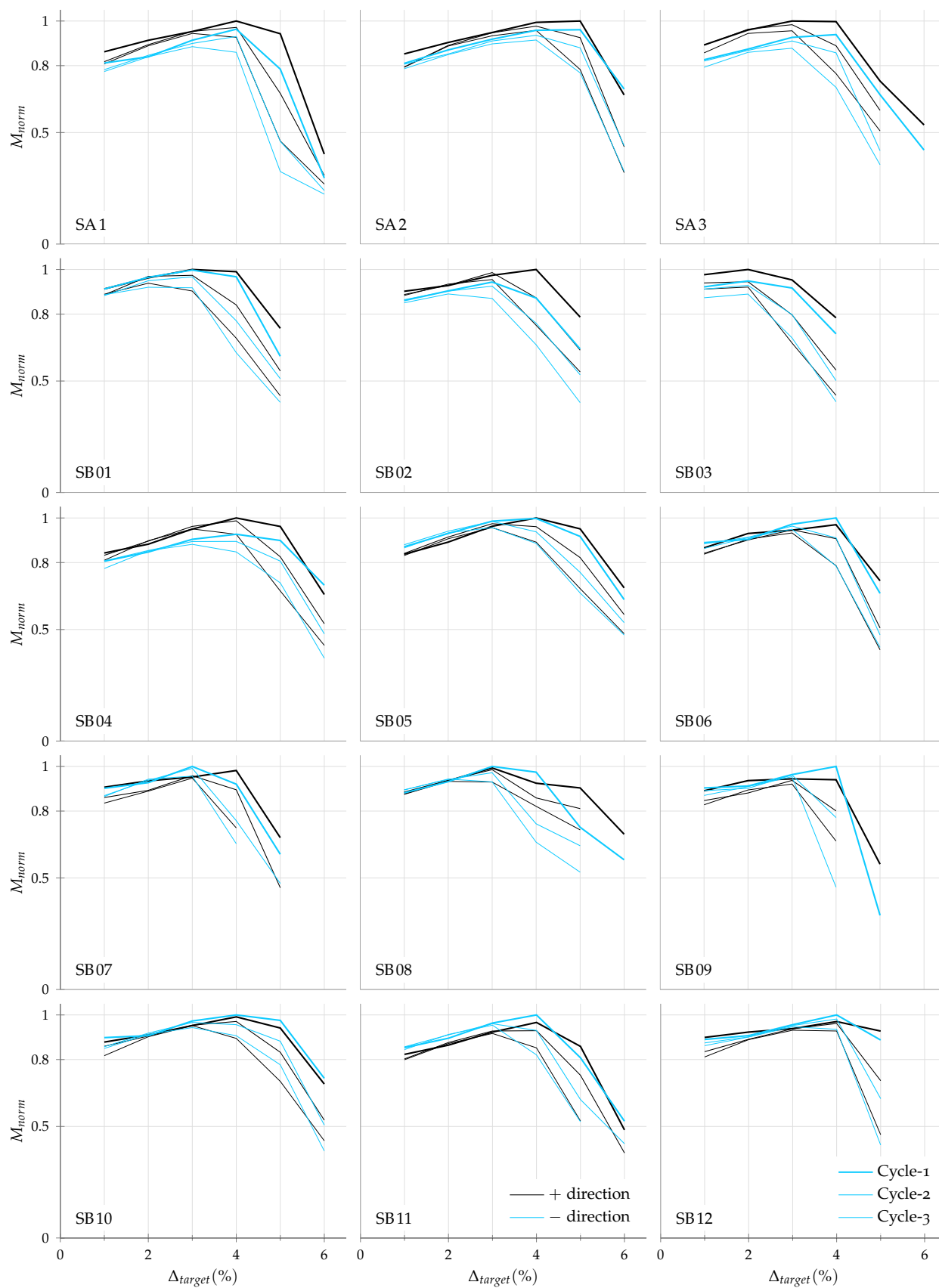
Figure 4.13: Degradation of peak moment strength over three cycles of loading (SA and SB series)
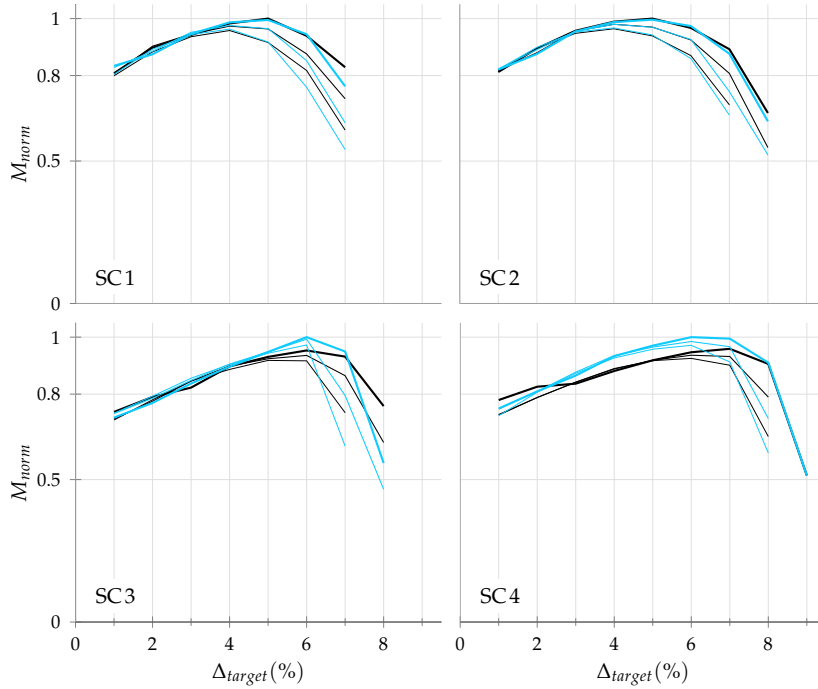
Figure 4.14: Degradation of peak moment strength over three cycles of loading (SC series)

Raw images are usually corrupted with lens distortions and unwanted inclinations. Pre-processing was performed to remove the distortions and prepare the raw images for photgrammetric analysis. Undistortion was first performed using the measured camera *parameters* to remove radial and tangential lens distortions using the procedure listed in Algorithm 4.2.

Require: camera *parameters*, all captured *images*
1: find *matrix* for the size of *images* using *parameters* and `getOptimalNewCameraMatrix`
2: **for all** *images* **do**
3:     undistort *images* using *matrix* and `undistort`
4: **end for**

Algorithm 4.2: Undistortion of captured images using OpenCV

Undistorted images were transformed to get rid of distortions due to initial camera inclination. Four rectangular points were identified on the specimen surface with known *coordinates* and perspective transformation to was applied using the procedure listed in Algorithm 4.3. Corners of the 500 mm × 200 mm specimen grid expressed in Figure 3.14 were used as known *coordinates* and were transformed to a *size* of 4000 px × 1600 px in image space.

4.3.2 *Image processing*

The set of transformed images from both specimen faces were processed to determine deformation fields using Method-A and Method-B image processing techniques.

Method-B processing was performed to determine deformations
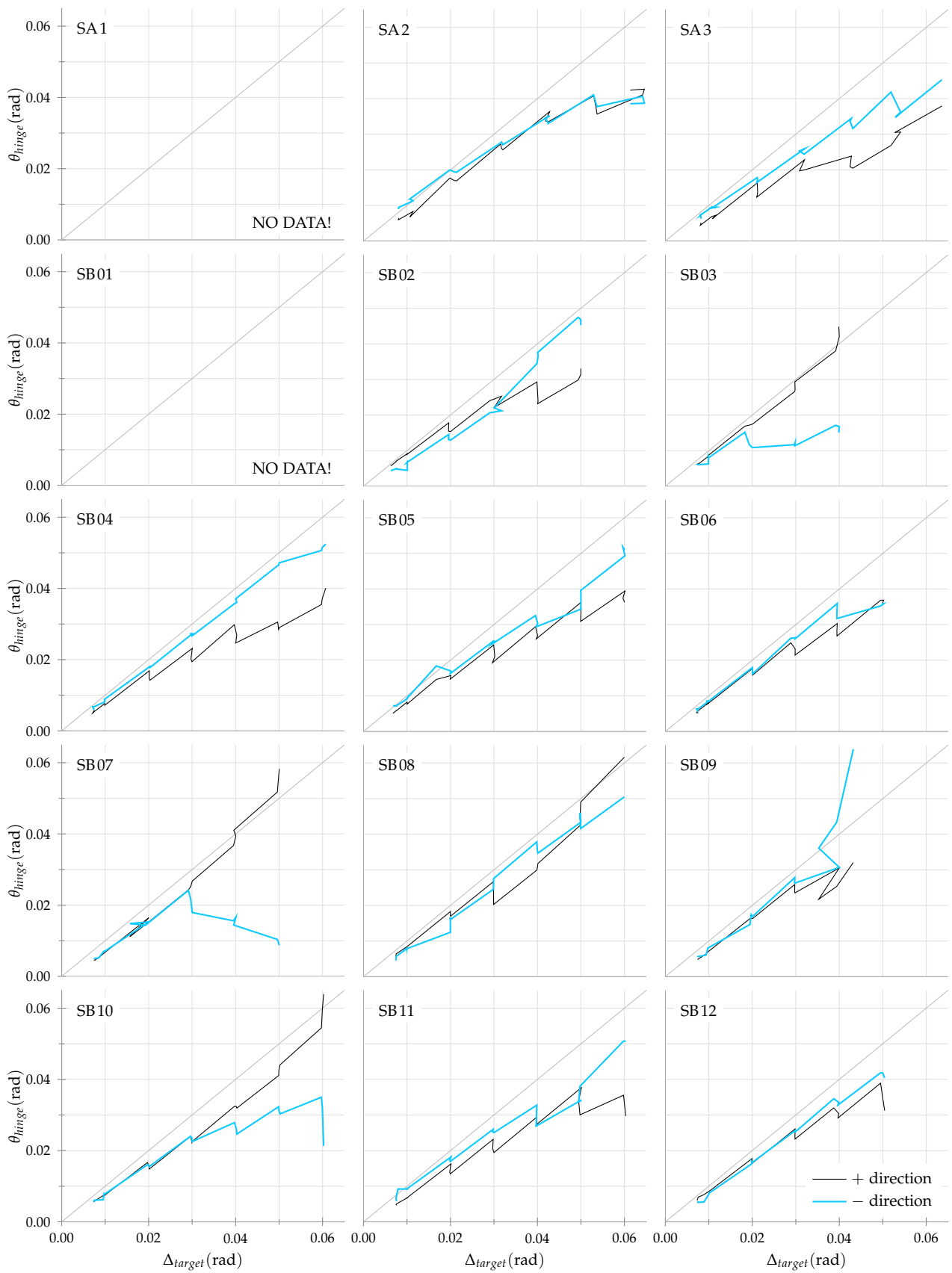
Figure 4.15: Contribution of hinge rotation to total chord rotation (SA and SB series)
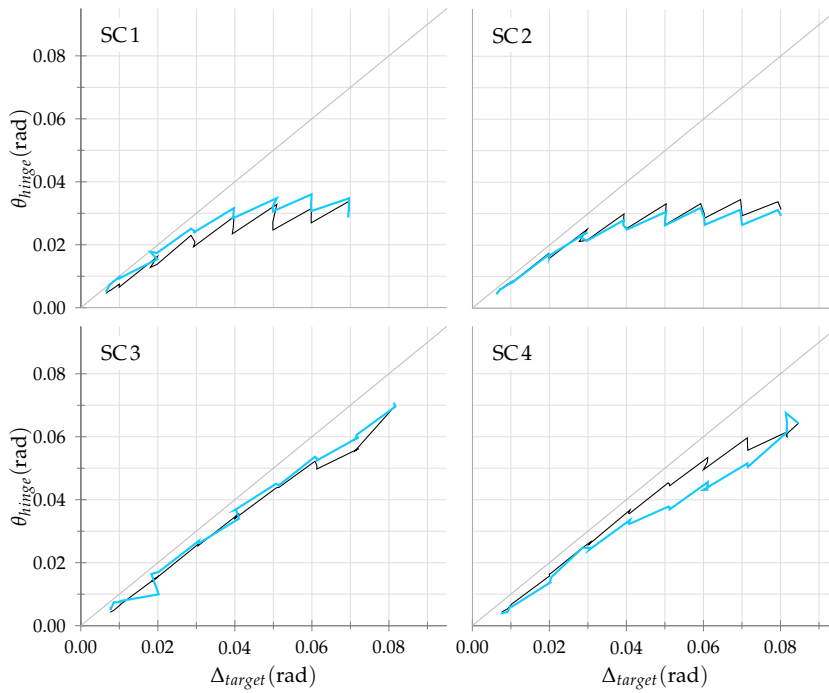
Figure 4.16: Contribution of hinge rotation to total chord rotation (SC series)
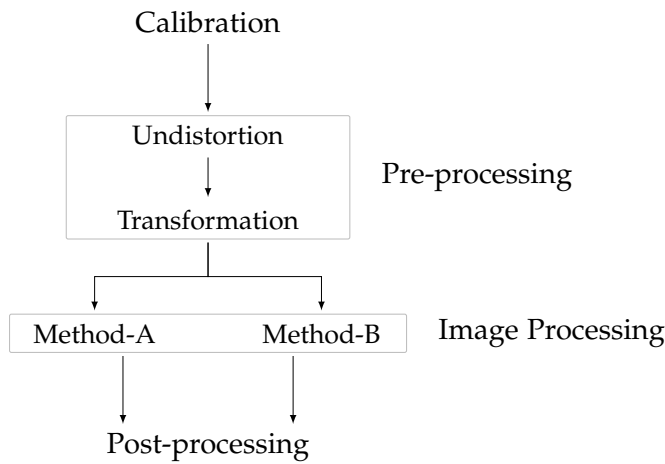
Figure 4.17: Flow of photogrammetric analysis to obtain surface deformation fields

Require: rectanguar specimen *coordinates*, transform *size*
1: find transformation *matrix* for *images* using *coordinates*, *size*, and `getPerspectiveTransform`
2: **for all** *images* **do**
3:     transform *images* using *matrix* and `warpPerspective`
4: **end for**

Algorithm 4.3: Perspective transformation of undistorted images using OpenCV
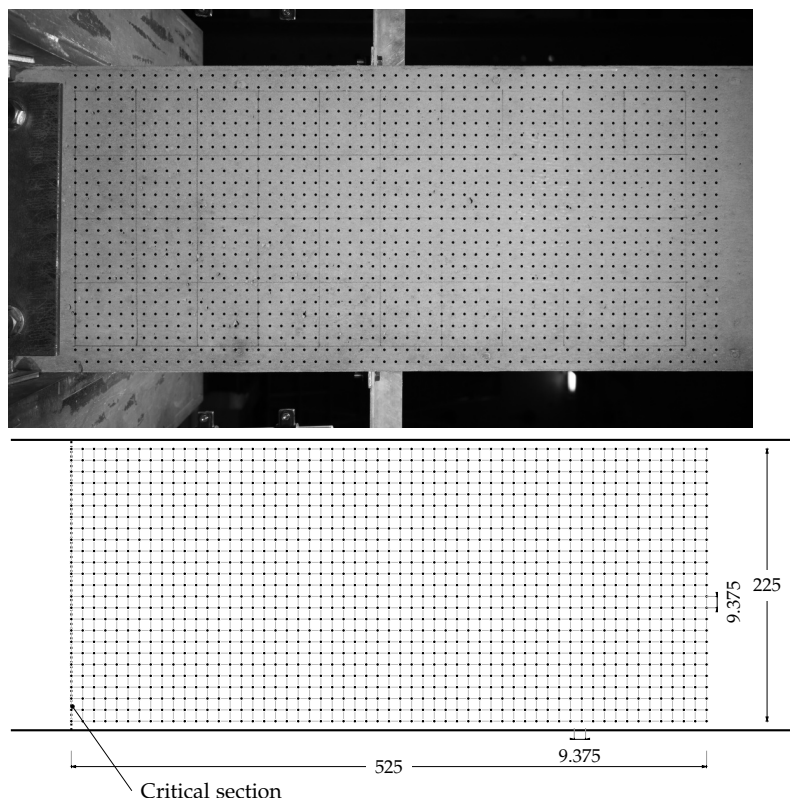
over a region of 525 mm × 225 mm by defining target coordinates at 75 px (9.375 mm) interval over the 4200 px × 1800 px image region as indicated in Figure 4.18. Surface displacement at each of these 1425 target coordinates over the series of photographic records captured throughout the experiment was performed using pattern matching as expressed in Algorithm 4.4. Typical pattern matching algorithms find the target in source image by calculating a mathematically defined correlation over the entire image size and identifying the location of maximum correlation. This fundamental procedure is implemented on lines 4 and 5 using OpenCV implementation of image matching with normalized cross-correlation.

Require: initial $coordinates_i$, undeformed $image_i$, new $image_n$, target *size*

1: convert $image_i$ and $image_n$ to $grayscale_i$ and $grayscale_n$ using `cvtColor`

2: read four *quadrants* of *size* around $coordinates_i$ in $grayscale_i$

3: **for all** *quadrants* **do**

4:     find *correlation* of *quadrants* over $grayscale_n$ using `matchTemplate`

5:     find *location* and *value* of maximum *correlation* using `minMaxLoc`

6: **end for**

7: identify new $coordinates_n$ as the *location* of maximum *correlation* among all four *quadrants*

Algorithm 4.4: Method-B of identifying target locations using OpenCV
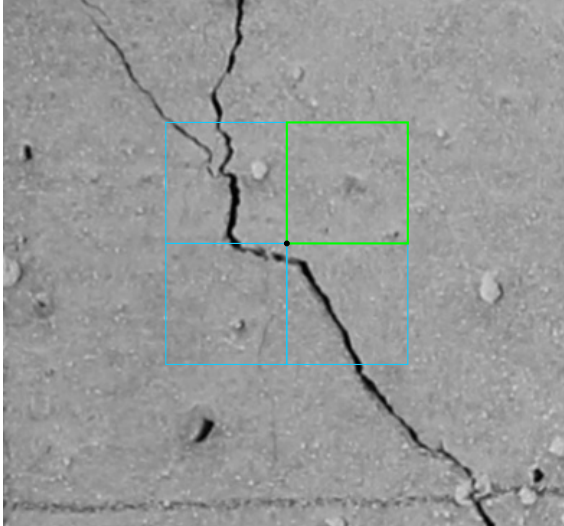
Figure 4.19: Four quadrants around a template coordinate used for template matching in Method-B

In this study, however, the fundamental procedure was adapted for application to concrete surfaces which exhibit cracking. Instead of the conventional method of using a single orientation for finding matching patterns, template images in four different orientations around a single coordinate were used as expressed in Figure 4.19. Although this methodology quadruples the processing time, it proves effective in accurately finding pattern matches even when concrete surface is excessively cracked. Inclusion of cracks in the template image significantly reduces the correlation and increases the probability of finding incorrect matches. Using four templates in four quadrants around the point-of-interest ensures at least one orientation resulting in correct match. Accuracy of pattern-matching algorithm for cracked concrete surfaces is thus ensured through Line 7 of Algorithm 4.4.

It must be noted that the modified template matching algorithm still fails when closely spaced multiple cracks appear on the surface or when fragments of concrete cover spall-off. Quadrants of 25 px (3.125 mm) *size* (on Line 2) were consistently used for finding pattern matches in all specimens.

Method-A processing was comparatively faster as deformations were measured on a coarser grid of 50 mm × 50 mm. Generalized procedure is listed in Algorithm 4.5. Same principles of pattern matching as Method-A were applied with some modifications. Use of only one template image for finding all target locations ensured speed by minimizing correlation calculations. The template image was the sectioned quadrant circular symmetric target patterns detailed previously in Section 3.3.4. In addition to the steps for pattern matching, additional sorting (Line 14) was also required in this method due to multiplicity of the targets. This requirement meant that the analysis could only be performed in the sequence in which photographs were recorded during the experiment.

Require: a quadrant of cropped *target* image, specimen *images*

1: convert *target* and *images* to *grayscale$_t$* and *grayscale$_i$* using `cvtColor`

2: **for all** *images* **do**

3:     convert image to to *grayscale$_i$* using `cvtColor`

4:     **for all** four orientations of *grayscale$_i$* **do**

5:         find *correlation* of *grayscale$_t$* over *grayscale$_i$* using `matchTemplate`

6:         apply a threshold on *correlation* to remove low amplitude peaks using `threshold`

7:         find all local peak *locations* using `imregionalmax`

8:     **end for**

9:     average over *locations* identified in four orientations

10: **end for**

11: sort peak *locations$_1$* from the first image in a rectangular sequence

12: **for all** *locations$_1$* **do**

13:     **for all** *images* **do**

14:         find *location$_n$* in *image* closest to *location$_{n-1}$*

15:     **end for**

16: **end for**

4.3.3 Post-processing

Deformation history measured at each coordinate can be expressed using the general representation illustrated in Figure 4.20. All deformations are defined with respect to the origin at the center of critical section. Vertical grids as denoted as X_i while horizontal grids are denoted as Y_j. Image frame corresponding to each deformation coordinate is indicated in superscript as $X_i Y_j^N$. An illustration of the data obtained through photogrammetric analysis is expressed in the form of cumulative deformation trace over all grid locations obtained using Method-B for specimen SB05 in Figure 4.21.

Easy comprehension of this enormous deformation data is enable by reducing to more conventional response parameters such as strains

$$X_i Y_j^N (x_{ij}^N, y_{ij}^N)$$

i : X grid
j : Y grid
N : Image frame
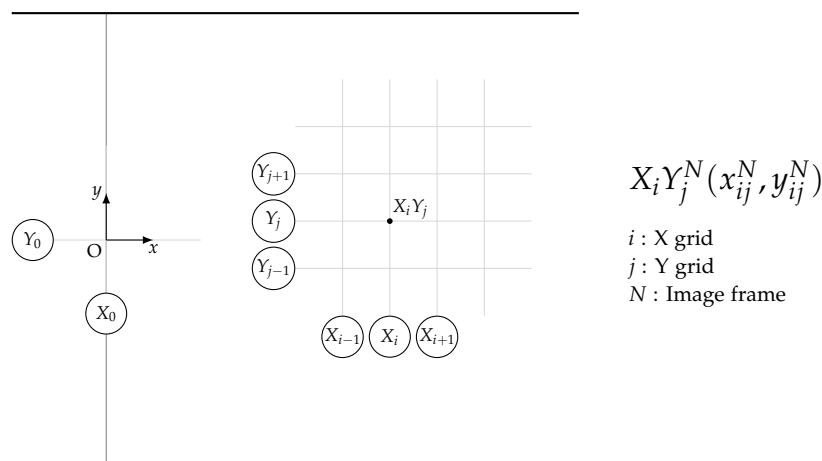
Figure 4.20: General representation of measured photogrammetric coordinates
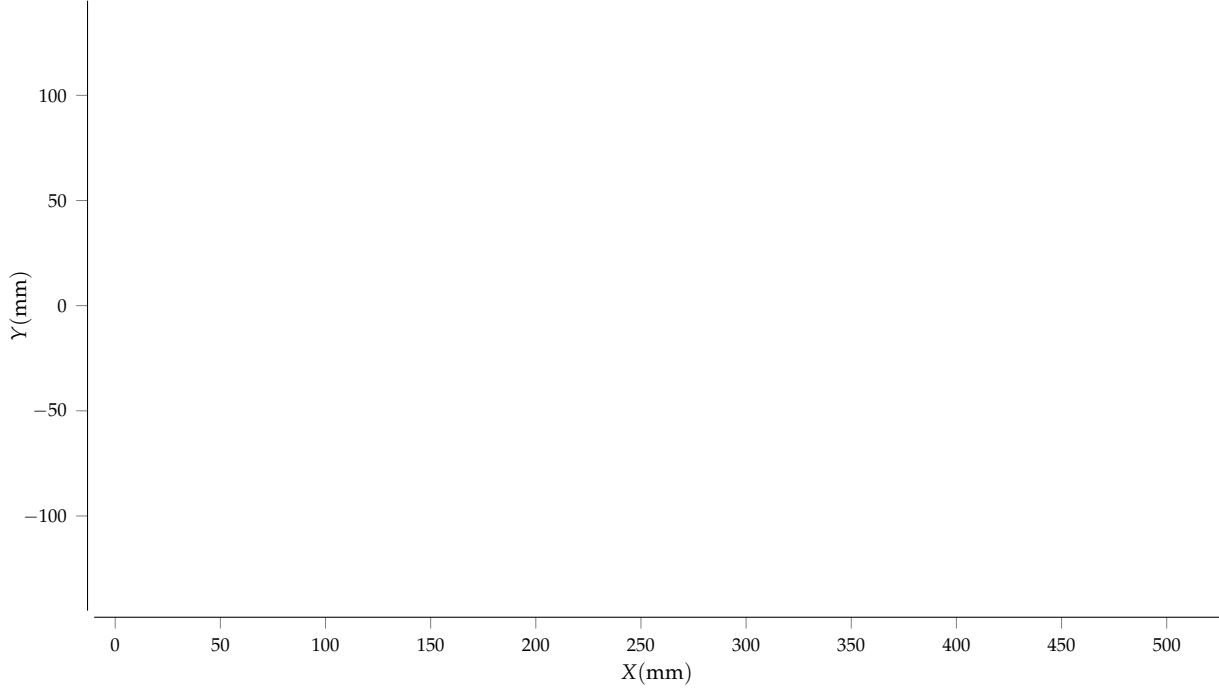
Figure 4.21: Trace of deformation measure at each target through the entire testing duration for specimen SB 05

and rotations. Distance between any two points X_aY_b and X_cY_d is determined at the respective image frame N as:

$$l_{abcd}^N = \sqrt{(x_{ab}^N - x_{cd}^N)^2 + (y_{ab}^N - y_{cd}^N)^2} \tag{4.1}$$

Lateral bulging of the specimen due to widening of inclined cracks is quantified as lateral strain ($\epsilon_{lateral}$). It is calculated at each vertical grid $X_i(i = 1 : U_x)$ by measuring deformation across two the extreme horizontal grids Y_{-U_y} and Y_{U_y} closest to bottom and top sides of the beam respectively. The calculation is mathematically expressed as:

$$\epsilon_{lateral_i}^N = \frac{l_{iU_yi-U_y}^N - l_{iU_yi-U_y}^1}{l_{iU_yi-U_y}^1} \tag{4.2}$$

Axial expansion of the specimen due to accumulation of flexural cracks is quantified as axial strain (ϵ_{axial}). It is calculated at each vertical grid $X_i(i = 1 : U_x)$ by measuring the average deformation across all horizontal grids $Y_j(j = -U_y : U_y)$ as:

$$\epsilon_{axial_i}^N = \frac{\sum_{j=-U_y}^{U_y} l_{ij0j}^N - l_{ij0j}^1}{\sum_{j=-U_y}^{U_y} l_{ij0j}^1} \tag{4.3}$$

Rotation (θ) across the section represented by vertical grid $X_i(i = 1 : U_x)$ is expressed as the inclination between two points on extreme horizontal grids Y_{-U_y} and Y_{U_y} as:

$$\theta_i^N = \tan^{-1}\left(\frac{x_{iU_y}^N - x_{i-U_y}^N}{y_{iU_y}^N - y_{i-U_y}^N}\right) \tag{4.4}$$

Lateral strains calculated as per these definitions over the length of the grid are expressed in figures 4.22 and 4.23. Strain profiles are shown representing the state of the specimen at zero deformation after the completion of 1, 2, and 3 loading cycles at 2 %, 3 % and 4 % target drift. Axial strain profile over the length of the specimen is similarly expressed in figures 4.24 and 4.25. Axial strains are calculated at the peak loading state of 1st, 2nd, and 3rd loading cycles at 2 %, 3 % and 4 % target drift.

Variation of rotation along the length of the member is expressed in Figure 4.26. Again, profiles recorded at peak loading state of each loading cycle at 2 %, 3 % and 4 % target drifts are expressed.

Validity of the photogrammetric data can also be established by comparing with axial strain in the hinge region measured through displacement sensors. Axial strain measured using Method-B at grid X_{27} at a distance of 253.125 mm from the critical section is compared with displacement sensor strain measured at a similar distance of 255 mm as expressed in Figure 4.27.

One of the advantages of expressing concrete surface deformation as photogrammetric data as compared simple photographs is that it enables convenient comparison between two images. Surface deformation data for SB01 obtained from images at peak states in different target drift cycles is imposed with a common origin as expressed in Figure 4.28. Similar representations for all other specimens are attached in Appendix E.

Several observations can be made on the presented photogrammetric specimen response as follows:

· Lateral strain in the hinge region was found to strongly relate to specimen performance. Specimens of SC series which sustained loading to the largest imposed drifts also resulted in the smallest lateral strains. SB series specimens with high ρ_s also developed smaller lateral strains as compared to other specimens. The length over which large lateral strains were observed was also small as compared to other specimens. Specimen SB03 which exhibited smallest drift capacity among all specimens also resulted in extra-ordinarily large later strains.

· Similarly, specimens exhibiting larger drift capacities also developed good axial strain profiles along the height. Increasingly large axial enlargement was observed over the length of the specimen in specimens with high ρ_s. Continuous development of axial strain can be associated with stable flexural performance. Increasing flexural deformations lead to increasingly large flexural cracks. Loss of axial strain accumulation also signals the initiation of strength degradation.

· Specimen rotation profiles exhibit concentration of curvatures in the hinge. Most of the development of rotation takes place in the hinge region while the specimen retains almost the same inclination beyond the hinge.

· Comparison of photogrammetric strain measurement with displacement sensor measurements implies generally similar measure-
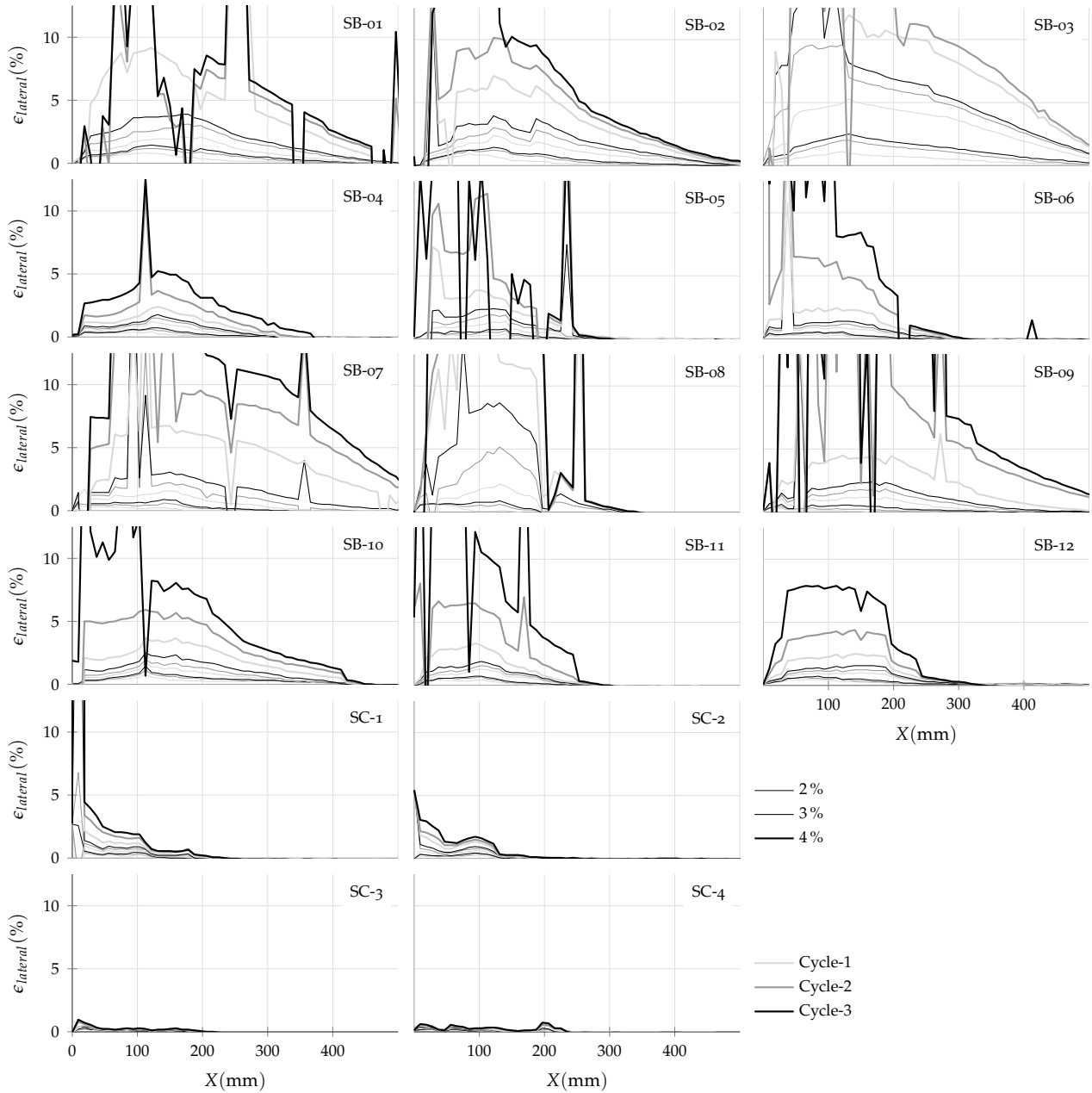
Figure 4.22: Lateral strain profile along the grid length using Method-B
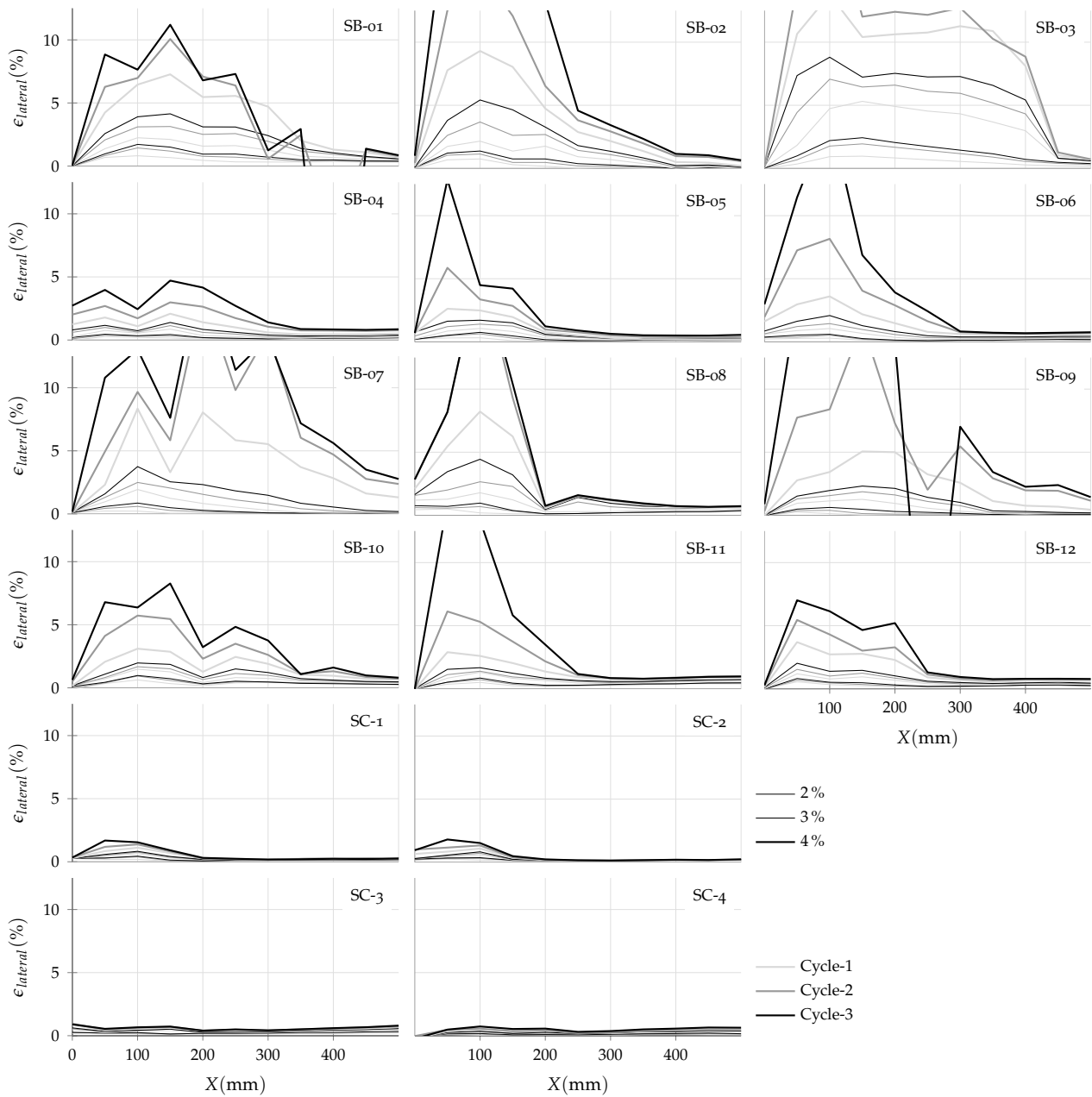
Figure 4.23: Lateral strain profile along the grid length using Method-A
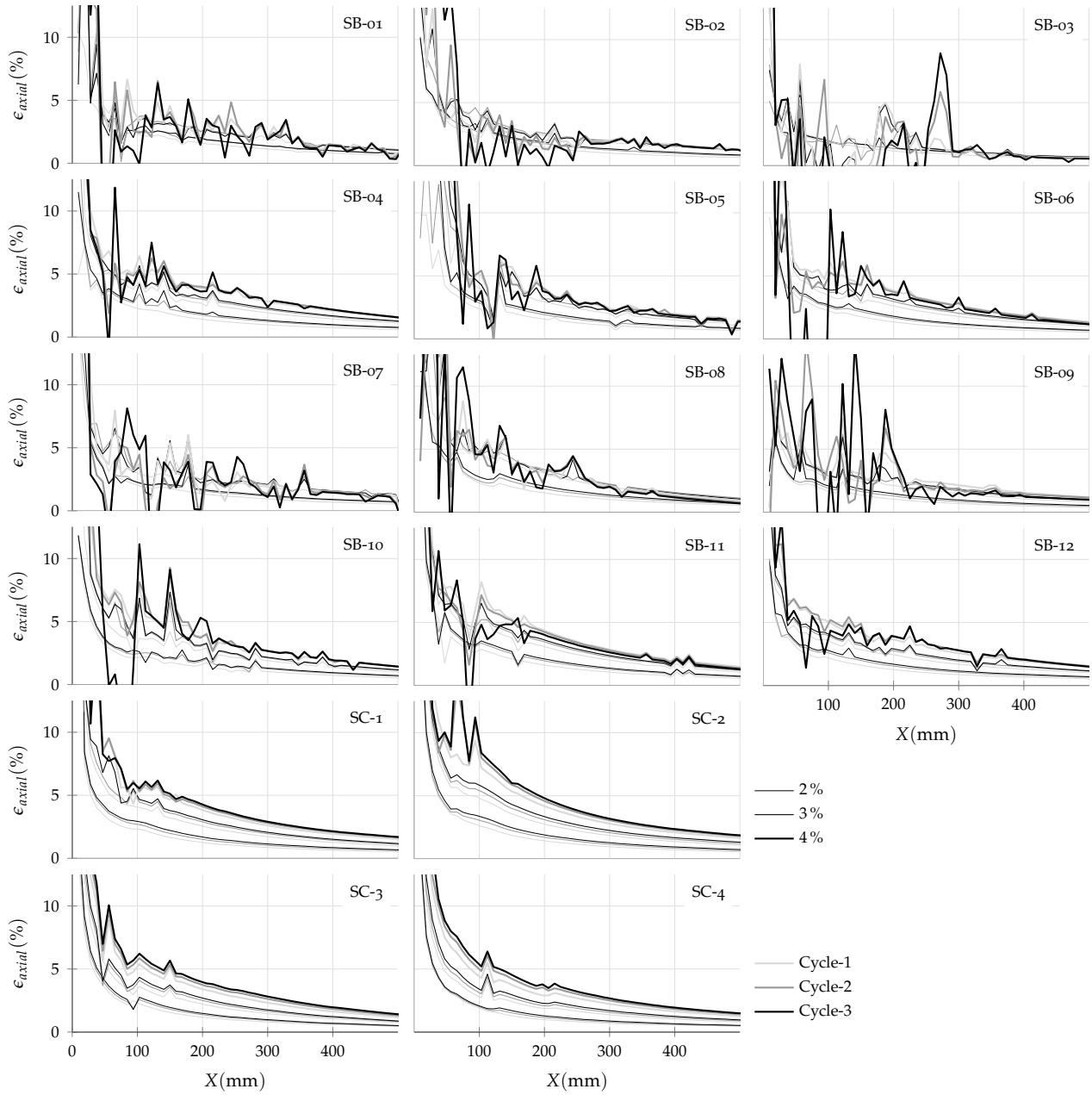
Figure 4.24: Axial strain profile along the grid length using Method-B
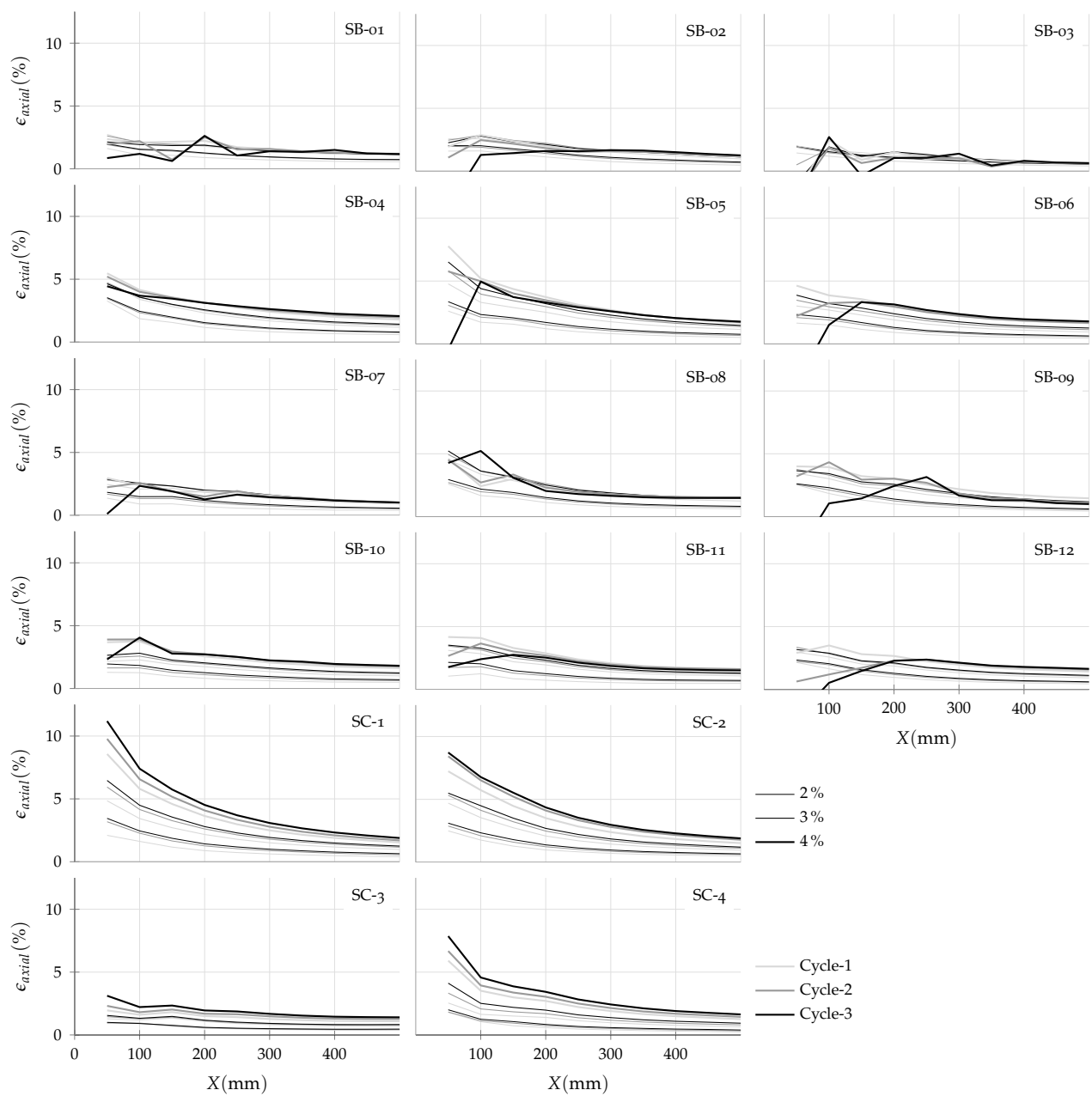
Figure 4.25: Axial strain profile along the grid length using Method-A
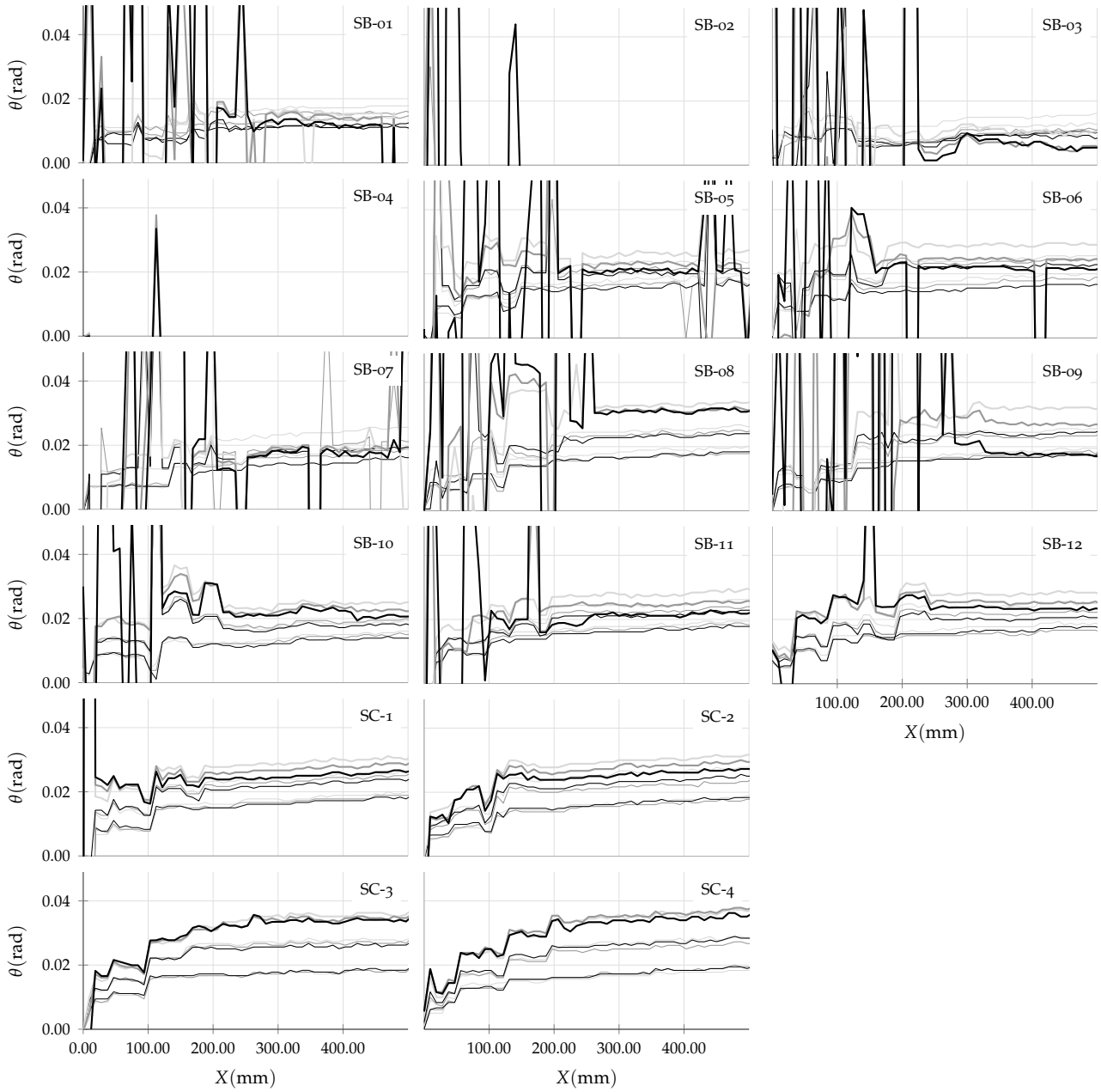
Figure 4.26: Rotation profile along the grid length using Method-B
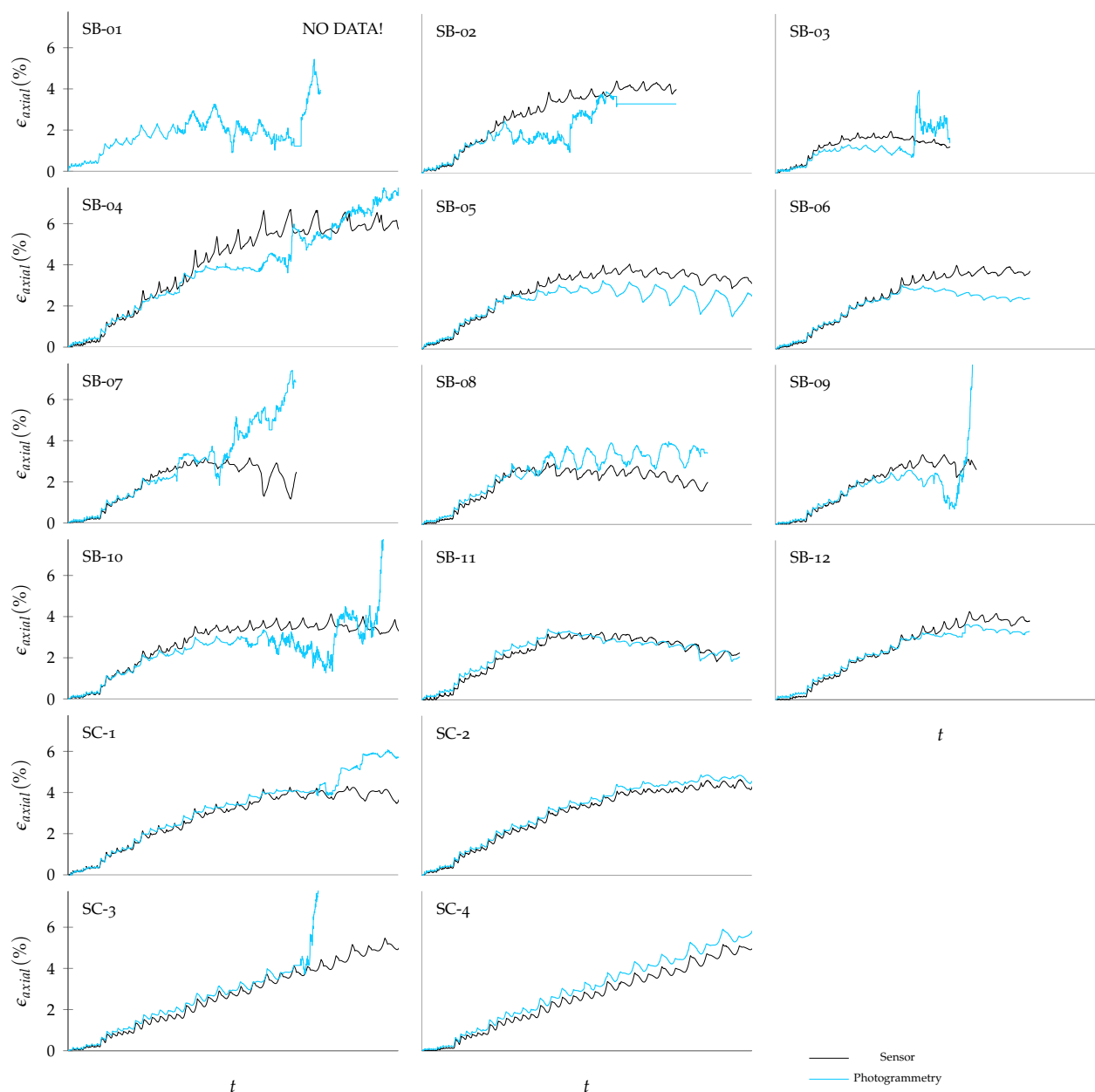
Figure 4.27: Validation of photogramme-tric measurements against displacement sensor measurements
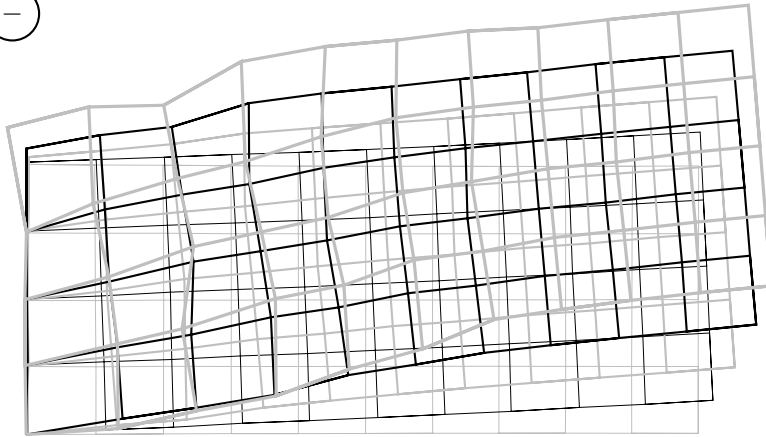
Figure 4.28: Deformed grid shape for specimen SB 04
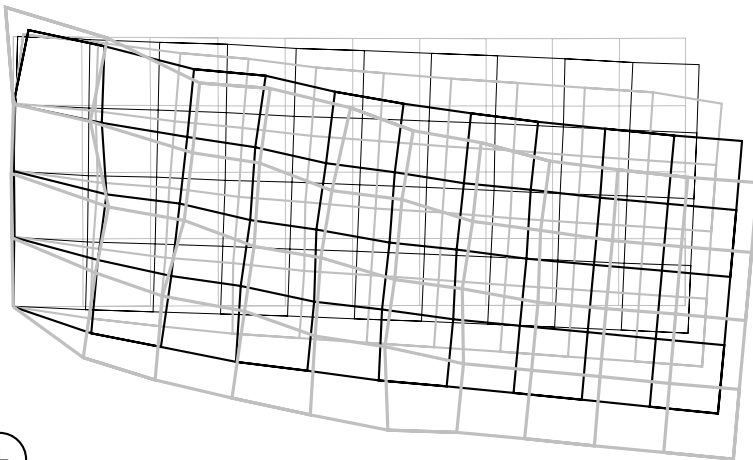
ments. Photogrammetric measurements seem to diverge at large deformations due to spalling of concrete. Also, since the quantity being measured is not exactly similar (average of deformation over top and bottom faces in the case of displacement sensors and average deformation over 24 grid lines across the beam depth in the case of photogrammetry), some deviation at large strains is expected.

5
Discussion

EXPERIMENT results were analyzed to better understand the response mechanism at the ultimate state. Response quantities related to ultimate state are systematically discussed leading to the final proposition on mechanism at ultimate state.

5.1   *Effect of parameters*

SPECIMENS were designed with multiple variations of parameters expected to affect drift capacity. Response of respective specimens are compared to understand the influence of parameters involved on the mechanism at ultimate state. For this comparison, peak cycle resistances and drifts are expressed to show the strength degradation characteristics similar to the one introduced in Figure 4.13. Mean curves are used to compare specimen-to-specimen response instead of two different positive and negative direction curves.

Effect of concrete strength (f_c') can be seen from the comparison expressed in Figure 5.1. Specimen pairs SB01 and SB02, SB04 and SB05, SB07 and SB08, and SB10 and SB11, constructed from normal and high strength concrete respectively, are compared against each other. No significant drift capacity improvement was observed when using high f_c' in most cases. Although the difference was small, even rapid strength deterioration was observed with high f_c' when comparing SB10 and SB11.

Effect of longitudinal reinforcement content (ρ) is explained using the comparison expressed in Figure 5.2. Specimens SB03, SB06, SB09, and SB12 reinforced an extra layer of rebars are compared against specimens SB02, SB05, SB08, and SB11. While an expected increase in strength was observed, deterioration in strength after reaching the peak strength was also more rapid in high ρ specimens. Degradation was also consistently observed at 1 % smaller drifts.

Effect of transverse reinforcement content (ρ_s) is illustrated through the comparison in Figure 5.3. In addition to the specimen pairs SB01 and SB04, and SB03 and SB06 with only two different variations of ρ_s, specimens SB02, SB05, SC1, and SC2 representing four ρ_s variations are also compared. An increase in ρ_s also resulted in larger drift capacities. Consequently, observed ultimate moment strength was also larger following almost constant post yielding stiffness.
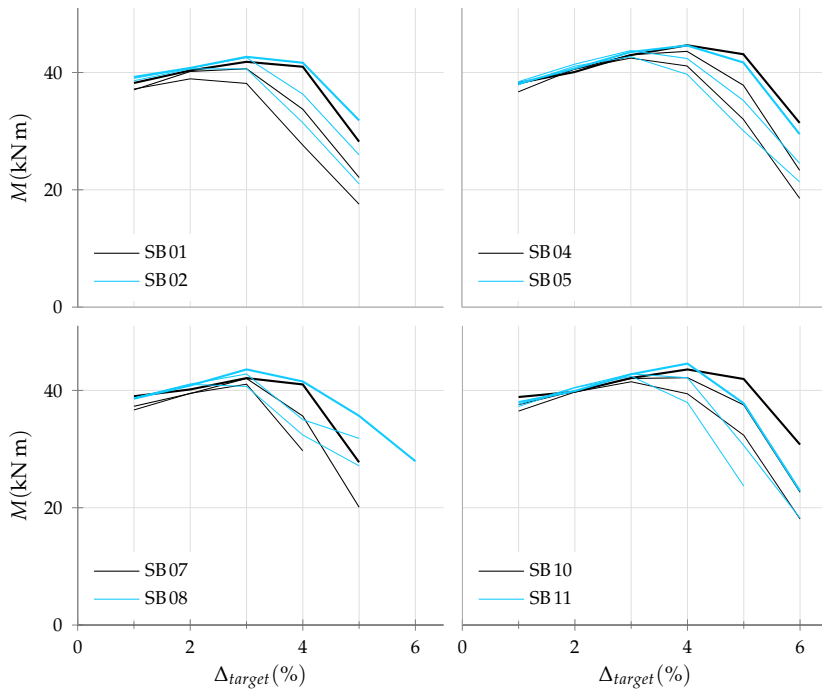
Figure 5.1: Comparison of specimens with different concrete strength
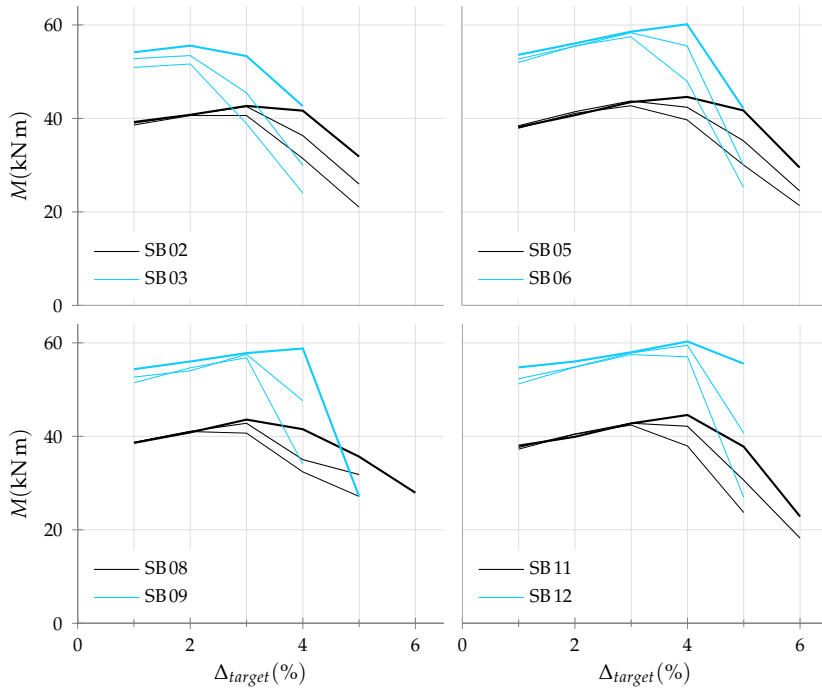
Figure 5.2: Comparison of specimens with different longitudinal reinforcement content
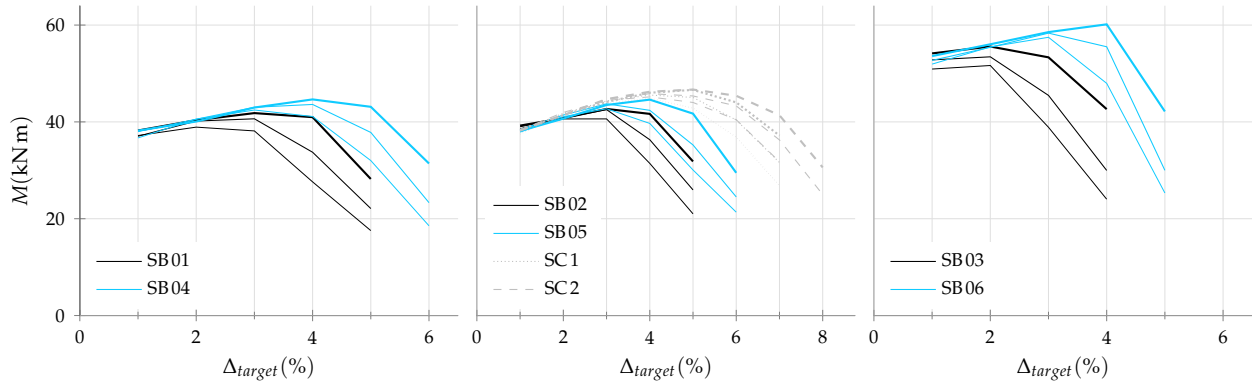
Figure 5.3: Comparison of specimens with different transverse reinforcement content

Effect of longitudinal reinforcement strength (f_{yt}) is explained using the comparison expressed in Figure 5.4. Specimen pairs SB04 and SB10, SB05 and SB11, and SB06 and SB12, having normal and high strength transverse reinforcement respectively, are compared against each other. All the presented comparisons imply almost similar deformation capacities and moment strengths in the specimen pairs.
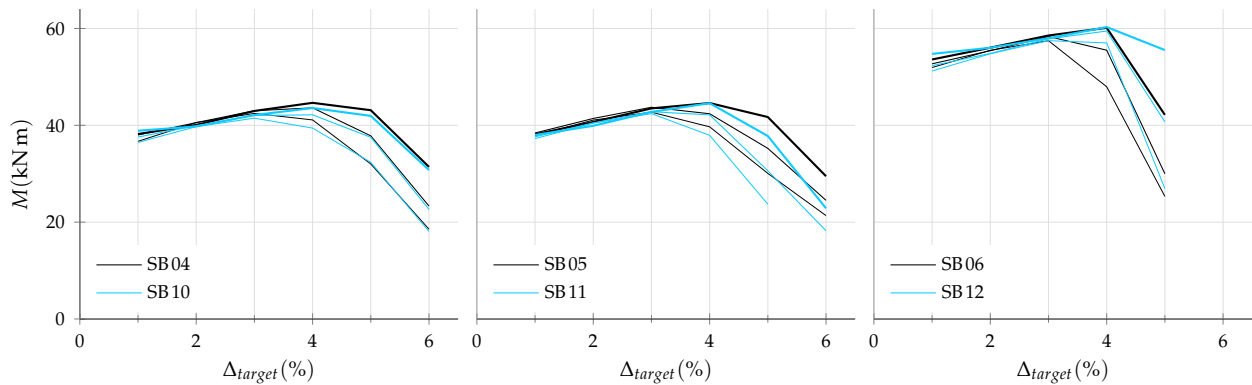
Figure 5.4: Comparison of specimens with different transverse reinforcement grade

Effect of shear-span ratio (l/D) is illustrated using the comparison in Figure 5.5. Between the specimen pairs SB01 and SB17, SB02 and SB08, and SB03 and SB09 no significant impact of l/D on response can be concluded. However, in the SC series specimen pairs SC1 and SC3, and SC2 and SC4, where an even greater difference in l/D was designed, improved drift capacities and strengths were observed with an increase in l/D.

Effect of bar diameter (d_b) is explained using the comparison expressed in Figure 5.6. Marginally smaller drift capacities can be observed in SA3. Note that the moment strength was smaller in SA3 due to difference in reinforcement yield strength.

5.2 Drift capacity

ONE of the main objectives of this study was to investigate the ultimate state response of RC beams. For the specimens such as tested in this study which exhibited stable fleuxral response after yielding,
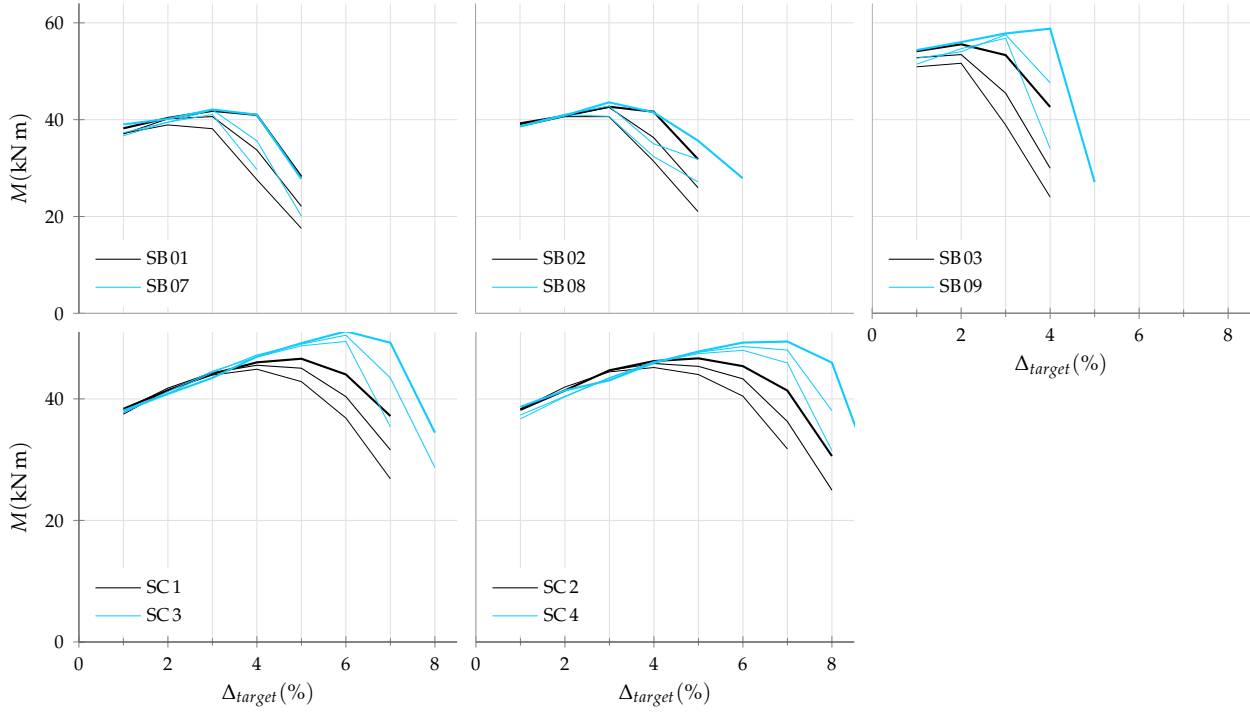
Figure 5.5: Comparison of specimens with different shear-span ratio
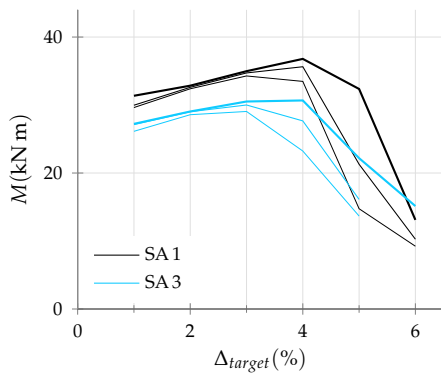
Figure 5.6: Comparison of specimens with different bar diameter

the ultimate drift capacity is the most significant indicator of ultimate state response. Experiment data was analyzed to systematically determine the exhibited drift capacity. Observations were also compared with existing methods for estimating drift capacity.

5.2.1 Definition

BEFORE any discussion on experimentally observed drift capacity can be organized, it is imperative to clearly define the drift capacity. Deformation characteristics of materials are often quantified by the deformation at a fractional loss of strength capacity. In reinforced concrete research, deformation at 10 % or 20 % loss of strength has often been reported as deformation capacity.

In monotonic loading tests, which is often the case for characterizing materials, this definition results in a clear and definitive value. For cyclic loading tests, however, multiple interpretations are possible. Disregarding the cyclic phenomenon and reporting deformation at 20 % loss of overall resistance as capacity (Δ_{cap}) is the commonly considered definition of deformation capacity. Since cyclic tests are aimed at quantifying the effects repeated loadings, it is arguable to consider resistance observed at the end of all cycles (Δ_{cap}^3) at a given deformation level as the representative resistance. This definition may result in slightly greater capacities as the reference peak resistance is itself smaller than the overall peak resistance due to the effects of cyclic strength deterioration. For load tests conducted in simulation of seismic events, it may be reasonable to ignore the effects of cyclic loading at large deformation since most earthquakes exhibit fewer oscillations of large deformation (Δ_{cap}^1). This definition also results in markedly greater capacities as cyclic strength deterioration at large deformation is neglected.

One inherent limitation of using fractional loss of resistance for quantifying deformation capacity in cyclic loading test is the lack of variability among different results. Since loading is always performed to discrete target deformation levels and peak resistance is also observed at peak deformation, the resulting deformation capacity is limited to the discrete values of target deformation adopted for the loading. Neither does this definition capture the effects of rapid or gradual loss of strength. In light of these limitations, using interpolations between discrete target deformations may be suggested as one possible way to define deformation capacity ($\Delta_{cap_i}^1$, $\Delta_{cap_i}^3$).

An alternative way to quantify deformation characteristics of materials may be found through the parameters used in the definition of hysteresis models. Also, given the fact that many recent design procedures allow the use of such models to analyze and quantify building performance, quantification of model parameters would be more useful than finding ultimate deformation capacities. Ibarra et al.[1] proposed a strength and stiffness degrading model defined around a capping point. While the capping point is defined on the monotonic loading curve, it is possible to identify the deformation

[1] L. F. Ibarra et al. "Hysteretic models that incorporate strength and stiffness deterioration". In: *Earthquake Engineering & Structural Dynamics* 34.12 (2005), pp. 1489–1511. DOI: 10.1002/eqe.495.

at capping point by observing the occurrence of negative loading stiffness in the hysteretic response curve ($\Delta_{cap_{cap}}$).

Finally, the classical definition of capacity, deformation at the peak resistance may be considered as another definition of drift capacity (Δ_{cap_m}, $\Delta^1_{cap_m}$, $\Delta^3_{cap_m}$).

ALL plausible definitions of drift capacity discussed above are illustrated through an example in Figure 5.7. Experimentally observed drift capacities accordingly deduced for all specimens in both positive and negative loading directions are listed in Table 5.1. Same data is also expressed graphically in figures 5.8 and 5.9. Note that $\Delta_{cap_{cap}}$ is not listed this data as throughout the experiments negative stiffness was not identified in any of the specimen tests.

Different definitions generally resulted in 2 % to 3 % variation in identified capacity. While the variation was small for specimens that exhibited rapid loss of strength (SB03, SB06, and SB−9), gradually degrading specimens resulted in larger variation of identified drift capacity. Identified drift capacities for SC2 were spread over a range as large as 4 %.

By definition, quantifying capacity as the deformation at the point of maximum resistance resulted in severest drift capacities (Δ_{cap_m}, $\Delta^1_{cap_m}$, $\Delta^3_{cap_m}$). Also unsurprisingly, ignoring cyclic effects is defining Δ^1_{cap} resulted in largest drift capacities in all specimens.

Comparatively smaller variations were noted in the drift capacities observed in negative loading direction. In fact, $\Delta^1_{cap_m}$ and $\Delta^3_{cap_m}$ were identical in negative loading direction for all specimens. Compared to the positive loading direction, drift capacities in negative direction were up to 1 % smaller.

5.2.2   *Comparison*

Numerous existing technologies on estimation of ultimate drift capacity of RC members were discussed in Chapter 2[2]. Drift capacity estimation equations available in the literature were used to calculate capacity for the specimens and compare with experimental observations.

[2] See page 15.

Panagiotakos and Fardis[3] proposed estimating ultimate capacity (Δ_{PF}) using an empirical relation considering the effects of concrete strength, shear span ratio, and confinement provided by transverse reinforcement. Although their formulation provides an optional parameter to include the contributions of reinforcement slip to total deformations, slip coefficient was set to zero in present calculations.

[3] Refer equation 9 on page 140 of Panagiotakos and Fardis, op. cit.

Haselton et al.[4] proposed another empirical relation by calibrating parameters of a mathematical hysteresis model. They determined plastic deformation at peak resistance using transverse reinforcement ratio, concrete strength, a rebar buckling coefficient defined by bar diameter, hoop spacing, and longitudinal reinforcement yield strength as parameters. An estimate of stiffness was proposed using shear span ratio as parameter. Deformation at peak resistance (Δ_H) was

[4] Refer equation 3.10 on page 40 of Haselton et al., op. cit.
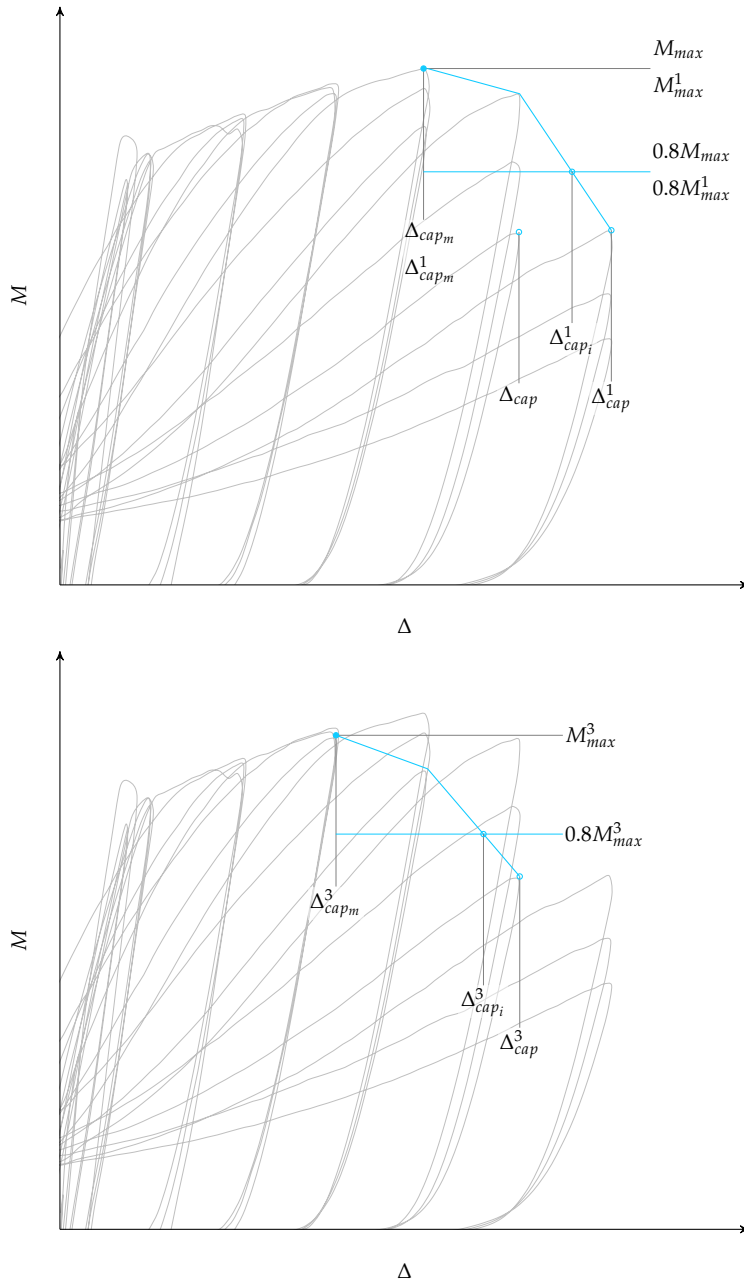
Figure 5.7: Definitions of drift capacity

Table 5.1: Experimentally observed drift capacity

	Overall		1st Cycle			3rd Cycle		
	Δ_{cap}	Δ_{cap_m}	Δ^1_{cap}	$\Delta^1_{cap_i}$	$\Delta^1_{cap_m}$	Δ^3_{cap}	$\Delta^3_{cap_i}$	$\Delta^3_{cap_m}$
SA1	5.37	4.28	6.05	5.25	3.94	5.01	4.37	2.97
	−5.04	−4.24	−6.01	−5.01	−2.97	−5.01	−4.30	−2.97
SA2	5.37	5.29	5.98	5.57	4.94	5.92	5.03	3.97
	−5.38	−5.32	−6.03	−5.75	−3.98	−6.03	−5.08	−3.98
SA3	4.31	3.20	5.08	4.80	2.98	3.99	3.99	2.99
	−4.15	−4.22	−5.03	−4.71	−3.02	−5.01	−4.03	−3.02
SB01	3.99	2.94	5.00	4.75	3.00	4.00	3.72	1.99
	−3.95	−2.97	−5.00	−4.48	−2.00	−4.00	−3.62	−2.00
SB02	4.01	3.99	5.00	4.94	4.00	4.01	3.94	3.01
	−4.01	−2.98	−5.00	−4.51	−2.00	−4.01	−3.77	−2.00
SB03	2.98	1.83	3.99	3.90	2.00	3.00	2.73	2.00
	−3.00	−1.99	−3.99	−3.76	−2.00	−3.00	−2.91	−2.00
SB04	5.00	3.97	6.00	5.53	4.00	5.00	4.66	3.00
	−5.03	−3.89	−6.01	−5.79	−3.01	−6.00	−5.01	−3.01
SB05	4.99	3.96	6.00	5.57	4.00	5.00	4.61	3.00
	−4.96	−3.97	−6.01	−5.42	−3.00	−5.01	−4.55	−3.00
SB06	4.95	3.95	5.00	4.77	4.00	5.01	4.11	3.00
	−4.01	−3.99	−5.00	−4.60	−3.01	−5.01	−4.06	−3.01
SB07	3.96	3.95	5.00	4.65	4.00	4.00	3.85	3.00
	−4.03	−2.97	−5.00	−4.38	−3.00	−4.00	−3.63	−3.00
SB08	5.00	2.99	6.00	5.52	3.00	5.00	4.70	2.00
	−3.99	−2.90	−5.00	−4.71	−2.00	−4.01	−3.66	−2.00
SB09	3.94	2.98	5.16	4.57	3.00	4.00	3.72	3.00
	−3.71	−3.91	−5.01	−4.30	−3.00	−4.00	−3.39	−3.00
SB10	5.02	3.97	6.00	5.59	4.00	5.00	4.69	3.00
	−5.00	−3.91	−5.99	−5.67	−3.00	−6.00	−5.05	−3.00
SB11	4.95	3.98	6.00	5.24	4.01	5.00	4.36	3.00
	−4.89	−3.98	−6.00	−5.03	−3.00	−5.01	−4.18	−3.00
SB12	5.00	3.87	5.01	5.01	4.00	5.00	4.40	3.00
	−5.04	−4.00	−5.02	−5.02	−3.00	−5.00	−4.34	−3.00
SC1	6.96	5.09	7.00	0.00	4.99	7.01	6.25	4.00
	−6.00	−4.99	−7.02	−6.83	−4.00	−6.00	−5.93	−4.00
SC2	7.01	5.03	8.00	7.41	5.01	7.01	6.58	4.01
	−6.96	−4.95	−8.01	−7.34	−4.00	−7.00	−6.44	−4.00
SC3	7.17	6.08	8.00	7.98	6.00	7.98	6.99	5.00
	−7.10	−6.09	−7.99	−7.38	−6.01	−7.01	−6.56	−6.01
SC4	8.14	7.14	8.97	8.34	7.00	8.01	7.64	6.00
	−8.17	−6.12	−8.97	−8.28	−5.99	−8.04	−7.44	−5.99
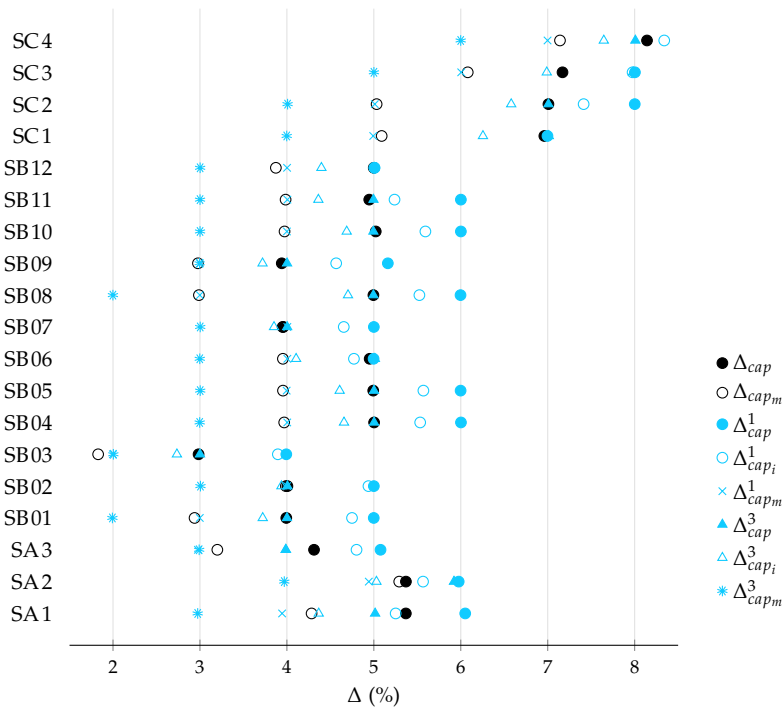
Figure 5.8: Experimentally observed drift capacity in positive direction loading
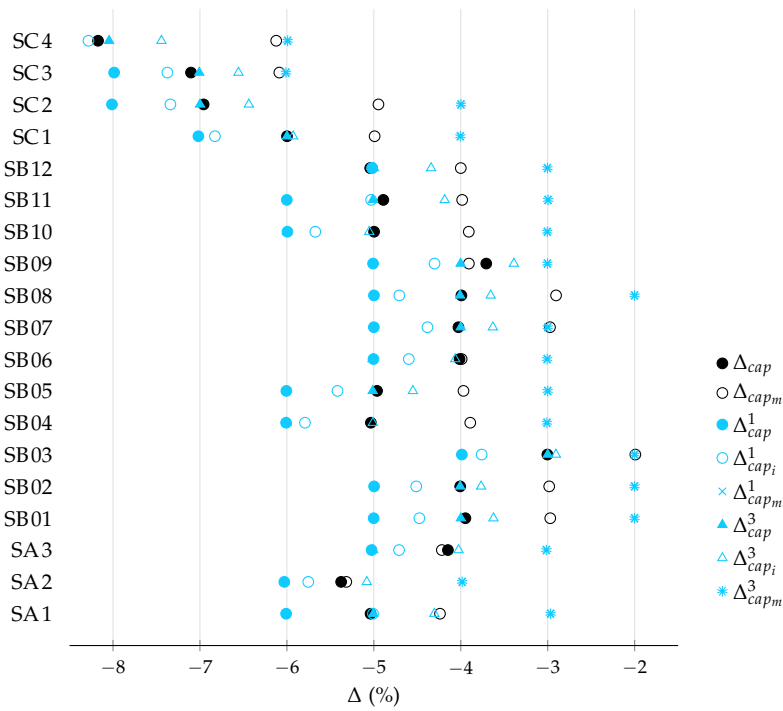
Figure 5.9: Experimentally observed drift capacity in negative direction loading

calculated as the sum of estimated plastic deformation and yield deformation. Yield deformation was calculated using the provided stiffness and yield moment calculated as per Panagiotakos and Fardis.[5]

Berry and Eberhard[6] used experimental data on bar buckling to empirically define deformation at the initiation of bar buckling (Δ_{BE}) in RC members. They used shear span ratio, bar diameter, transverse reinforcement ratio, concrete strength, and transverse reinforcement yield strength as parameters.

ASCE 41-13[7] provided guidelines for estimation of modelling parameters for RC beams. For flexure controlled members plastic rotation at peak resistance is defined based on a shear stress coefficient and conformity or non-conformity of the transverse reinforcement. Total deformation at peak (Δ_{ASCE}) was estimated as the sum of plastic and yield deformations. Suggested effective stiffness[8] and yield moment calculated in Section 4.1 were used to determine deformation at yield.

Architectural Institute of Japan[9] proposed estimating ultimate state of an RC member on the concept of shear strength deterioration with increasing plastic deformation. Shear strength defined in terms of the plastic deformation is used to back-calculate the plastic deformation at which the shear strength deteriorates below the level at maximum moment. Total deformation (Δ_{AIJ}) is calculated as the sum of plastic and yield deformations.

It must be noted that none of the presented above consider the effect of number of cyclic repetitions on drift capacity.

RESULTS of the calculated drift capacities for all the specimens are listed in Table 5.2. Same data is also expressed graphically in Figures 5.10 and 5.11. Also indicated for reference is the experimentally observed capacity Δ_{cap} (average of the capacity observed in positive and negative loading directions). ASCE 41-13 predictions were consistently the most conservative and also the only predictions that were uniformly conservative for all specimens. Except for Berry and Eberhard's estimates which were also generally conservative, all other estimates revolved around the mean. AIJ predicted drift capacities were consistently more close to the experimental observations than any of the considered estimates. For specimens of SC-series which exhibited largest drift capacities in the experiment, however, Haselton et al.'s or Panagiotakos and Fardis's predictions were comparatively closer.

Direct comparison among various estimates discussed above makes little sense since respective definitions of ultimate capacity are not directly comparable. Panagiotakos and Fardis interpreted drift capacity with "distinct reduction of the reloading slope, and the area of the hysteresis loops and the peak force, in comparison with those of the preceding cycle(s)" which was typically found to "coincide with a drop in peak force exceeding 15 % of the ultimate force". This definition would seem to correspond to Δ_{cap}. Haselton et al.'s estimates plastic deformation capacity correspond to the capping point on the monotonic response curve, identified as $\Delta_{cap_{cap}}$ in the discussion

[5] Refer equation 6 on page 137 of Panagiotakos and Fardis, op. cit.

[6] Refer equation 3.10 on page 1066 of Berry and Eberhard, op. cit.

[7] Refer Table 10-7 on page 192 of American Society of Civil Engineers. *Seismic evaluation and retrofit of existing buildings (ASCE/SEI 41-13)*. Reston, VA, 2013. ISBN: 978-0-7844-7791-5.

[8] Refer Table 10-5 on page 186 of ibid.

[9] Refer section A5 of Architectural Institute of Japan. *Guidelines for performance evaluation of earthquake resistant reinforced concrete buildings (Draft)*. Tokyo, Japan, 2004. ISBN: 978-4-8189-0552-8.

	Δ_{PF}	Δ_H	Δ_{BE}	Δ_{ASCE}	Δ_{AIJ}
SA1	4.53	4.72	3.41	2.96	4.63
SA2	4.53	4.68	3.38	2.95	4.65
SA3	4.52	3.86	3.22	2.87	4.74
SB01	4.32	4.03	3.16	2.50	3.13
SB02	4.59	3.08	3.05	2.26	3.47
SB03	4.60	3.35	3.05	2.25	2.84
SB04	4.77	5.78	3.37	3.03	4.38
SB05	4.78	4.57	3.16	2.76	4.65
SB06	4.79	4.92	3.15	2.81	4.40
SB07	4.81	4.23	4.94	3.29	4.81
SB08	5.15	3.14	4.77	2.86	4.96
SB09	5.16	3.44	4.77	2.51	3.90
SB10	5.90	5.74	3.80	3.03	4.40
SB11	5.19	4.54	3.38	2.76	4.65
SB12	5.20	4.89	3.38	2.81	4.45
SC1	5.15	5.60	3.29	2.74	4.87
SC2	6.31	7.66	3.73	2.74	4.90
SC3	6.16	5.53	7.26	2.94	5.49
SC4	7.22	7.55	8.17	2.93	5.51

Table 5.2: Drift capacity (in %) predictions from literature
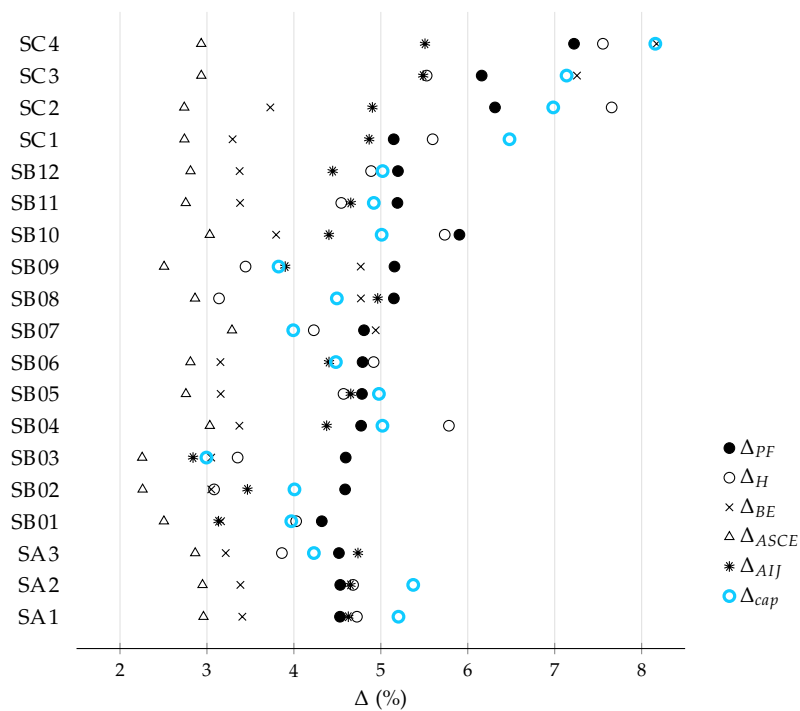
Figure 5.10: Predictions of drift capacity from literature
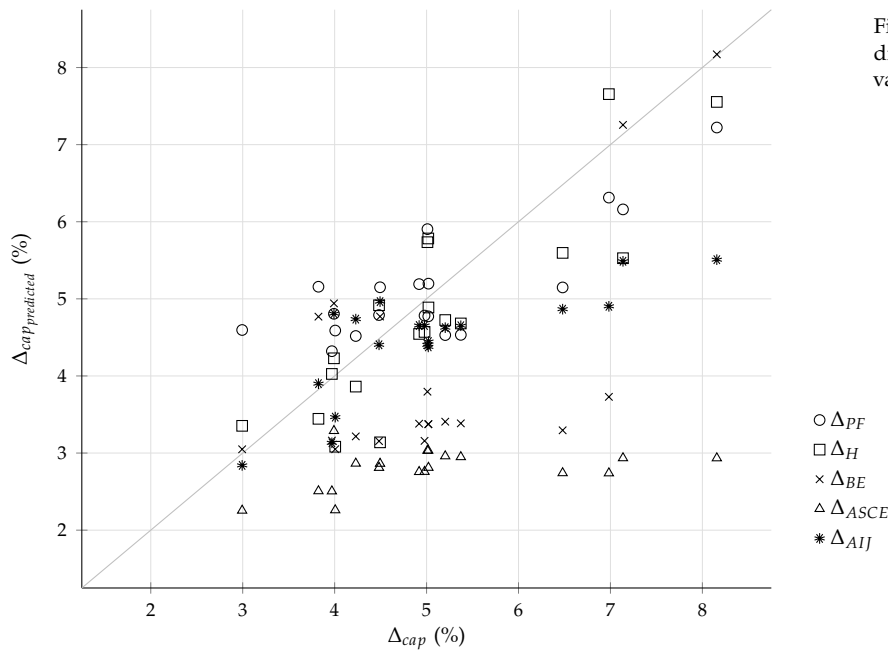
Figure 5.11: Comparison of predicted drift capacity with experimental observation

on drift capacity definitions. Since Berry and Eberhard's estimates determine the point of initiation of bar buckling, it is reasonable to identify their definition with the capacity observed just before loss of strength (Δ_{cap_m}). ASCE 41-13 modelling parameters correspond to the envelope of element response. Plastic rotation at peak thus determined therefore naturally corresponds to Δ_{cap_m}. Similarly, AIJ estimate of drift capacity as deformation at the occurrence of shear failure also corresponds to Δ_{cap_m}.

Comparison of respective predictions against the adjusted drift capacities is expressed in Figure 5.12. Scatter in the observed data is visibly increased as compared to Figure 5.11. And AIJ predictions no longer offer the closest approximations to the experimental observations. Note that Haselton et al.'s estimates are not indicated since the corresponding experimental value $\Delta_{cap_{cap}}$ was not observed in any of the experiments.

PREDICTION of response at ultimate state is not limited to a single drift capacity value. Indeed, some of the literature listed above discuss the response envelope or post-yield characteristics in addition to drift capacity. Such quantities are further deduced to enable better comprehension predicted response in contrast to the experimental observations.

Haselton et al. provide empirical estimates for all relevant quantities on the backbone curve including post-yielding stiffness and post-capping stiffness. Similary, AIJ guidelines also provide clear definitions for all points on the load-response curve including the cracking point. For the definition of maximum moment strength, however, proposed equations for estimating ultimate concrete strain resulted in ridiculously small values due to small confining factor

in current specimen sections. An approximate of ultimate strain as 0.45 % was use instead. ASCE 41-13 also defines plastic rotations at the peak and post capping limit but ignores any stiffness in the post-capping branch. Post-yielding branch was constructed using $1.25M_{nm}$ as the peak moment since no specific post-yielding stiffness values were available.

Resulting backbone curves are displayed against experimentally observed moment-drift response in figures 5.13 and 5.14. As before, ASCE 41-13 predicted backbone is largely conservative in terms of the deformation capacity. Haselton et al.'s backbone curve forms an envelope over the experiment response. AIJ predicted stiffness of the post-yielding branch was inappropriate due to unrealistically low estimation of maximum moment.

Since it was demonstrated in Section 4.2 that the hinge rotation (θ_{hinge}) is not the same as member drift (Δ), it might be reasonable to compare ASCE 41-13 backbone curve with experimentally observed moment-hinge rotation response as ASCE 41-13 defines plastic hinge rotation as the generalized deformation parameter.[10] This comparison is expressed in figures 5.32 and 5.33. ASCE 41-13 backbone curve provides a conservative envelope to the specimen response. The conservatism seems especially pronounced for specimens with high transverse reinforcement content. Note that on the rotation response curve, however, ASCE 41-13 enforced limiting deformation offer a better representation of the experimental response.

[10] Refer Clause 10.4.2.2 on page 193 of American Society of Civil Engineers, op. cit.

5.3 Ultimate strength and post-yielding stiffness

ULTIMATE moment reported in Section 4.1 was observed to be consistently lower than the estimated value. Ultimate strength was
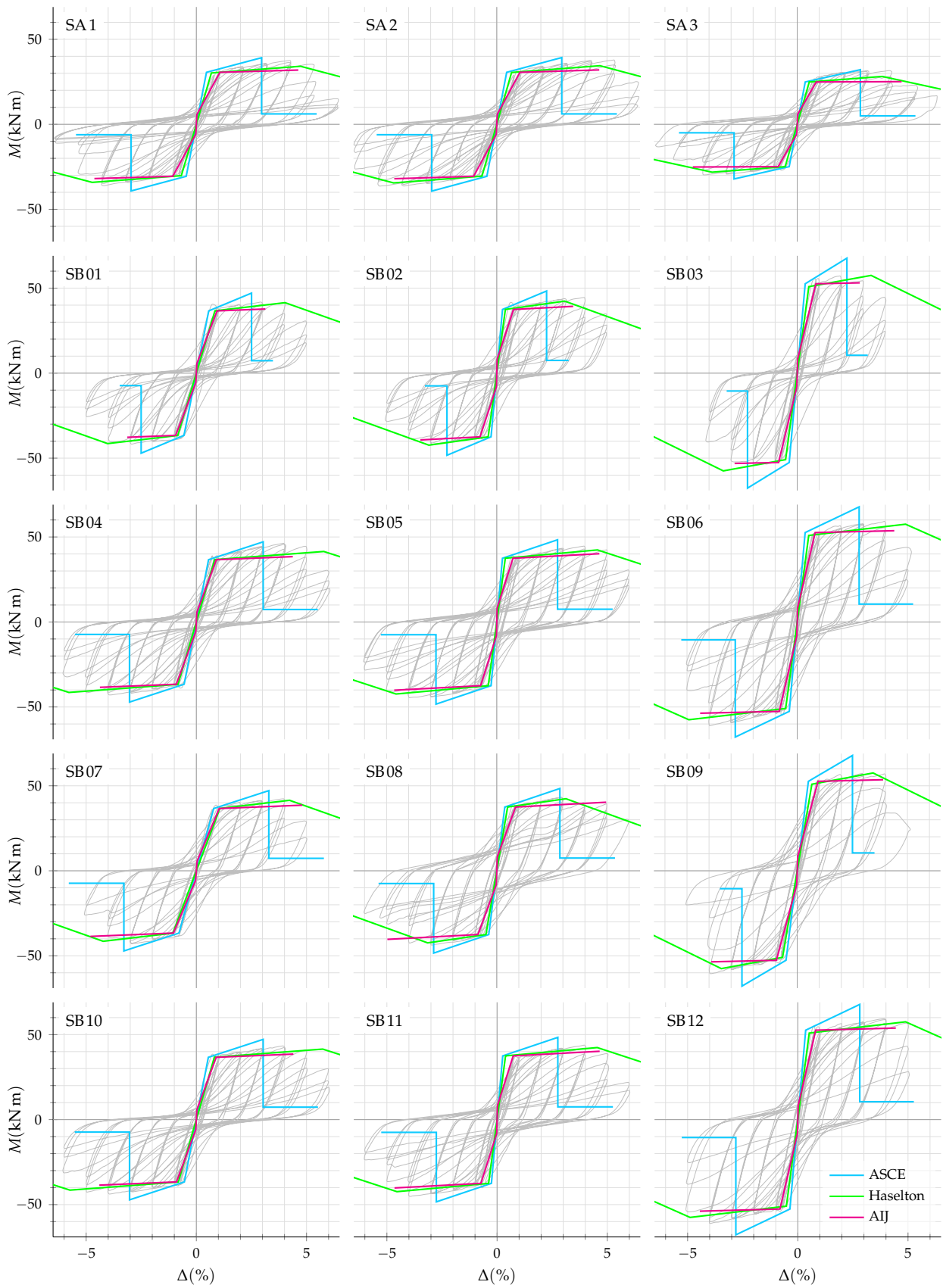
Figure 5.13: Moment-drift response and estimated capacity models (SA and SB series)
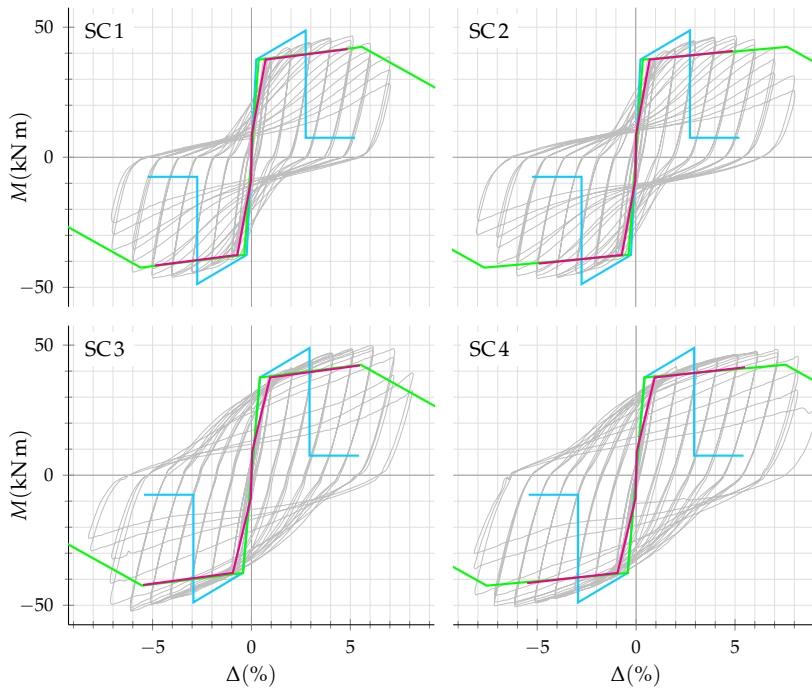
Figure 5.14: Moment-drift response and estimated capacity models (SC series)

estimated as 1.25 times the nominal moment strength as a reflection of ACI 318-14 code[11] where steel stress equal to 1.25 times the yield stress is required to be used to estimate the maximum moment that can develop in flexural members. Alternate strategies were therefore considered to better estimate the ultimate moment strength.

First alternate (M_{u_1}) was simply based on using a fixed maximum concrete strain and steel stress to estimate strength at ultimate state. Concrete material tests suggested a maximum strain larger than the code recommended 0.3 %, a larger value of 0.45 % was used. And since the actual steel stress to yield stress (f_s/f_y) value of 1.25 was previously illustrated to result in larger ultimate strengths, a smaller value of 1.15 was used. Ultimate strength was then calculated based on section analysis using the code defined stress block and Bernoulli's assumption.

In the second alternative (M_{u_2}), similar section analysis was performed but using actual stress strain distribution of steel and concrete instead. Concrete stress-strain distribution was based on Mander et al.[12]'s unconfined concrete model and stress-strain recorded from tensile tests of rebars was used as steel stress-strain distribution.

In the third alternative (M_{u_3}), confined model of concrete as proposed by Mander et al.[13] was used to represent the state of stess of core concrete. Instead of using the defined expressions[14] for finding the confining strength ratio, the chart[15] suggested for sections such as beams with low confinement was used of fig.4 was used. Resulting confinement effectiveness was of the order of 2 % to 5 %.

Resulting moment strengths for each specimen section are indicated in Table 5.3. Also indicated alongside are the resulting ratio of steel stress at ultimate state of yield stress (f_s/f_y) and the maximum

[11] Clause R18.6.5 on page 279 in American Concrete Institute, op. cit.

[12] J. B. Mander et al. "Theoretical stress-strain model for confined concrete". In: *Journal of Structural Engineering, ASCE* 114.8 (1988), pp. 1804–1826. DOI: 10.1061/(ASCE)0733-9445(1988)114:8(1804).

[13] Ibid.

[14] See equation 29 on page 1812 of ibid.

[15] See fig.4 on page 1813 of ibid.

strain of compressive concrete (ϵ_c). The same data is also expressed in the from of a graph in Figure 5.15 for comparison. While the unconfined model results in a rather low estimate of ultimate strength, confined model estimates are higher and closer to experimentally observed strengths. Some estimates for the confined case significantly exceed the observed strength. This may be attributed to the fact that the adopted confined was developed for column applications and does not result in good representations for beams.

Table 5.3: Post-yielding stiffness and ultimate moment strength

	k_y/EI		k_s/k_y(%)		M_{u_1}			M_{u_2}			M_{u_3}		
					M_u	ϵ_c%	f_s/f_y	M_u	ϵ_c%	f_s/f_y	M_u	ϵ_c%	f_s/f_y
SA1	0.16	0.17	5	5.2	33.4	0.45	1.15	32.3	0.4	1.09	44.7	0.84	1.27
SA2	0.15	0.18	4.2	3.6	33.5	0.45	1.15	32.1	0.4	1.08	39.4	0.82	1.27
SA3	0.16	0.22	4.8	2.5	25.3	0.45	1.15	23.8	0.4	1	29	0.8	1.22
SB01	0.26	0.27	3.2	3	40.3	0.45	1.15	39	0.4	1.07	45	0.67	1.24
SB02	0.14	0.12	2.2	3.2	42.6	0.45	1.15	40.9	0.4	1.12	44.3	0.53	1.21
SB03	0.16	0.14	1.7	2.3	54	0.45	1.15	51.6	0.4	1.01	56.3	0.53	1.1
SB04	0.25	0.27	4.6	3.3	40.4	0.45	1.15	39.1	0.4	1.07	49.8	1.09	1.37
SB05	0.12	0.21	4.2	1.9	42.7	0.45	1.15	41.2	0.4	1.13	47.2	0.75	1.3
SB06	0.15	0.19	2.8	2.6	54.2	0.45	1.15	52.1	0.4	1.02	60.3	0.74	1.19
SB07	0.3	0.32	2.2	4.2	40.4	0.45	1.15	39.1	0.4	1.07	44.9	0.66	1.23
SB08	0.16	0.19	4.4	3.9	42.7	0.45	1.15	41.1	0.4	1.12	44.3	0.53	1.21
SB09	0.17	0.2	2.7	2.9	54.4	0.45	1.15	52	0.4	1.02	56.4	0.53	1.1
SB10	0.25	0.22	3	3.2	40.6	0.45	1.15	39.2	0.4	1.07	52.5	1.77	1.44
SB11	0.1	0.14	4.7	3.5	42.8	0.45	1.15	41	0.4	1.12	50.2	1.1	1.38
SB12	0.16	0.15	1.8	3.2	54.5	0.45	1.15	52	0.4	1.02	65.4	1.09	1.3
SC1	0.12	0.15	3.6	2.5	44.8	0.45	1.15	43.6	0.4	1.12	52.2	1.27	1.38
SC2	0.12	0.14	3.5	3	41.6	0.45	1.15	43.6	0.4	1.12	62.9	2.34	1.43
SC3	0.16	0.18	5.2	5.7	45.2	0.45	1.15	43.9	0.4	1.12	52.1	1.22	1.37
SC4	0.15	0.16	3.6	5.7	42	0.45	1.15	44	0.4	1.12	55.4	2.24	1.43

Also indicated in Table 5.3 are the experimentally observed post-yielding stiffness values. Estimation methodology of the same is illustrated in Figures 5.16 and 5.17. First cycle peaks at all target drifts 2 % onwards and until the maximum moment were extracted from the recorded experiment data and a linear fit curve was deduced as the approximation of post yielding stiffness. As can be seen from the figure, linear fit approximates the behavior well enough over the range considered. Values are indicated in Table 5.3 for stiffness in both positive and negative directions. Post-yielding stiffness is reported as fraction of the stiffness before yielding. The table data is also expressed as graphs in Figures 5.18 and 5.19 for illustration.

It must be noted at the end of this discussion that although the three quantities representing ultimate state response, drift capacity, ultimate strength, and post-yielding stiffness, were evaluated and discussed independently, they are indeed closely related. In fact, estimation of any two of them is sufficient to represent ultimate state response as
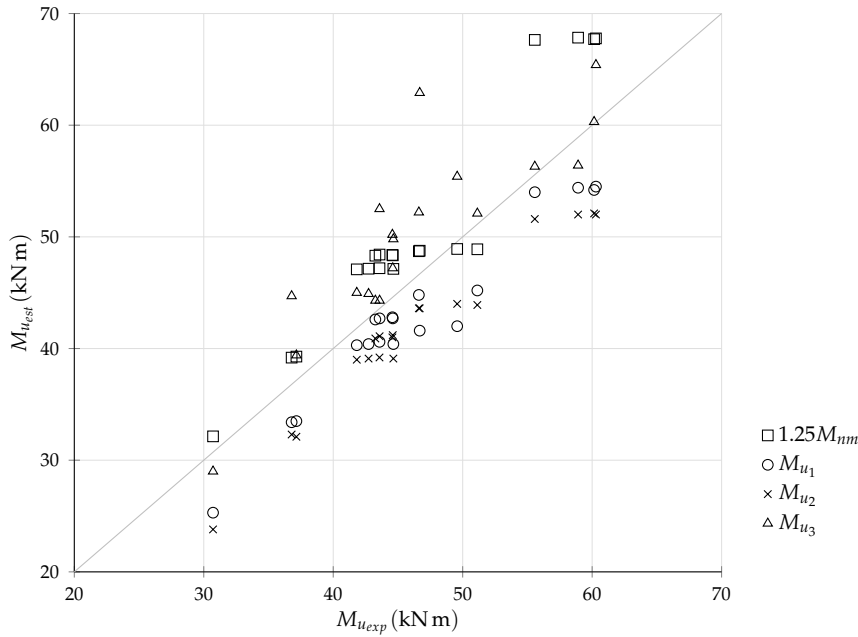
Figure 5.15: Comparison of experimentally observed ultimate moment strength with various estimation procedures

the third quantity can always be expressed in terms of the other two.

5.4 Ultimate state mechanism

KEY observations on the experiment response are noted and implications on existing mechanism are critically discussed. In conclusion, a new mechanism to explain experiment observations is defined and its application is discussed.

5.4.1 Observations

As previously discussed in Section 5.1, parameters f_c' and f_{yt} were observed to have no influence on the ultimate drift capacity of test specimens. This observation directly conflicts with the philosophy of shear-strength degradation based mechanism. Since concrete strength and stirrup strength are two sole contributors to section shear strength, increase in either or both of those results in enhancement of the shear carrying capacity of the section. High initial shear strength would therefore be expected to delay failure with increasing drifts if an equal degrading slope is assumed. Absence of corresponding observations from the test results implies that either the failure was not caused by the degradation of shear resistance or the rate of shear strength degradation was not constant for differing initial conditions.

One factor that was consistently found to affect drift capacity was ρ_s. Both spacing and bar size of stirrups were modified to achieve varying ρ_s. Increasing ρ_s resulted in not just larger drift capacities but also higher moment strength. Better flexural behavior and delayed failure was ensured by the transverse reinforcements. This observation is not unique in the context of reinforced concrete behavior. Efficiency
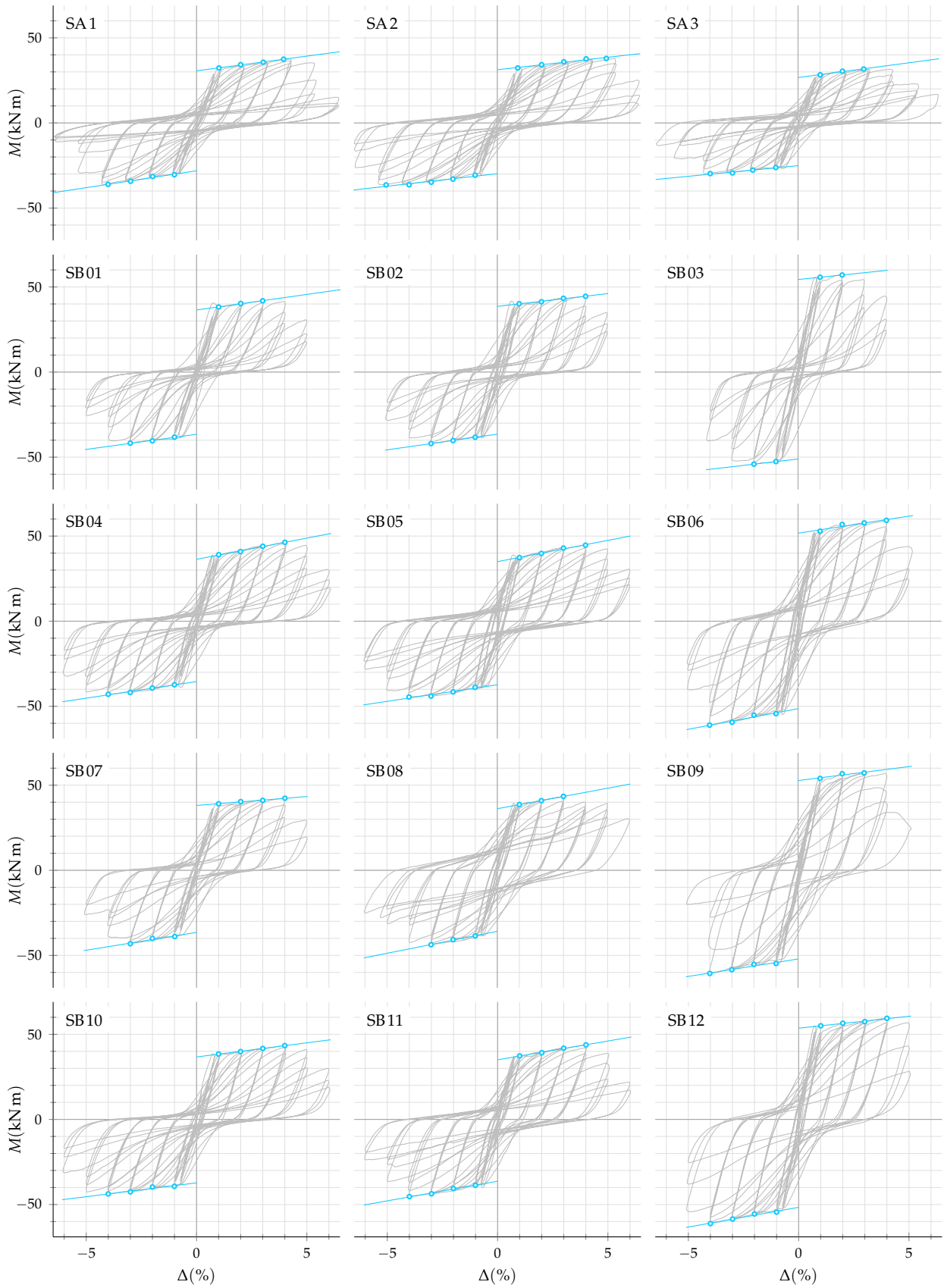
Figure 5.16: Estimation of post-yielding stiffness from moment-drift response (SA and SB series)
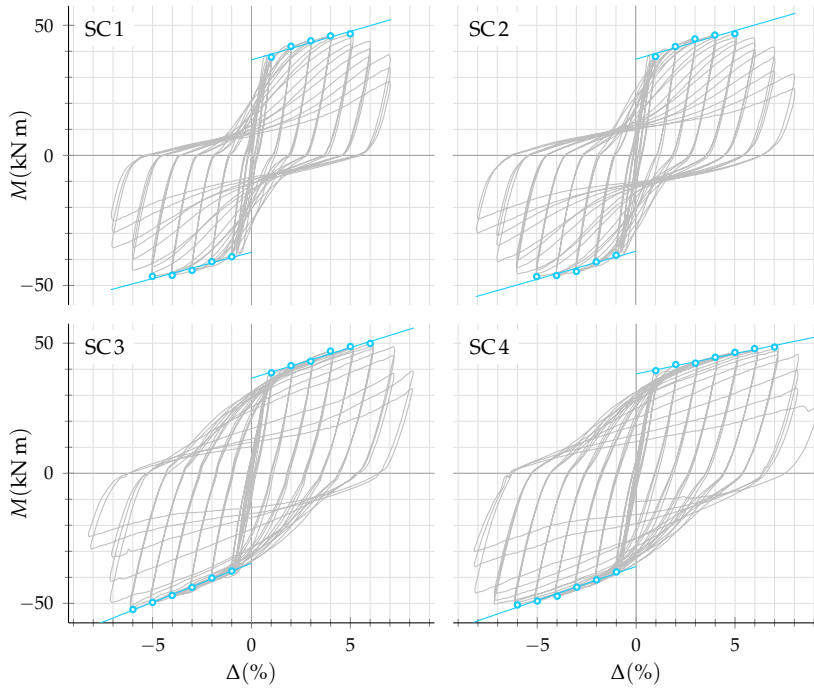
Figure 5.17: Estimation of post-yielding stiffness from moment-drift response (SC series)
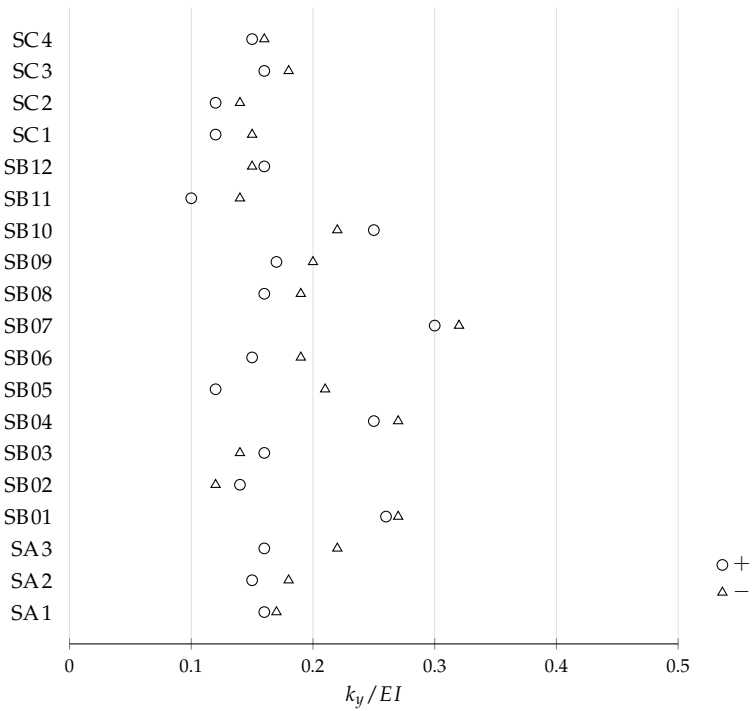
Figure 5.18: Experimentally observed pre-yielding stiffness expressed as a fraction of EI

of transverse reinforcement in improving lateral response is usually explained with effective confinement of the concrete core or contribution to shear strength or restraint of the compressive reinforcement. In the context of this experiment program however, it can be concluded that shear strength contribution of transverse reinforcement is not the prime reason for its effectiveness in improving earthquake response.

Coupled with the fact that d_b was also observed to have some influence on ultimate state response, it is reasonable to explore mechanism approaches related to lateral stability of longitudinal reinforcement. Buckled shape in longitudinal bars was often observed as illustrated through post experiment photographs in Figure 5.20. As also noted by Berry and Eberhard,[16] it is difficult to precisely identify the occurrence of buckling during the experiment as the reinforcements are hidden by concrete cover. The images presented here represent the specimen state at the end of the loading where several loading cycles have been applied since the loss of strength started. It is therefore not correct to identify bar buckling as the mechanism responsible for loss of strength solely on the evidence of these post experiment images.

[16] Berry and Eberhard, op. cit.

In-experiment lateral deformation behavior of longitudinal reinforcements was studied using photogrammetric data. Although the data is a direct measurement of concrete surface deformation, it is reasonable to approximate reinforcement displacement with concrete surface deformations until concrete spalling occurs. Surface deformation grid at peak and zero states at increasing target drift levels is expressed for SB02 in Figure 5.21 as an example. At the zero state, hinge region of specimen can be observed to start to bulge after cyclic loading at large target drift. When loaded towards positive or negative direction from the bulged state, the compression side can be observed to furt-
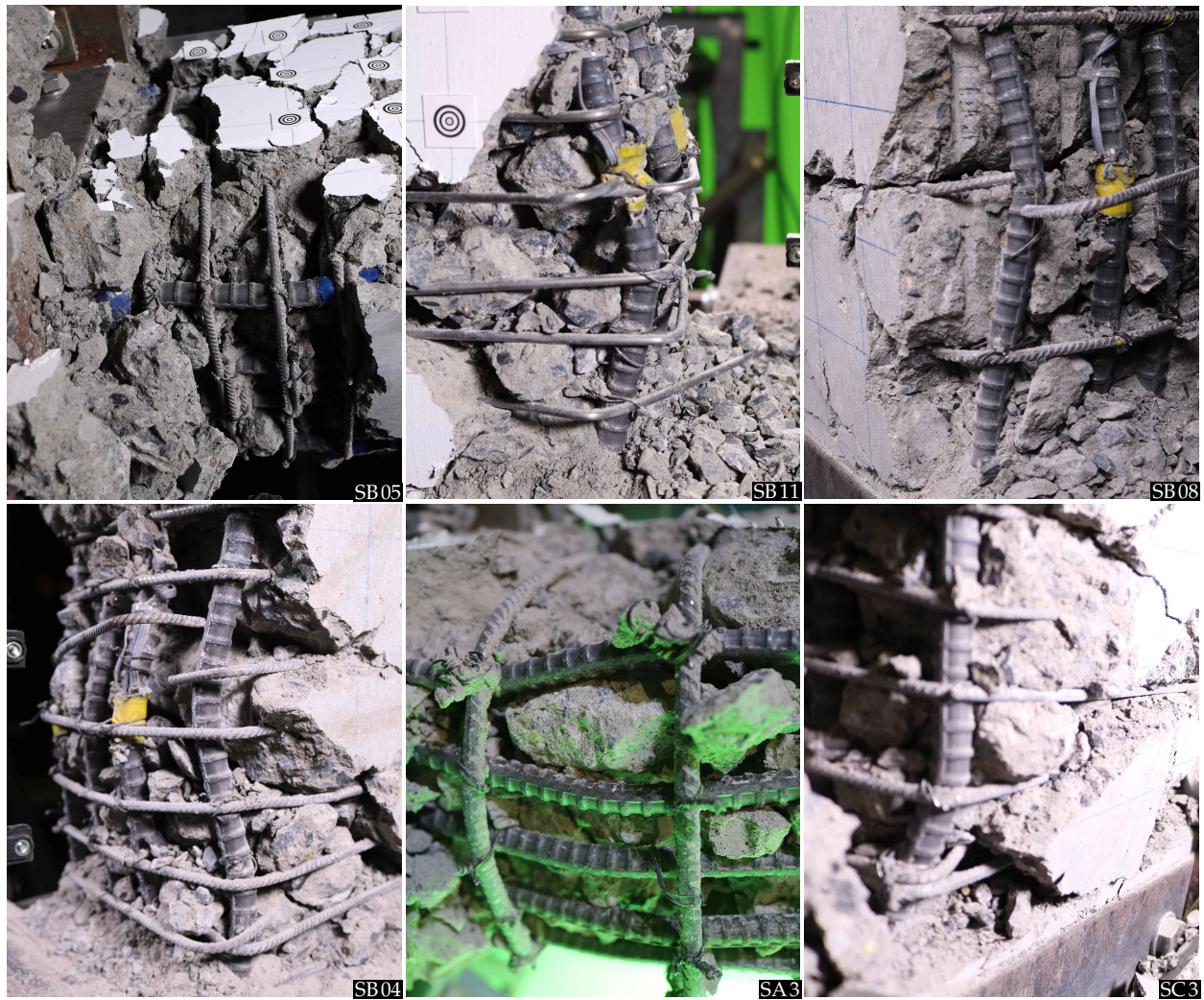
Figure 5.20: Buckled bar shapes observed in post loading inspection

her outwards inclination. With repetitive loading, the bulging and inclination are seen increase on both sides.

While it was not possible to record meaningful photogrammetric observations at large drifts, this was observation was confirmed from the inclined shape of reinforcing bars exposed after spalling of concrete cover as expressed in Figure 5.22.

On the evidence of these observations it is now possible to define a new mechanism to determine the initiation of loss of strength based on lateral inelastic deformations of longitudinal reinforcement.

5.4.2   Mechanism definition

CYCLIC loading response of reinforced concrete beams designed with sufficiently high shear strength consists of stable flexural response in initial stages. High initial stiffness of the concrete section quickly degrades with increasing deformation as tension concrete cracks and tensile reinforcements yield. Hysteresis loops at this stage are full in shape and exhibit good energy dissipation characteristics. When beam is loaded to **a** in post-yielding range, thin flexural cracks open close to the critical section signifying yield of longitudinal reinforcement in tension. Upon unloading from **a**, deformation decreases at almost pre-yield stiffness leaving significant residual plastic deformation at **b**. Loading further in the opposite direction, stiffness gradually decreases as the longitudinal reinforcement in opposite direction also enters post-yielding range. When peak is reached at **c**, nearly same resistance as at **a** is achieved and similar pattern of flexural cracks is reproduced on the opposite side of the beam. Repeated cycling produces accumulation of residual strain in reinforcement and axial expansion of beam due to widening of flexural cracks.

As repetitive loading cycles at increasingly large deformations are applied, flexural cracks increase in extent and length forming a pattern of diagonal intersections in the middle portion of the section. As successive loading is performed on the beam in this state, hysteresis loops begin to pinch due deterioration of mechanical interlock along the cracks and slipping deformations. Minor degradations in stiffness also accompany slipping deformations but no loss in peak resistance is observed as yet. Resistance at peak deformation **f** is a continuous increment from previous peak as reinforcement stresses increase due to strain hardening. Concrete section develops increasingly wide cracks at this stage. Unloading from **f** occurs at a slightly reduced stiffness following the hysteretic pattern of reinforcing steel. At zero resistance point **g**, cracks on the tension side are not fully closed. As loading is continued in opposite direction, large deformations have to take place until the cracks close at **h**. From **g** to **h**, very small stiffness is observed as a result of small resistance provided by the compressive reinforcement and large slips that occur across the diagonal cracks with deteriorated interlock. As a result, hysteresis loops become increasingly pinched.

With increasing deterioration of the resistance along the diagonal
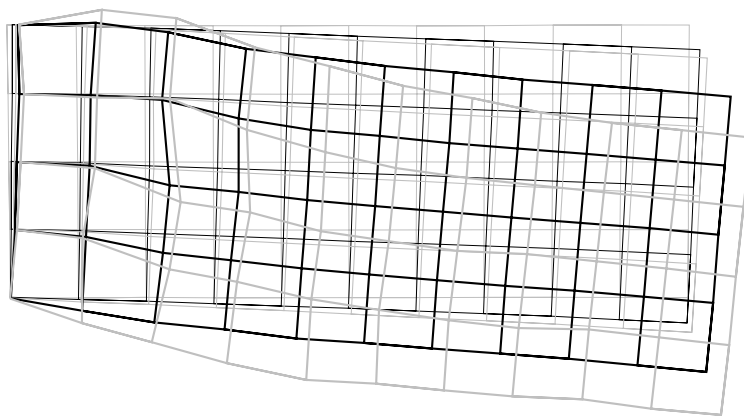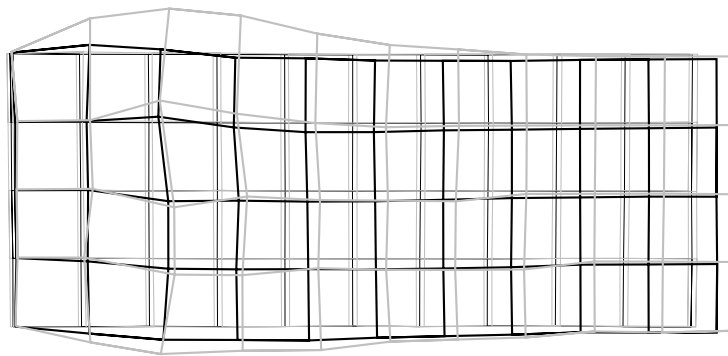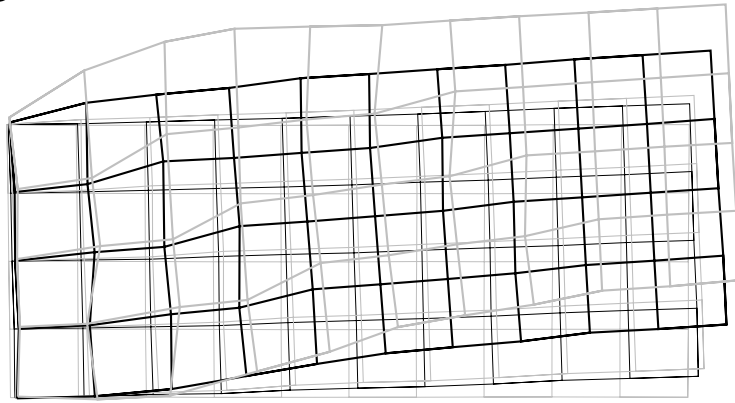
Figure 5.21: Deformation pattern of SB02 at peak and zero states over increasing target drift levels
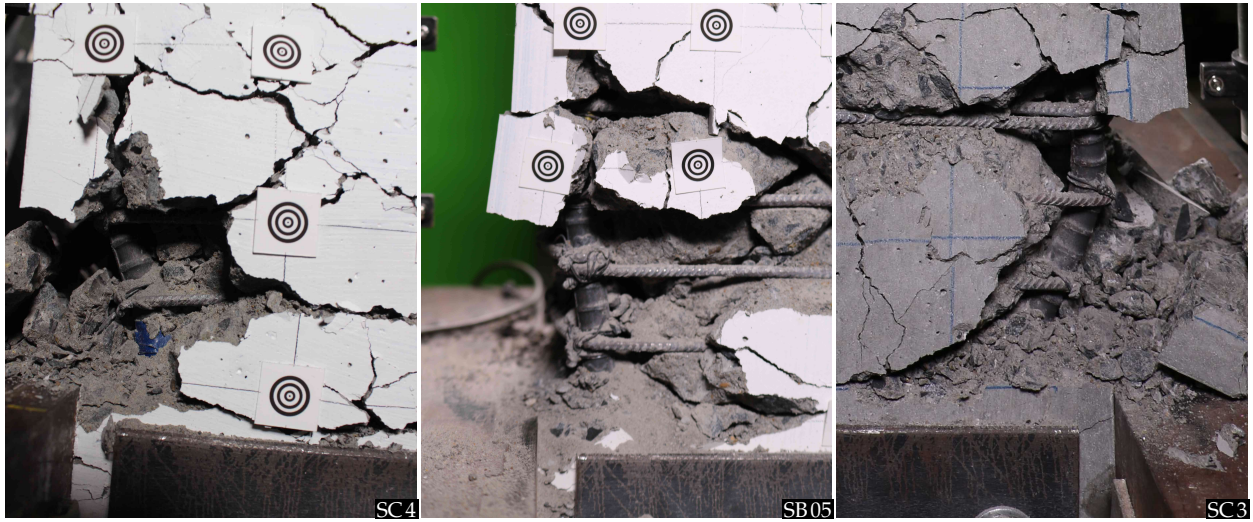
Figure 5.22: Inclined state of longitudinal reinforcement at the critical section
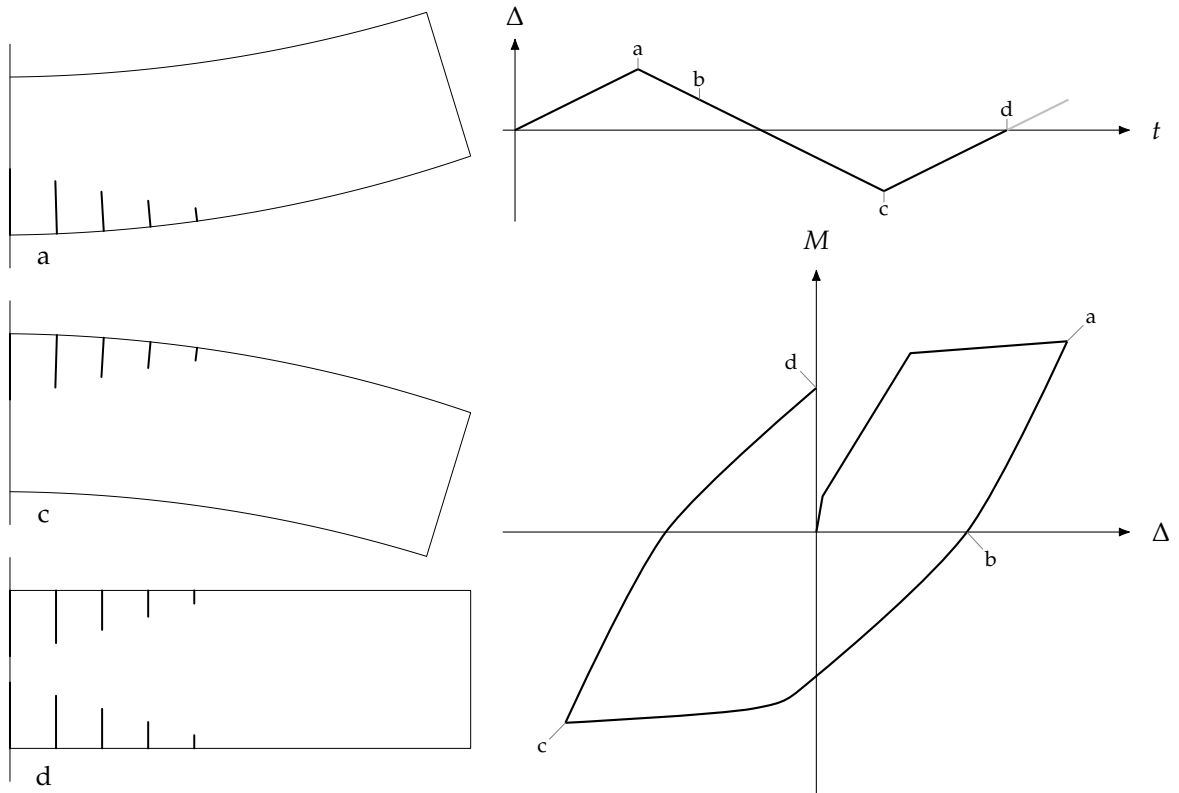
Figure 5.23: Response at small deformations
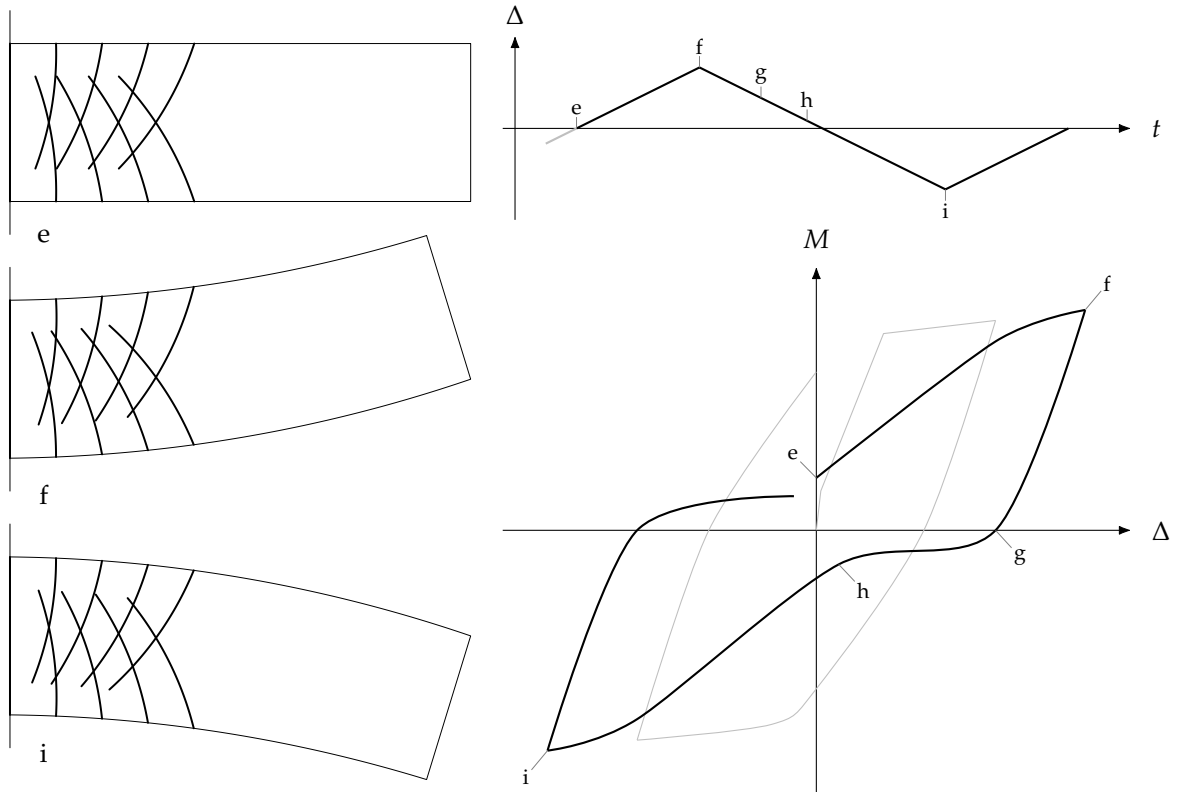
Figure 5.24: Response at intermediate deformations

cracks, shear resistance of concrete also degrades. As a result, applied shear is increasingly born by the stirrups and the dowel action of longitudinal reinforcement. Yielding and subsequently increasing plastic deformations of stirrups in the hinge zone leads to lateral expansion of the concrete core in hinge region. This lateral expansion of concrete and stirrups also leads to lateral deformations in the longitudinal reinforcement. Since the reinforcements are already in plastic state after yielding in tension, they fail to return to perfectly straight configuration under lateral pressure from expanding core.

When loaded from this laterally bulged core state, longitudinal reinforcements on the compressive are subjected to bending moments in addition to compressive axial force. As the bending moments increase with increasing deformation, compressive load carrying capacity of reinforcements decreases due to interaction of axial force and moment. Finally, the peak resistance starts degrading when the inclined longitudinal reinforcement cannot bear the required axial force due to the presence of moments imposed by the inclined bar geometry. Upon further loading from this state, increased inclination of reinforcement leads to the formation of buckled shape and rapid degradation in peak resistance.

Thus, ultimate drift capacity of the beam is determined by the lateral inelastic deformations of longitudinal reinforcement.

Figure 5.25: Bulging of hinge region
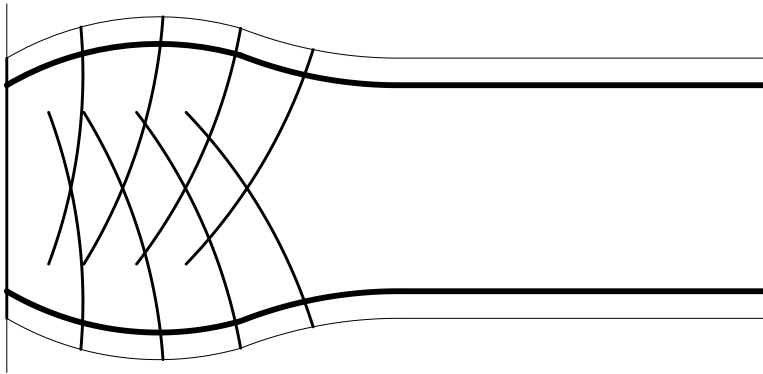
5.4.3   *Application*

In the proposed mechanism, load resistance at ultimate state is dependent on the performance of inclined longitudinal reinforcement under compression. Characterization of P-M interaction behavior of rebars is therefore essential for estimating drift capacity determined by the mechanism.

Formulation for P-M interaction of rebar is based on Yang.[17] Rebar is assumed to have a perfectly circular cross-section with diameter d_b and be under fully plastic stress conditions as illustrated in Figure 5.26. At the material limit state f_y, permissible combinations of axial load (P_{bar}) and moment (M_{bar}) supported by the bar can be estimated from stress resultants as:

[17] Refer Section 2.6.1 on page 2-10 of Y. Yang. "Research on post shear failure residual axial strength evaluation of reinforced concrete columns". PhD thesis. Tokyo, Japan: University of Tokyo, 2016.
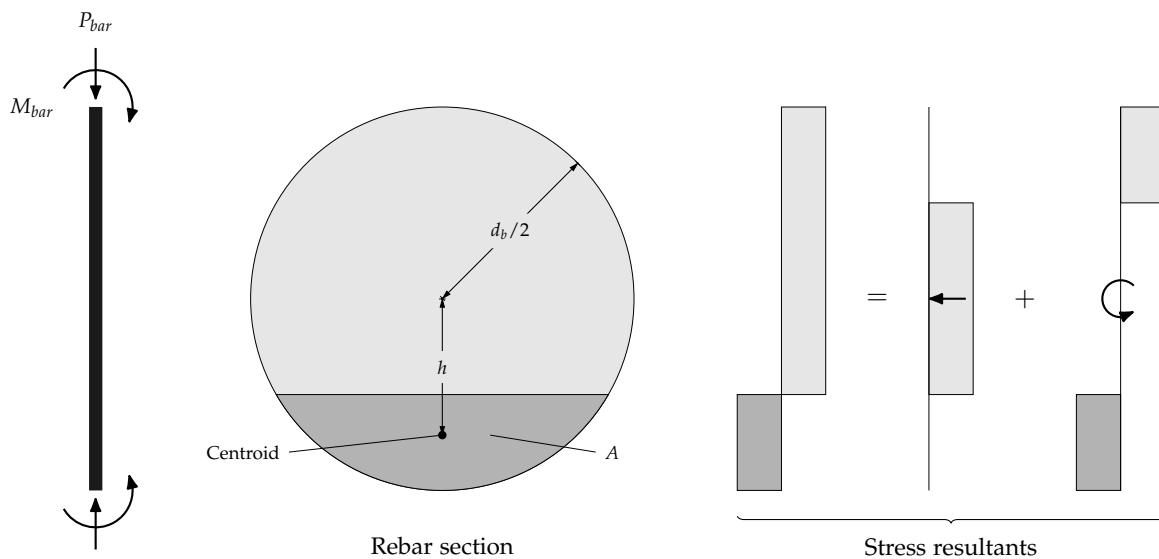
Figure 5.26: P-M interaction model of circular rebar

$$P_{bar} = \left(\frac{\pi d_b^2}{4} - 2A \right) f_y \tag{5.1}$$

$$M_{bar} = 2A f_y h \tag{5.2}$$

P-M interaction diagram can thus be drawn by evaluating equations (5.1) and (5.2) for all possible neutral axis depths ($x = 0 : d_b/2$). Resulting interaction diagram is expressed in Figure 5.27.
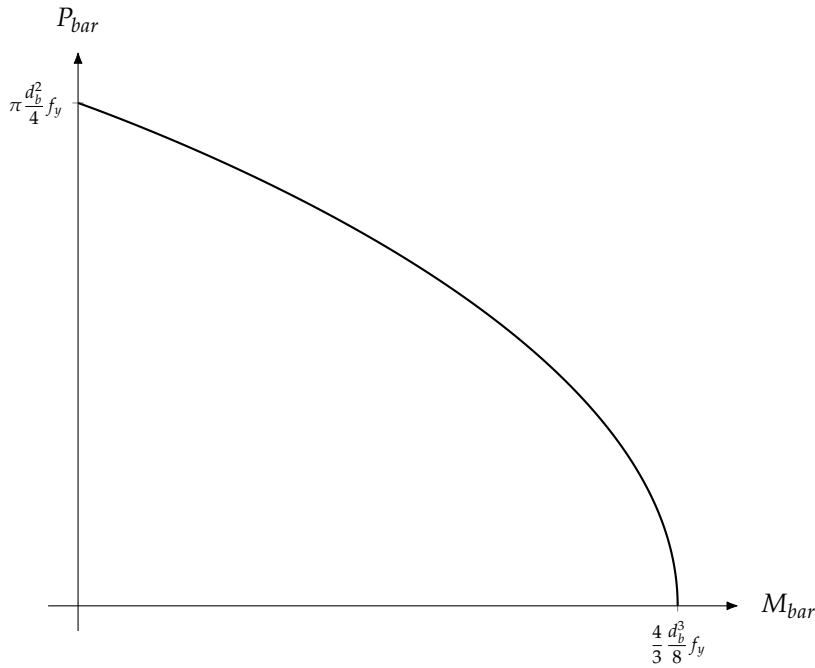
Figure 5.27: P-M interaction for circular rebar sections

In the case of compressive longitudinal reinforcement where the rebar is subjected to bending moments resulting from an eccentrically applied axial load, P-M interaction curve can be expressed in terms of P-e. Evaluating the interaction equations (5.1) and (5.2) for the D13 bars used in the specimens and expressing P_{bar} as normalized axial load, the interaction curve can be drawn as displaed in Figure 5.28. It can be inferred that the axial load carrying capacity of rebars drops to less than 70 % at an eccentricity of about 2 mm.

APPLICABILITY of the proposed mechanism can now be verified using rebar P-M interaction model and photogrammetric measurements. Considering any general deformed geometry as indicated in Figure 5.29, coordinates of the grid points ①, ②, and ③ representing the inclined end of compressive reinforcement can be obtained from photogrammetric analysis.

Geometric quantities associated with the deformed shape can be obtained using the photogrammetric coordinates as:
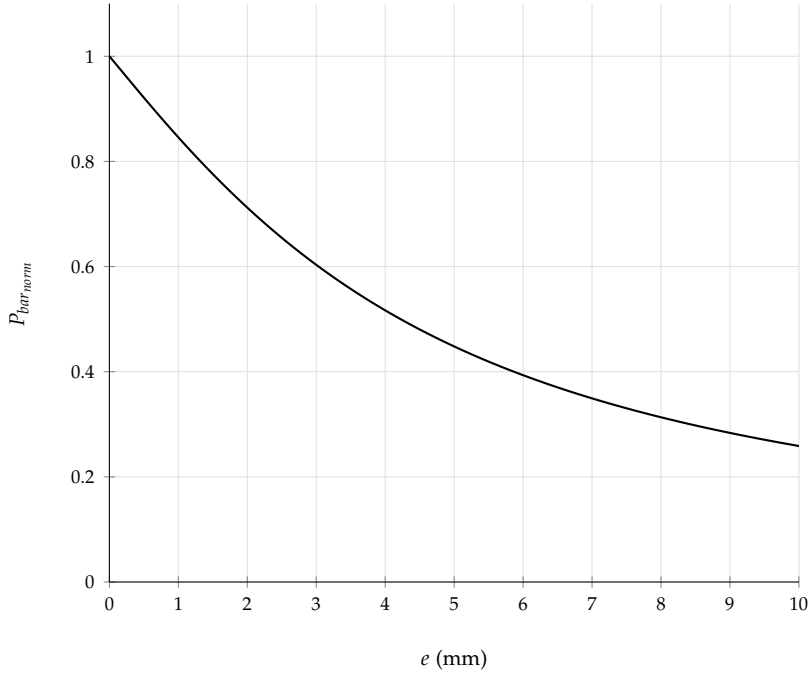
$$l_{12} = \sqrt{(y_2 - y_1)^2 + (x_2 - x_1)^2} \tag{5.3}$$

$$\theta_{12} = \tan^{-1}\left(\frac{x_2 - x_1}{y_2 - y_1}\right) \tag{5.4}$$

$$\theta_{23} = \tan^{-1}\left(\frac{x_3 - x_2}{y_3 - y_2}\right) \tag{5.5}$$

Differential inclination between the segments can then be calculated as:

$$\theta = \theta_{23} - \theta_{12} \tag{5.6}$$

If the segment ②-③ is compressed to an axial load F, force actions transmitted to segment ①-② can be given as:

$$F_1 = F \cos\theta \tag{5.7}$$

$$F_2 = F \sin\theta \tag{5.8}$$

These force actions can be resolved in to equivalent axial force and moment as:

$$P_{12} = F_1 \tag{5.9}$$

$$M_{12} = F_2 l_{12} \tag{5.10}$$

Eccentricity of the applied combination of axial load moment can thus be obtained as:

$$e = \frac{M_{12}}{P_{12}} \tag{5.11}$$
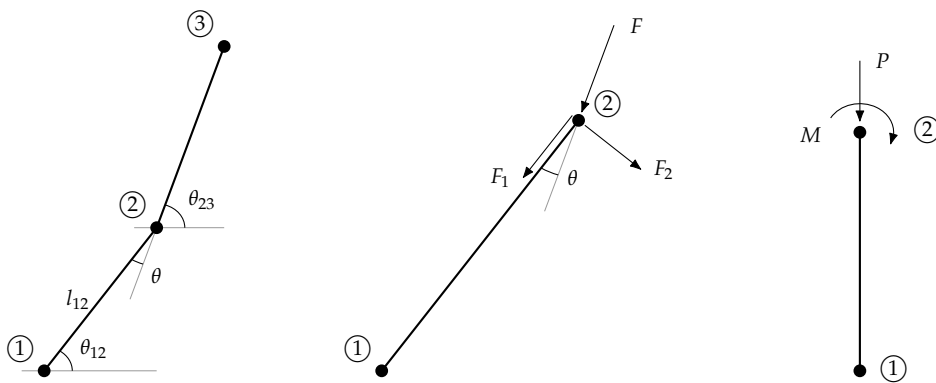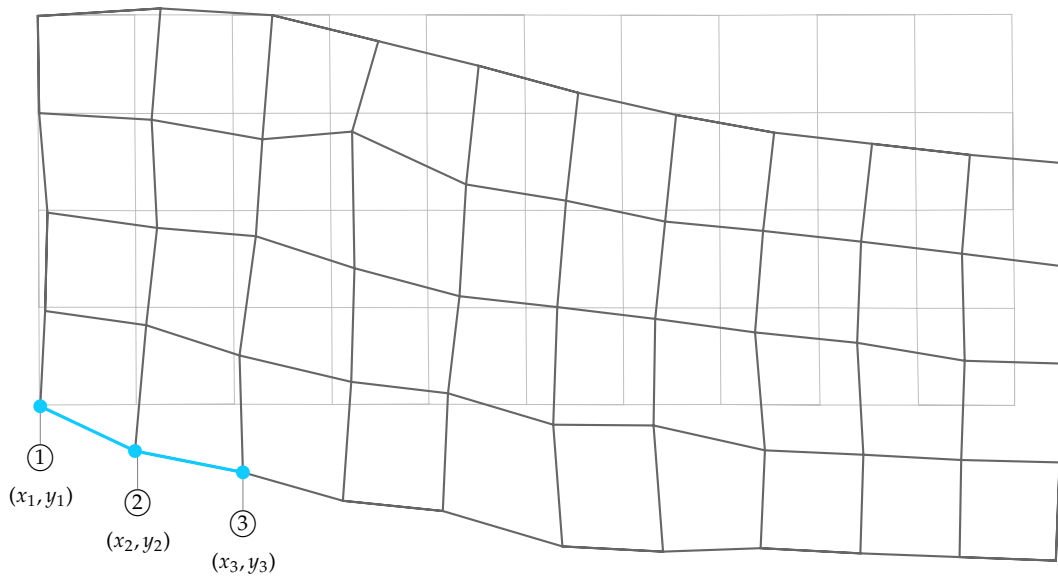
Figure 5.29: Calculation of rebar eccentricity from photogrammetric measurements

Resolving the eccentricity expression, we can evaluate e using only the photogrammetric coordinates as:

$$e = l_{12} \tan \theta \qquad (5.12)$$

USING the eccentricity formulation derived above, critical specimen eccentricity was calculated for all specimens at peak loading states using photogrammetric analysis data. Results are plotted in figures 5.30 and 5.31. Gradual increment in rebar eccentricity is noted in all specimens. Close to the point where loss of strength was usually observed, sudden jump in eccentricity is noted. These observations suggest that loss of strength was indeed initiated by loss of axial force resistance in inclined rebars.

5.4.4   Discussion

COMMON experiment observations and reported effect of parameters on response can be explained through the proposed mechanism.

Cyclic loading: One of the key differences between cyclic and monotonic loading is the symmetry of response. Monotonic loading does not induces symmetric cracking pattern and alternating symmetric states of stress in reinforcements as produced in cyclic loadings. Consequently, there is no lateral expansion or bulging of the hinge region. As per the proposed mechanism, therefore, loss in resistance does not happen even at very large deformations and the compression reinforcement maintains its integrity without any instability.

Loading reversals: A similar argument may be stated for the role of loading reversals in producing deterioration of strength. When cyclic loading is applied without reversals, symmetric cracks patterns do not form as only one side is subjected to tensile stresses. Also, as the compression side reinforcement is never subjected to tensile stress, plastic state of stress is not reached in the compression reinforcement. Since there no bulging is induced in this way, no loss of strength can take place due to reinforcement lateral deformations as proposed by this mechanism.

Transverse reinforcement: Role of transverse reinforcement in ensuring stable inelastic response in reinforced concrete members is one of the most common observation in cyclic loading experiments. While its contribution to shear strength or concrete confinement is often attributed as the reason for its effectiveness, a different explanation can be give in the context of the proposed mechanism. When diagonal intersecting cracks appear in the hinge region, lateral expansion of the core is restrained solely by the legs of transverse reinforcement. Higher reinforcement content thus ensures integrity of the hinge region. Lateral stability of rebars is also provided by restraint of transverse reinforcement. As the lateral expansion of core pushes longitudinal reinforcement to larger inclinations, the dowel action of stirrups effectively delays loss of strength by supporting the rebars. Closely spaced stirrups and ties to each longitudinal rebars are there-
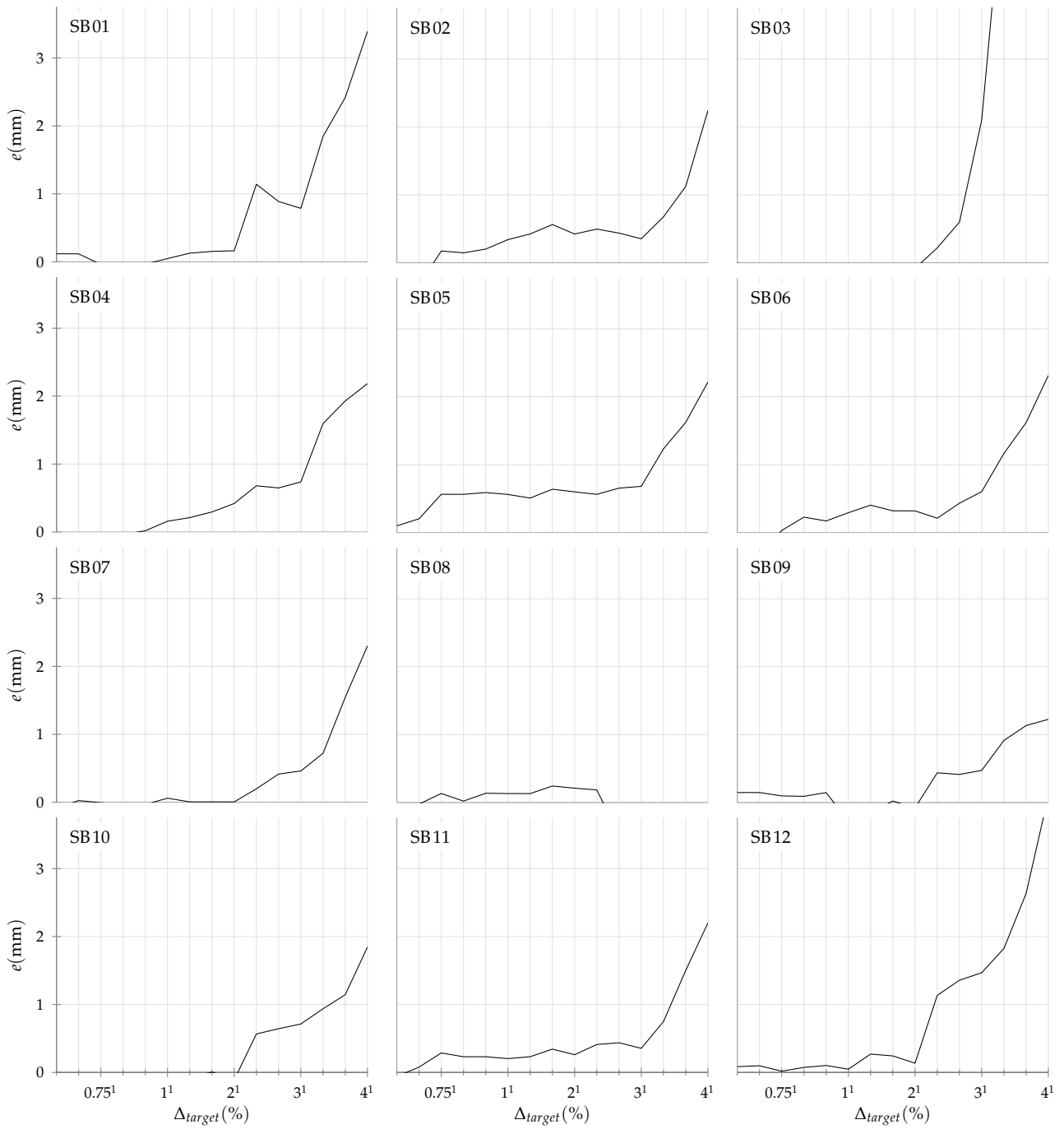
Figure 5.30: Rebar eccentricity at peak loading states (SB series)
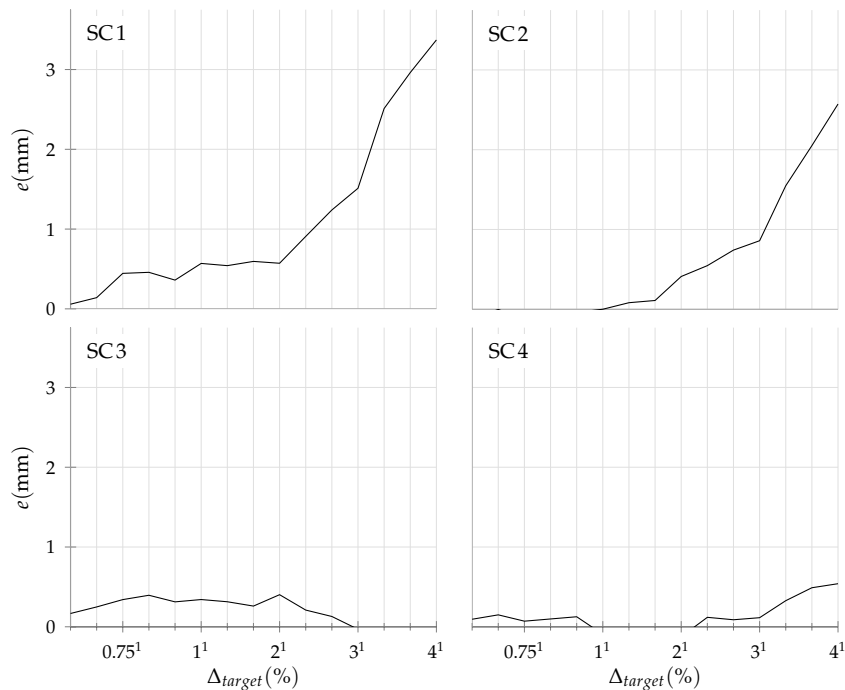
Figure 5.31: Rebar eccentricity at peak loading states (SC series)

fore more effective in improving ultimate drift capacity according to this mechanism.

Shear stress: State of stress in the section also plays an important role in initiating loss of strength according to this mechanism. When larger shear stresses are induced in the section, set of diagonal intersecting cracks are formed early in the loading cycle. Lateral expansion of core due to deterioration of shear resistance across the cracks thus proceeds at a faster pace. In comparison, when flexural stresses dominate the section, development of intersecting cracks requires larger cyclic deformations leading to delayed loss of resistance according to the proposed mechanism.

Bar-buckling: Role of the so called bar-buckling may also discussed in the context of the proposed mechanism. Classic treatment of rebar buckling in RC members usually considers lateral instability in straight inelastic rebars with initial imperfections. It was postulated in the proposal of the new mechanism and also demonstrated with photogrammetric data that the initally straight rebars turn to a bulged shape as result of concrete latera expansion. Therefore it may not be reasonable to assume a straight rebar to formulate buckling mechanism. In fact the phenomenon of bulging of rebars described in the proposed mechanism may not be interpreted as buckling.

5.5 *Performance states*

ONE of the key features of performance-based design is the freedom of choice afforded to the clients and designers in selecting target building performance levels. Photographic data obtained from the

experiment is organized in terms of the available performance criteria definitions and presented to establish greater comprehension of expected performance.

5.5.1   Criteria definition

BASIC definitions of structural performance objectives in the context of performance-based seismic design first appeared in the Vision 2000[18] report. Four performance levels, *fully operational*, *operational*, *life safe*, and *near collapse* were defined in global terms. Acceptance criteria was given in terms of total building drift but no element level performance was identified. More detailed definitions of these performance levels with a slightly modified terminology were introduced in FEMA 356.[19] Acceptance criteria for individual structural elements in terms of allowable plastic were also listed for respective performance levels. Latest edition of this standard, ASCE 41-13[20] enforces the same provisions.

ASCE 41-13 defines overall and component specific damage states at four performance levels: *operational*, *immediate occupancy* (IO), *life safety* (LS), and *collapse prevention* (CP). Relevant description of the damage states from tables C2-3 and C2-4 of the standard with reference to RC frame structural elements is listed in Table 5.4. Operational and IO levels effectively imply elastic or near-elastic response in beams. At LS, cracking and stiffness degradation are expected without any significant loss of strength. CP implies the state before imminent collapse due to the initiation of one of the failure mechanisms. Acceptance criteria for IO, LS, and CP are defined in terms of plastic member rotations in Table 10-7 of the standard.

Table 5.4: Performance levels as per ASCE 41-13

Collapse Prevention	Life Safety	Immediate Occupancy	Operational
Severe damage	Moderate damage	Light damage	Very light damage
Large permanent drifts	Some permanent drift	No permanent drift	No permanent drift
Little residual strength and stiffness	Some residual strength and stiffness	Full strength and stiffness retained	Full strength and stiffness retained
Extensive cracking and hinge formation	Spalling of cover and shear cracking	Minor cracking with limited yielding	–

AIJ performance evaluation guidelines[21] define performance at three levels: *serviceability*, *reparability*, and *safety* limit states. Reparability limit state is subdivided in to two levels based on the degree of repairs required. Acceptance criteria for serviceability and reparability limit states are provided in terms of residual crack width. Serviceability limit is defined as the initiation of yielding in longitudinal reinforcement and associated with a residual crack with of 0.2 mm. The two reparability states are associated with 1 mm and 2 mm residual crack widths respectively. Safety limit is identified at ultimate state before the initiation of failure mechanisms associated with shear or longitudinal reinforcement fracture.

PEER performance-based design guidelines[22] provide criterion to evaluate performance at only two levels: *service level earthquake* (SLE)

and *maximum considered earthquake* (MCE). Component level acceptance criteria at SLE is required to be estimated through laboratory testing. However, use of ASCE 41-13 IO performance acceptance criteria is also permissible in its lieu. At the MCE level, components are expected to reach their ultimate deformation capacity.

5.5.2   *Experiment data*

OCCURRENCE of ASCE 41-13 performance states IO,LS, and CP in each specimen test was identified according to the accepted plastic rotations for each level. Specimen state corresponding to each level is expressed as the state at the conclusion of all three loading cycles at the largest target drift level before the exceedance of accepted plastic rotation. Identification of the performance level through specimen response is illustrated in figures 5.32 and 5.33. Residual specimen state before the exceedance of performance criteria for all specimens are expressed in figures 5.34 to 5.36. Also indicated on the figures are the target drift level during which the images were recorded. IO level was reached during the 2 % target drift cycle for all specimens except SB02 and SB07. Similarly, all specimens reached LS level during the 4 % target drift cycle except specimens SB02, SB06, and SB07. For the specimens which did not reach the CP level during the test, images from the final loading cycle are used instead and indicated with a * in Figure 5.36.

At the IO level, all specimens had already yielded. Minor residual cracks, especially at the critical section remained in most specimens. At the LS level, extensive cracking was observed in the hinge region of all specimens but no spalling or crushing of concrete was prominent. At the CP level, all specimens had suffered extensive spalling and crushing of concrete. Large lateral deformation were frequently noted in the rebars.

ASSESSMENT of AIJ performance states requires evaluation of crack widths at the residual state. To facilitate estimation of residual crack widths corresponding to the loading level, specimen images at zero force state following the conclusion of all displacement cycles at each target drift level are provided in Appendix D.
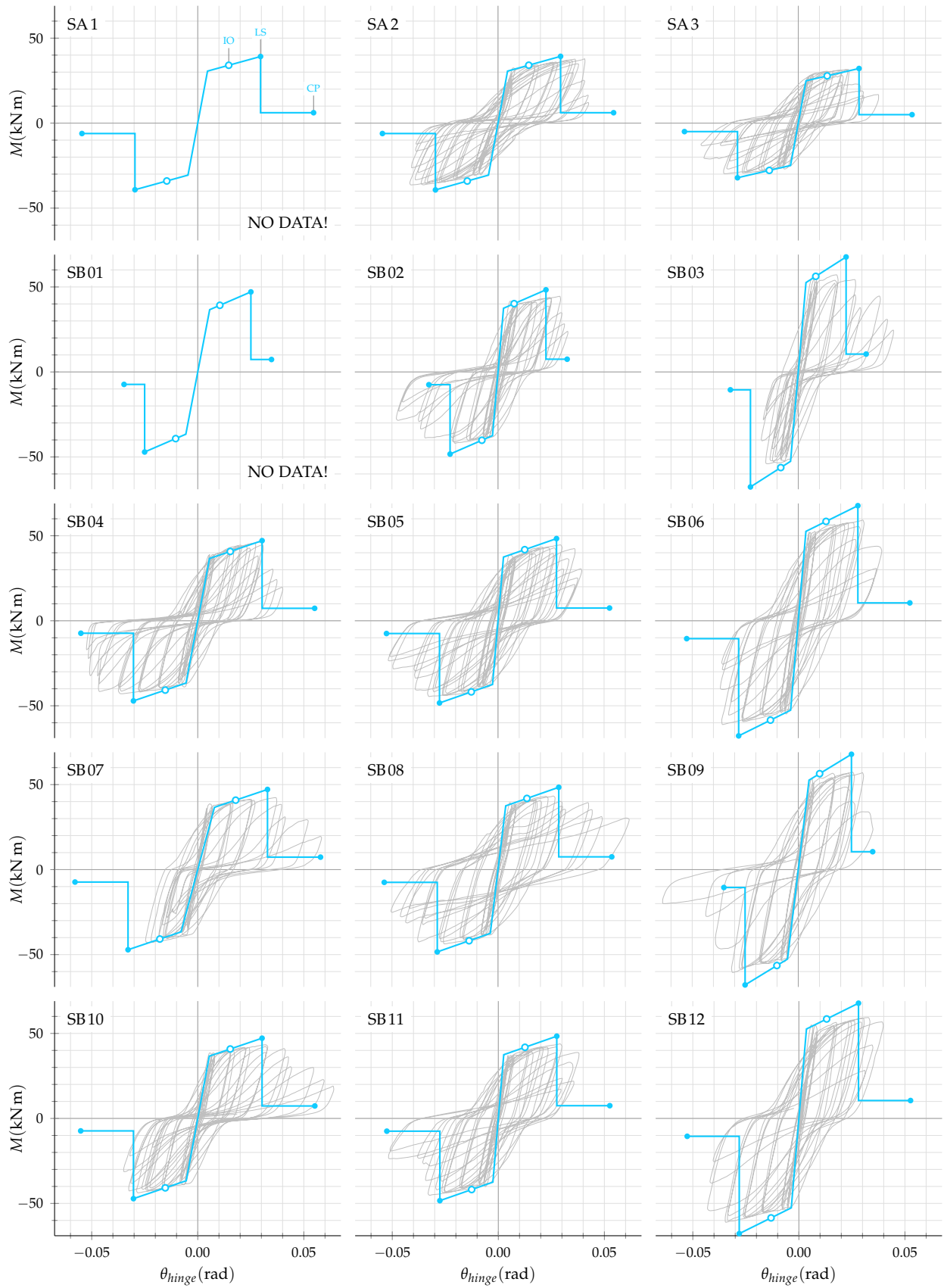
Figure 5.32: ASCE defined performance states on experimentally hinge rotation response (SA and SB series)
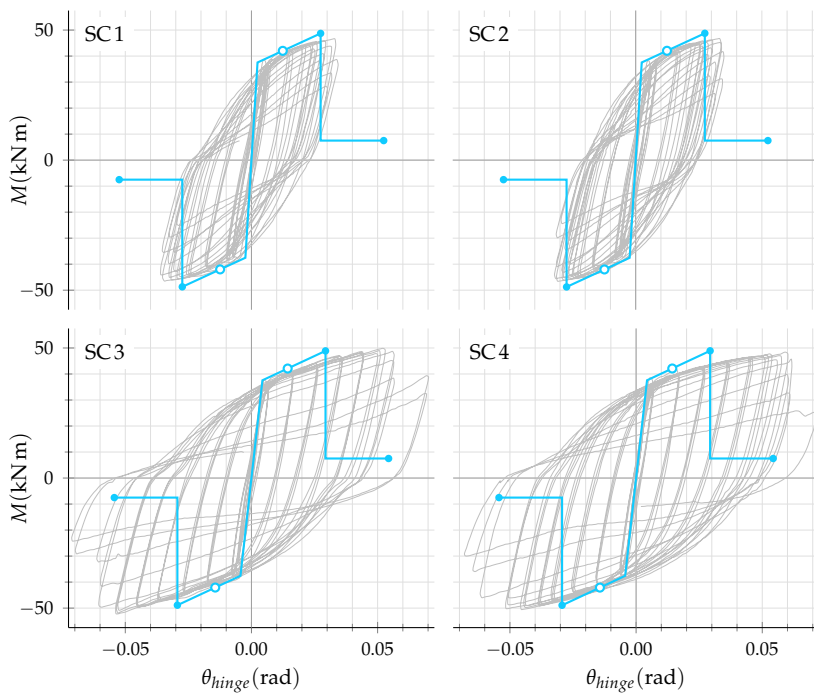
Figure 5.33: ASCE defined performance states on experimentally hinge rotation response (SC series)
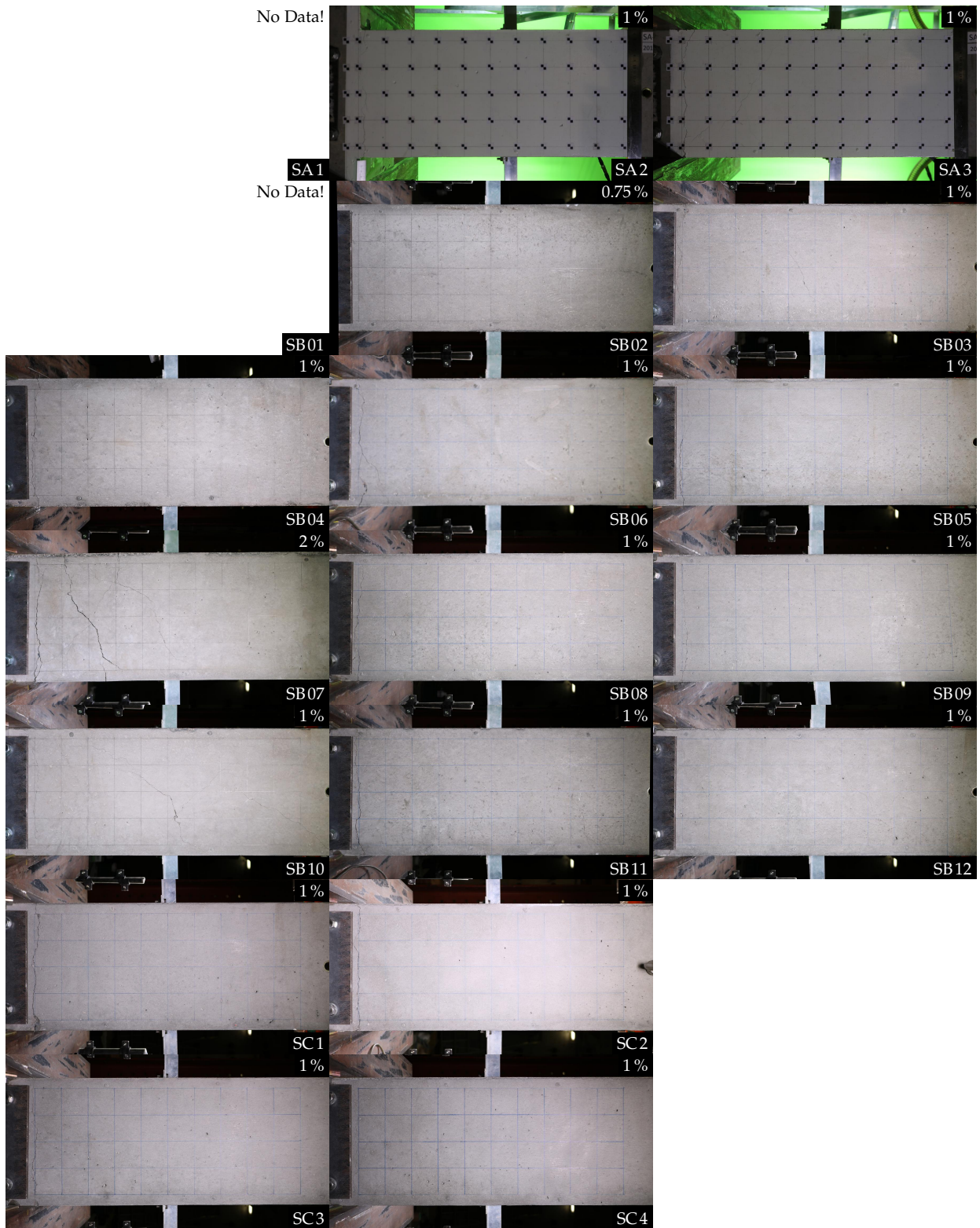
Figure 5.34: Comparison of damage states for all specimens at IO performance state
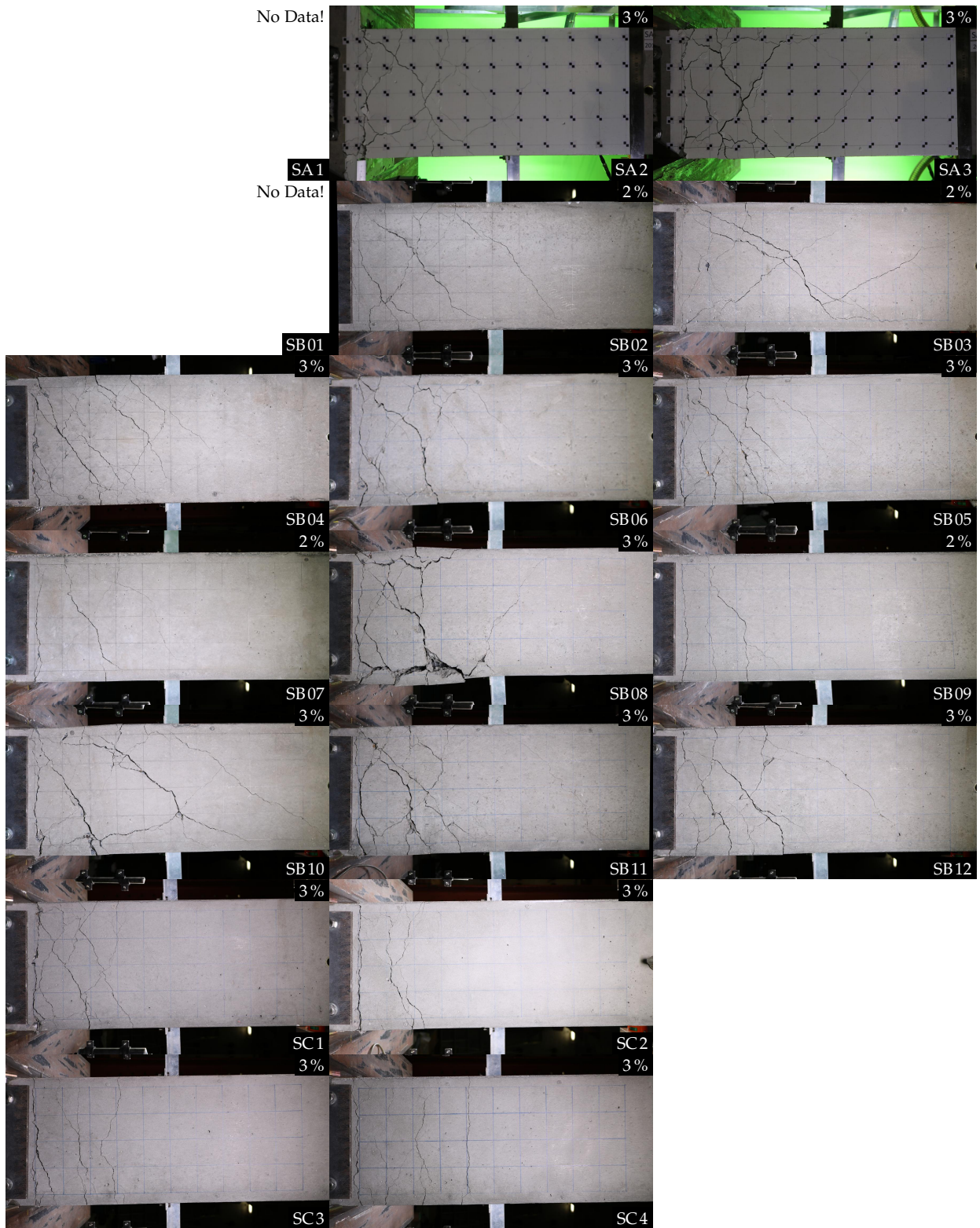
Figure 5.35: Comparison of damage states for all specimens at LS performance state
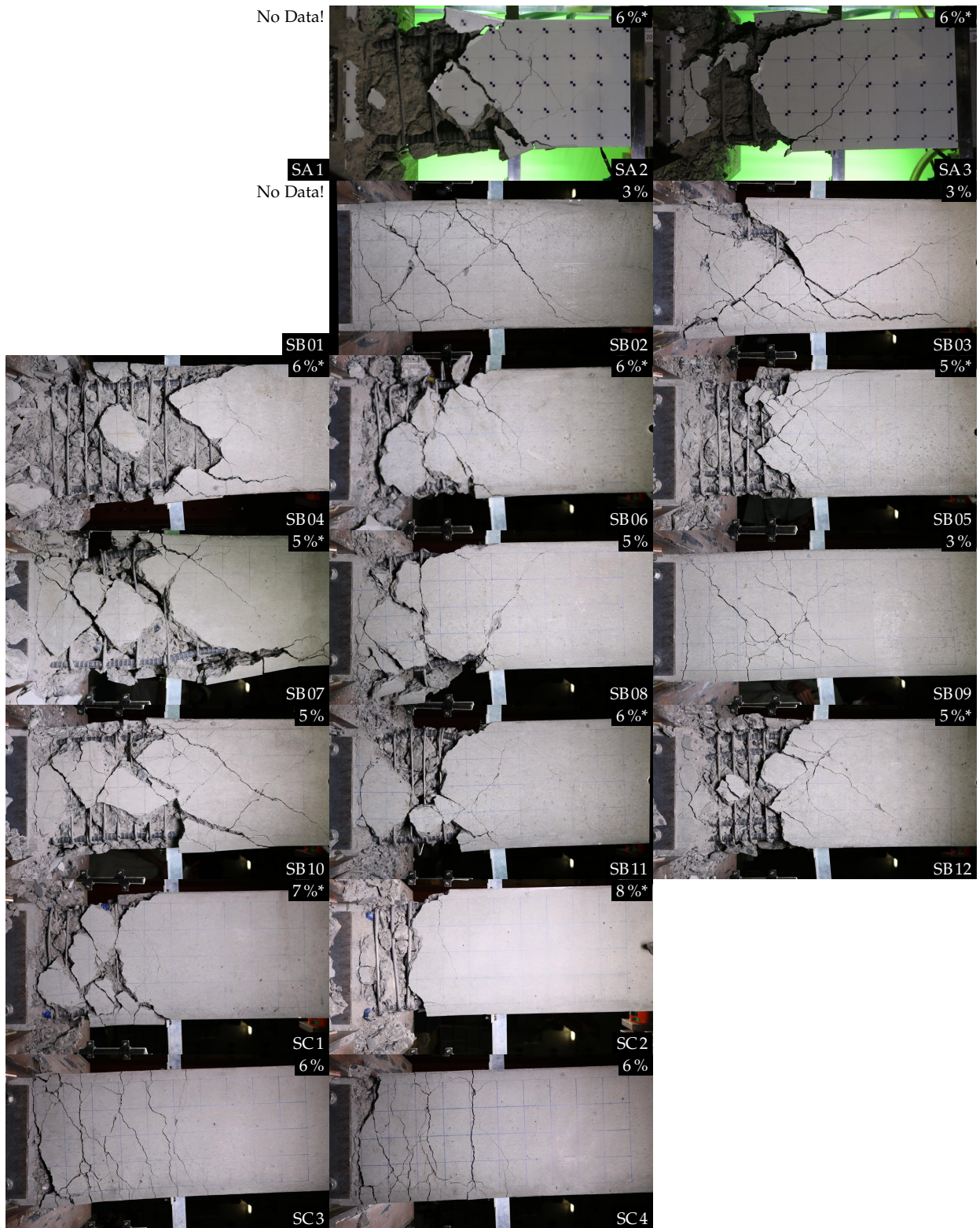
Figure 5.36: Comparison of damage states for all specimens at CP performance state

6
Conclusion

Ultimate state response of RC beams under reversed cyclic loading was investigated through a large experimental program consisting of nineteen beam specimens. In addition to conventional measurements, photogrammetry was used to study specimen response to a greater level of detail. Recorded data was analyzed and the performance of relevant parameters was compared to evaluate the performance of existing explanations of mechanism at ultimate state. As experimental findings showed divergence from the existing mechanism, a new mechanism based on lateral inclination of inelastic rebar sections was proposed as an alternative mechanism definition. Photogrammetric measurements were used to qualitatively validate the mechanism and its correlation with ultimate drift capacity. Specific conclusions from each chapter are discussed in detail followed by some suggestions on possible future directions that may be followed from this study.

6.1   *Chapter-wise conclusions*

Conclusions drawn from the respective chapters and important sections can be stated as follows:

· Previous research related to drift capacity of RC beams was reviewed in *Chapter 2*[1]. Detrimental effect of cyclic loading on drift capacity of RC elements was known from experiments as early as 1970s. Numerous experiments were conducted over the next few decades investigating parameters that affect drift capacity. Transverse reinforcement content (ρ_t) was consistently reported to be the single most influential parameter. However, since stirrups contribute to the enhancement of many aspects of section characteristics such as shear strength, concrete confinement, and rebar restraint, it has not been possible to isolate the precise mechanism behind this observation. Existing analytical methods to estimate drift capacity can be broadly separated into four categories. Concrete compressive strain limit based estimates are attractive because of their ease of application but do not accurately represent the effects of cyclic loading. Shear strength deterioration based methods have attracted significant research interest due to its strong correlation with experimental observations. Accurate drift capacity estimation

has not been possible with this approach due to the inherent limitations of strength-based principle in determining deformations. Bar-buckling based methods are also supported by experimental observations but are limited in terms of accuracy because of the inability to explicitly identify the point of initiation of buckling from experiments. Finally, the empirical estimation methods do provide good mean values of drift capacity over the limited range of considered dataset but the accuracy of these estimates is severely restricted by the scatter in dataset.

· Details of the tested specimens, experiment setup and corresponding instrumentation were provided in *Chapter 3*[2]. Large number of specimens (19 in total) with multiple parametric variations ensured systematic and comprehensive evaluation of the influence of respective parameters on drift capacity. Innovative three-point loading setup adopted to simulate cantilever response afforded greater economy and ease of construction in fabricating specimens. However, this arrangement also resulted in greater instrumentation complications as all sensors had to be installed against the same reference close to the critical section of the specimen in the stub region. Successful testing protocol for photogrammetry could be designed using a free camera controller program but the lack of functional and stable applications for this purpose was a significant hurdle.

[2] See page 25.

· Results obtained from the testing program and the reduced response quantities were presented in *Chapter 4*[3] General behavior and cracking pattern observed was very similar in all specimens. After yielding at 0.75 % or 1 % drift cycles and stable strength gain due to strain hardening in tensile reinforcement over next few cycles, rapid deterioration in strength was observed. Drift capacity, defined as the point of more than 20 % deterioration in peak strength, was reached in the narrow range of 4 % to 5 % for most specimens. Specimen state at the conclusion of the loading program was dominated by severe concrete spalling and bulging of rebars in most specimens. Moment-drift response loops exhibited significant pinching for most specimens, especially for loading cycles at larger drifts. Moment-hinge rotation response loops exhibited much less pinching at similar drift levels. Hinge-rotation response was also noted to become increasingly asymmetric as damage starts concentrating on one of the beam edges. Photogrammetry facilitated detailed analysis of specimen response not previously possible with conventional sensors but a meaningful utilization of the measurements was possible nly over a smaller range of the loading history. Excessive cracking and spalling typically observed starting at 4 % target drift cycles limited the utility of photogrammetry beyond that point. Of the two photogrammetry approaches implemented on opposite specimen faces, Method-A provided similar observations on specimen response while costing less analysis time and allowing easier comprehension of test data.

[3] See page 43.

Comparison of results with displacement sensor data successfully demonstrated the validity of photogrammetric measurements.

· Finally, all the gathered experiment results were analyzed and discussed in *Chapter 5*[4]. Major conclusions from respective sections can be listed as follows:

   · Influence of respective parameters on response was investigated by comparing sets of similar specimens in *Section 5.1*[5]. Transverse reinforcement content (ρ_t) was found to have the greatest influence on drift capacity. Although very large increments in ρ_t did not produce proportionally high drift capacities after about 1 % ρ_t values. Shear strength related parameters, concrete strength (f'_c) and transverse reinforcement strength (f_{yt}), were consistently found to have no impact on drift capacity as specimens with more than 100 % difference in f'_c or f_{yt} exhibited nearly similar moment-drift response loops. Shear-span ratio (l/D) was also found to affect drift capacity. Although only small improvements were observed in the drift capacity for specimens with higher l/D, the pinched shape of moment-drift response loops was significantly improved. Specimens with larger longitudinal reinforcement content (ρ) were found to consistently exhibit lower drift capacities and resulted in rapid loss of strength after reaching the drift capacity. Although only one set of specimens were available for comparison, larger rebar diameter (d_b) resulted in slightly larger drift capacities.

   · Evaluation of experimentally observed drift capacities and comparison with existing estimates was carried out in *Section 5.2*[6]. While many different definitions of drift capacity are possible for a loading program with multiple repetitions, it was observed that they are generally related and any definition may be reasonably adopted depending on the type of application or the overall objective. Variations in the resulting drift capacity as large as 4 % were, however, noted over all the considered drift capacity definitions. Drift at peak response (Δ_{cap_m}) was noted as the severest definition of drift capacity, consistently resulting in the smallest capacity values. This estimate is also not influenced by post-peak behavior as the rapidity of strength loss is not reflected in the capacity value. Of the various estimates evaluated from literature, ASCE estimate was consistently conservative while other estimates were, on average, close to the experimentally observe values. For the specimens of SC series which exhibited drift capacities exceeding 6 % and reaching up to 8 %, most estimates ended on the conservative side.

   · Experimentally observed ultimate moment strength and post yielding stiffness were analyzed in *Section 5.3*[7]. ACI recommended estimate of 1.25 times the nominal moment strength was found to consistently over-predict the ultimate moment strength in all specimens. Using accurate material models, however, was

found to result in much improved estimates in some cases. On the basis of this observation, it was concluded that reasonable estimates of concrete confinement must be included in the material model to accurately estimate the ultimate strength. Post-yielding stiffness approximated with a single linear branch was found to closely represent the specimen response from yield to maximum strength. Expressed as a fraction of the stiffness before yield, most specimens were observed to have post-yielding stiffness in the range of 3 % to 5 %. It was noted that if a linear post-yielding behavior is assumed, entire response to the ultimate state may be reasonably represented with any two of the following three quantities: ultimate moment strength, post-yielding stiffness and drift capacity.

· Based on the observed response and failure patterns a new mechanism defining resistance at the ultimate state was proposed in *Section 5.4*[8]. Observing that shear strength related parameters did not influence the drift capacity and large lateral expansion on concrete core before reaching the ultiamte state was recorded using photogrammetry, the new mechanism was formulated based on the lateral inclination capacity of inelastic rebar sections. It was argued that repeated loading cycles cause deepening of inclined cracks which leads to gradual build up of residual slips and lateral bulging of concrete core. P-M interaction curve of inclined rebars at the edge of bulging concrete sections was deduced and it was found that more than 40 % of axial load carrying capacity of rebars is lost at an eccentric inclination of about 3 mm (for the rebar size used in this experiment). Rebar eccentricity approximated with concrete surface deformations measured using photogrammetry was also found to strongly corelate with the initiation of loss of strength. Validity of the proposed mechanism was thus qualitatively confirmed using photogrammetric measurements.

[8] See page 93.

· Finally, using the recorded response and systematically shot photographs from the experiment, various performance states were identified in *Section 5.5*[9]. Using the ASCE defined envelope and the recorded response, the three performance states defined by ASCE could be identified from the experiment. Conservatism of ASCE in predicting the drift capacity was also reflected in the identified performance states. Collapse prevention performance state could not be accurately determined in all specimens since the loading program was often terminated before reaching very large deformations.

[9] See page 108.

6.2   *Scope for future work*

QUALITATIVE definition of a new mechanism determining resistance at the ultimate limit state of deformation was formulated in this study. The ideas introduced through this mechanism may be refined to

develop appropriate tools for estimating drift capacity of RC beams. Few of the plausible next steps can be listed as follows:

· A *mechanical model* relating the ultimate drift capacity with rebar eccentricity may be derived to accurately determine drift capacity of RC beams depending on the reinforcement arrangement. Strength characteristics of inclined rebar sections developed in this thesis allow accurate determination of load resistance based on the inclination of the rebars at the peak deformation state. Now, if the development of rebar inclination can be established in terms of the applied tip deformations, accurate estimation of tip deformation capacity can be readily obtained. The mechanics of diagonally cracked section may be analyzed to relate the development of lateral strain or core expansion with the application of cyclic loadings at increasingly large displacements.

· Further *experiments* may be conducted to obtain refined data on rebar deformation which may also be used to calibrate the mechanical model. In the current study, photogrammetric measurements at specific grid locations on concrete surface were used to approximate rebar deformations. Better ways to experimentally measure rebar deformations may be devised to obtain more accurate estimates. Examples may include refined photogrammetry grid, instrumentation to directly measure rebar deformations, reinforcement cage only experiments or even radiographic imaging. Such experimental data would also be valuable for calibration of the mechanical model developed to estimate drift capacity as the experimental data on this phenomenon is currently very limited.

· The mechanism proposed for the simple case of beams in flexure may be expanded to the more complicated case of *columns*. While the proposed mechanism was validated for only beams with no axial load, the basic mechanics associated with inclination of rebars are expected to be the same in case of columns. The presence of axial load may limit expansion of concrete but at the ultimate state, large rebar eccentricity is expected to lead to a loss of resistance in a similar mechanism. Experimental investigation may be pursued to test the validity of this mechanism in the case of columns.

A
Design drawings

SPECIMEN construction drawings are included to show the general layout, reinforcement details, insert locations, and strain gauge placement. Full page figures in the following pages show sets of respective detail drawings for each specimen.

Drawings for specimens with only minor differences such as the material grades are omitted for brevity. Details are included for specimens SA1, SA2, SA3, SB01, SB03, SB04, SB07, SC1, SC2, and SC3. Following four designated drawings are included for each of these specimens:

101 : Layout and section details

102 : Reinforcement details

103 : Strain gauge arrangement

104 : Insert arrangement

配筋・形状図

断面図

※注記
・寸法単位はミリメートルとする。
・コンクリートの配合は別途打ち合わせによる
・主筋はSD345とする。
・せん断補強筋はSD295とする。
・プレート・ナットは東京鉄鋼製とする。
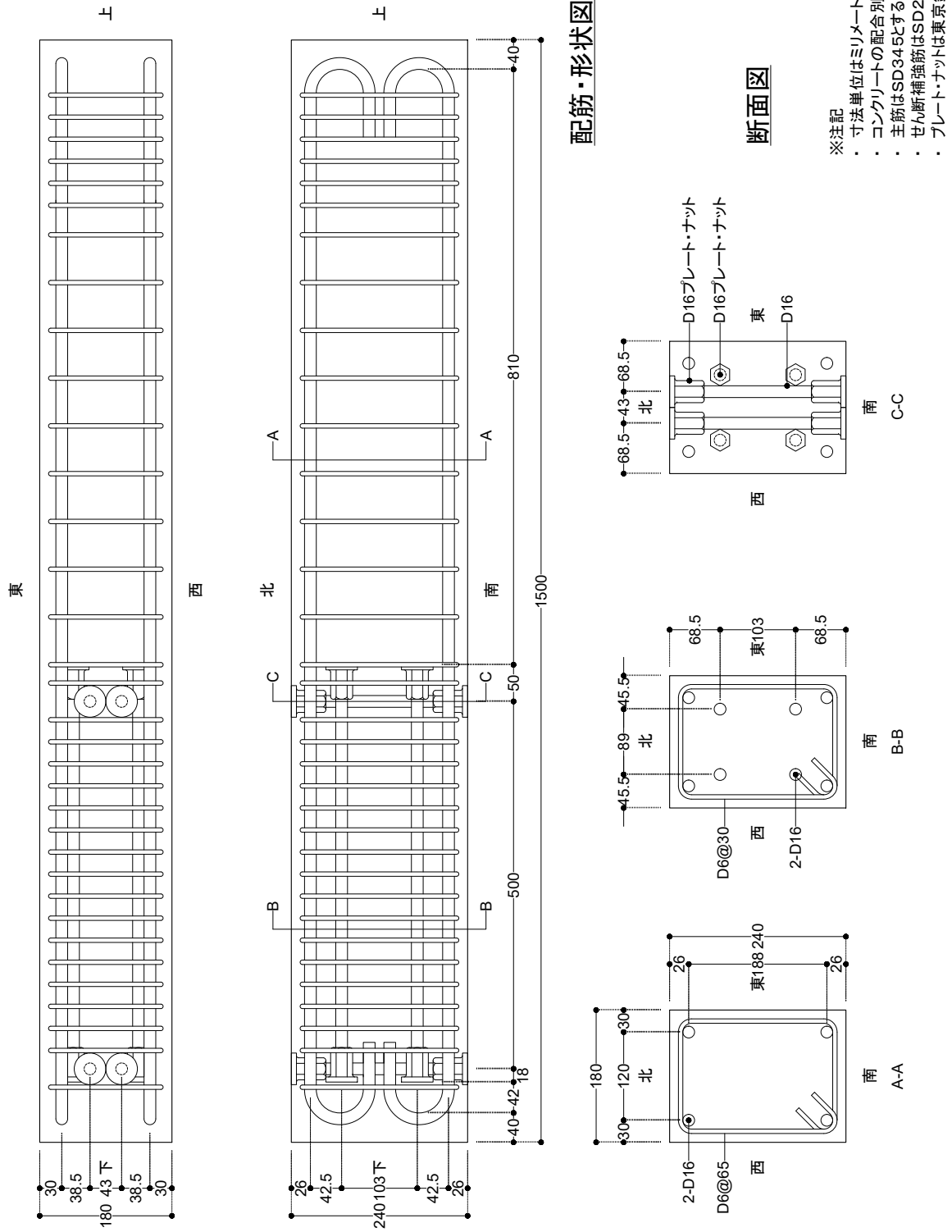
Figure A.1: SA1-101 Layout and section details
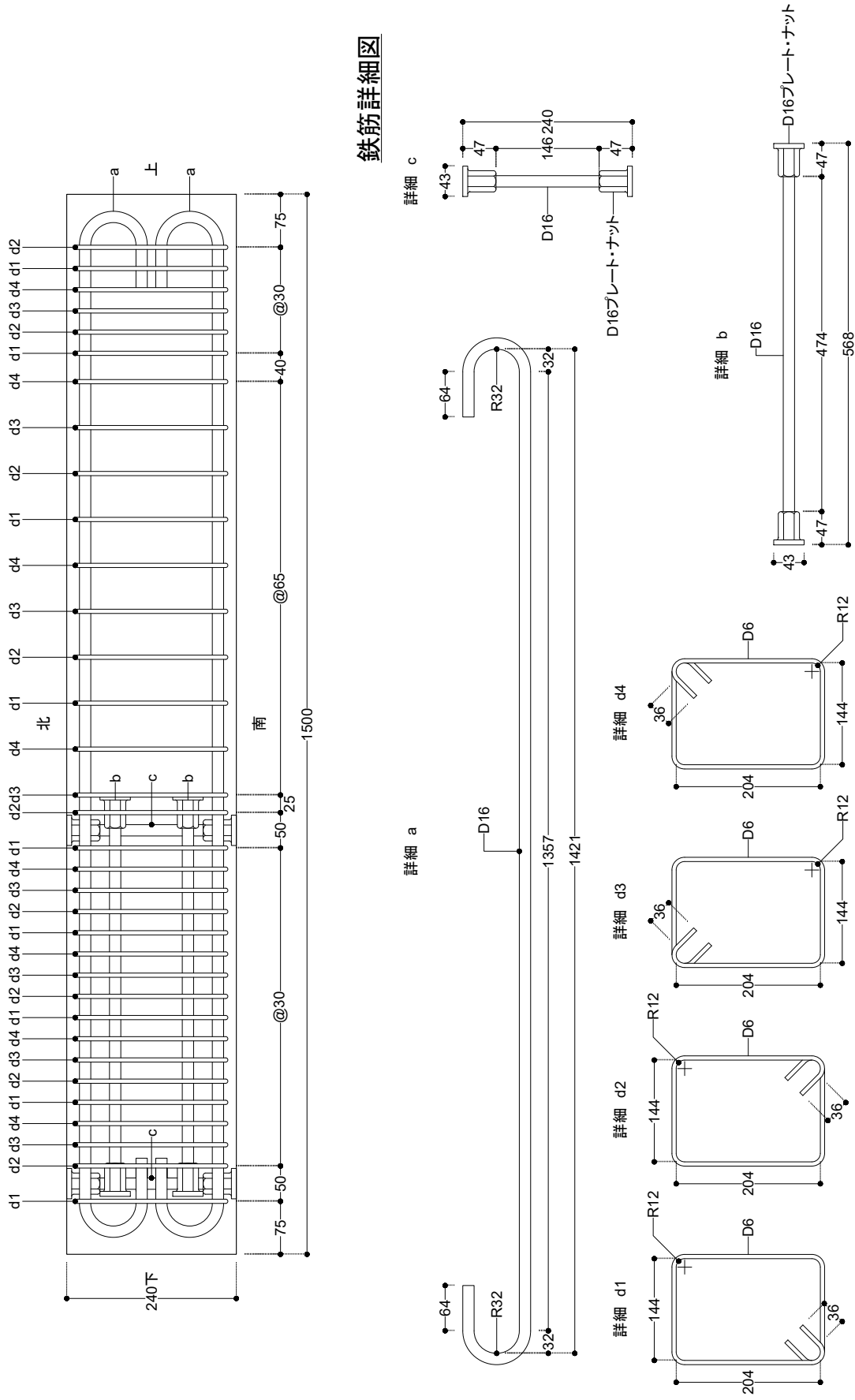
鉄筋詳細図

Figure A.2: SA1-102 Reinforcement details

Figure A.3: SA1-103 Strain gauge arrangement

インサート位置
縮尺 1:6

インサート詳細
縮尺 1:4

Figure A.4: SA1-104 Insert arrangement

Figure A.5: SA2-101 Layout and section details

鉄筋詳細図

詳細 b

詳細 c

詳細 a

詳細 d1

詳細 d2

詳細 d3

詳細 d4

詳細 e1

詳細 e2

詳細 e3

詳細 e4
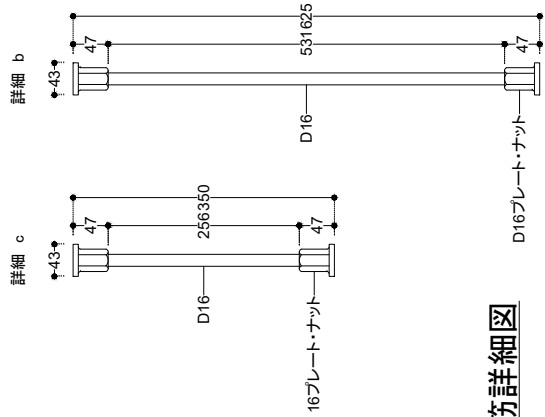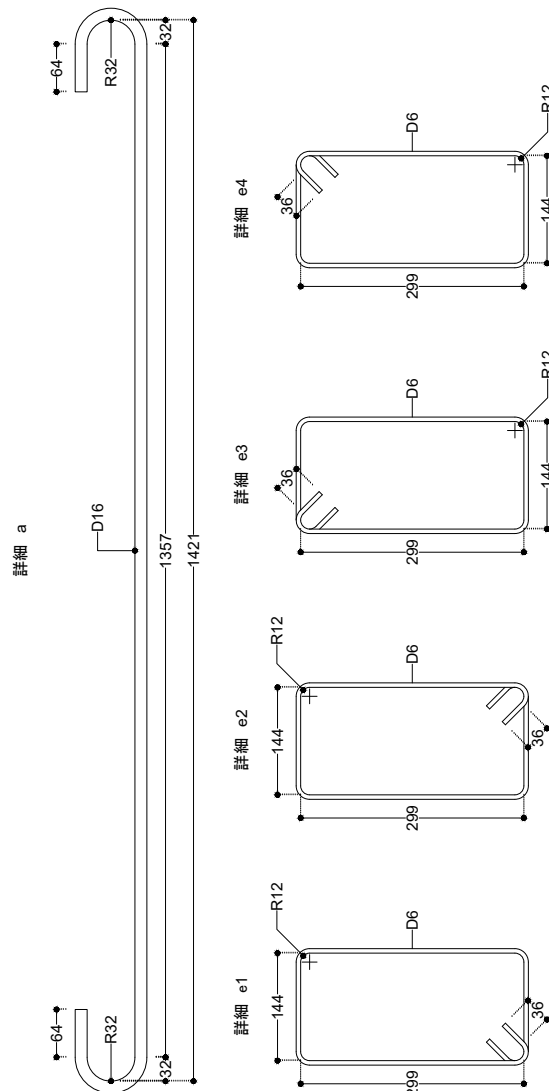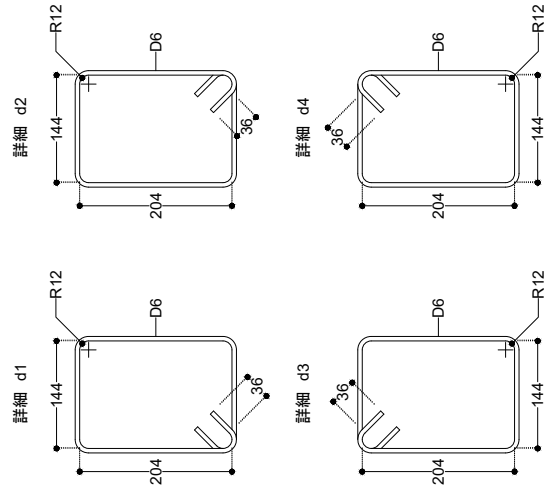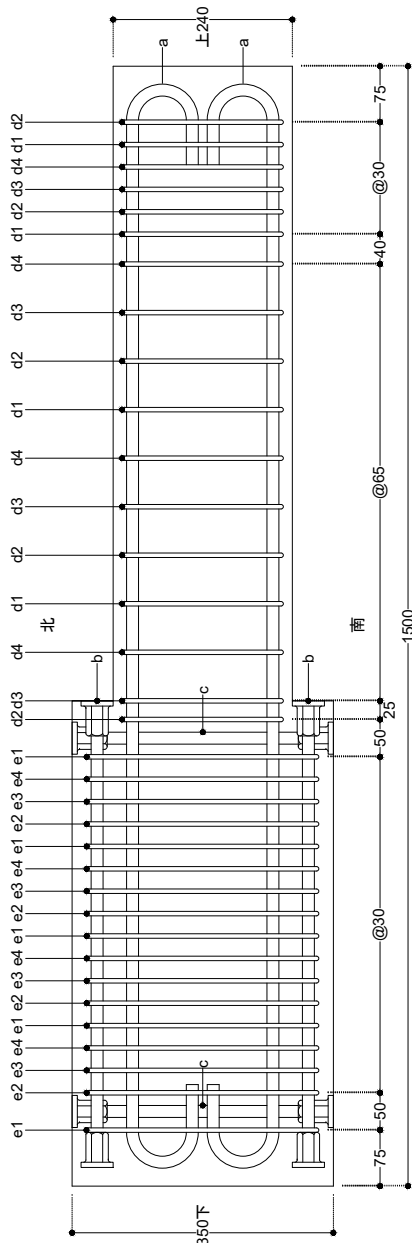
Figure A.6: SA2-102 Reinforcement details
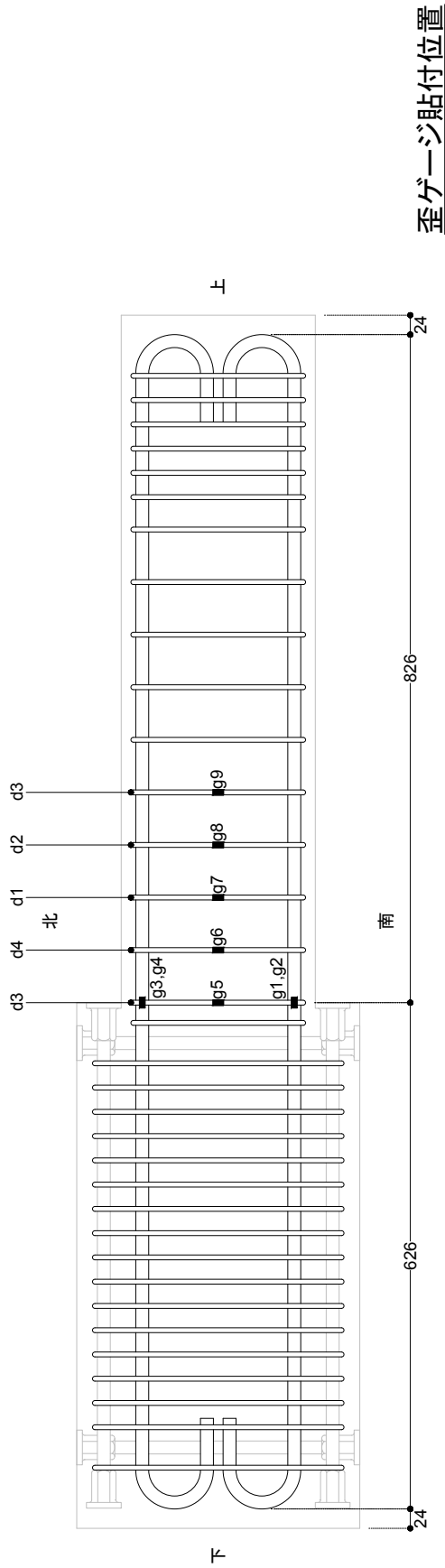
歪ゲージ貼付位置
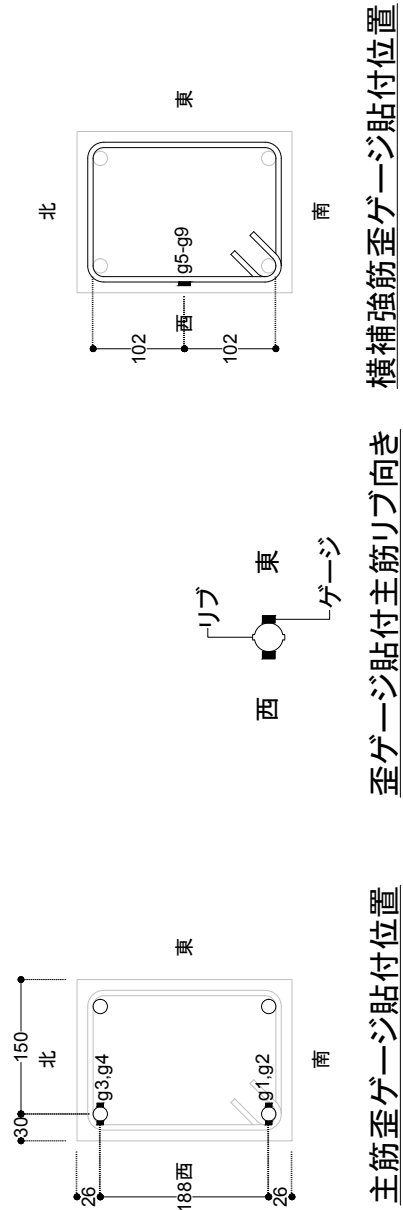
横補強筋歪ゲージ貼付位置

歪ゲージ貼付主筋リブ向き

主筋歪ゲージ貼付位置

※注記
・詳細d1−d4は図面番号105による。
・主筋の歪ゲージは東京測器製のFLA−3とする。
・横補強筋の歪ゲージは東京測器製のFLA−2とする。

Figure A.7: SA2-103 Strain gauge arrangement

インサート位置

縮尺 1:6

インサート詳細

縮尺 1:4

※注記
・寸法単位はミリメートルとする。

東 / 西 / 北 / 南 / 上 / 下

M20B
M12B
M12A
M16
M12C
M12B
M20A

120 120
90 90
90 90
150
160
590
160
270
170
750
500
100
30
150
100 150 100
175 175

M16
(本数=4)
75
22

M20A
(本数=1)
75
30

M20B
(本数=1)
100
30

M12A
(本数=1)
50 50
18
10.5

M12B
(本数=10)
50
17

M12C
(本数=4)
18
10.5
鋼板
1X40X40
鋼線
1X50
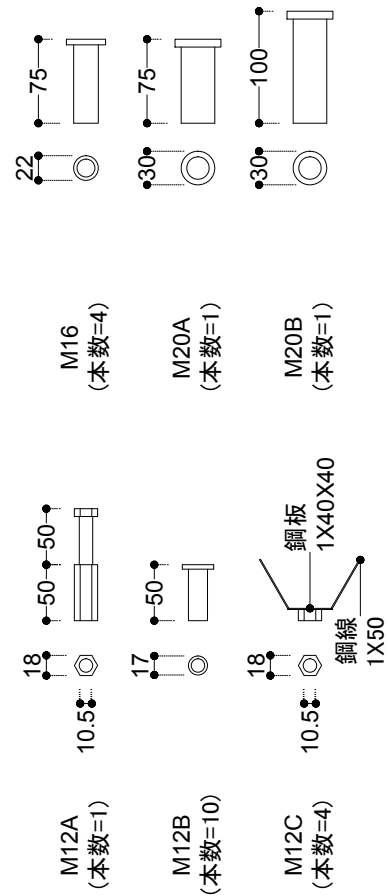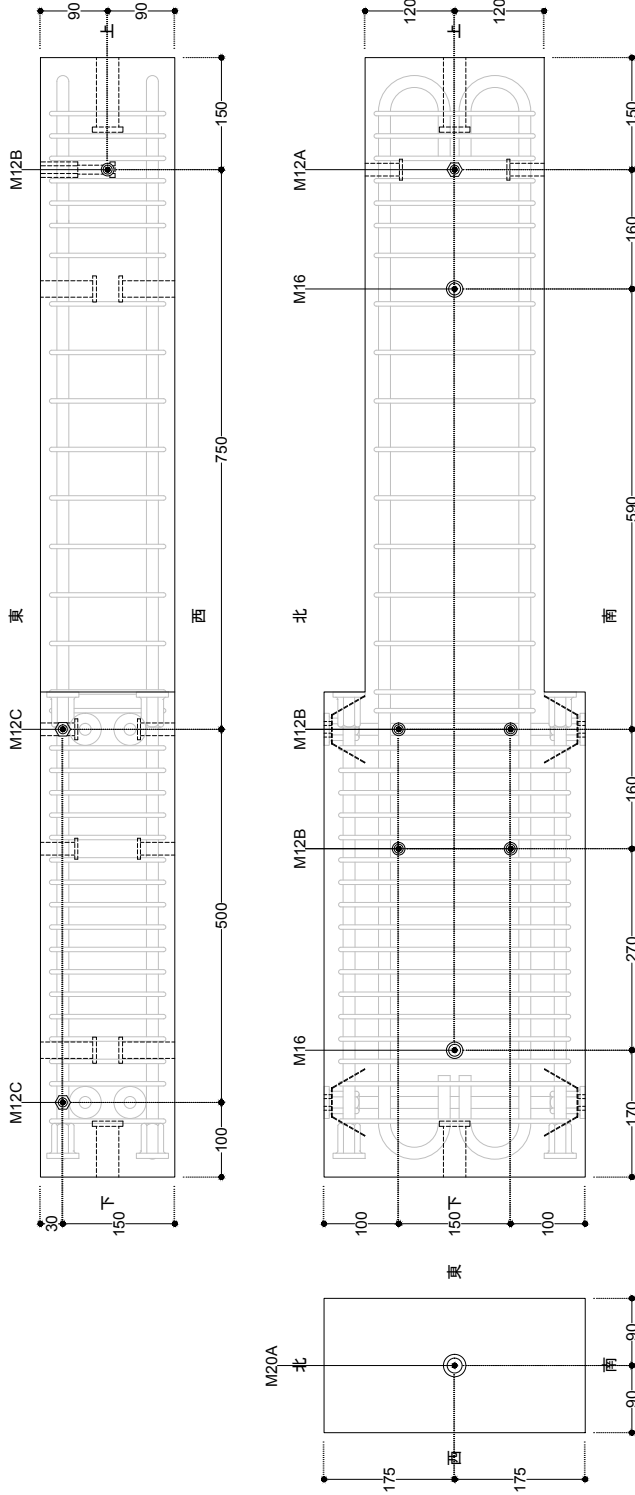
Figure A.8: SA2-104 Insert arrangement

Figure A.9: SA3-101 Layout and section details

鉄筋詳細図

詳細 c

詳細 b

詳細 a

鋼板 9

D16

詳細 d1

詳細 d2

詳細 d3

詳細 d4
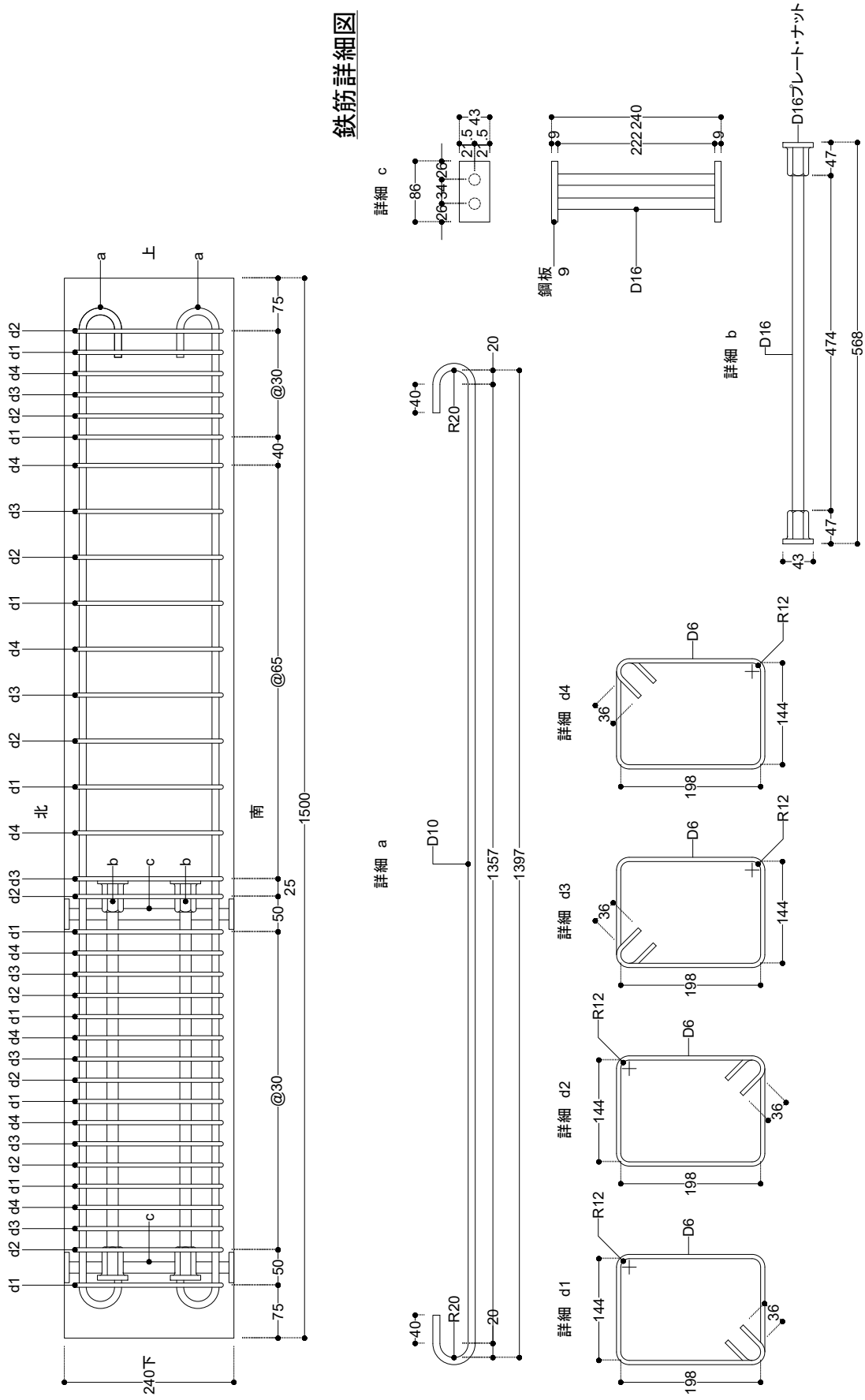
Figure A.10: SA3-102 Reinforcement details

Figure A.11: SA3-103 Strain gauge arrangement

インサート位置
縮尺 1:6

インサート詳細
縮尺 1:4

※注記
・寸法単位はミリメートルとする。

M12A
(本数=1)

M12B
(本数=8)

M12C
(本数=6)

M16
(本数=4)

M20A
(本数=1)

M20B
(本数=1)

鋼板
1X40X40

鋼線
1X50
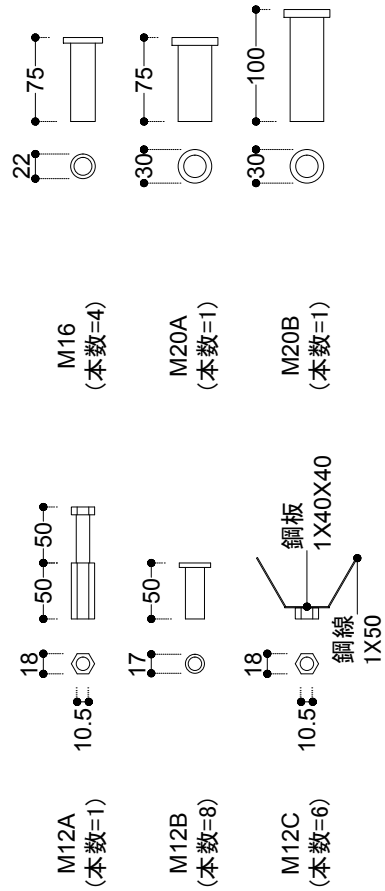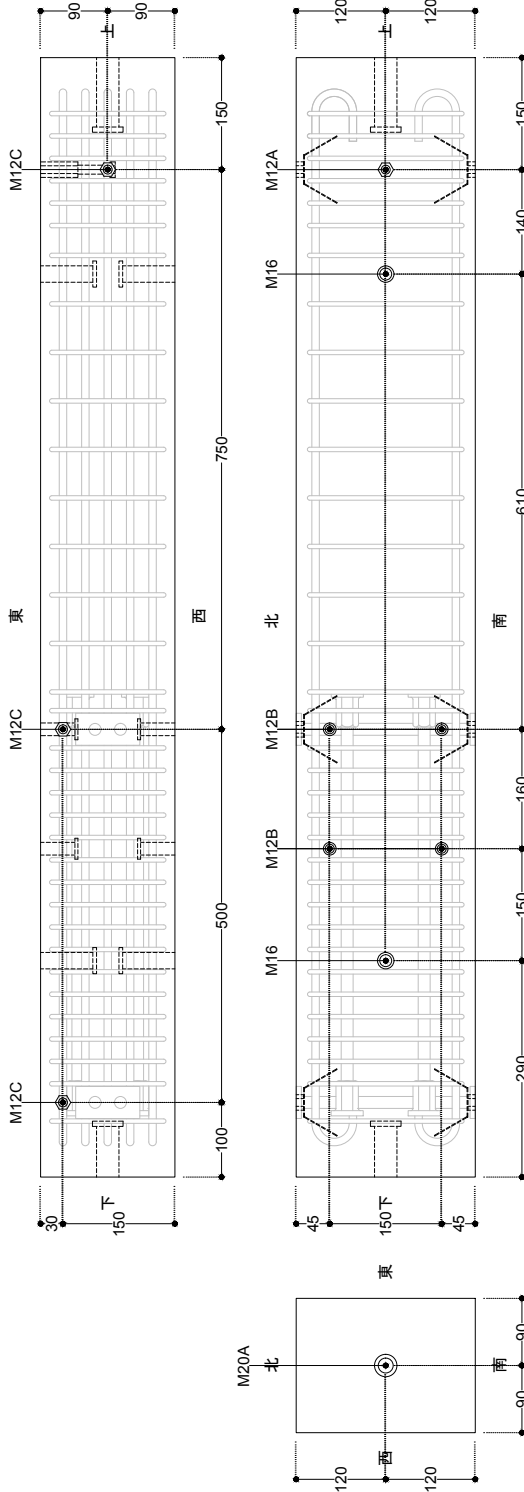
Figure A.12: SA3-104 Insert arrangement

Figure A.13: SB01-101 Layout and section details
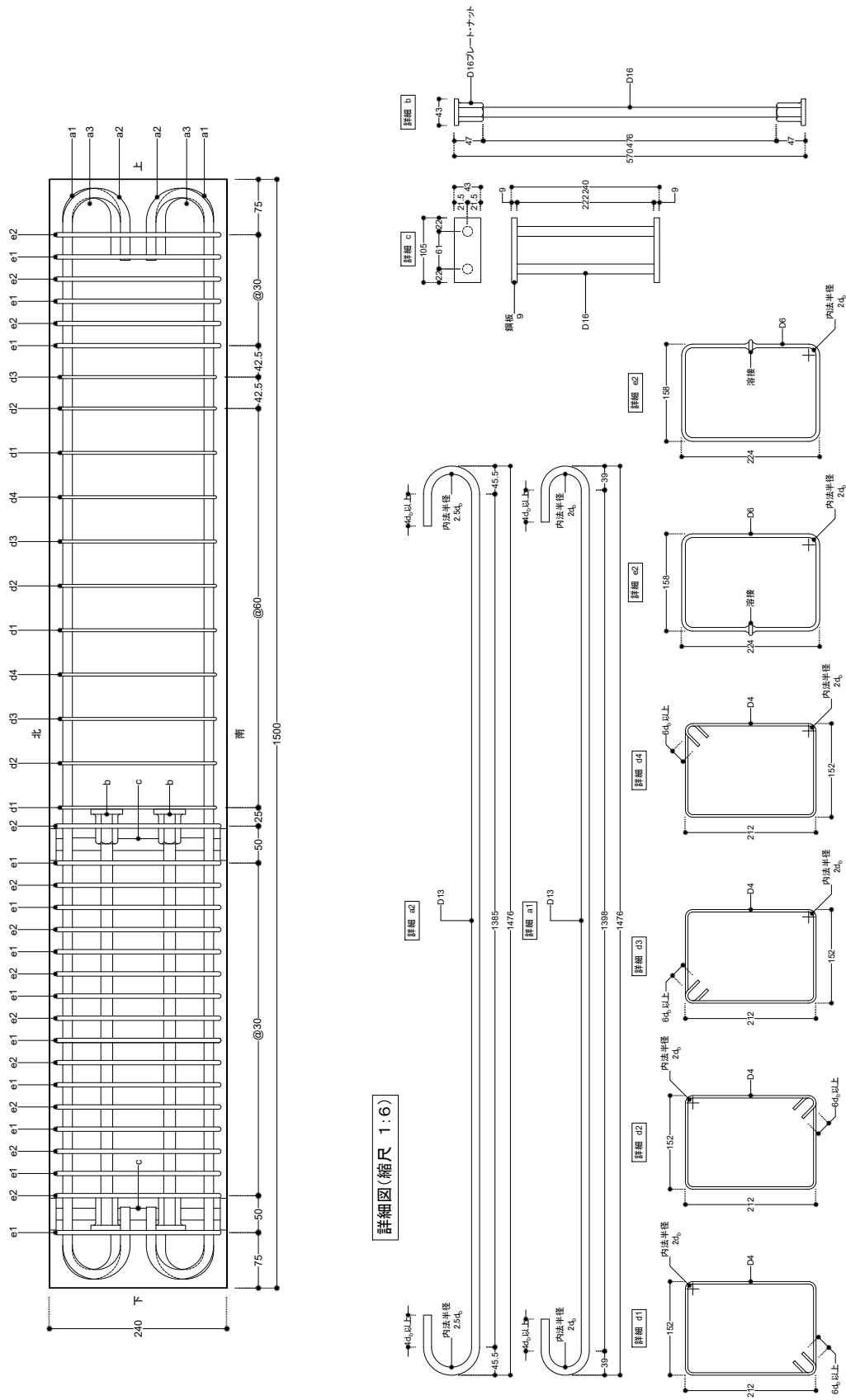
Figure A.14: SB01-102 Reinforcement details
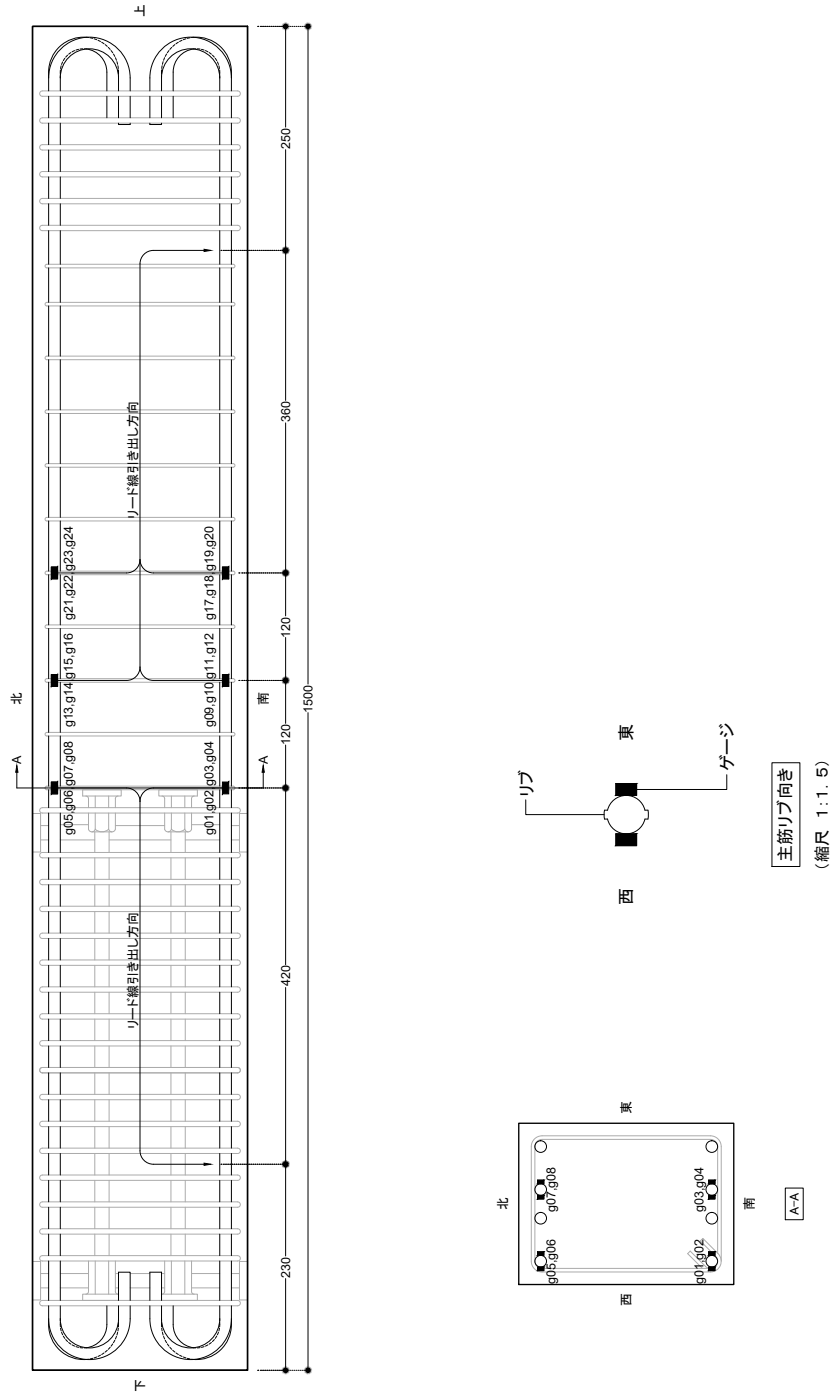
Figure A.15: SB01-103 Strain gauge arrangement
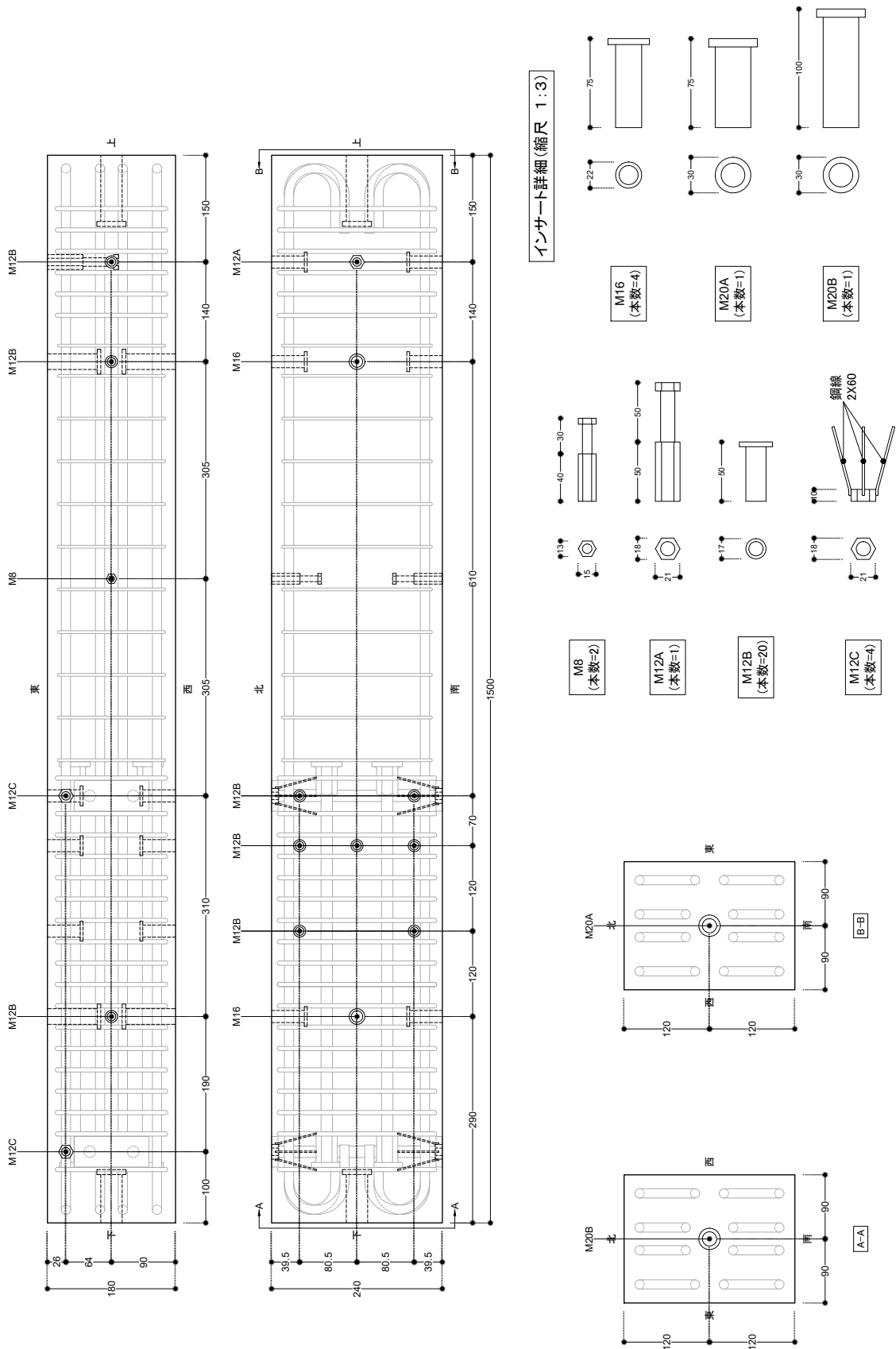
Figure A.16: SB01-104 Insert arrangement

Figure A.17: SB03-101 Layout and section details

Figure A.18: SB03-102 Reinforcement details
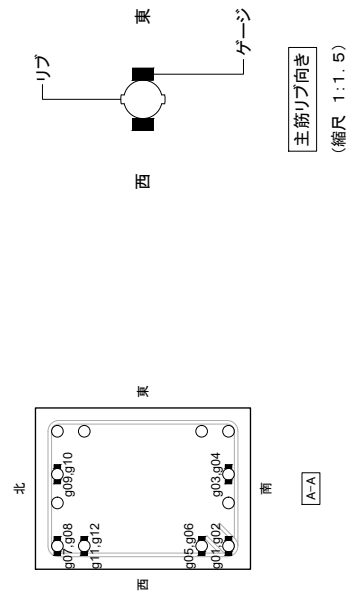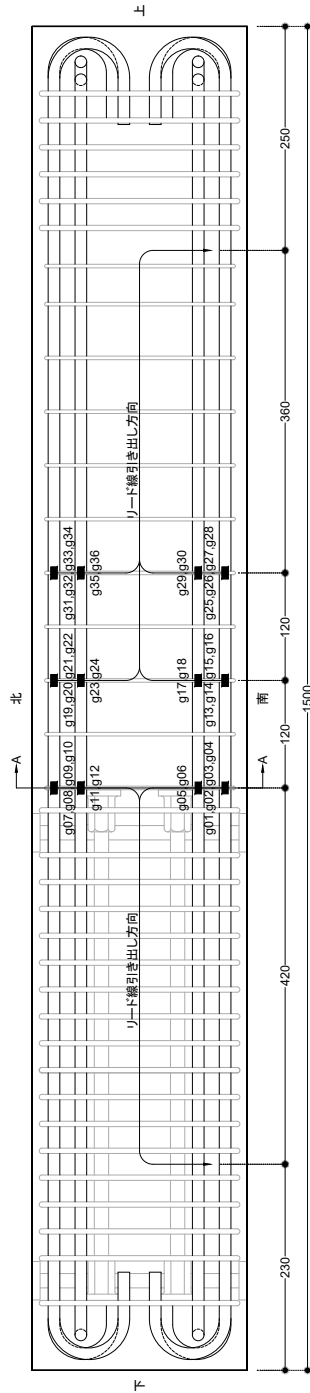
Figure A.19: SB03-103 Strain gauge arrangement
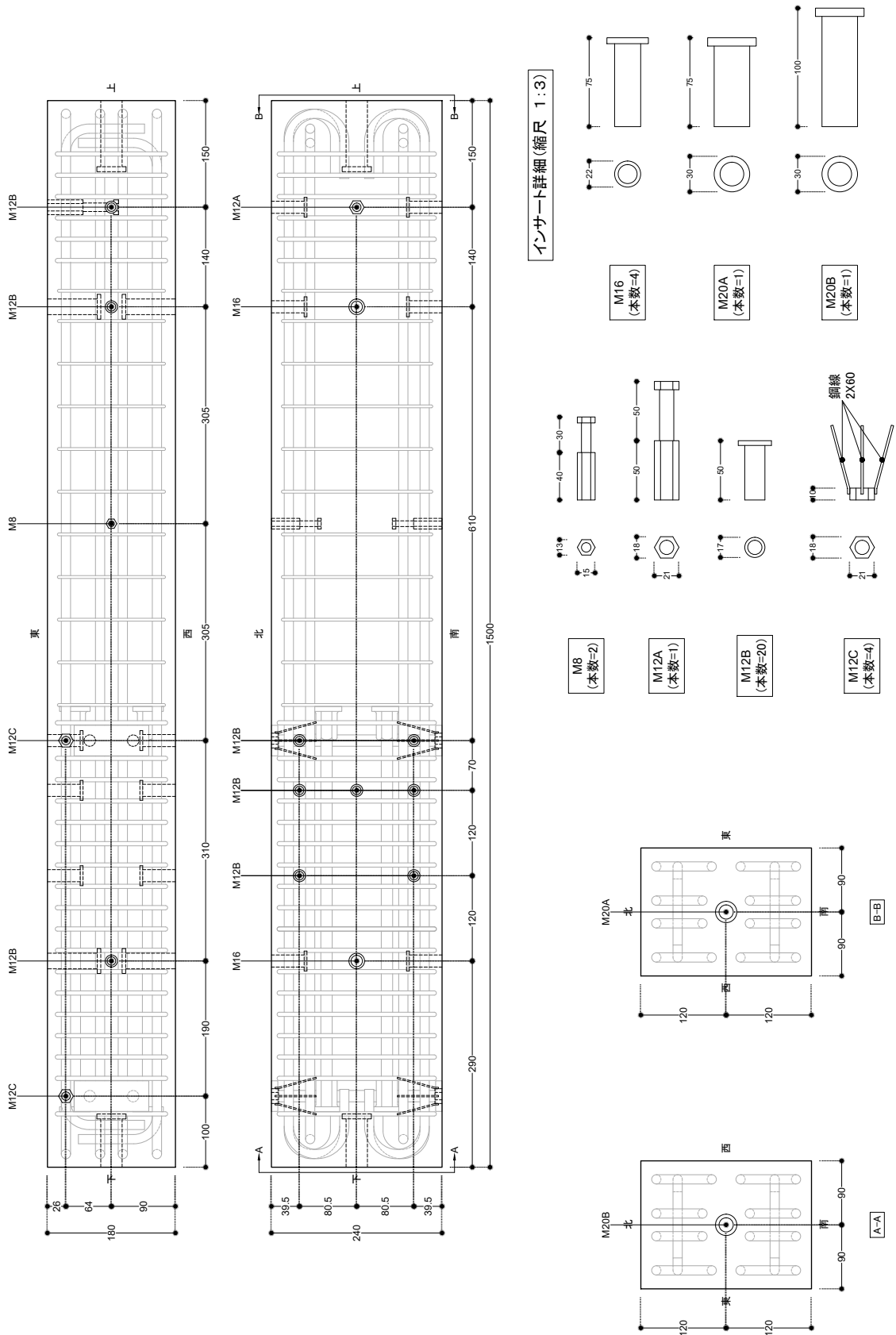
Figure A.20: SB03-104 Insert arrangement

Figure A.21: SB04-101 Layout and section details
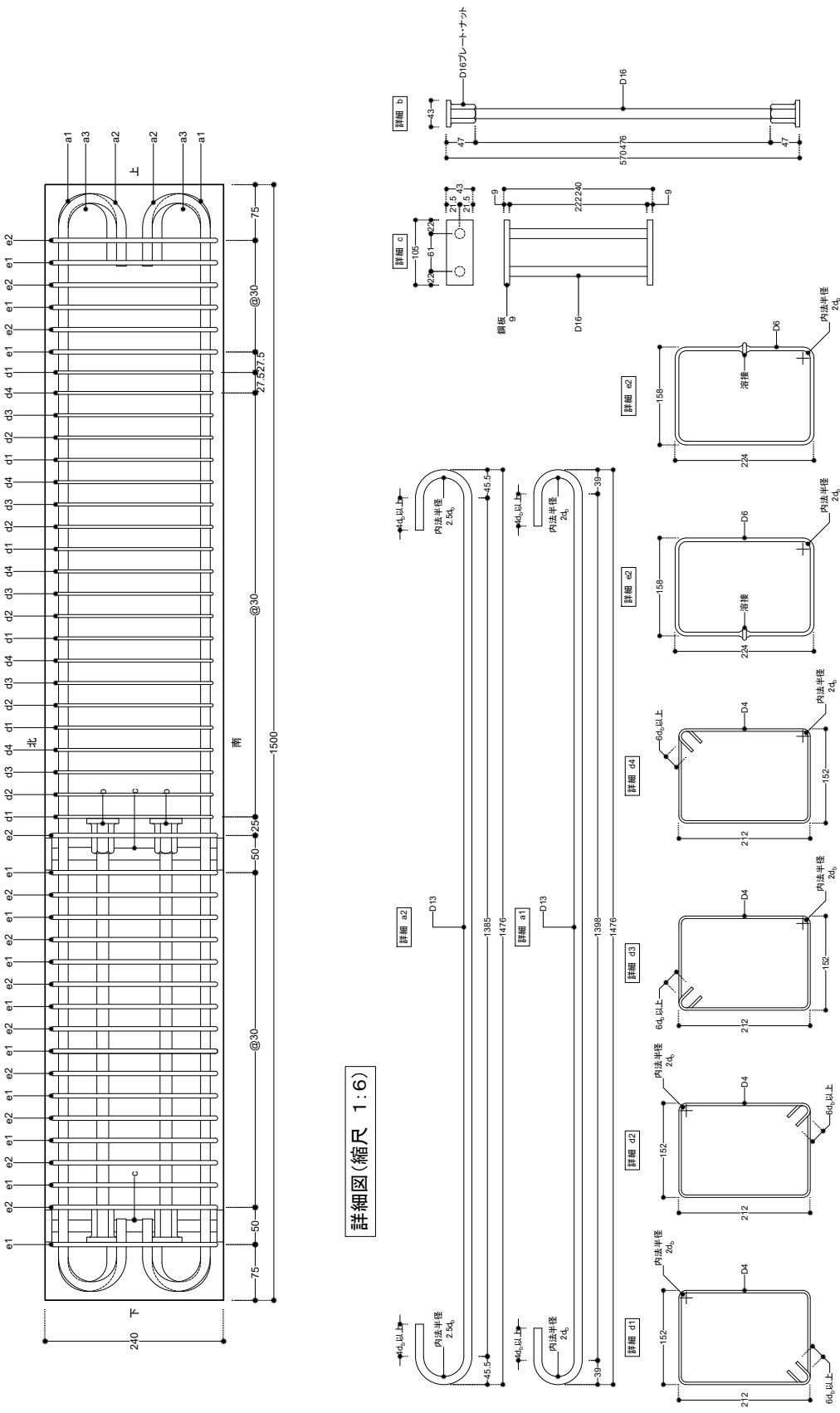
Figure A.22: SB04-102 Reinforcement details
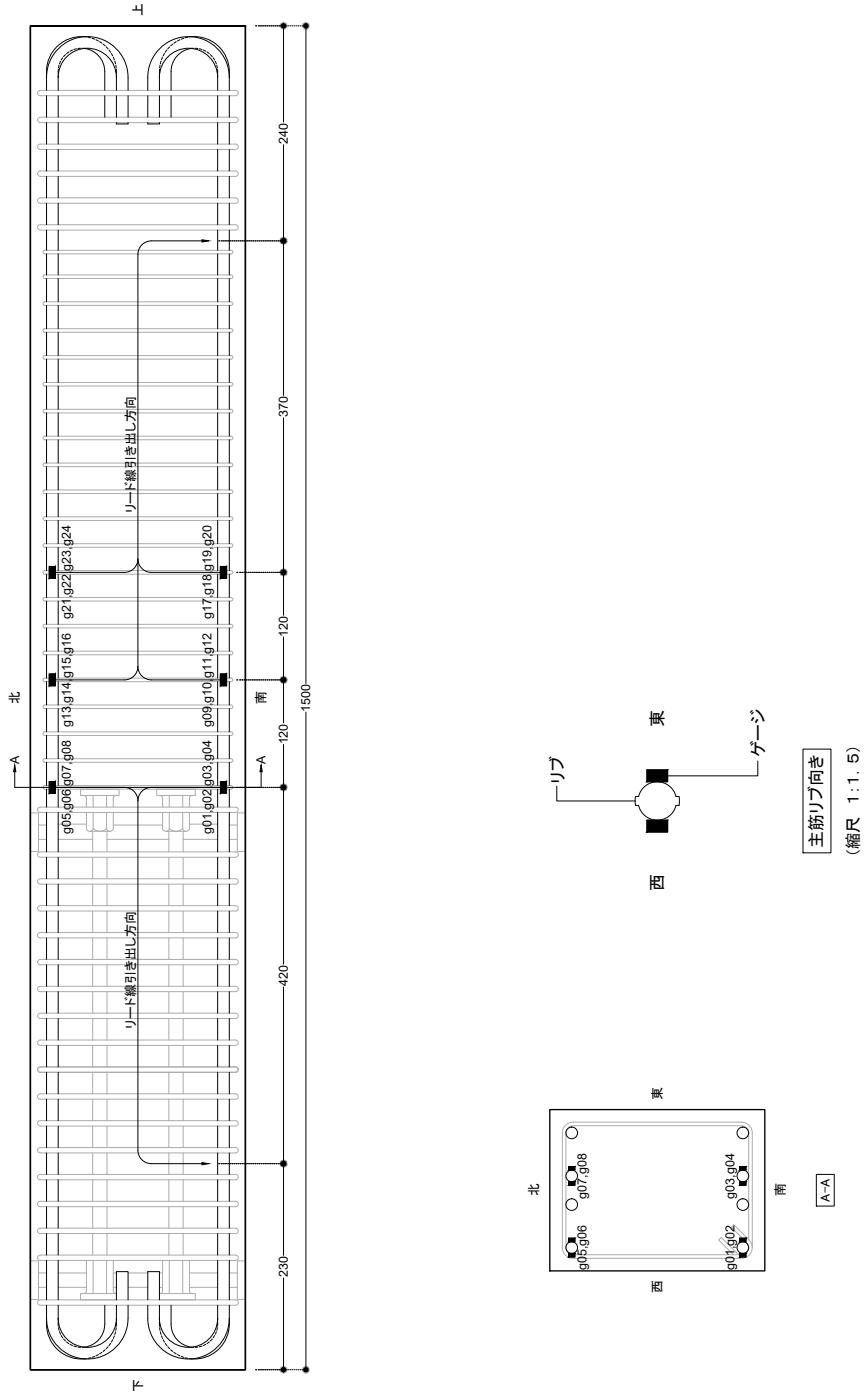
Figure A.23: SB04-103 Strain gauge arrangement
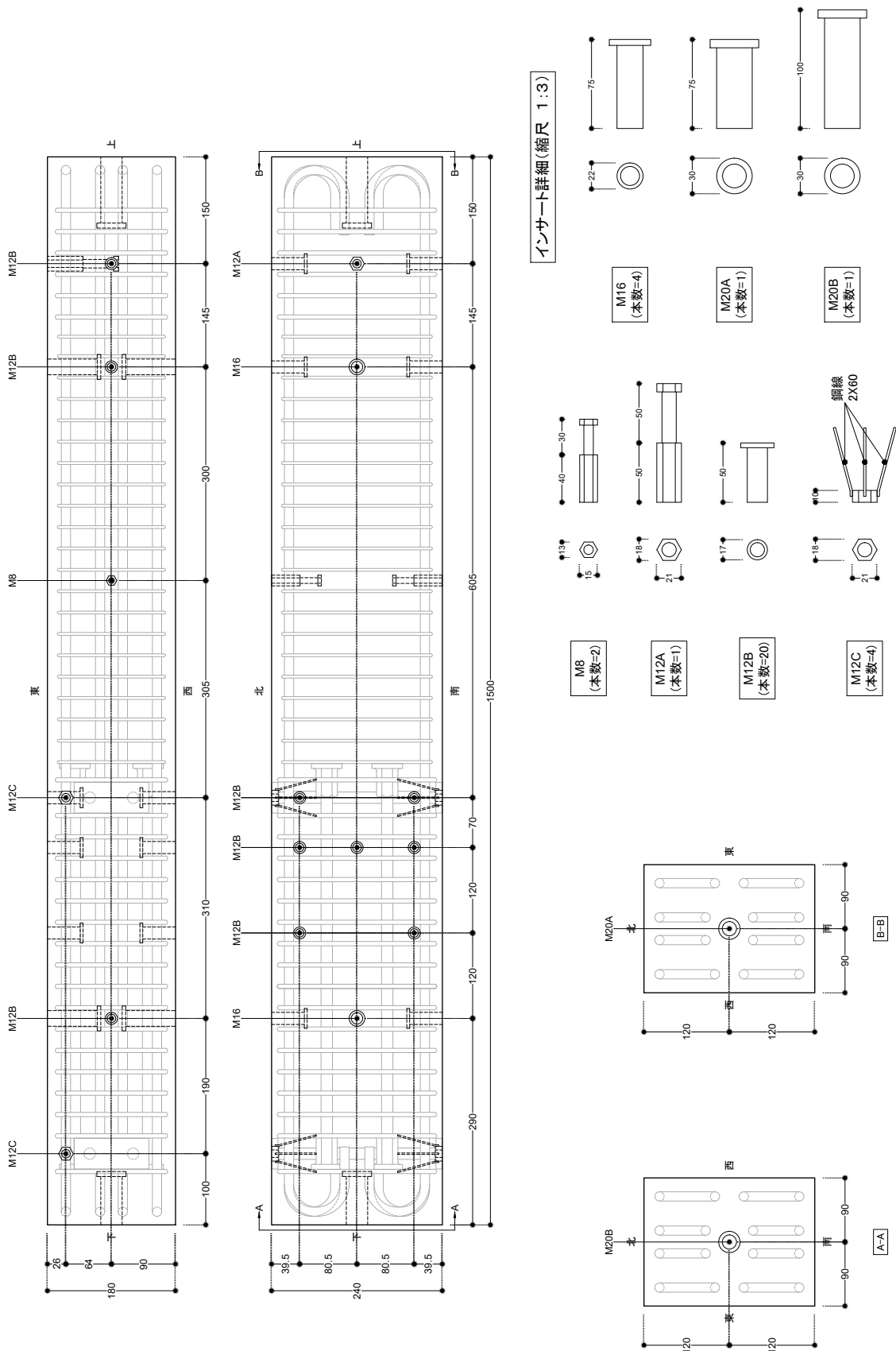
Figure A.24: SB04-104 Insert arrangement

Figure A.25: SB07-101 Layout and section details
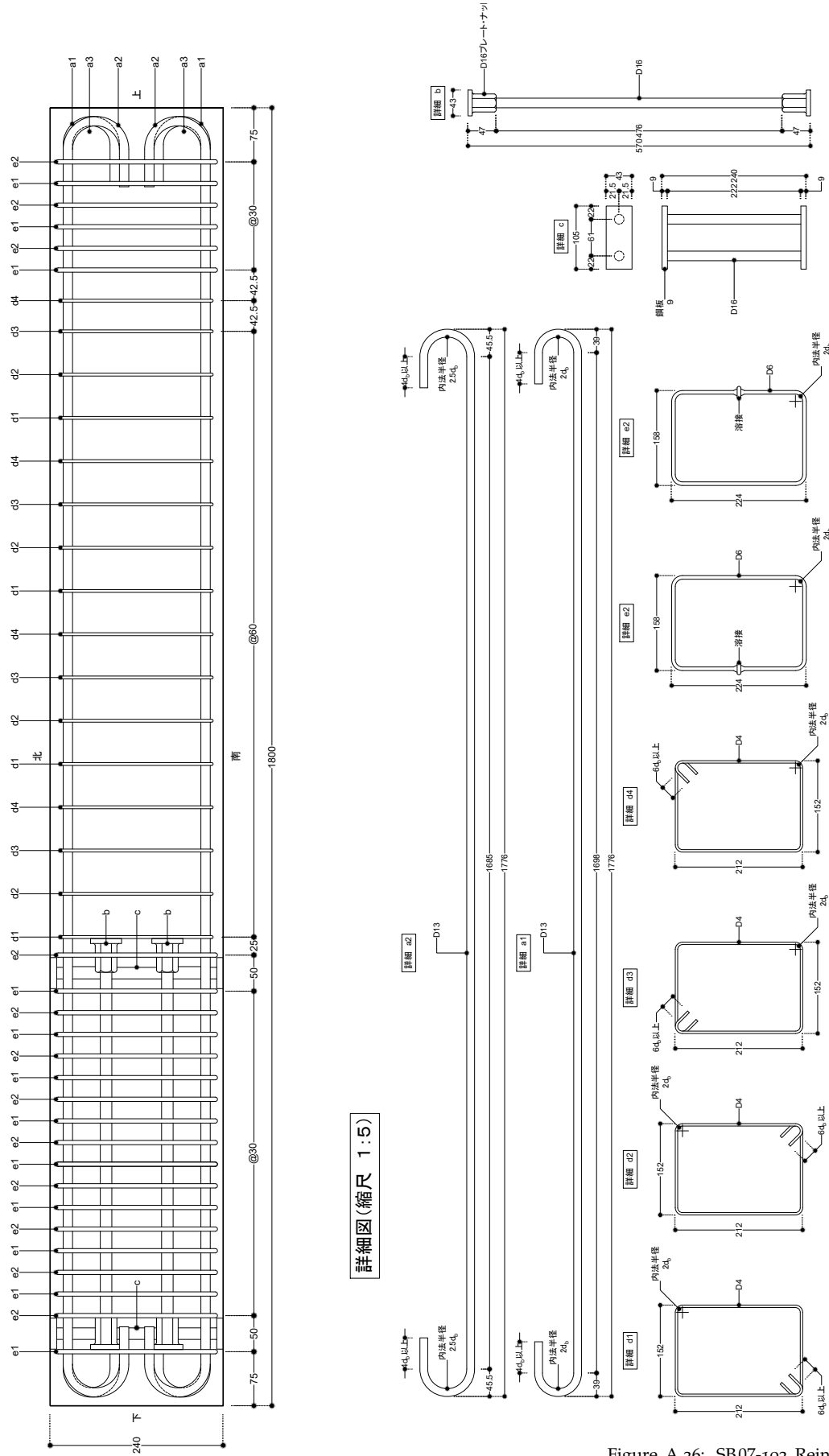
Figure A.26: SB07-102 Reinforcement details
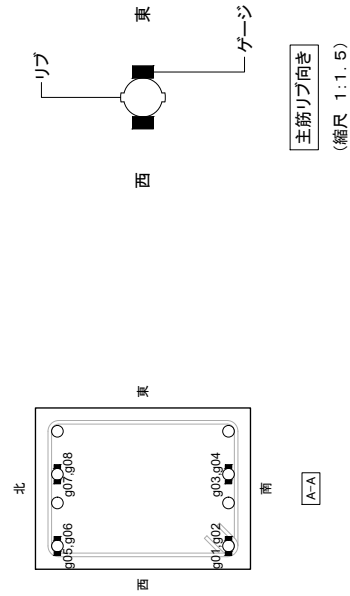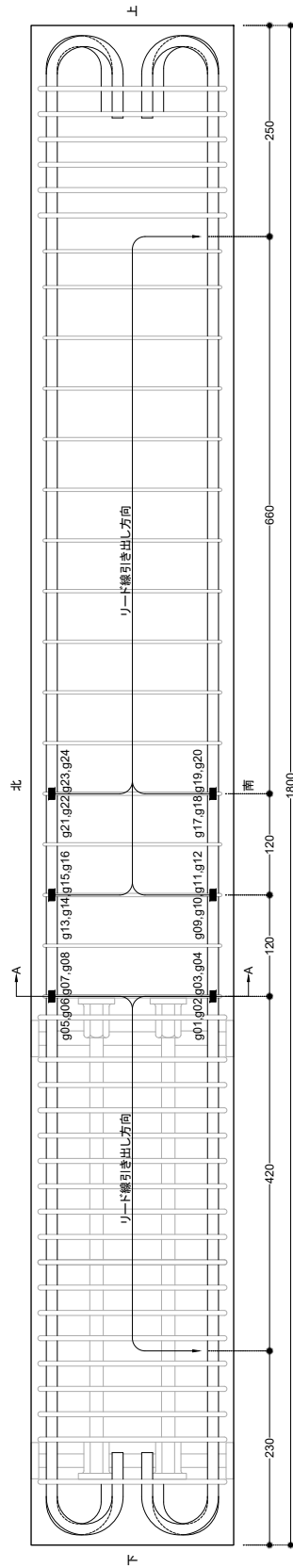
Figure A.27: SB07-103 Strain gauge arrangement
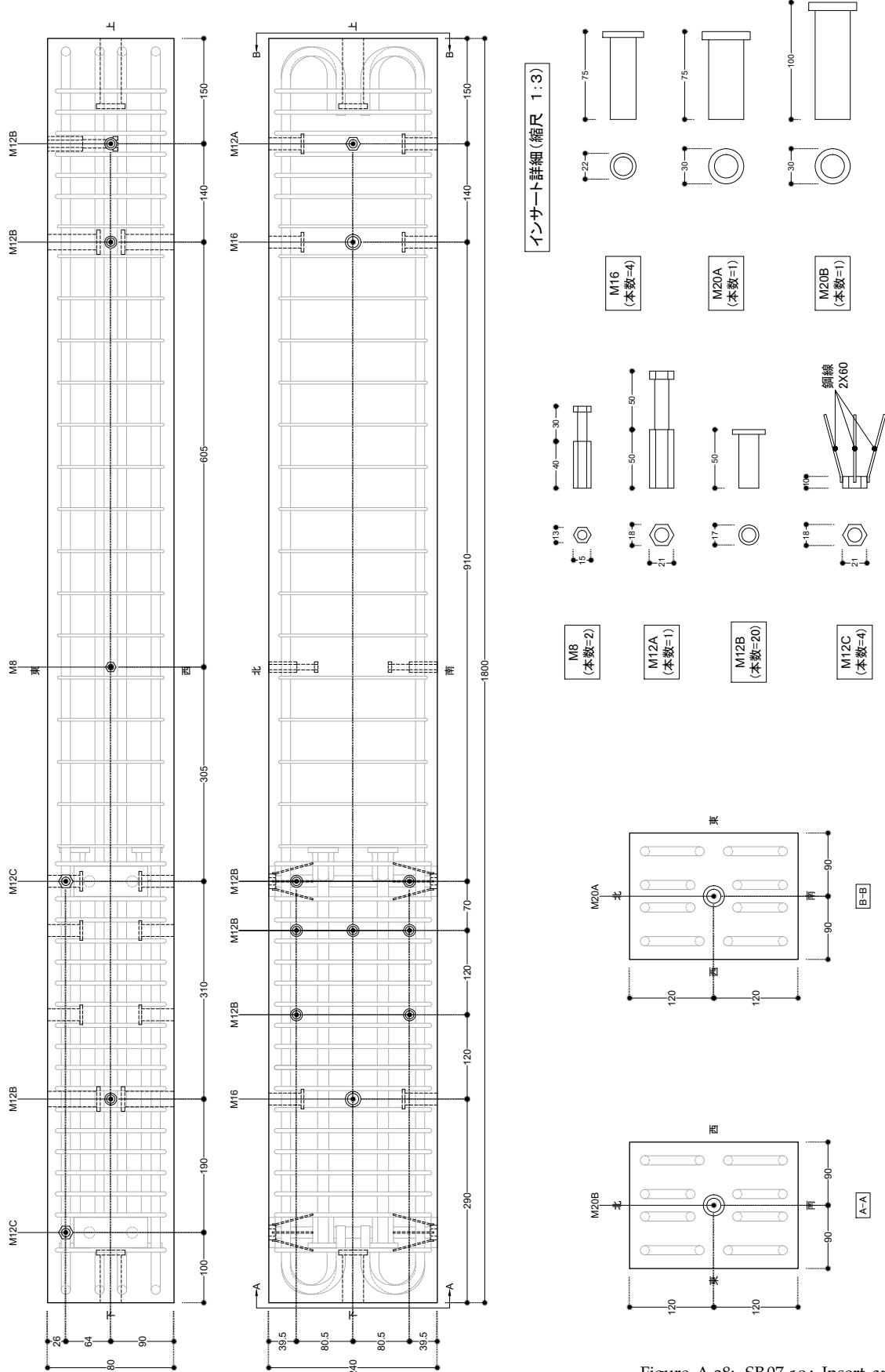
Figure A.28: SB07-104 Insert arrangement
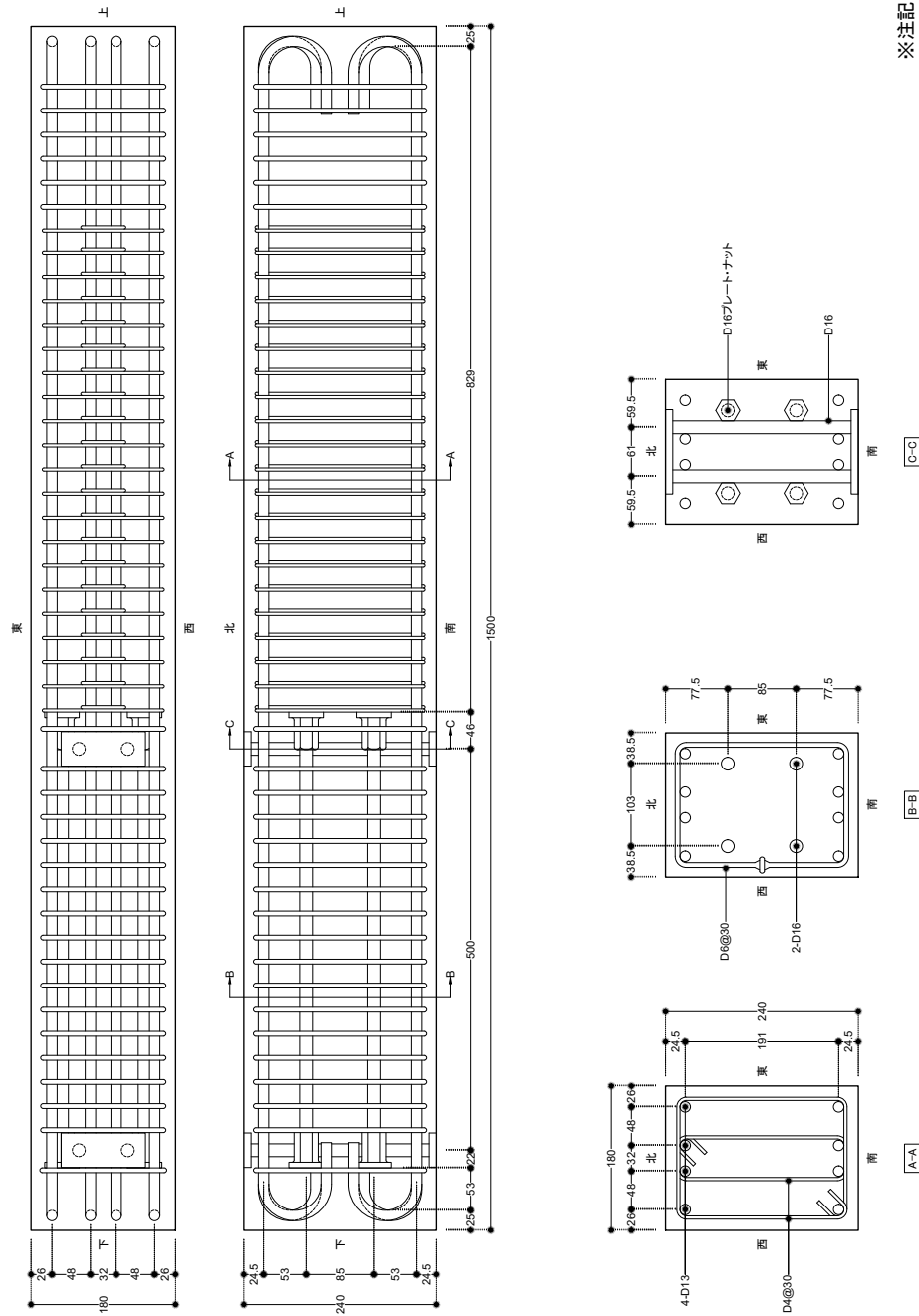
Figure A.29: SC1-101 Layout and section details
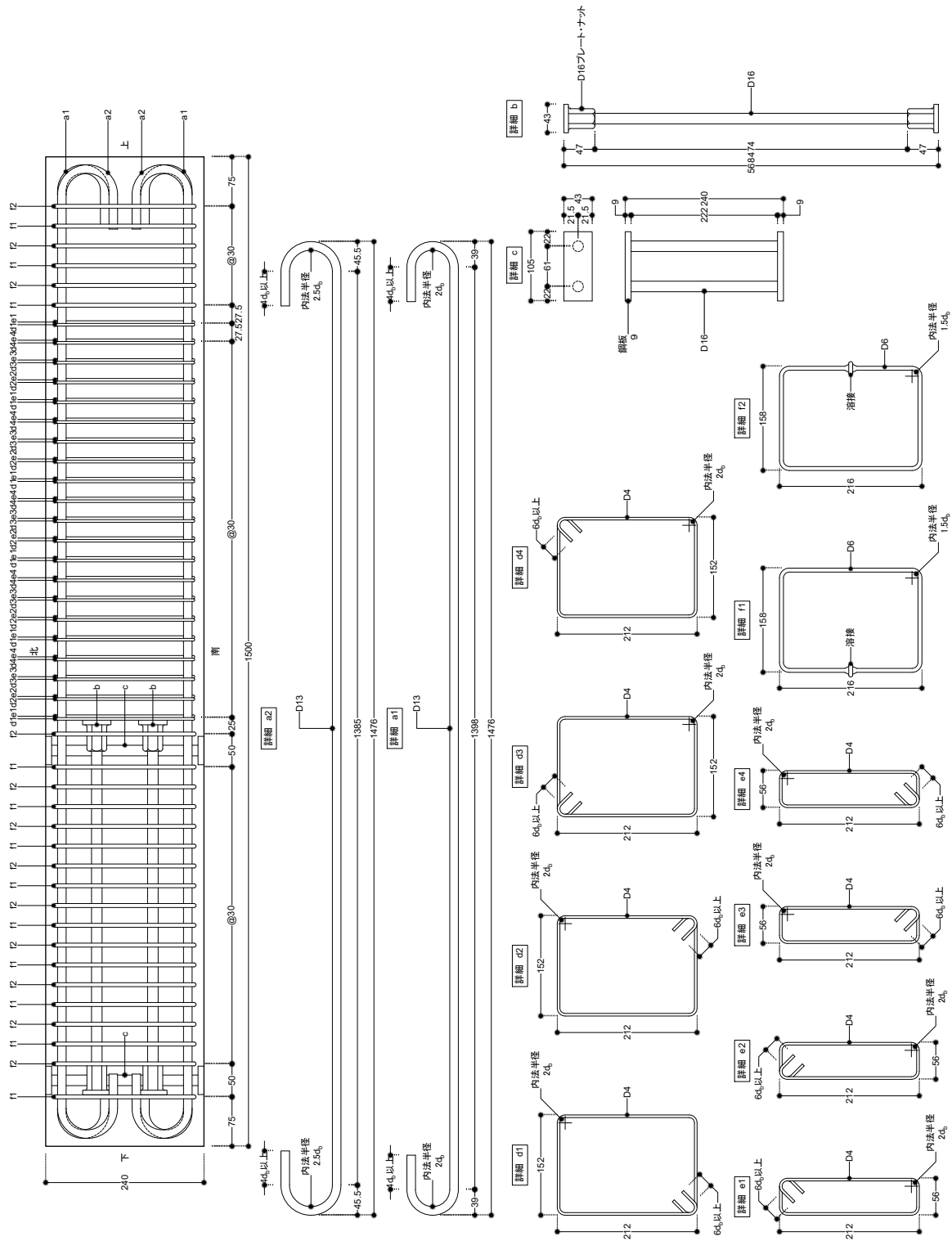
Figure A.30: SC1-102 Reinforcement details
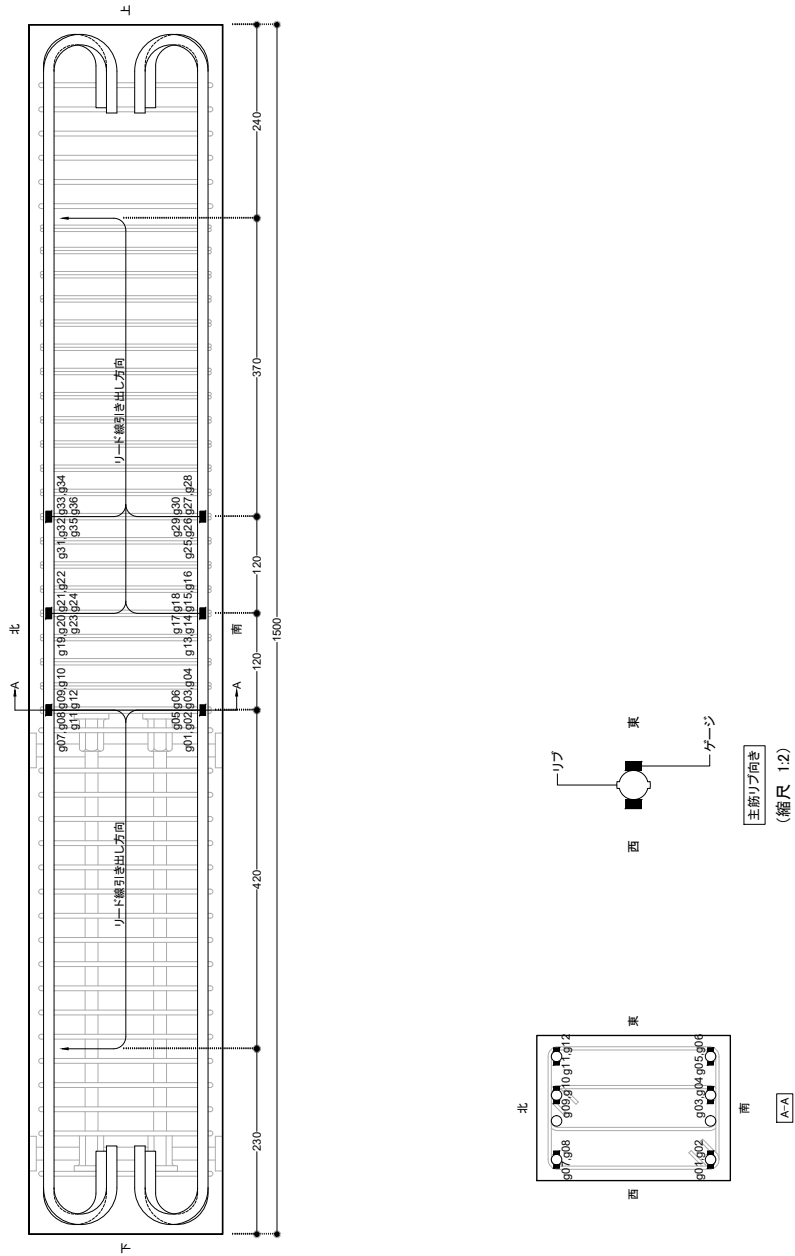
Figure A.31: SC1-103 Strain gauge arrangement
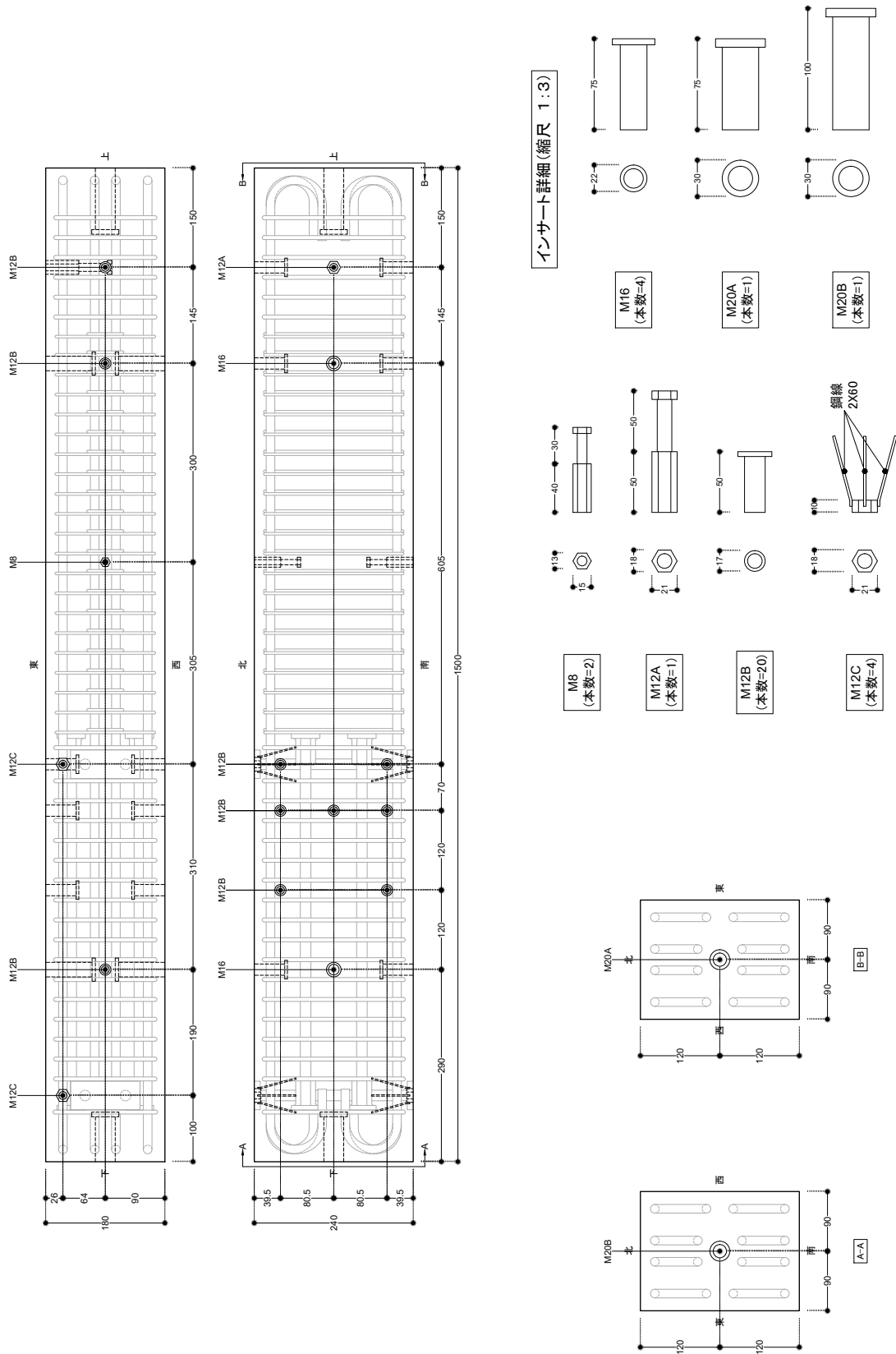
Figure A.32: SC1-104 Insert arrangement
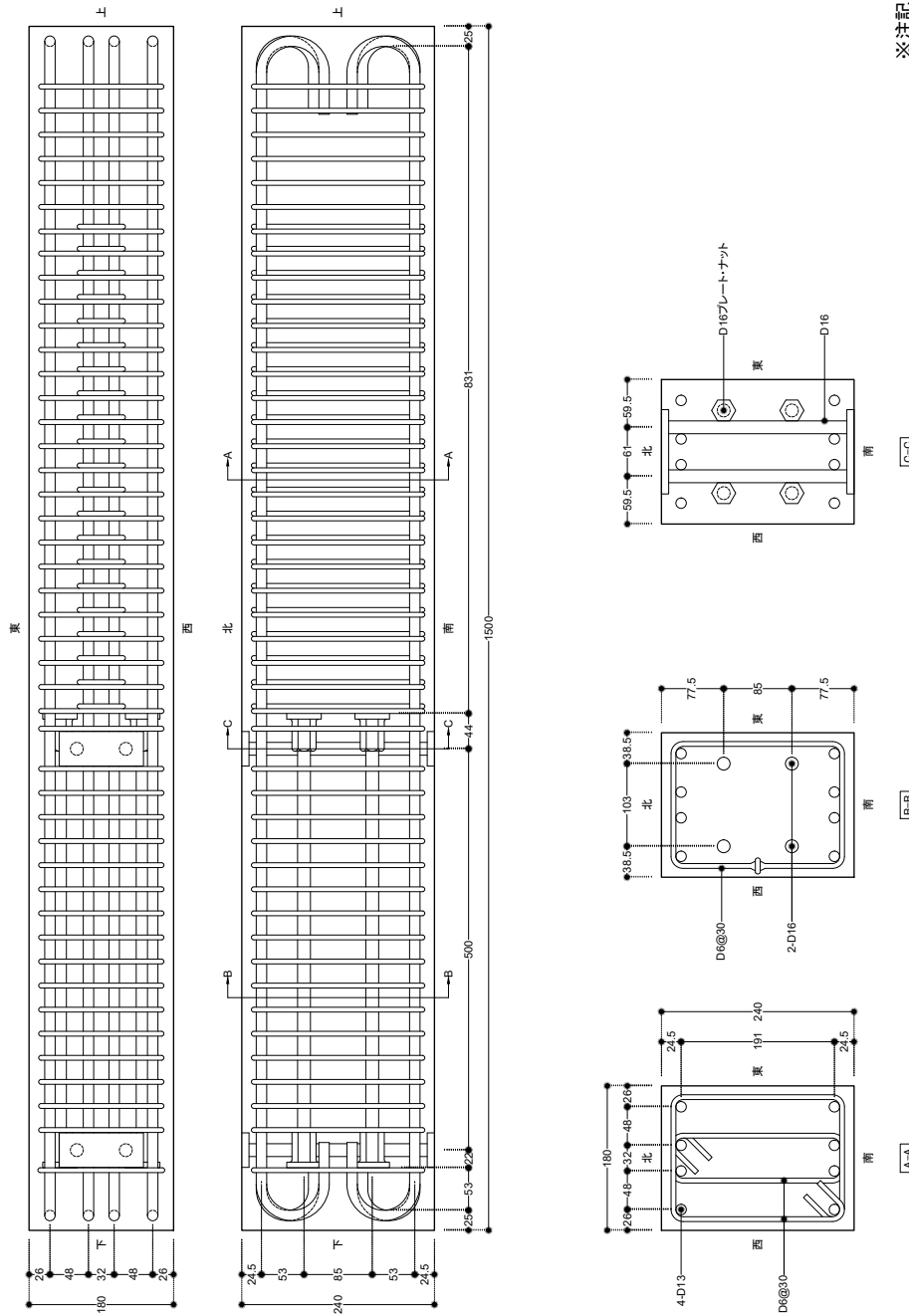
Figure A.33: SC2-101 Layout and section details
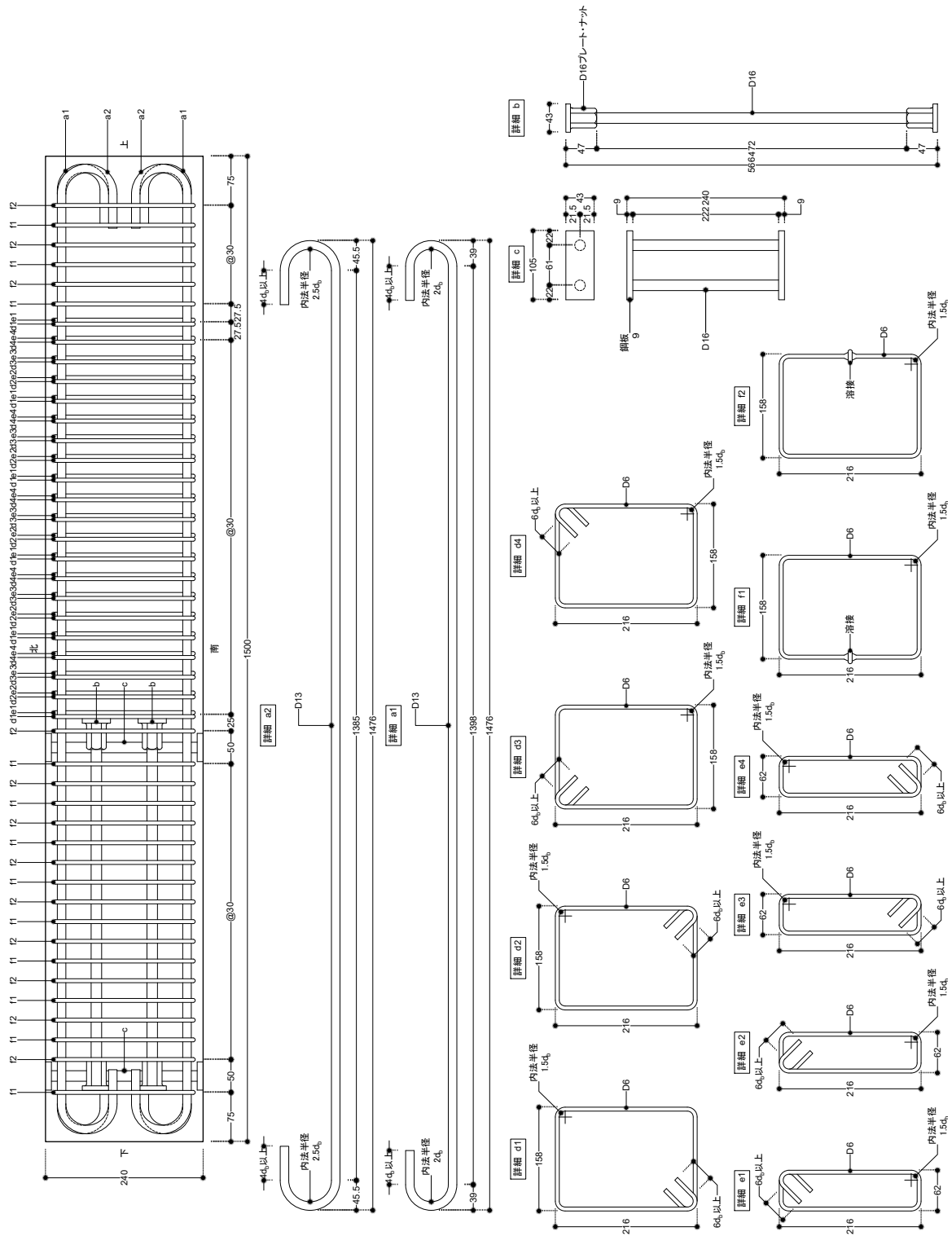
Figure A.34: SC 2-102 Reinforcement details
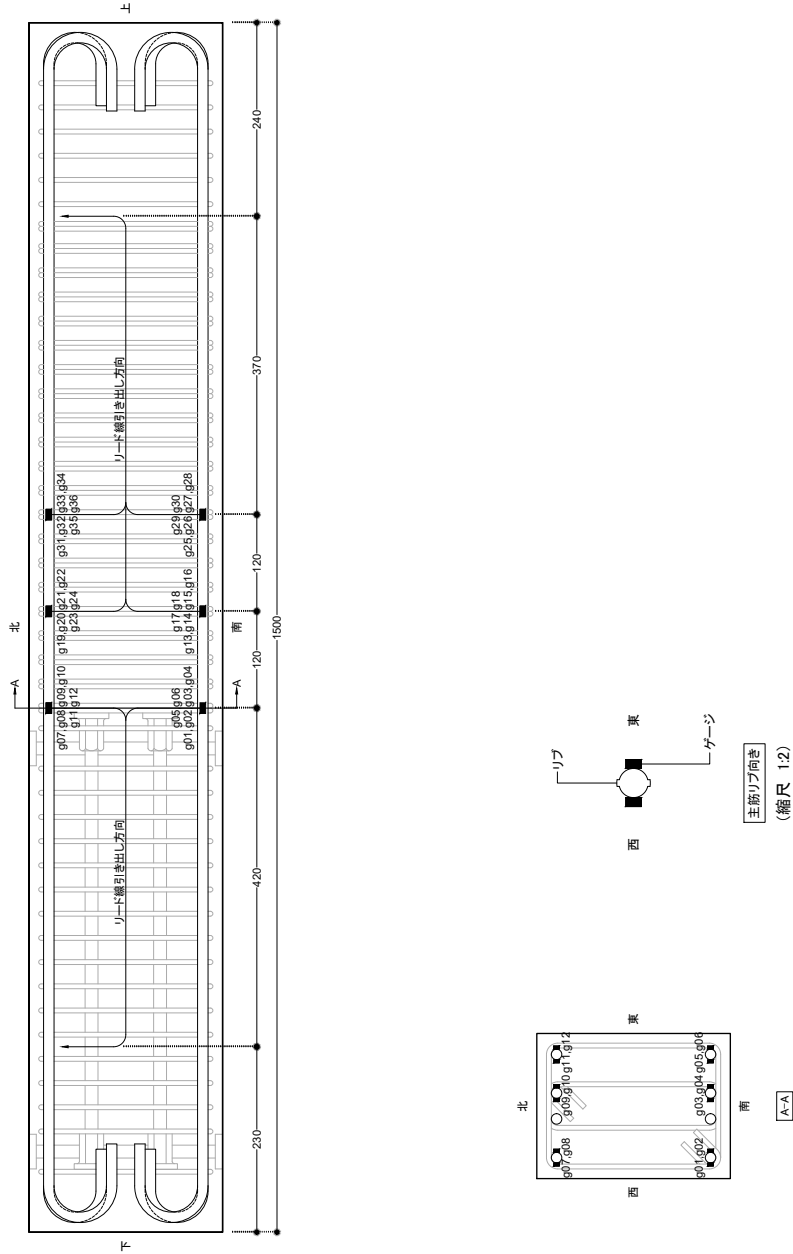
Figure A.35: SC2-103 Strain gauge arrangement
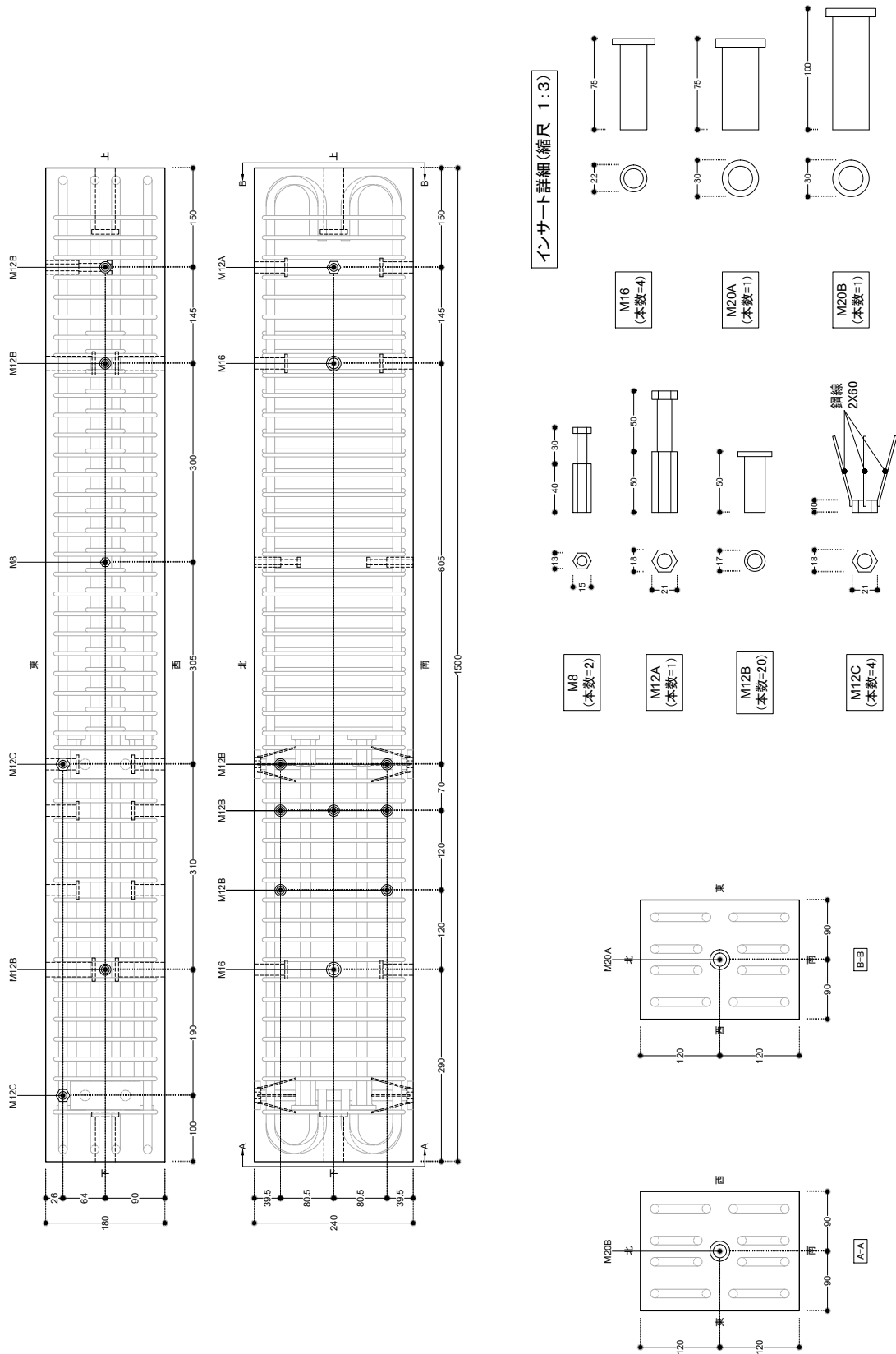
Figure A.36: SC2-104 Insert arrangement
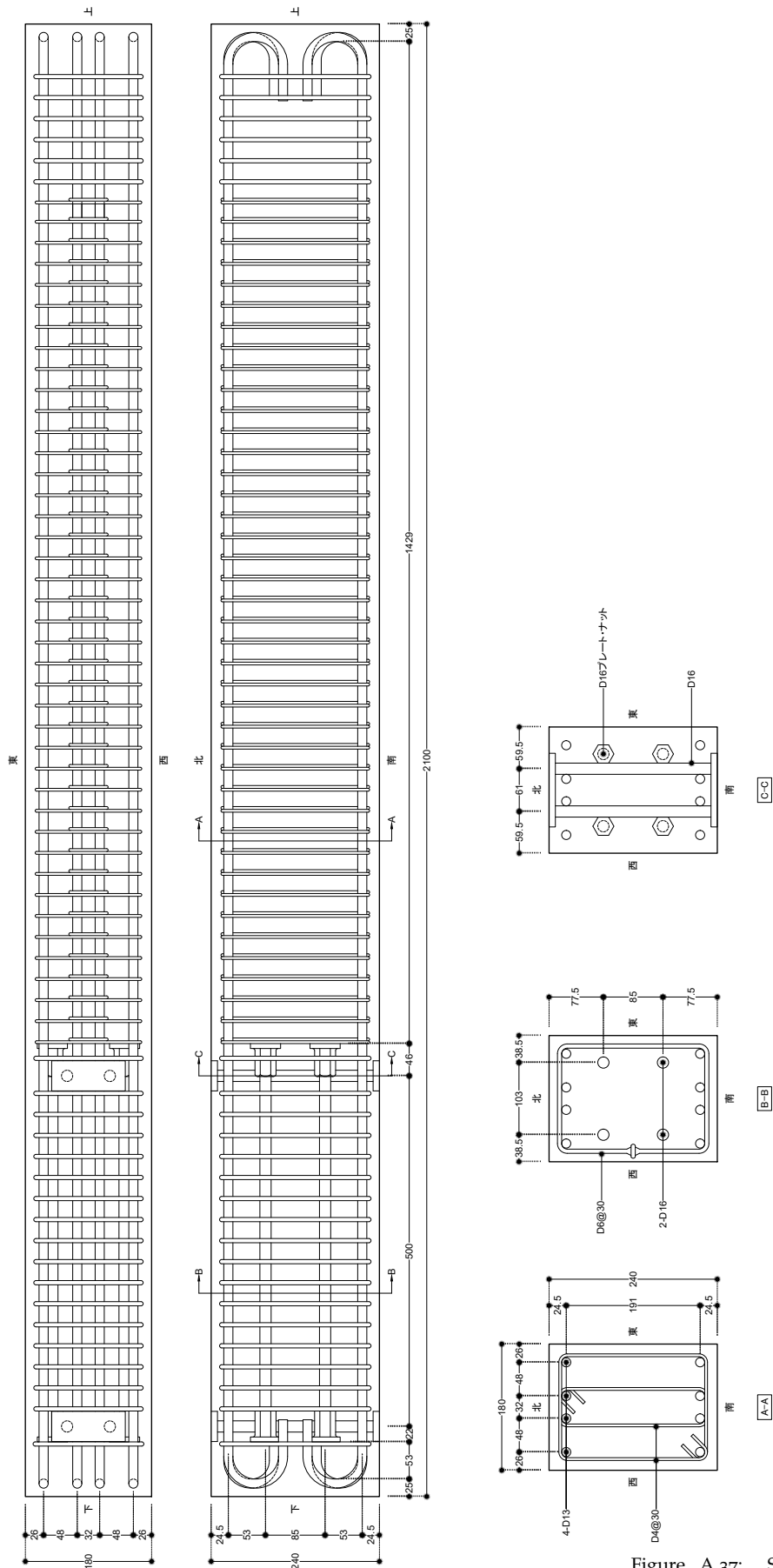
Figure A.37: SC3-101 Layout and section details
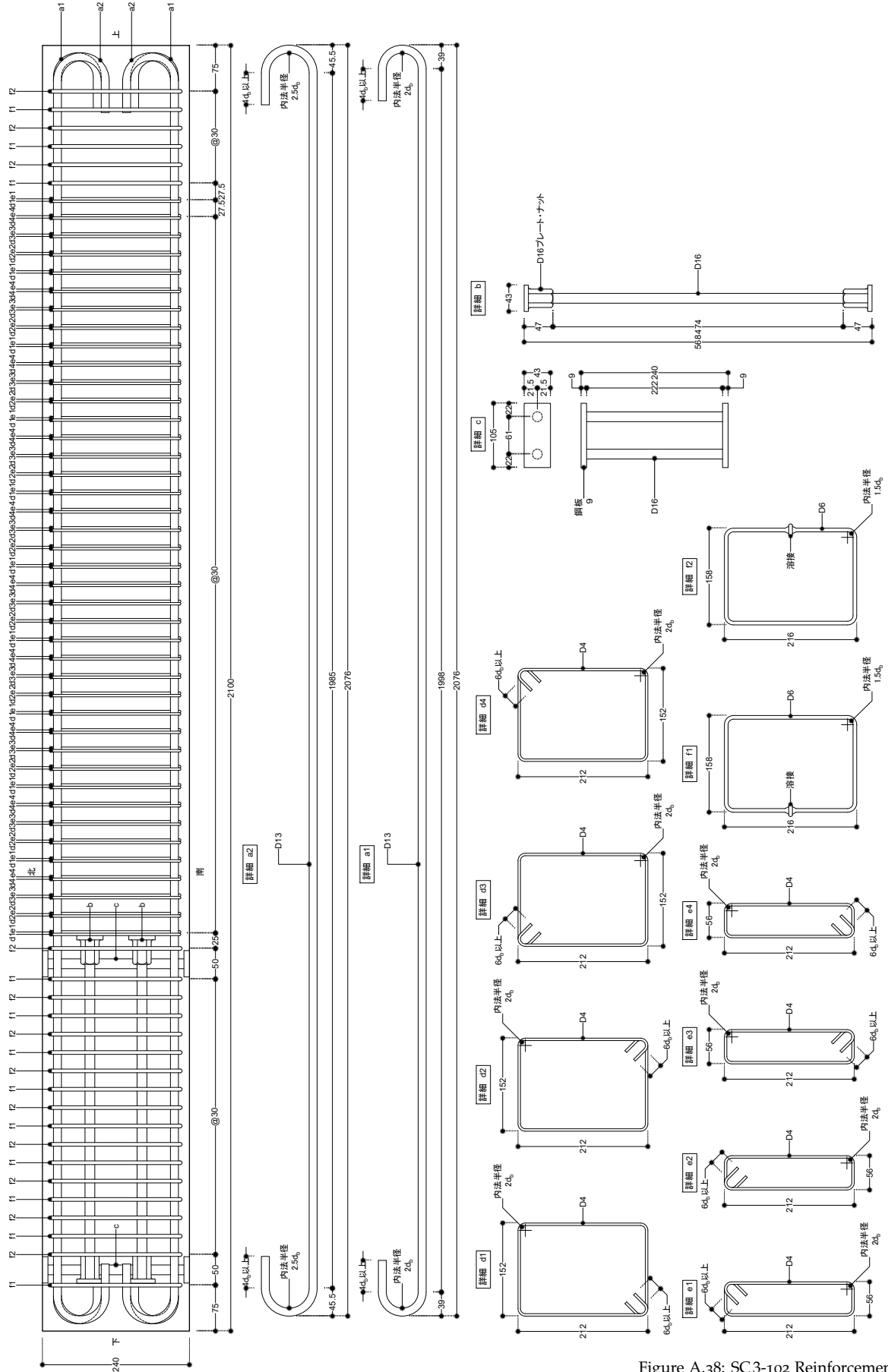
Figure A.38: SC 3-102 Reinforcement details
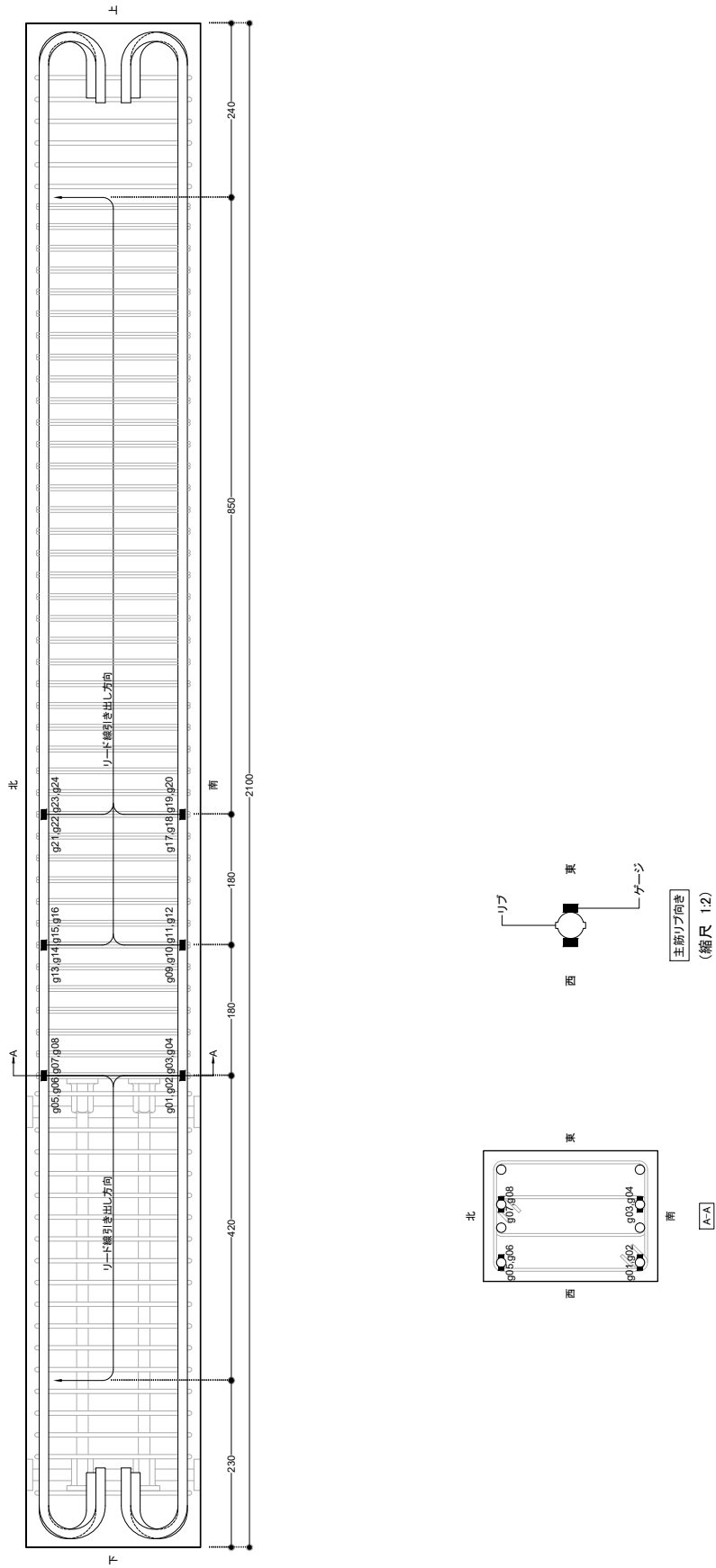
Figure A.39: SC3-103 Strain gauge arrangement
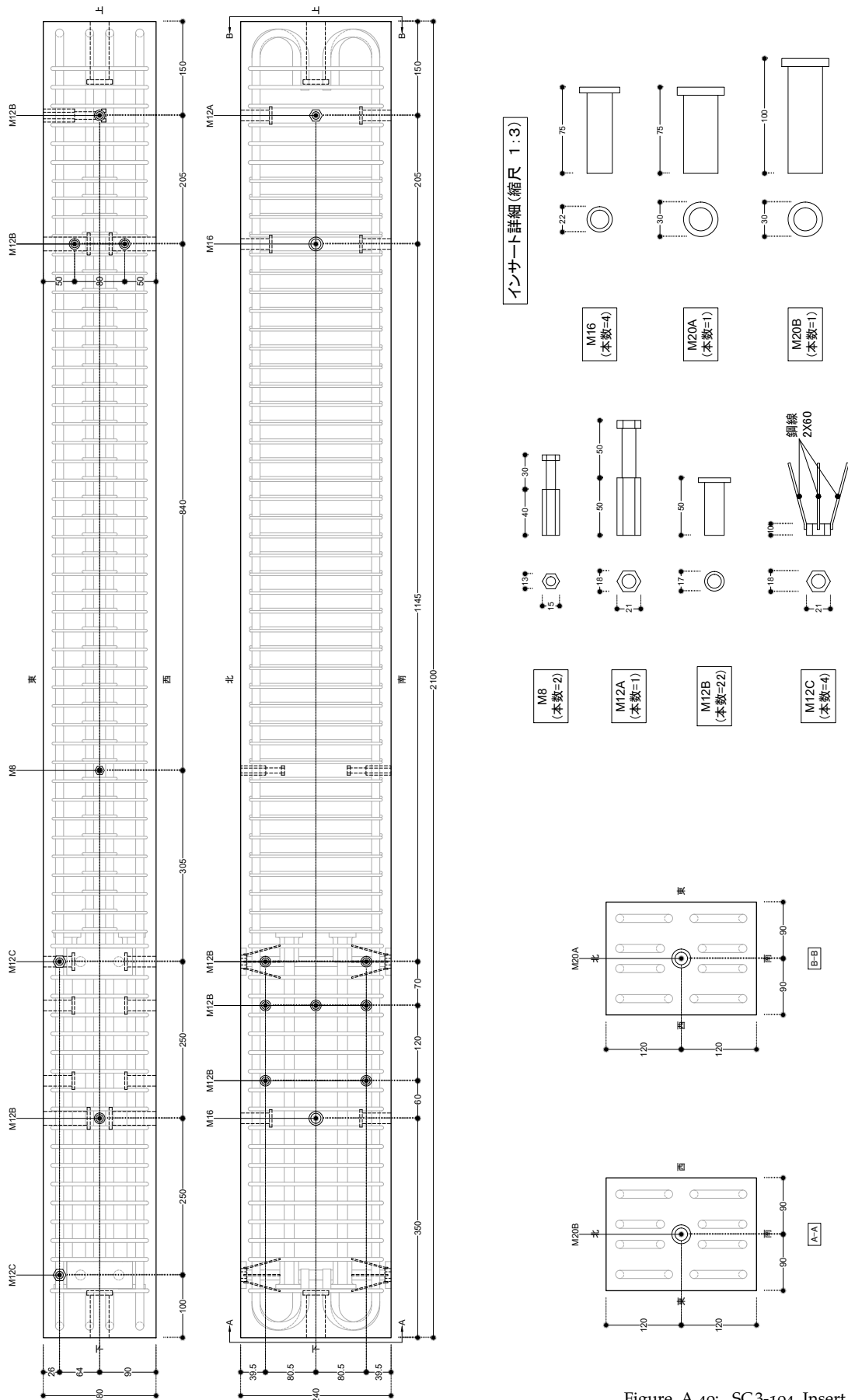
Figure A.40: SC3-104 Insert arrangement

B

Material testing

B.1 *Steel reinforcement*

STRESS-strain curves obtained from the tensile strength test of each bar are expressed in Figure B.1 along with the mean curve in bold. Yield stress and strain and other quantities determined from the same data are listed in tables B.1 to B.6 for each rebar grade.

	f_y (MPa)	ϵ_y (%)	E_s (GPa)	f_u (MPa)
Test piece #1	396.2	0.19	199.1	575.4
Test piece #2	396.8	0.25	195.6	573.5
Test piece #3	396.1	0.22	192.8	572.9
Test piece #4	398.9	0.19	211.3	576.2
Test piece #5	397.2	0.21	185.3	578.1
Average	397.1	0.21	196.8	575.2
Mean curve	396.0	0.21	197.0	578.1

Table B.1: D16 bar tensile strength test results

	f_y (MPa)	ϵ_y (%)	E_s (GPa)	f_u (MPa)
Test piece #1	373.7	0.21	187.8	540.3
Test piece #2	374.1	0.21	184.5	543.5
Test piece #3	375.1	0.20	189.1	546.0
Test piece #4	371.6	0.20	192.3	538.5
Test piece #5	372.2	0.21	184.9	539.8
Average	373.4	0.20	187.7	541.6
Mean curve	371.8	0.21	188.1	546.0

Table B.2: D13 bar tensile strength test results

B.2 *Concrete*

COMPRESSIVE-strength test results for SA, SB-M30, SB-M60, and SC concrete casting batches are expressed in figures B.2 to B.5 respectively. Stress-strain curves of the individual tests a mean curve determined by taking the mean stress over the common strain range of the individual tests are presented. Compressive strength (f_c') and elastic modulus (E_c) determined from each of these curves are listed in tables B.7 to B.29 along with the dimensions of each test cylinder ($D \times H$).
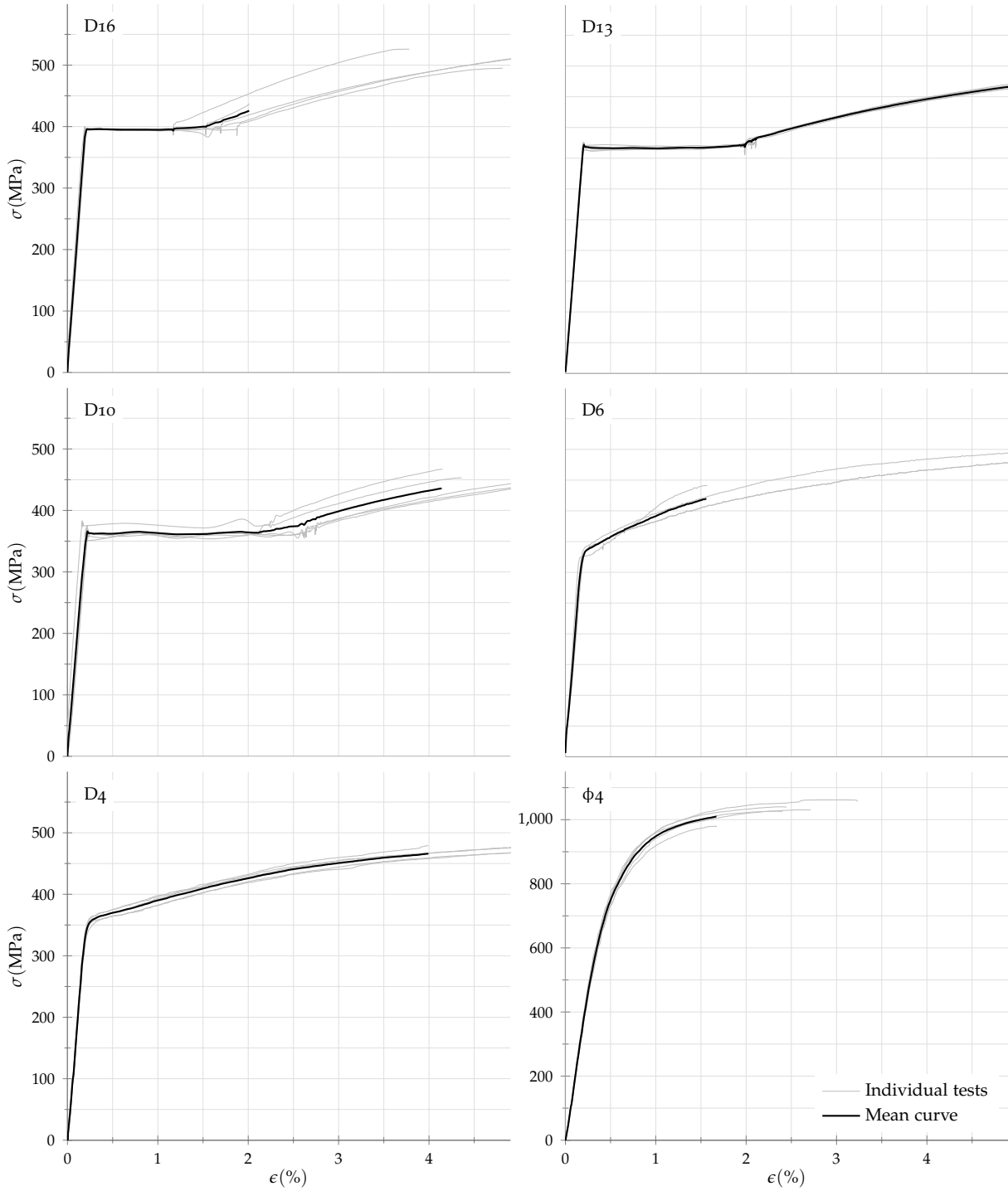
Figure B.1: Steel reinforcement bars tensile strength tests

Table B.3: D10 bar tensile strength test results

	f_y (MPa)	ϵ_y (%)	E_s (GPa)	f_u (MPa)
Test piece #1	368.4	0.23	167.9	518.5
Test piece #2	364.7	0.22	174.8	516.6
Test piece #3	373.8	0.22	186.2	517.3
Test piece #4	364.9	0.24	173.6	516.8
Test piece #5	379.8	0.17	224.3	539.6
Average	370.3	0.21	185.4	521.8
Mean curve	365.7	0.22	181.0	539.6

	f_y (MPa)	ϵ_y (%)	E_s (GPa)	f_u (MPa)
Test piece #1	356.6	0.39	187.3	520.2
Test piece #2	351.2	0.42	160.5	503.1
Test piece #3	335.5	0.36	214.8	470.6
Average	348.6	0.40	180.8	499.2
Mean curve	348.8	0.39	180.5	520.2

Table B.4: D6 bar tensile strength test results

	f_y (MPa)	ϵ_y (%)	E_s (GPa)	f_u (MPa)
Test piece #1	366.2	0.40	180.4	496.9
Test piece #2	371.3	0.41	174.6	492.9
Test piece #3	371.1	0.41	179.8	503.9
Test piece #4	360.0	0.39	194.1	486.2
Test piece #5	360.7	0.40	182.3	488.6
Average	365.9	0.40	182.2	493.7
Mean curve	365.8	0.40	182.0	503.9

Table B.5: D4 bar tensile strength test results

	f_y (MPa)	ϵ_y (%)	E_s (GPa)	f_u (MPa)
Test piece #1	805.5	0.63	189.0	1031.1
Test piece #2	851.5	0.65	188.5	1040.3
Test piece #3	832.4	0.62	196.4	1061.7
Test piece #4	793.5	0.61	191.1	979.6
Test piece #5	838.9	0.61	202.1	1026.8
Average	824.4	0.63	193.4	1027.9
Mean curve	824.0	0.63	193.3	1061.7

Table B.6: φ4 bar tensile strength test results

Results of the split-cylinder tensile strength tests are expressed in the same tables.
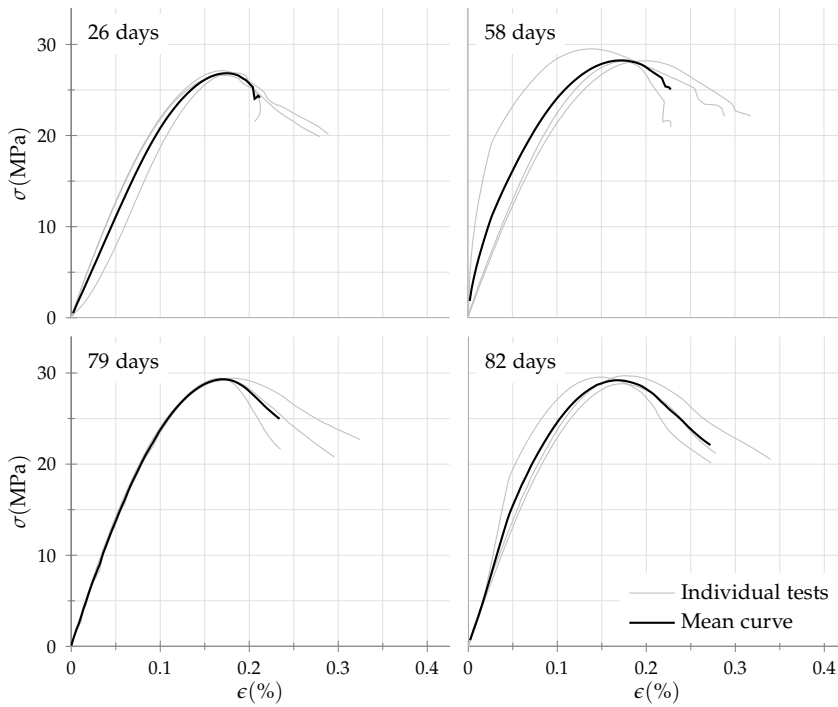
Figure B.2: Concrete material test results for SA batch

Table B.7: SA batch concrete test results at 26 days

	D_c (mm)	H_c (mm)	f'_c (MPa)	E_c (GPa)	D_t (mm)	H_t (mm)	f_t (MPa)
Test piece #1	100.16	200.07	26.9	17.4	100.11	199.94	2.2
Test piece #2	100.22	200.61	27.1	25.6	99.96	200.01	2.1
Test piece #3	99.88	200.15	26.6	25.2	100.10	198.87	2.3
Average	–	–	26.9	25.4	–	–	2.2
Mean curve	–	–	26.8	22.0	–	–	–
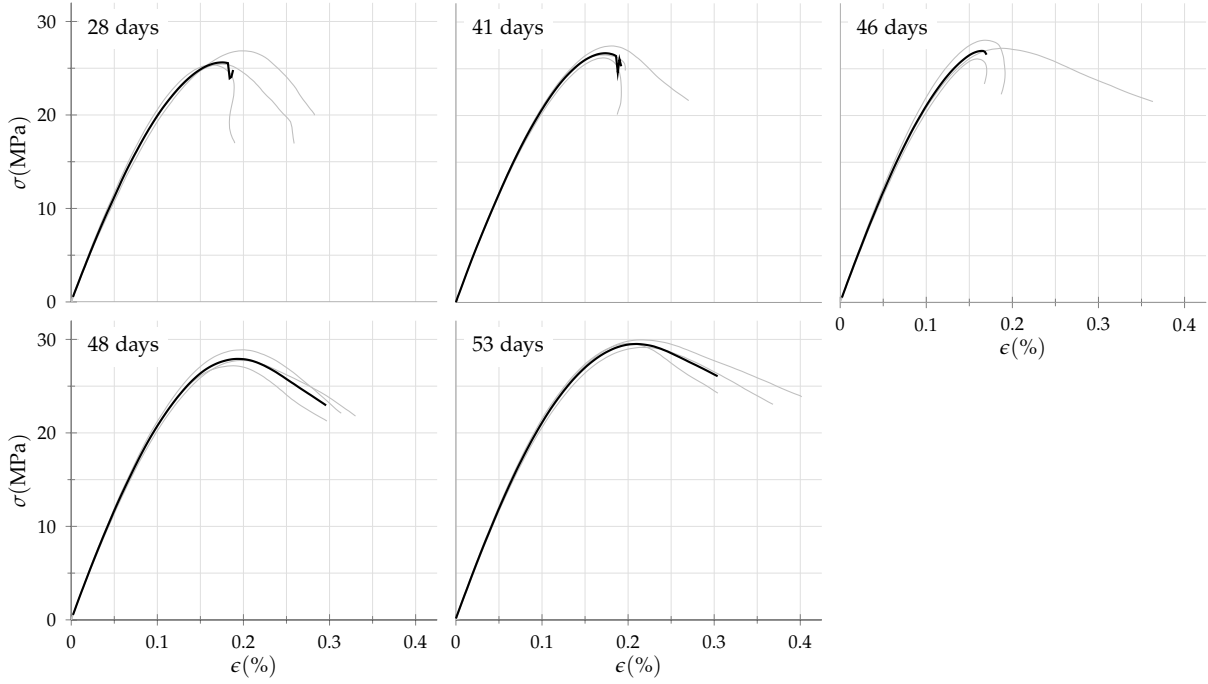
Figure B.3: Concrete material test results for SB-M30 batch
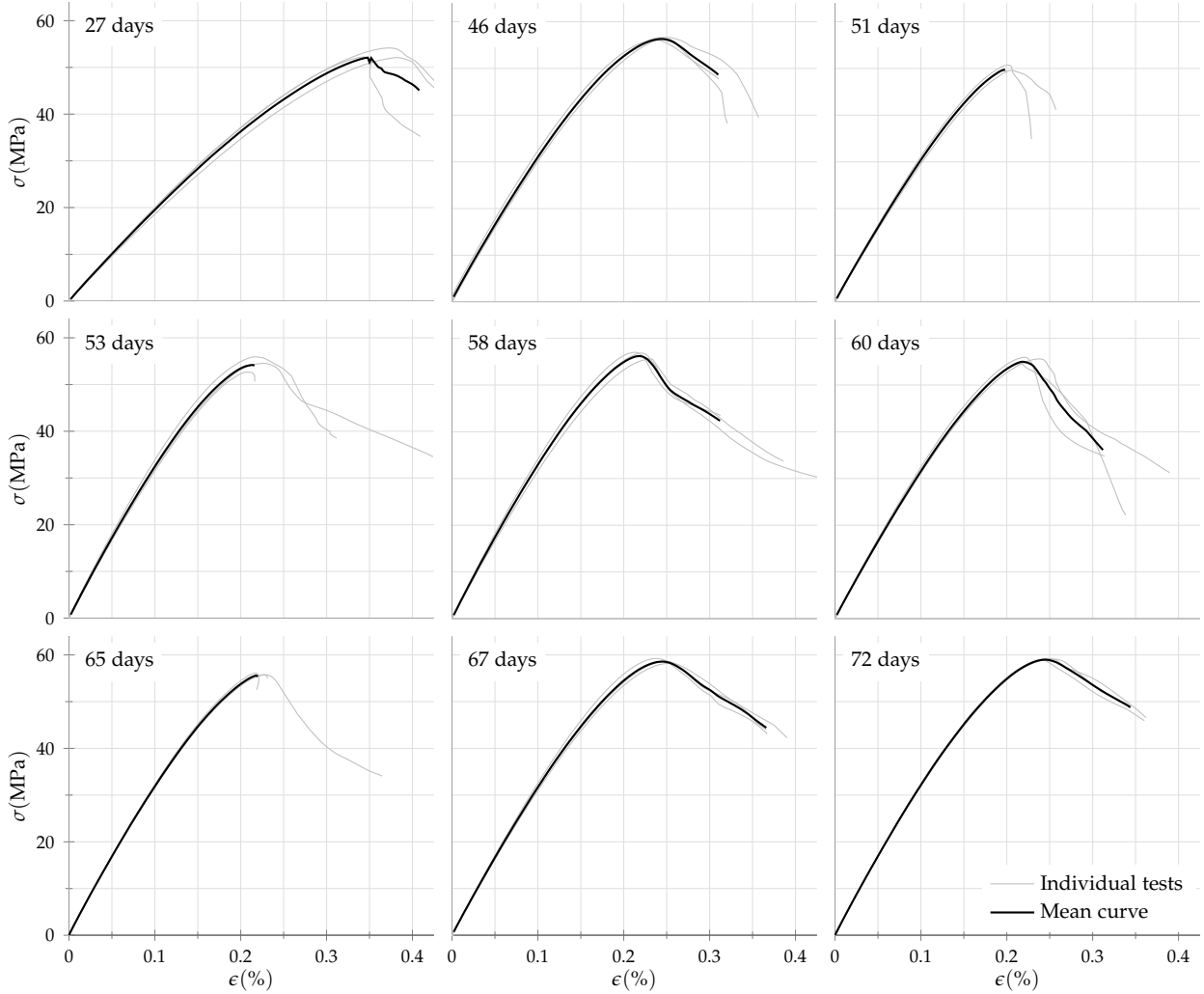
Figure B.4: Concrete material test results for SB-M60 batch
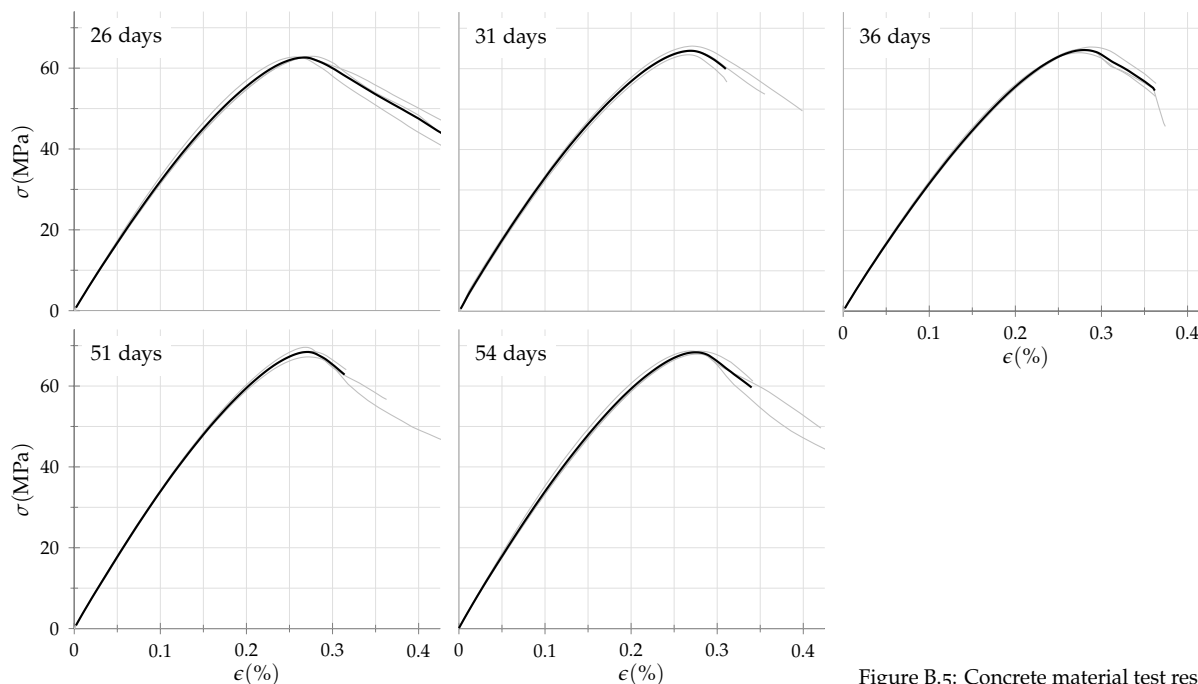
Figure B.5: Concrete material test results for SC batch

Table B.8: SA batch concrete test results at 58 days

	D_c (mm)	H_c (mm)	f'_c (MPa)	E_c (GPa)	D_t (mm)	H_t (mm)	f_t (MPa)
Test piece #1	100.08	201.17	28.2	24.4	99.50	200.94	2.3
Test piece #2	100.01	199.73	28.1	25.5	100.00	199.68	2.4
Test piece #3	99.57	199.69	29.5	72.5	99.84	200.42	2.1
Average	–	–	28.6	25.0	–	–	2.3
Mean curve	–	–	28.2	34.7	–	–	–

Table B.9: SA batch concrete test results at 79 days

	D_c (mm)	H_c (mm)	f'_c (MPa)	E_c (GPa)	D_t (mm)	H_t (mm)	f_t (MPa)
Test piece #1	100.06	201.72	29.4	27.4	100.18	199.87	2.4
Test piece #2	100.01	199.24	29.4	28.6	100.33	199.70	2.6
Test piece #3	100.09	200.80	29.2	26.8	99.84	200.80	2.0
Average	–	–	29.4	27.6	–	–	2.3
Mean curve	–	–	29.3	27.6	–	–	–

Table B.10: SA batch concrete test results at 79 days

	D_c (mm)	H_c (mm)	f'_c (MPa)	E_c (GPa)	D_t (mm)	H_t (mm)	f_t (MPa)
Test piece #1	99.72	199.92	29.5	39.1	99.56	200.62	2.2
Test piece #2	100.16	199.95	29.7	27.3	100.21	200.78	2.1
Test piece #3	100.10	199.78	28.8	26.3	99.97	200.16	2.4
Average	–	–	29.4	26.8	–	–	2.2
Mean curve	–	–	29.2	31.6	–	–	–

	D_c (mm)	H_c (mm)	f'_c (MPa)	E_c (GPa)	D_t (mm)	H_t (mm)	f_t (MPa)
Test piece #1	100.13	201.04	26.9	21.1	100.09	200.22	2.4
Test piece #2	100.15	201.44	25.4	22.8	100.21	199.81	2.4
Test piece #3	100.09	200.66	25.4	23.2	100.07	200.11	2.5
Average	–	–	25.9	22.4	–	–	2.4
Mean curve	–	–	25.6	22.4	–	–	–

Table B.12: SB-M30 batch concrete test results at 41 days

	D_c (mm)	H_c (mm)	f'_c (MPa)	E_c (GPa)	D_t (mm)	H_t (mm)	f_t (MPa)
Test piece #1	100.10	199.92	26.5	23.3	100.11	199.69	2.2
Test piece #2	100.15	199.75	26.2	22.8	100.07	200.72	2.4
Test piece #3	100.31	198.06	27.4	23.4	100.35	198.60	2.2
Average	–	–	26.7	23.2	–	–	2.2
Mean curve	–	–	26.7	23.2	–	–	–

Table B.13: SB-M30 batch concrete test results at 46 days

	D_c (mm)	H_c (mm)	f'_c (MPa)	E_c (GPa)	D_t (mm)	H_t (mm)	f_t (MPa)
Test piece #1	100.18	202.41	27.2	23.4	100.04	201.69	2.3
Test piece #2	99.97	201.64	26.1	22.9	100.09	202.58	2.3
Test piece #3	99.96	200.68	28.1	24.6	100.13	200.53	2.1
Average	–	–	27.1	23.6	–	–	2.2
Mean curve	–	–	26.9	23.6	–	–	–

Table B.14: SB-M30 batch concrete test results at 48 days

	D_c (mm)	H_c (mm)	f'_c (MPa)	E_c (GPa)	D_t (mm)	H_t (mm)	f_t (MPa)
Test piece #1	99.98	200.47	28.9	23.6	100.19	202.17	2.3
Test piece #2	100.16	201.64	27.7	22.5	99.98	202.04	2.3
Test piece #3	100.16	201.62	27.2	23.5	100.05	201.35	2.1
Average	–	–	27.9	23.2	–	–	2.2
Mean curve	–	–	27.9	23.2	–	–	–

Table B.15: SB-M30 batch concrete test results at 53 days

	D_c (mm)	H_c (mm)	f'_c (MPa)	E_c (GPa)	D_t (mm)	H_t (mm)	f_t (MPa)
Test piece #1	100.02	198.77	29.6	23.8	100.00	200.00	2.4
Test piece #2	100.05	198.38	30.0	23.3	100.00	200.00	2.4
Test piece #3	100.11	201.77	29.1	23.0	100.00	200.00	2.4
Average	–	–	29.6	23.4	–	–	2.4
Mean curve	–	–	29.5	23.4	–	–	–

Table B.16: SB-M60 batch concrete test results at 27 days

	D_c (mm)	H_c (mm)	f'_c (MPa)	E_c (GPa)	D_t (mm)	H_t (mm)	f_t (MPa)
Test piece #1	100.09	201.99	52.2	19.8	100.16	202.32	4.3
Test piece #2	100.00	202.36	52.1	18.4	99.97	201.75	4.8
Test piece #3	99.95	201.38	54.2	19.7	100.18	202.00	3.8
Average	–	–	52.8	19.3	–	–	4.3
Mean curve	–	–	52.1	19.3	–	–	–

Table B.17: SB-M60 batch concrete test results at 46 days

	D_c (mm)	H_c (mm)	f'_c (MPa)	E_c (GPa)	D_t (mm)	H_t (mm)	f_t (MPa)
Test piece #1	100.11	200.55	56.0	32.1	100.13	199.99	3.5
Test piece #2	100.06	202.00	56.6	31.2	100.22	200.85	3.3
Test piece #3	100.32	200.49	56.6	30.7	100.17	200.95	3.0
Average	–	–	56.4	31.3	–	–	3.3
Mean curve	–	–	56.3	31.4	–	–	–

Table B.18: SB-M60 batch concrete test results at 51 days

	D_c (mm)	H_c (mm)	f'_c (MPa)	E_c (GPa)	D_t (mm)	H_t (mm)	f_t (MPa)
Test piece #1	100.03	199.94	50.7	32.2	99.94	200.04	4.2
Test piece #2	100.08	201.34	49.6	31.0	100.06	201.28	4.3
Test piece #3	99.90	199.89	49.6	30.4	100.07	201.05	3.8
Average	–	–	50.0	31.2	–	–	4.1
Mean curve	–	–	49.8	31.3	–	–	–

Table B.19: SB-M60 batch concrete test results at 53 days

	D_c (mm)	H_c (mm)	f'_c (MPa)	E_c (GPa)	D_t (mm)	H_t (mm)	f_t (MPa)
Test piece #1	100.07	199.30	54.5	33.0	100.02	201.68	2.8
Test piece #2	99.92	198.57	52.7	32.7	100.10	201.39	4.2
Test piece #3	100.08	198.99	55.9	35.0	100.06	201.43	4.6
Average	–	–	54.4	33.6	–	–	3.8
Mean curve	–	–	54.2	33.7	–	–	–

Table B.20: SB-M60 batch concrete test results at 58 days

	D_c (mm)	H_c (mm)	f'_c (MPa)	E_c (GPa)	D_t (mm)	H_t (mm)	f_t (MPa)
Test piece #1	100.09	198.66	56.8	34.1	100.10	198.27	3.3
Test piece #2	100.09	200.67	57.0	35.5	99.91	198.56	3.3
Test piece #3	99.94	200.38	55.6	32.6	100.18	201.54	3.5
Average	–	–	56.5	34.0	–	–	3.4
Mean curve	–	–	56.2	34.0	–	–	–

Table B.21: SB-M60 batch concrete test results at 60 days

	D_c (mm)	H_c (mm)	f'_c (MPa)	E_c (GPa)	D_t (mm)	H_t (mm)	f_t (MPa)
Test piece #1	99.64	200.67	55.6	31.8	100.15	199.11	2.9
Test piece #2	100.12	200.25	54.6	31.7	100.12	201.05	2.9
Test piece #3	100.08	200.72	55.9	33.2	100.12	199.18	2.9
Average	–	–	55.4	32.3	–	–	2.9
Mean curve	–	–	55.0	32.3	–	–	–

Table B.22: SB-M60 batch concrete test results at 65 days

	D_c (mm)	H_c (mm)	f'_c (MPa)	E_c (GPa)	D_t (mm)	H_t (mm)	f_t (MPa)
Test piece #1	100.06	199.30	56.1	33.1	100.16	198.66	4.6
Test piece #2	100.06	199.44	55.8	32.6	100.14	199.32	4.7
Test piece #3	100.05	200.45	55.7	32.5	100.23	198.95	4.2
Average	–	–	55.9	32.7	–	–	4.5
Mean curve	–	–	55.6	32.8	–	–	–

Table B.23: SB-M60 batch concrete test results at 67 days

	D_c (mm)	H_c (mm)	f'_c (MPa)	E_c (GPa)	D_t (mm)	H_t (mm)	f_t (MPa)
Test piece #1	99.95	199.61	58.7	32.3	100.08	200.87	3.1
Test piece #2	100.06	200.89	59.2	33.1	100.13	198.64	3.0
Test piece #3	100.06	201.14	58.2	31.6	100.08	199.85	3.6
Average	–	–	58.7	32.4	–	–	3.2
Mean curve	–	–	58.6	32.4	–	–	–

Table B.24: SB-M60 batch concrete test results at 72 days

	D_c (mm)	H_c (mm)	f'_c (MPa)	E_c (GPa)	D_t (mm)	H_t (mm)	f_t (MPa)
Test piece #1	100.07	199.35	59.3	32.6	100.07	200.44	3.2
Test piece #2	100.04	199.09	59.1	33.1	100.06	199.63	3.1
Test piece #3	100.12	199.67	58.9	33.0	100.13	201.08	3.5
Average	–	–	59.1	32.9	–	–	3.3
Mean curve	–	–	59.0	32.9	–	–	–

Table B.25: SC batch concrete test results at 26 days

	D_c (mm)	H_c (mm)	f'_c (MPa)	E_c (GPa)	D_t (mm)	H_t (mm)	f_t (MPa)
Test piece #1	99.91	200.55	62.9	31.7	100.22	198.63	3.4
Test piece #2	100.09	198.14	62.8	33.9	100.19	197.52	3.5
Test piece #3	100.05	198.50	62.7	31.9	100.09	198.11	2.9
Average	–	–	62.8	32.5	–	–	3.3
Mean curve	–	–	62.6	32.6	–	–	–

Table B.26: SC batch concrete test results at 31 days

	D_c (mm)	H_c (mm)	f'_c (MPa)	E_c (GPa)	D_t (mm)	H_t (mm)	f_t (MPa)
Test piece #1	100.19	201.09	64.3	34.3	100.10	197.26	3.8
Test piece #2	100.10	200.56	63.4	33.1	100.21	199.45	4.1
Test piece #3	100.12	200.92	65.6	34.3	100.13	199.92	4.2
Average	–	–	64.4	33.9	–	–	4.0
Mean curve	–	–	64.4	34.0	–	–	–

Table B.27: SC batch concrete test results at 36 days

	D_c (mm)	H_c (mm)	f'_c (MPa)	E_c (GPa)	D_t (mm)	H_t (mm)	f_t (MPa)
Test piece #1	100.07	200.89	64.8	31.8	100.05	201.29	3.5
Test piece #2	100.16	199.93	65.4	31.6	100.10	201.25	3.3
Test piece #3	100.16	198.92	63.9	32.7	100.13	199.88	3.2
Average	–	–	64.7	32.0	–	–	3.3
Mean curve	–	–	64.6	32.1	–	–	–

Table B.28: SC batch concrete test results at 51 days

	D_c (mm)	H_c (mm)	f'_c (MPa)	E_c (GPa)	D_t (mm)	H_t (mm)	f_t (MPa)
Test piece #1	100.08	200.32	68.6	34.3	100.12	200.22	4.2
Test piece #2	100.06	200.26	67.2	34.0	100.10	200.34	4.4
Test piece #3	100.07	198.66	69.6	34.7	100.17	199.47	4.5
Average	–	–	68.5	34.3	–	–	4.4
Mean curve	–	–	68.4	34.4	–	–	–

Table B.29: SC batch concrete test results at 54 days

	D_c (mm)	H_c (mm)	f'_c (MPa)	E_c (GPa)	D_t (mm)	H_t (mm)	f_t (MPa)
Test piece #1	100.06	200.59	67.9	33.5	100.06	200.53	3.4
Test piece #2	100.12	199.44	68.6	33.6	100.18	200.54	3.2
Test piece #3	100.24	198.79	68.7	35.8	100.03	199.64	3.2
Average	–	–	68.4	34.3	–	–	3.3
Mean curve	–	–	68.3	34.4	–	–	–

C
Data processing

EXPERIMENT data was first processed to deduce peak locations of
force and drifts over load and deformation controlled ranges respecti-
vely. Loading cycles were then defined as data between the ranges of
identified cycle peaks. Zero force and zero drift locations were then
deduced over each half cycle. This completed the initial processing of
data. Extracted data was then used for evaluating various response
quantities as discussed in Chapter 4.

In addition to the raw sensor data, photographic data also needed
to be appropriately processed to enable photogrammetric analysis
and other uses. Time stamp of associated with each photograph was
used to identify the location of image in the sensor data stream. Time
stamp of each image was compared with time stamp of each data
point on the sensor data stream and image location in data stream
which sandwiched the image data stamp. For all further references,
the sensor data identified with an image was the most recent data
point occurring before the image point in the data stream.

D
Response states

RESPONSE states of the specimen at various loading states are expressed in the form of photos captured using the digital camera. Progression of damage is illustrated through response states at peak and end of cycle images as expressed in figures D.1 to D.19.

Residual damage states are illustrated through specimen images recording the zero condition when returning from both positive and negative cycles. All specimen images are expressed in figures D.20 to D.26.
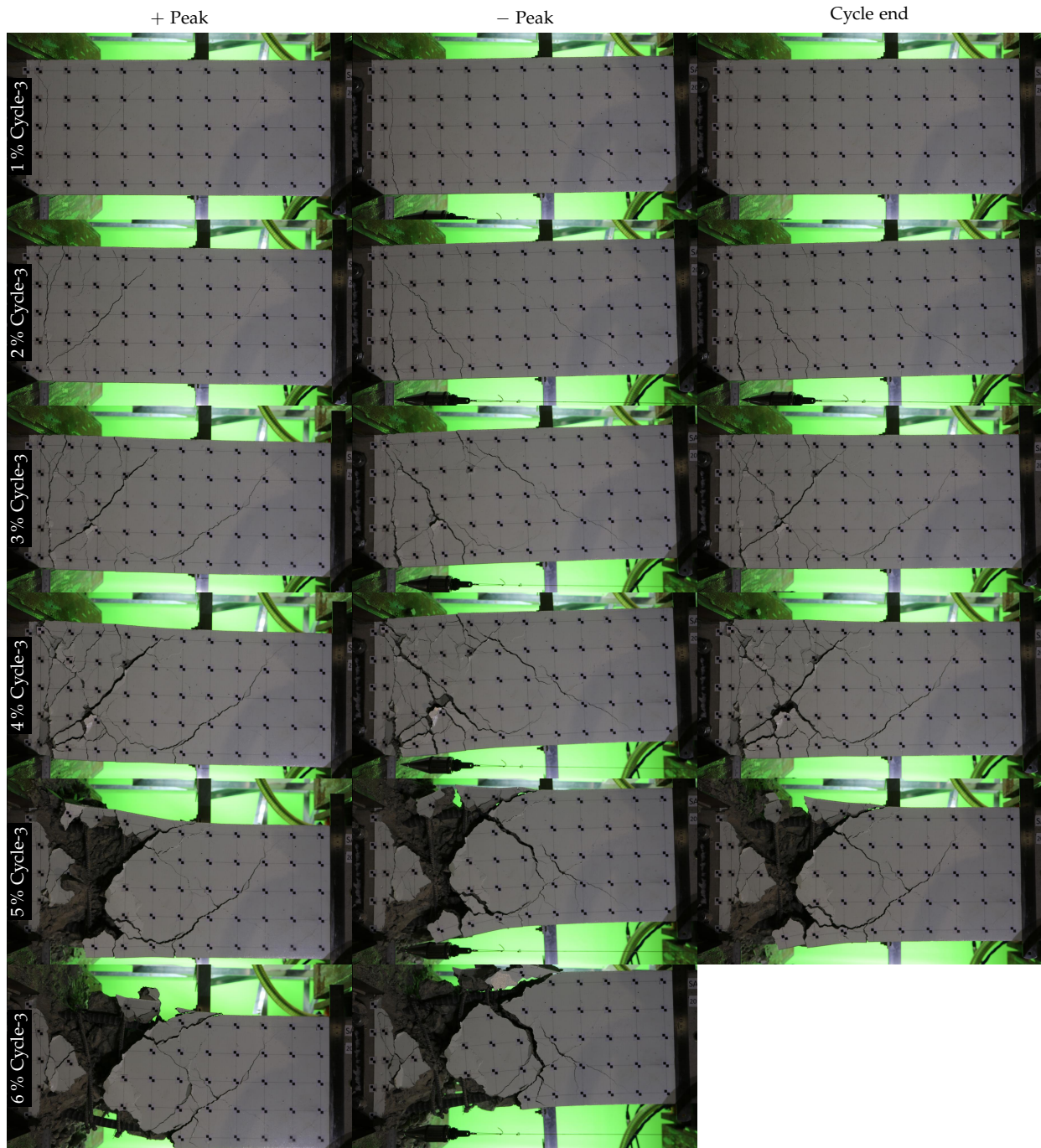
Figure D.1: Damage states at peak and cycle completion loading states (SA1)
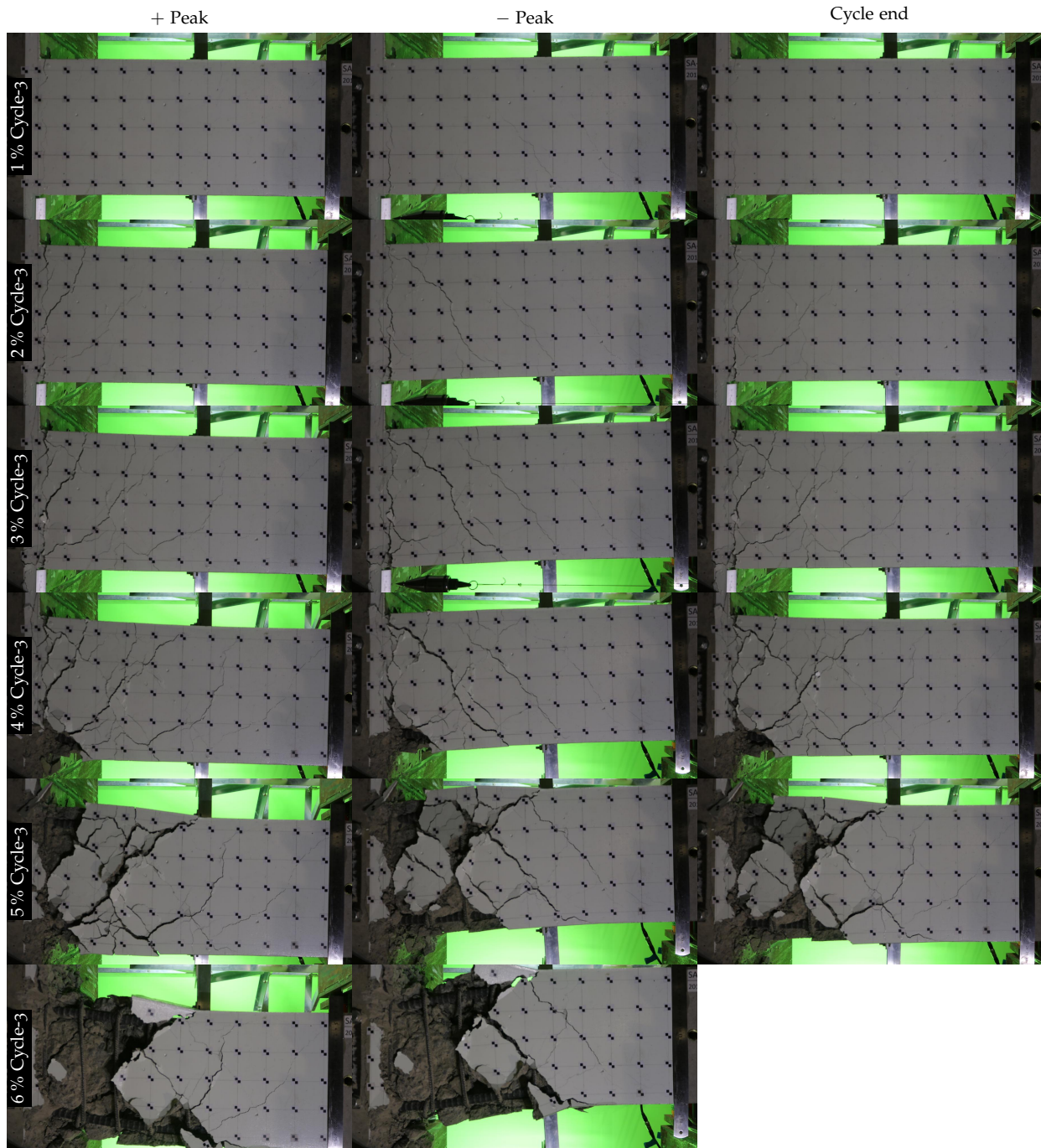
Figure D.2: Damage states at peak and cycle completion loading states (SA 2)
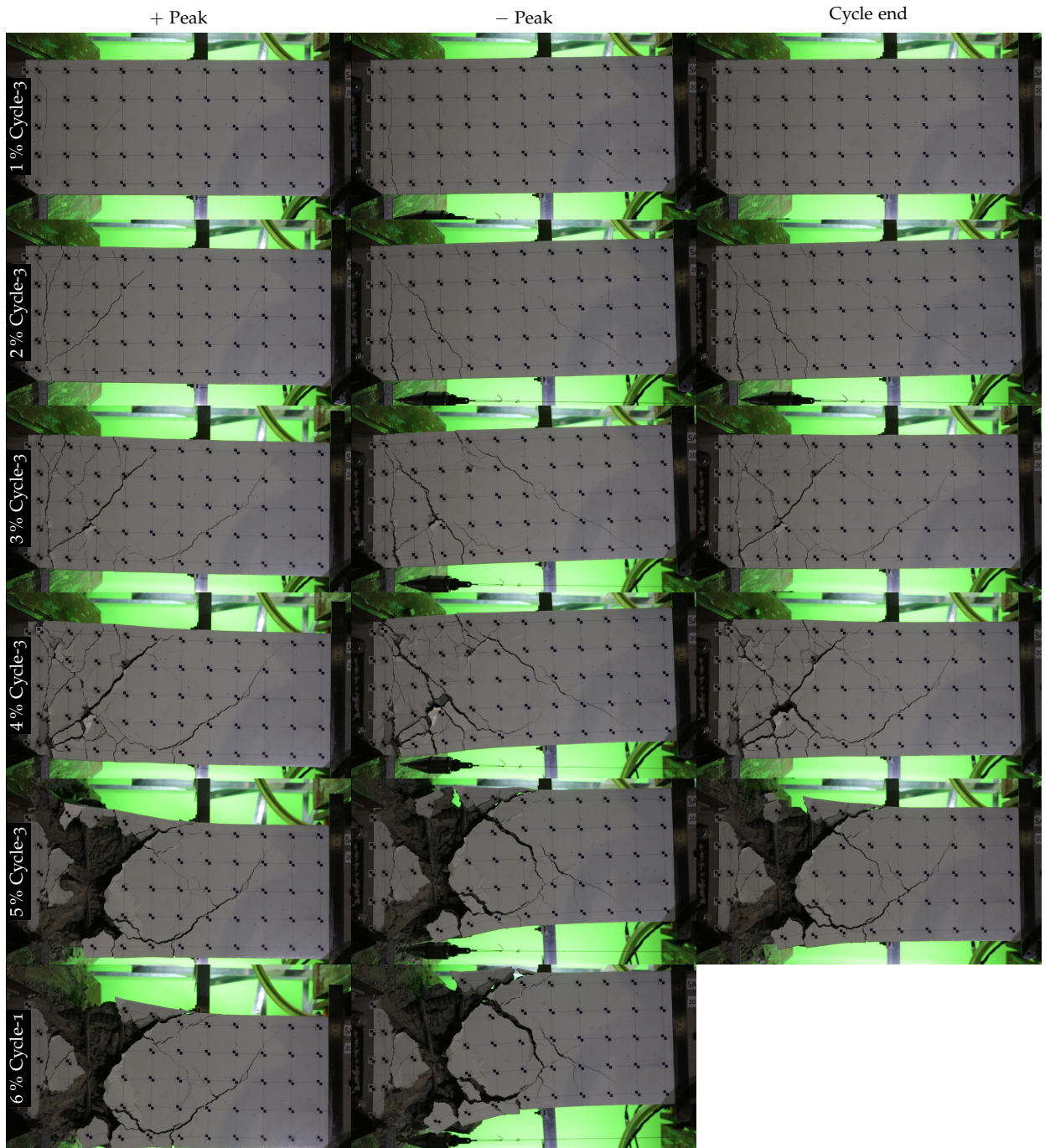
Figure D.3: Damage states at peak and cycle completion loading states (SA 3)

Figure D.4: Damage states at peak and cycle completion loading states (SB01)
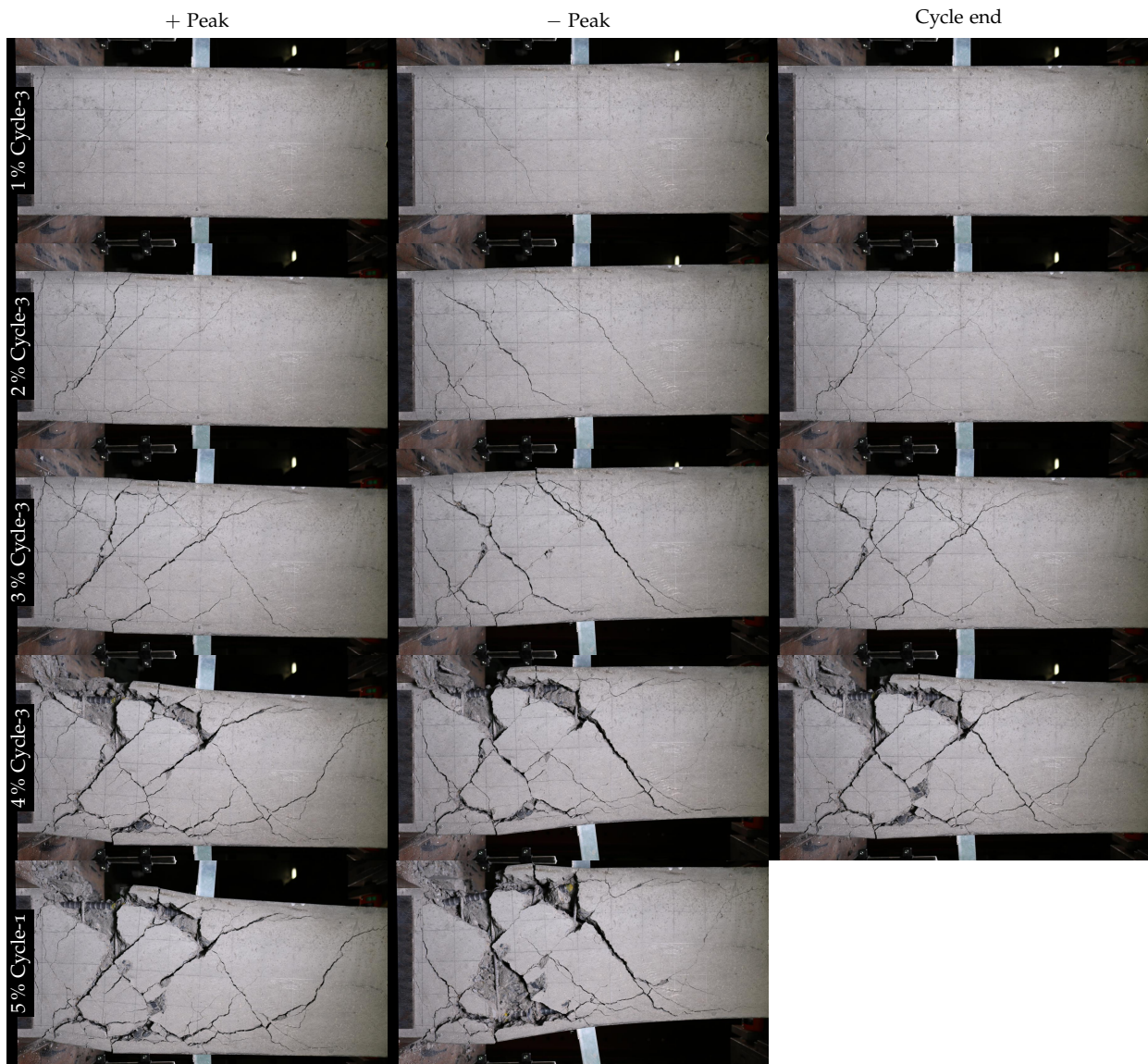
Figure D.5: Damage states at peak and cycle completion loading states (SB 02)
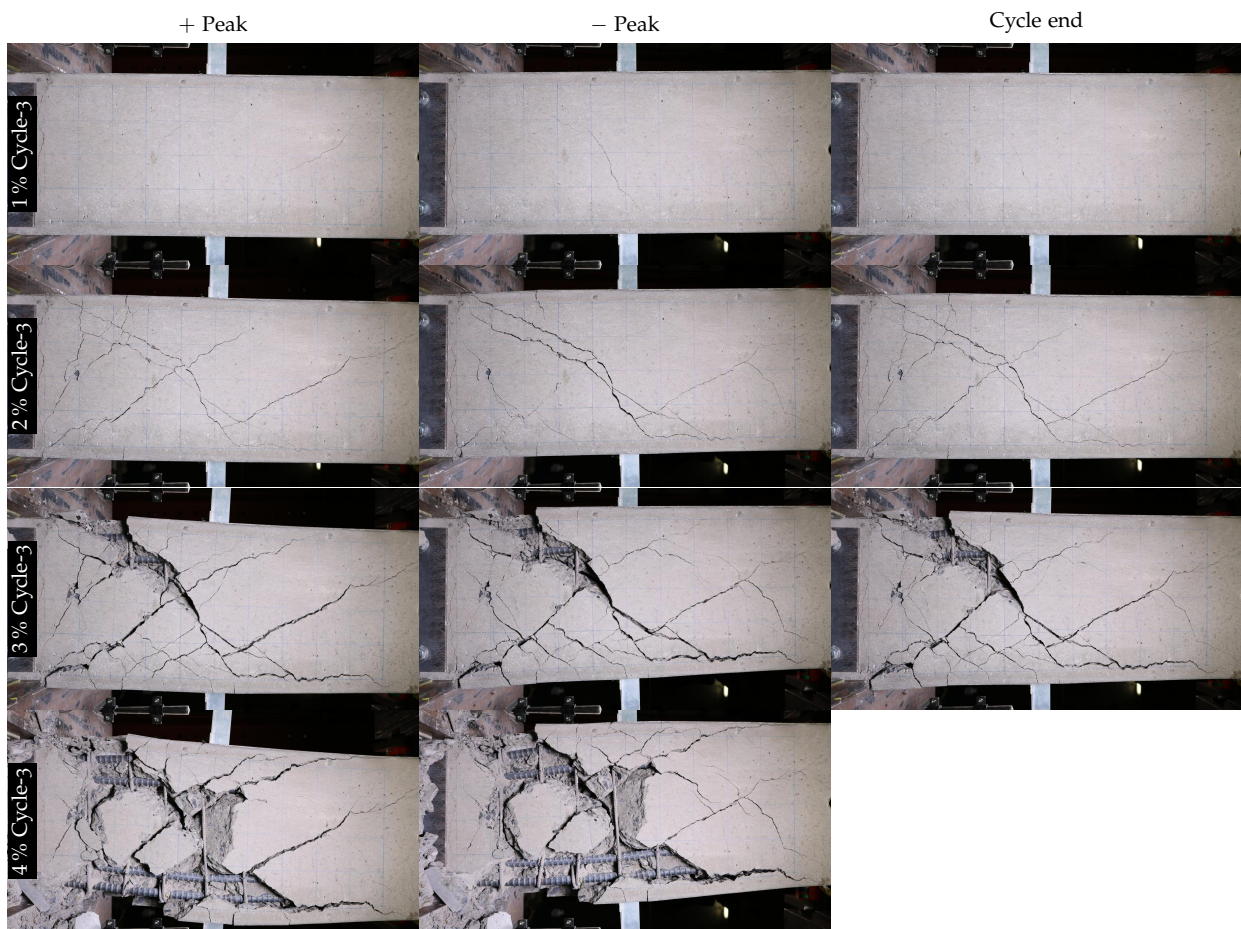
Figure D.6: Damage states at peak and cycle completion loading states (SB 03)
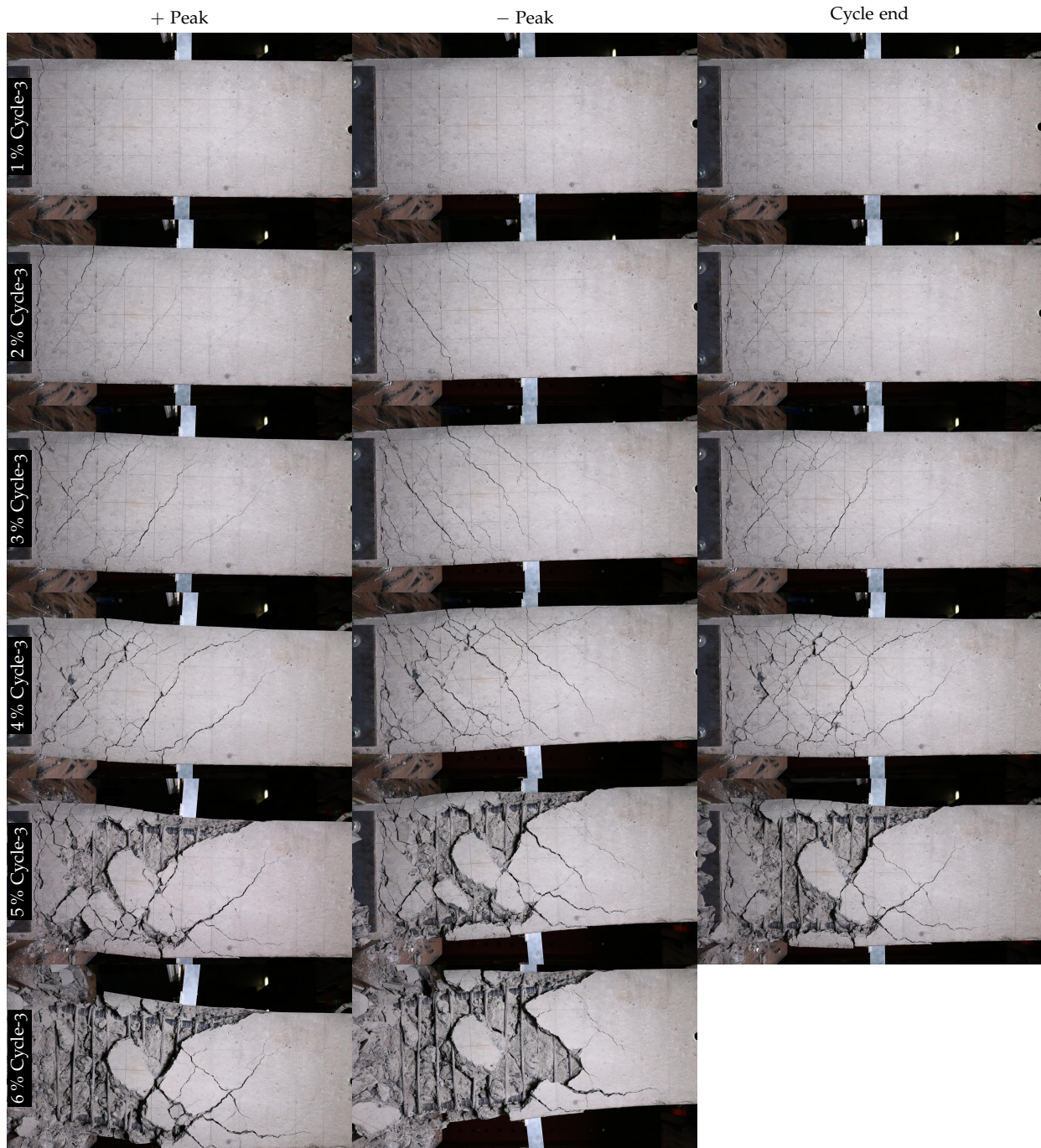
Figure D.7: Damage states at peak and cycle completion loading states (SB 04)

+ Peak

− Peak

Cycle end

1 % Cycle-3

2 % Cycle-3

3 % Cycle-3

4 % Cycle-3

5 % Cycle-3

6 % Cycle-3
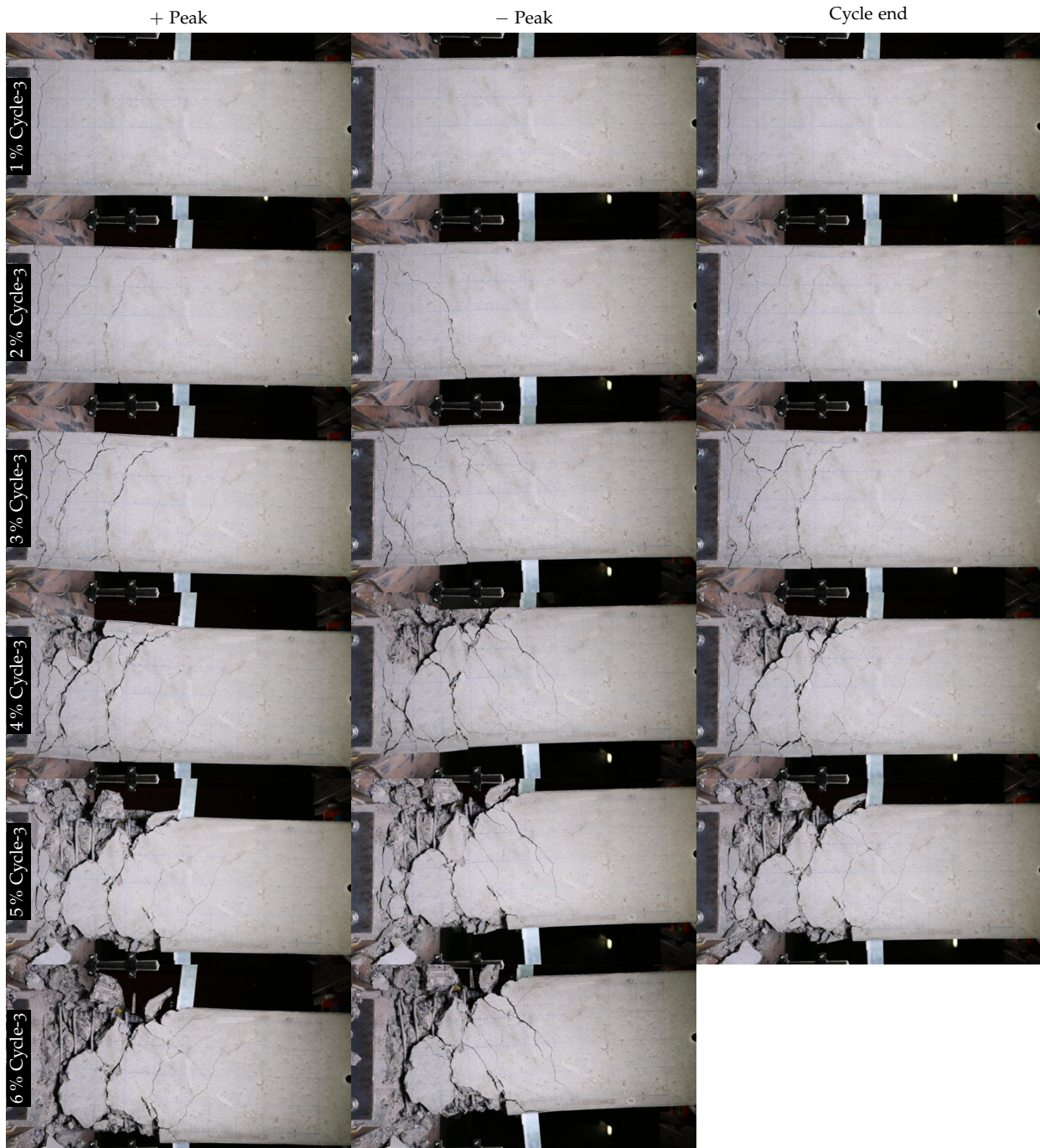
Figure D.8: Damage states at peak and
cycle completion loading states (SB 05)
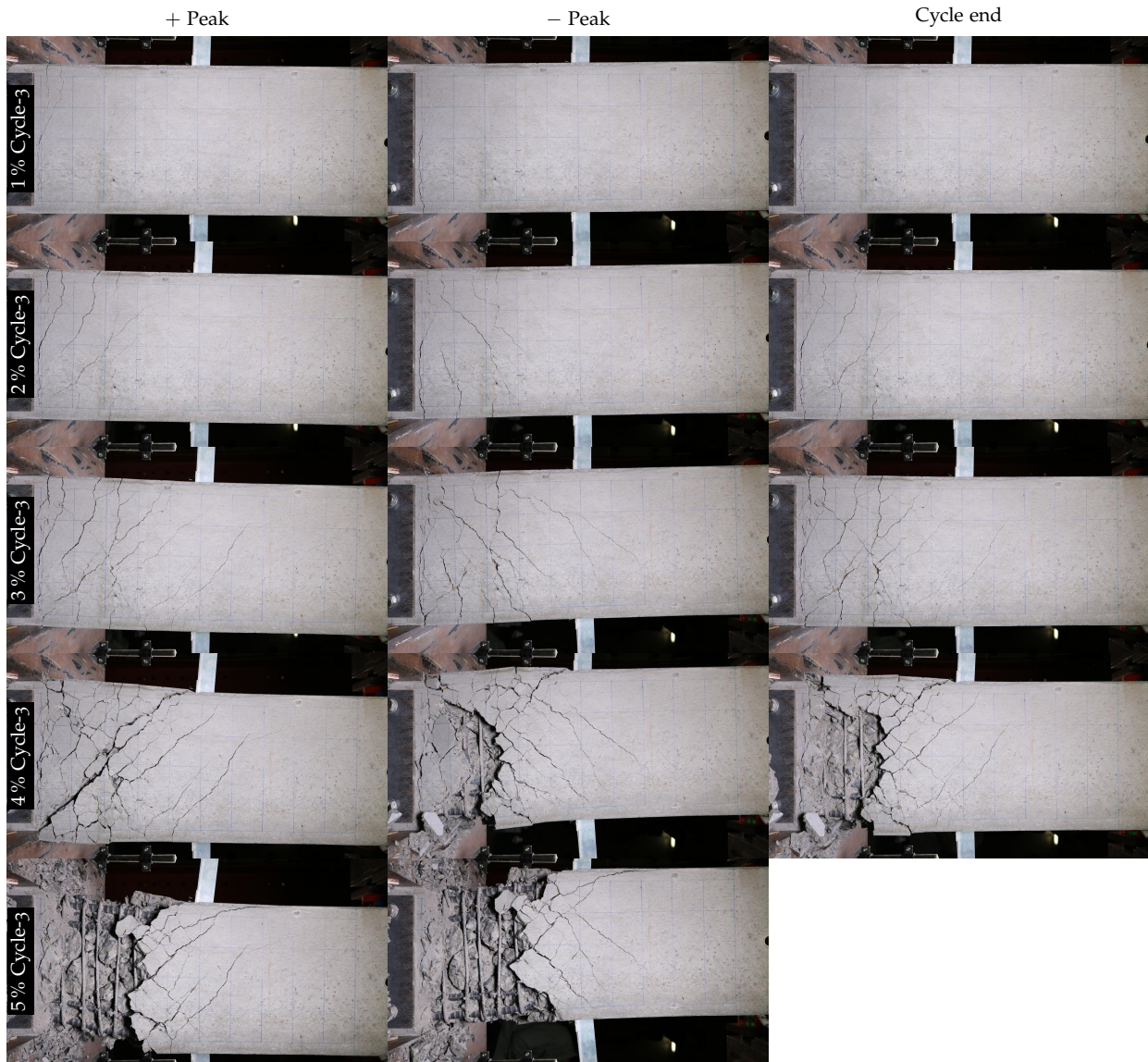
Figure D.9: Damage states at peak and cycle completion loading states (SB06)
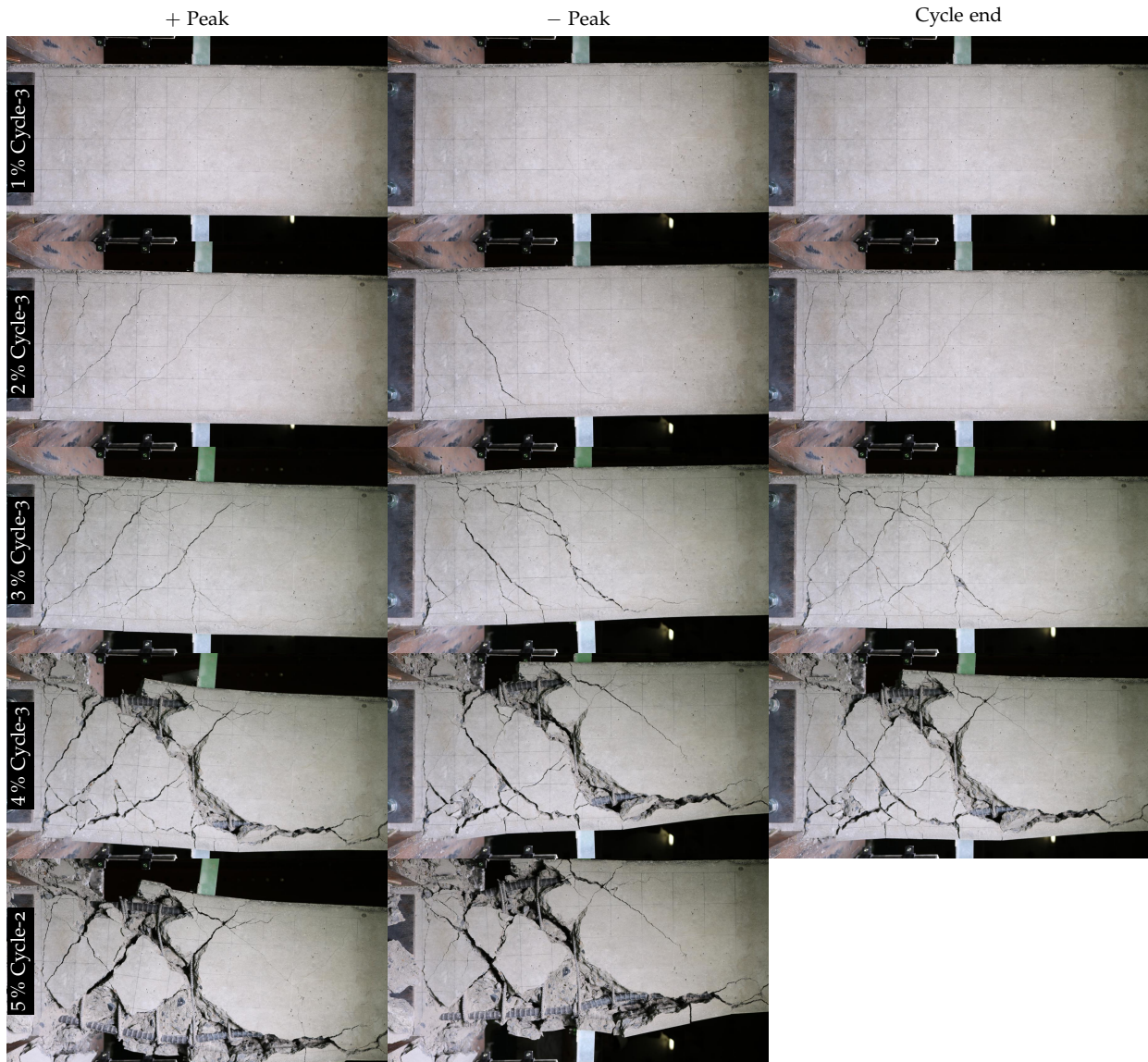
Figure D.10: Damage states at peak and cycle completion loading states (SB07)
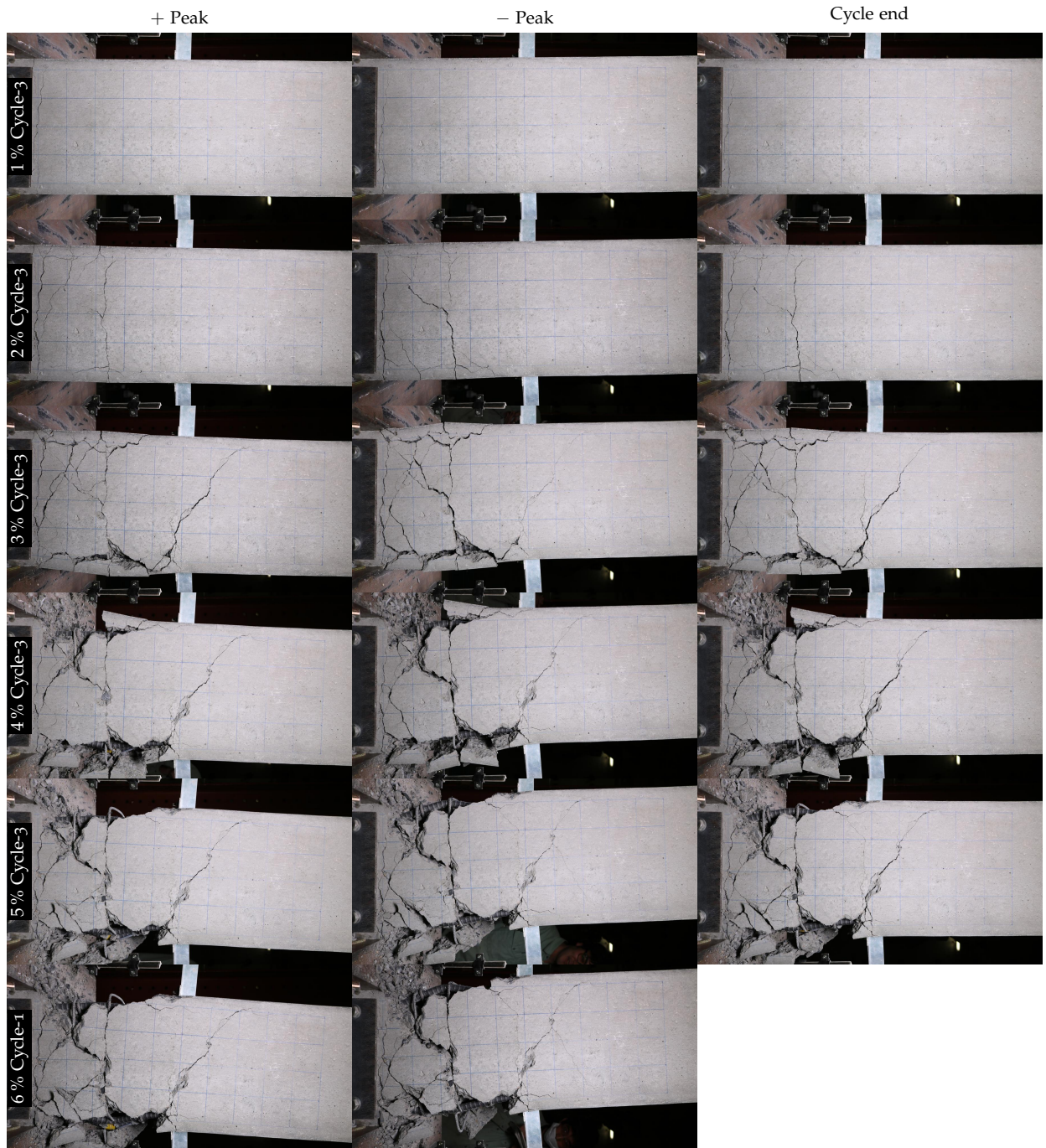
Figure D.11: Damage states at peak and cycle completion loading states (SB 08)

+ Peak   − Peak   Cycle end
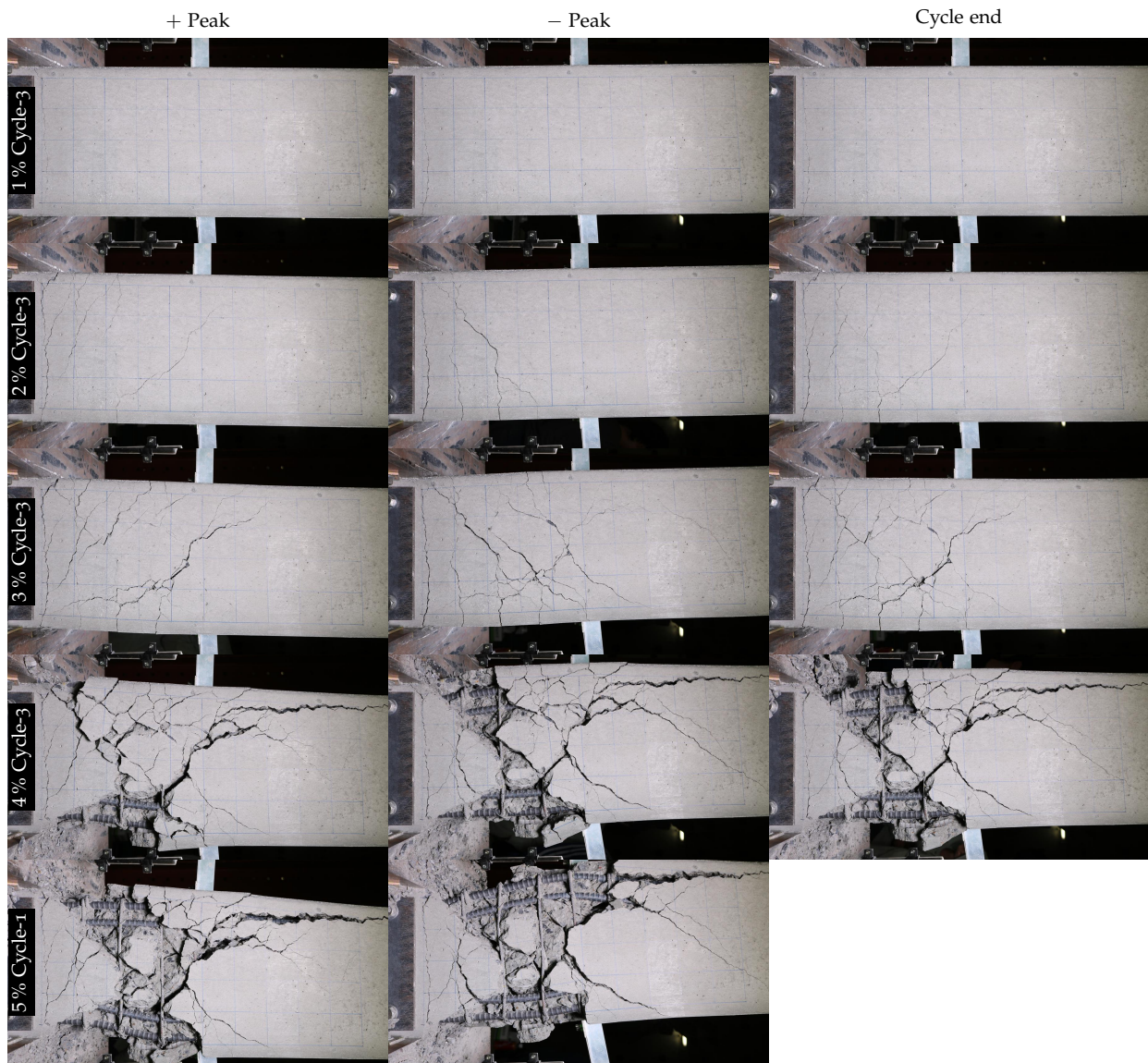
Figure D.12: Damage states at peak and
cycle completion loading states (SB 09)
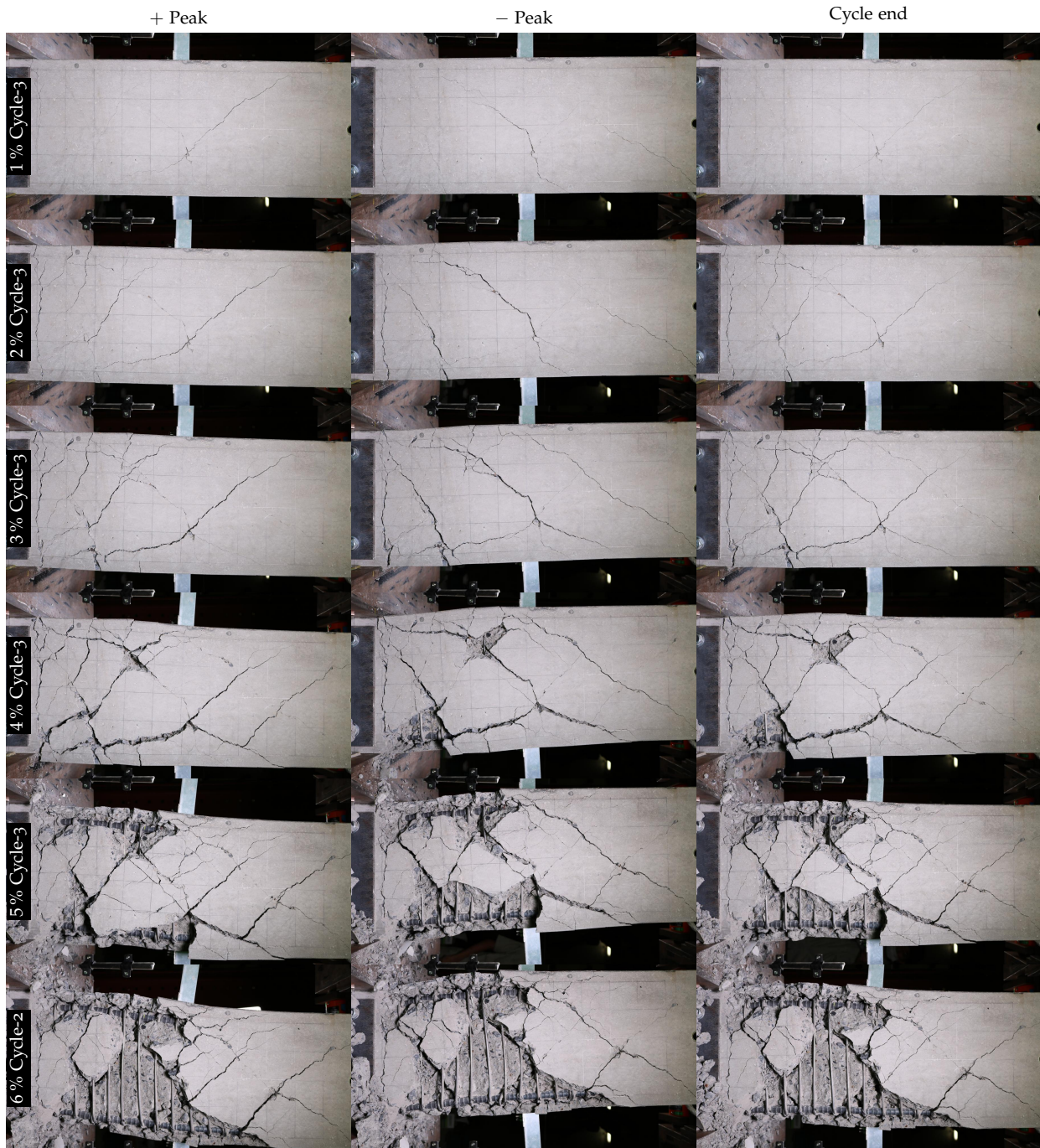
Figure D.13: Damage states at peak and cycle completion loading states (SB 10)
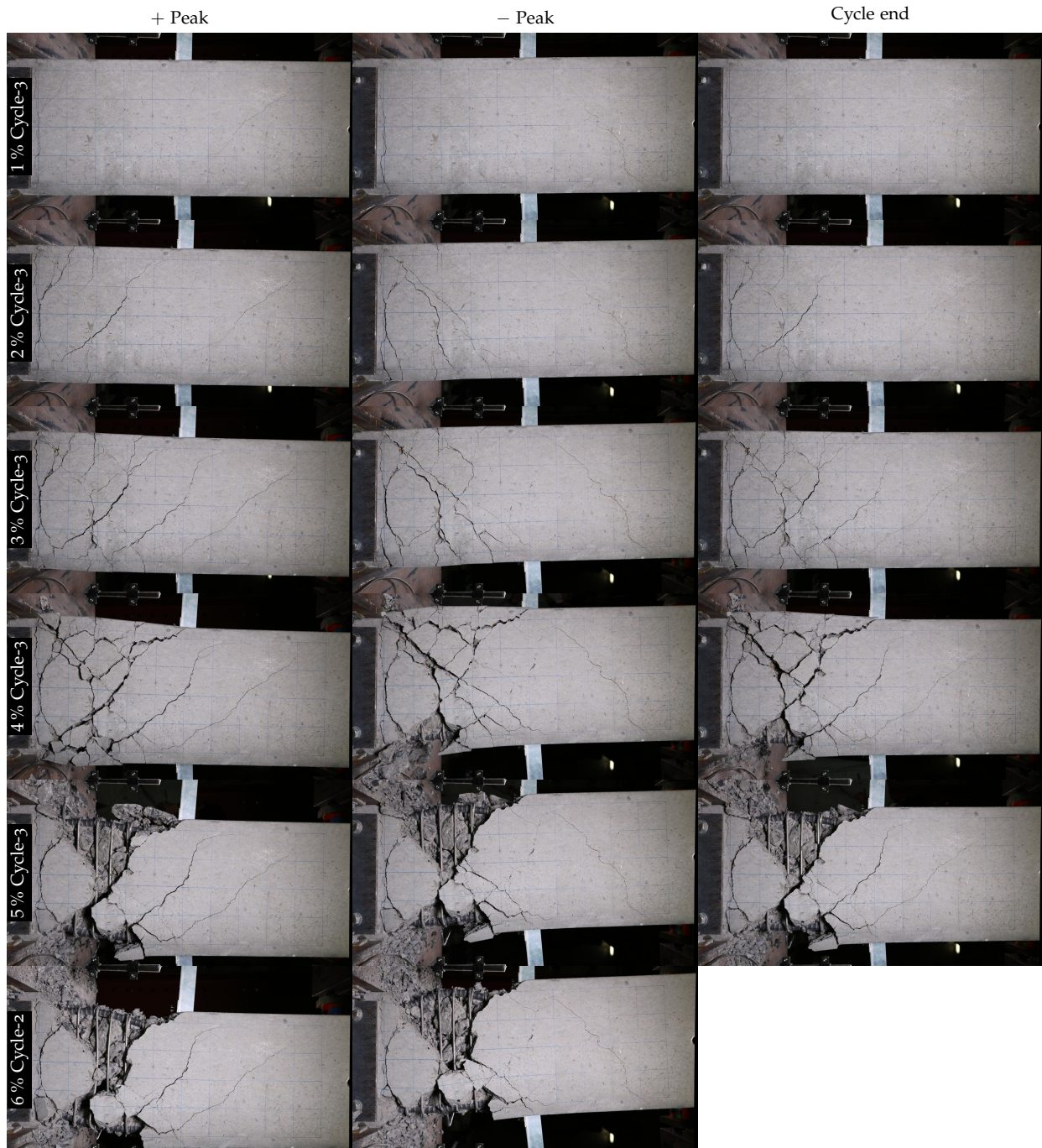
Figure D.14: Damage states at peak and cycle completion loading states (SB11)
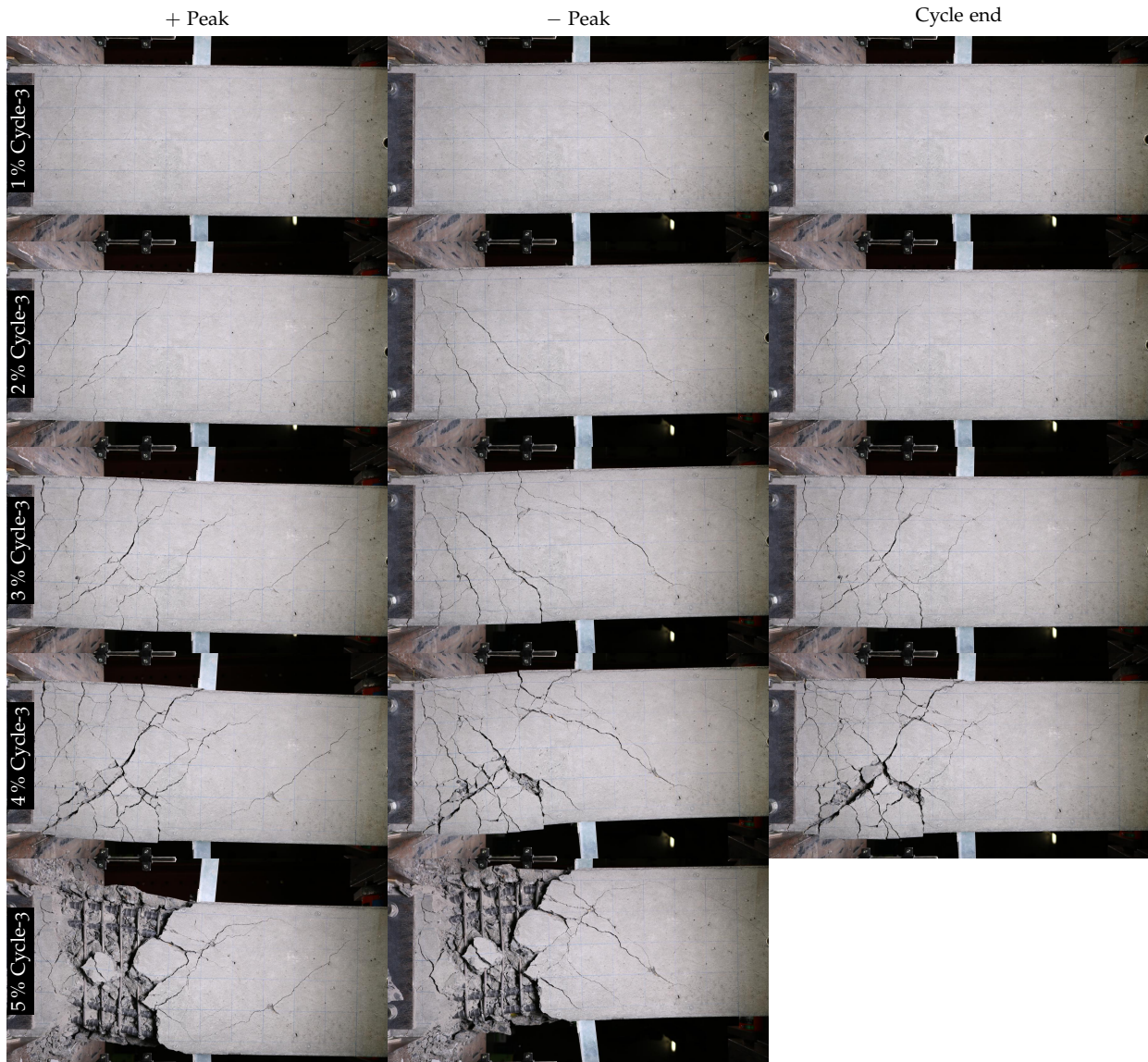
Figure D.15: Damage states at peak and cycle completion loading states (SB 12)

+ Peak   − Peak   Cycle end
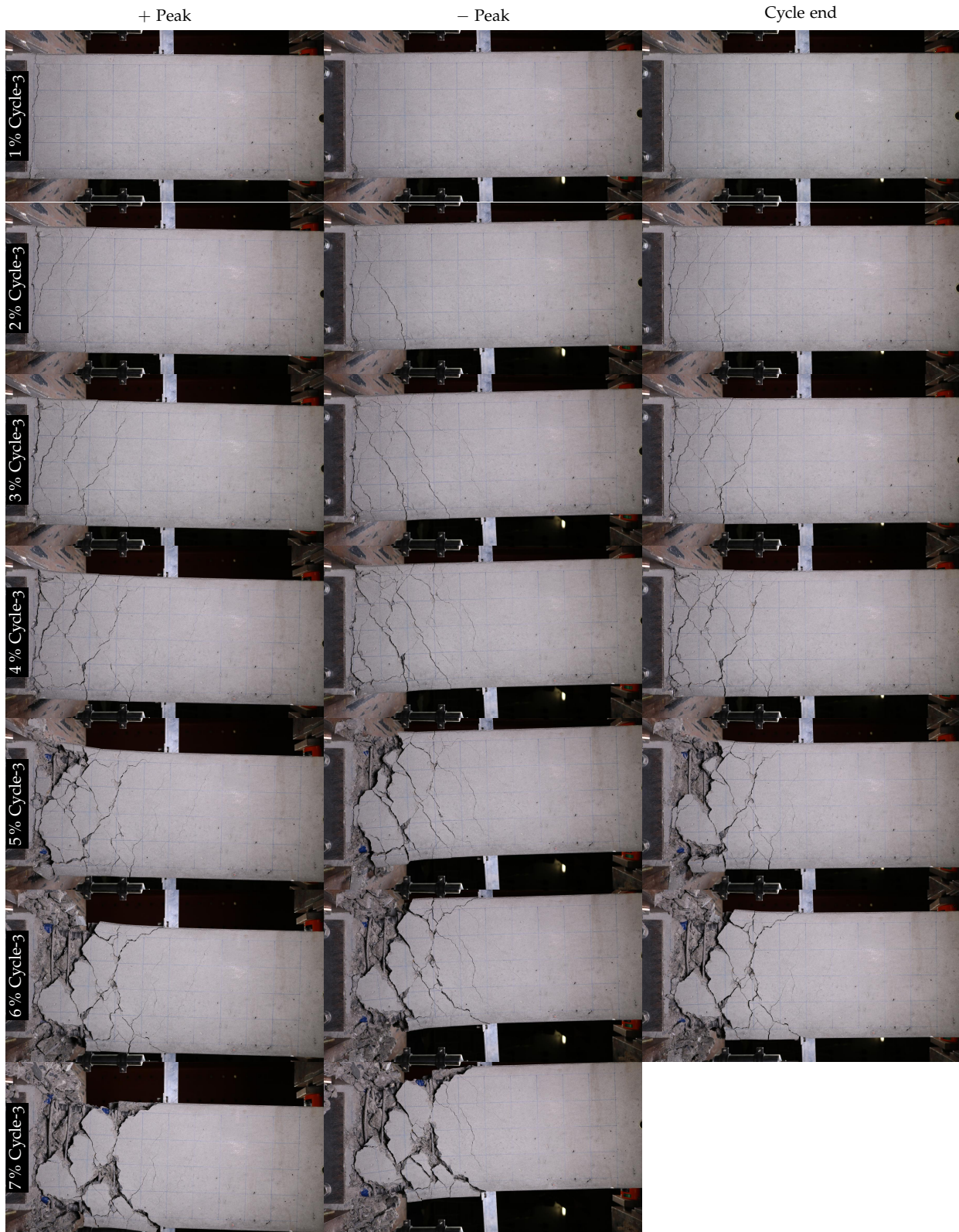
Figure D.16: Damage states at peak and cycle completion loading states (SC1)
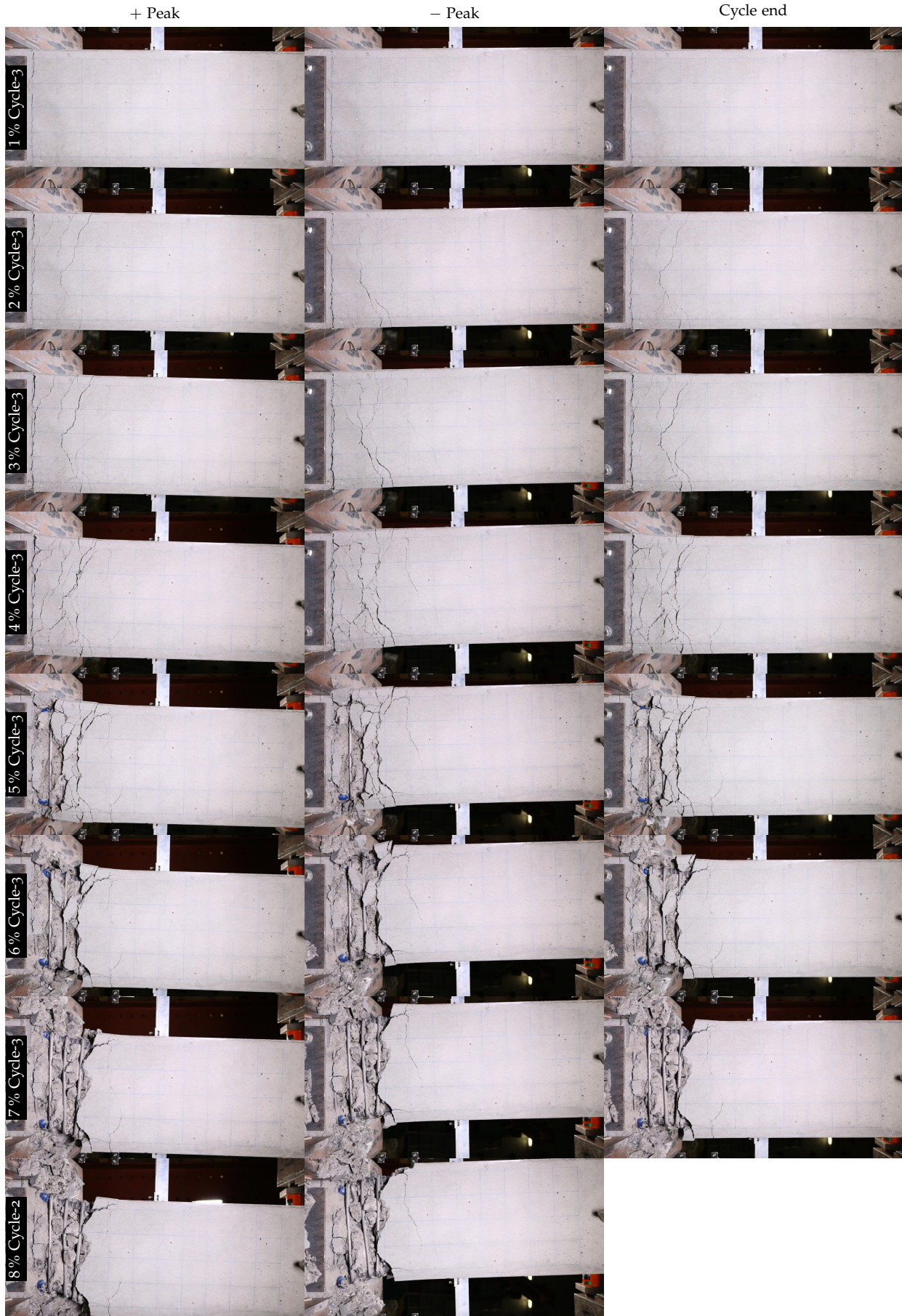
Figure D.17: Damage states at peak and cycle completion loading states (SC2)

+ Peak   − Peak   Cycle end
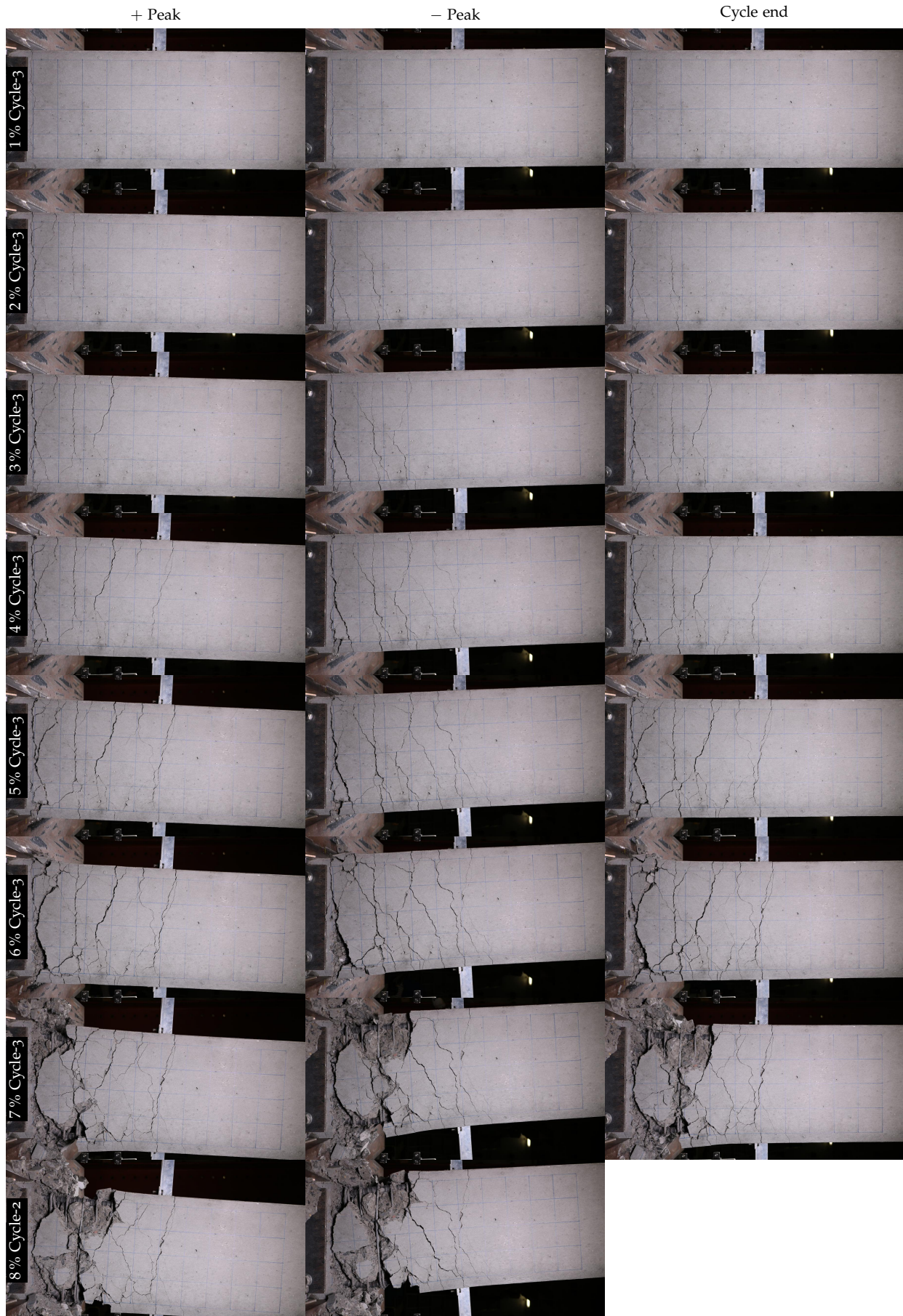
Figure D.18: Damage states at peak and
cycle completion loading states (SC 3)
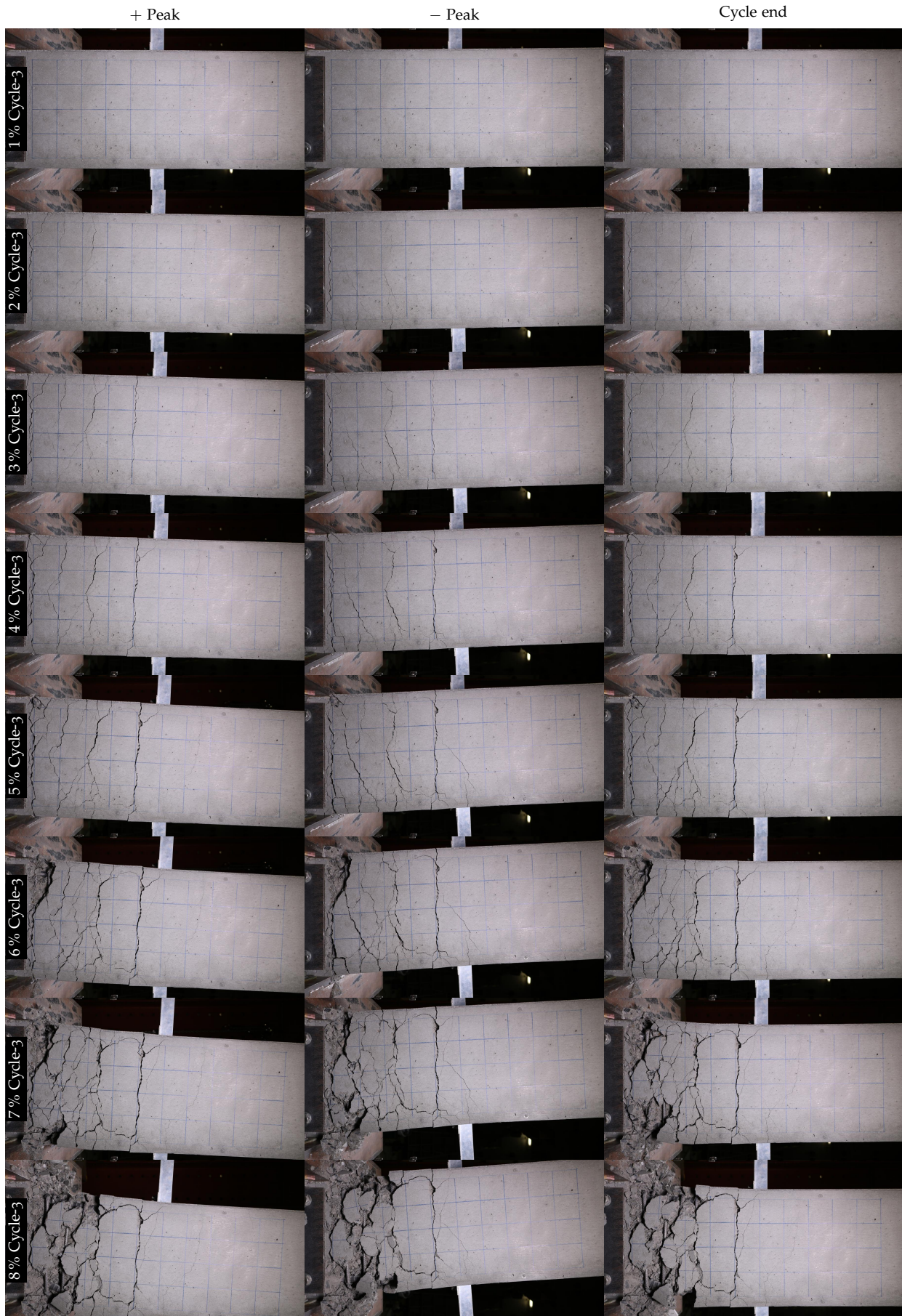
Figure D.19: Damage states at peak and cycle completion loading states (SC 4)
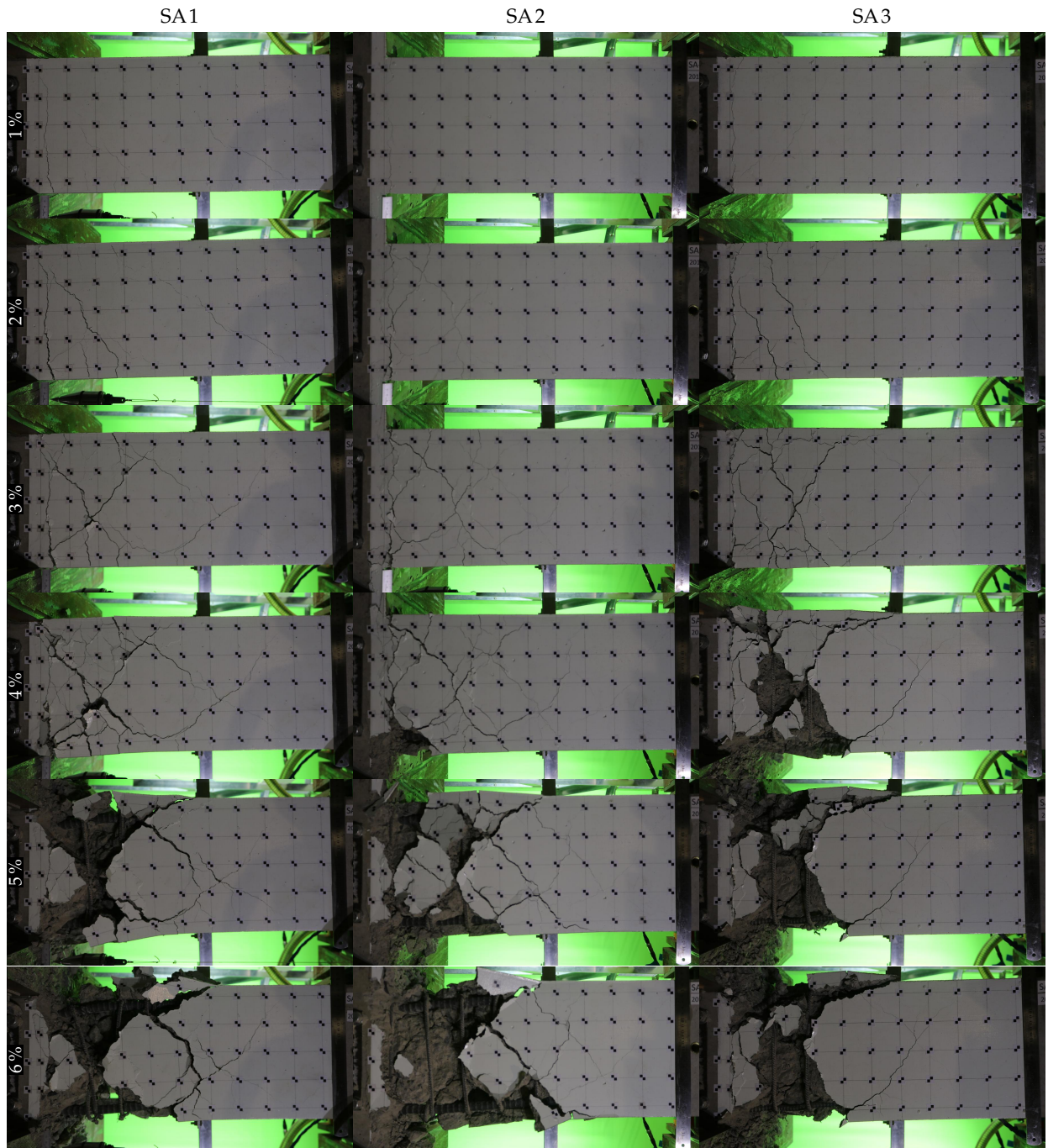
Figure D.20: Residual damage state at the end of cycle completion (SA1, SA2, and SA3)
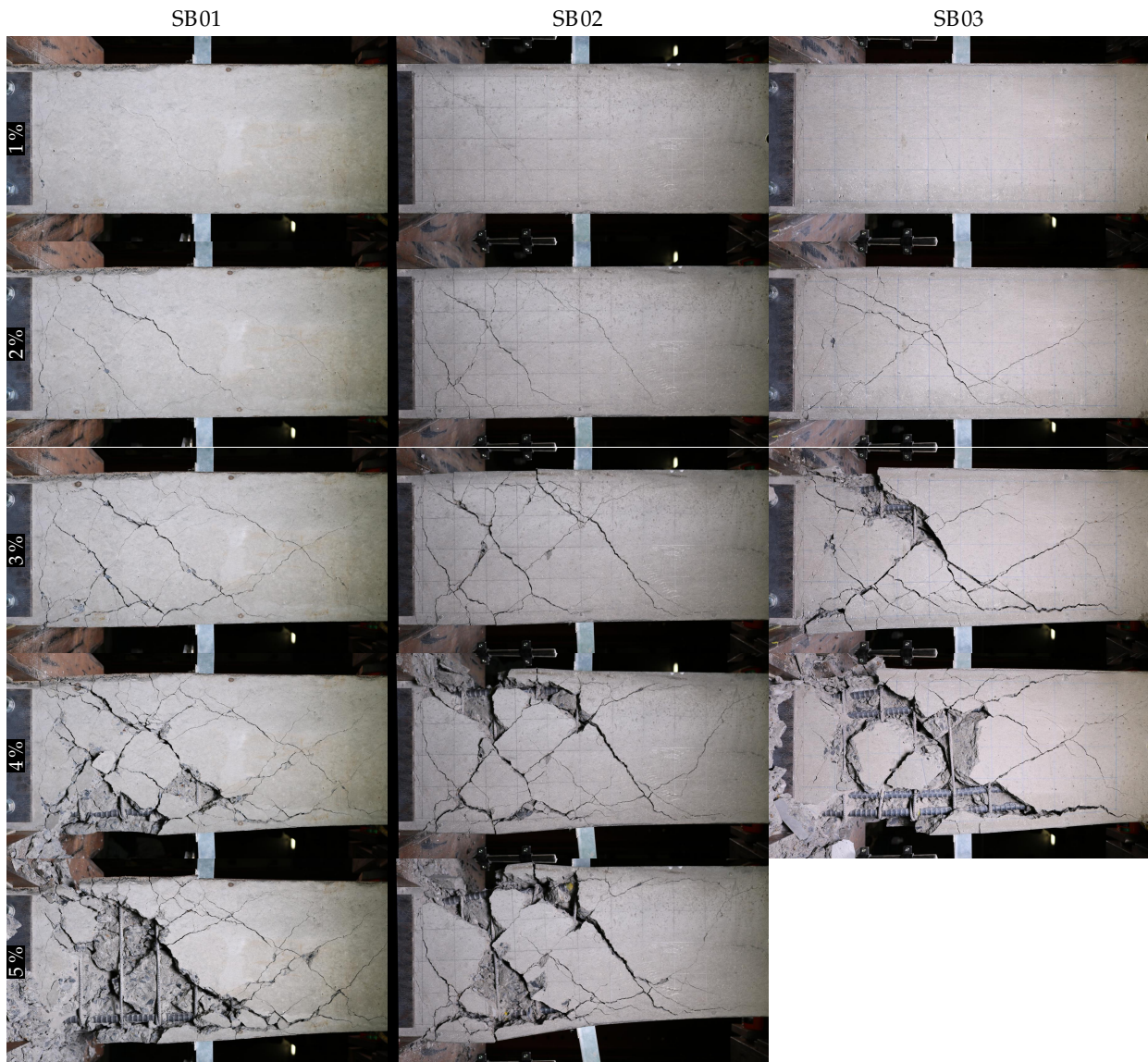
Figure D.21: Residual damage state at the end of cycle completion (SB01, SB02, and SB03)
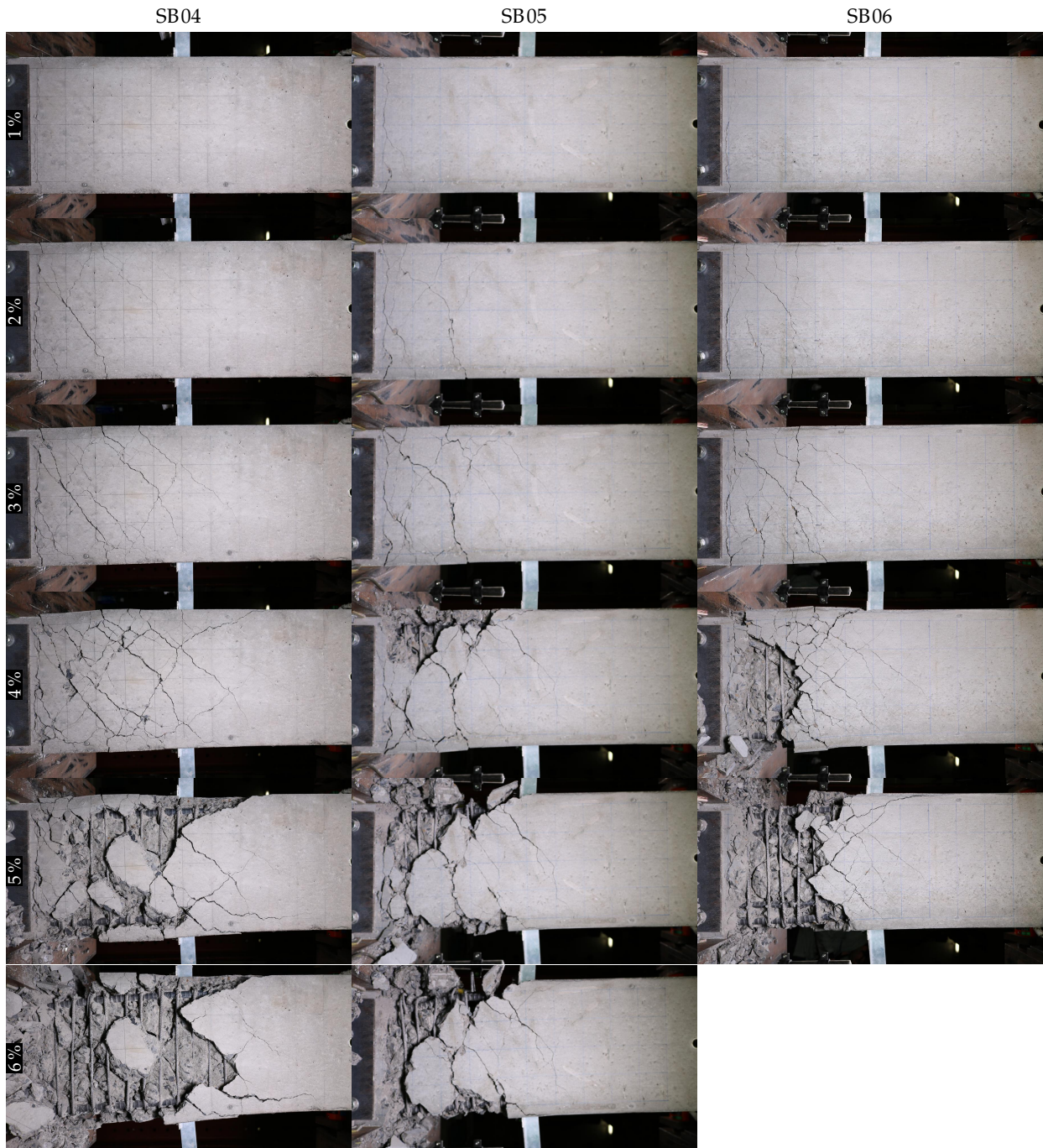
Figure D.22: Residual damage state at the end of cycle completion (SB04, SB05, and SB06)
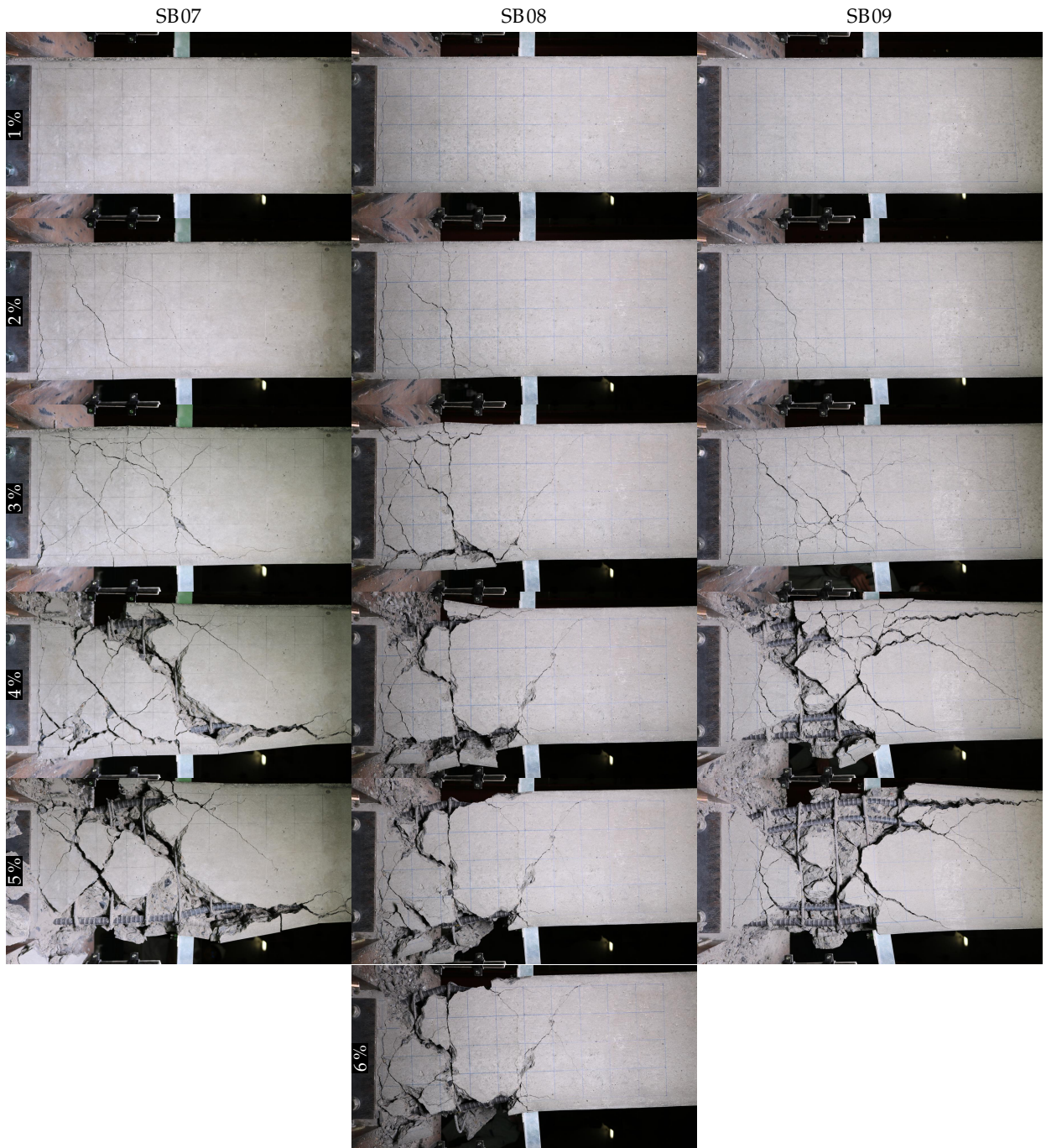
Figure D.23: Residual damage state at the end of cycle completion (SB07, SB08, and SB09)
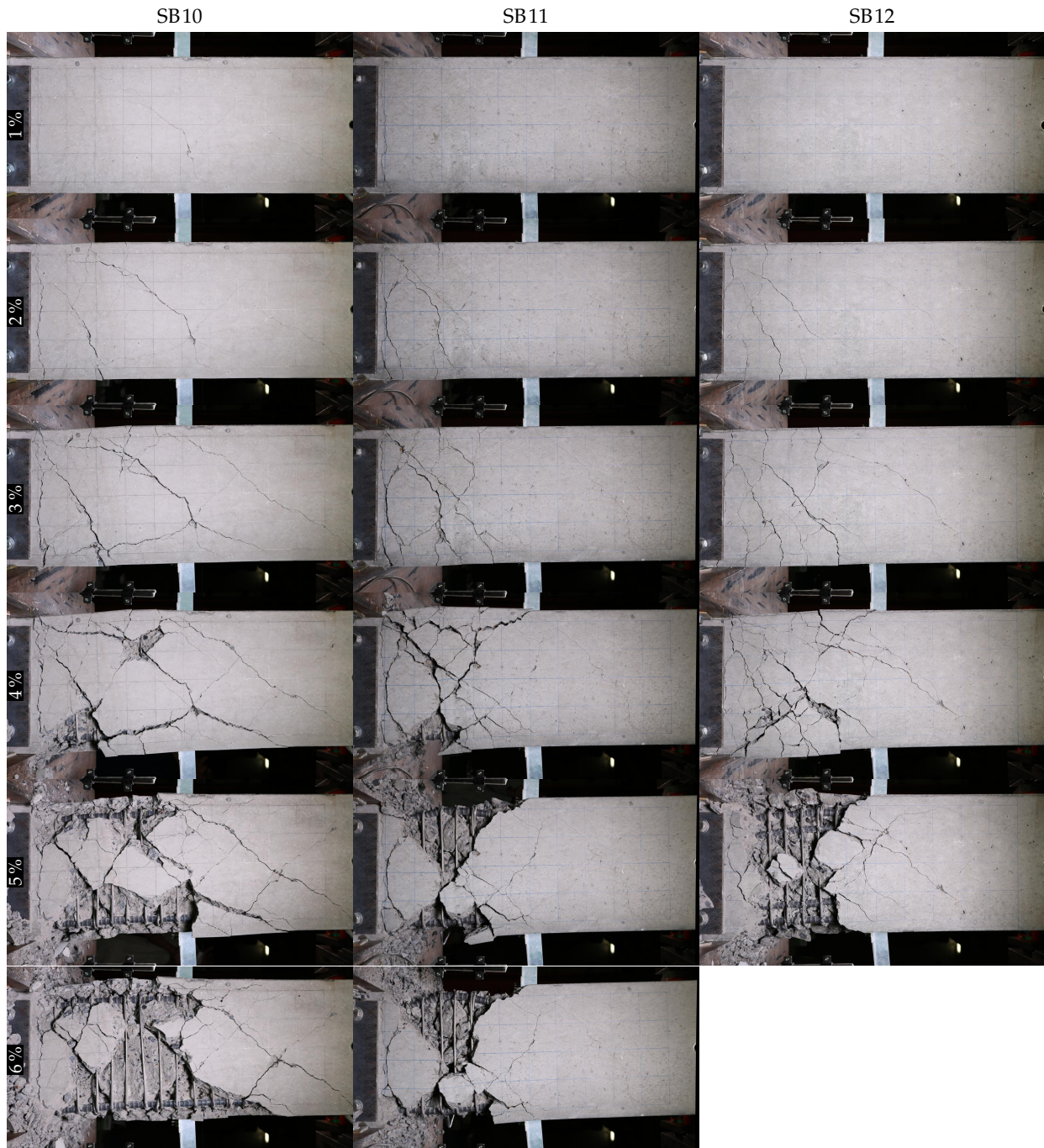
Figure D.24: Residual damage state at the end of cycle completion (SB10, SB11, and SB12)

Figure D.25: Residual damage state at the end of cycle completion (SC1 and SC2)

SC 3   SC 4
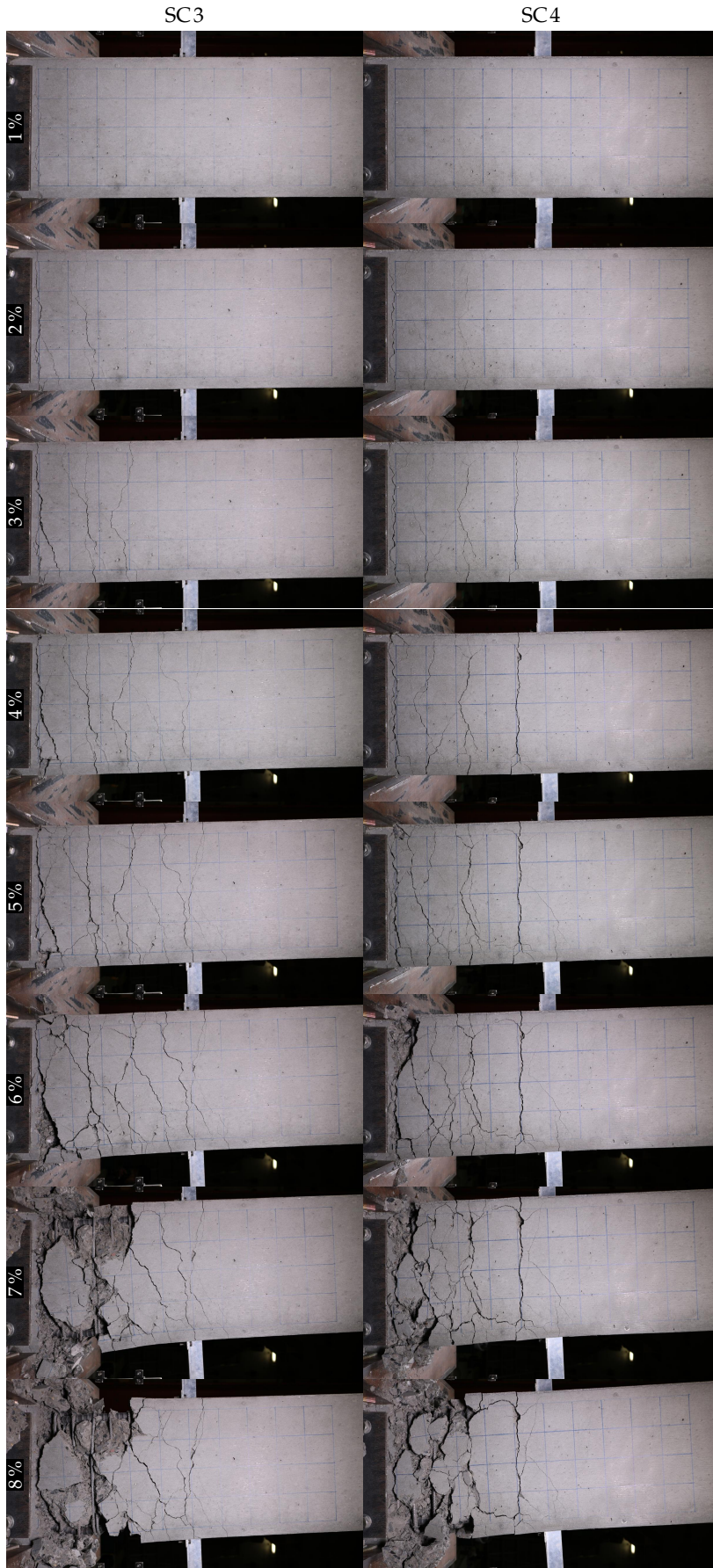
Figure D.26: Residual damage state at the end of cycle completion (SC 3 and SC 4)

E
Photogrammetric plots

Results of photogrammetric analysis using Method-A are expressed in the form of deformation grids. Deformations at peak positive, zero, and peak negative states over increasing target drift levels are expressed for all specimens in figures E.1 to E.16. The deformations expressed are *five* times magnified to enable easier understanding. Meaningful data was captured only up to about 3 % or 4 % target drift levels for most specimens as increased concrete spalling at large drifts resulted in fewer valid targets remaining intact on the surface.

Figure E.1: Deformation pattern of SB01 at peak and zero states over increasing target drift levels

Figure E.2: Deformation pattern of SB 02 at peak and zero states over increasing target drift levels
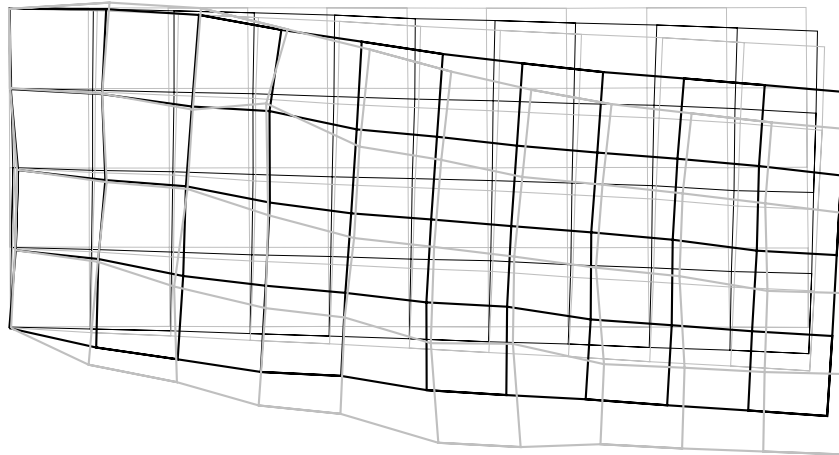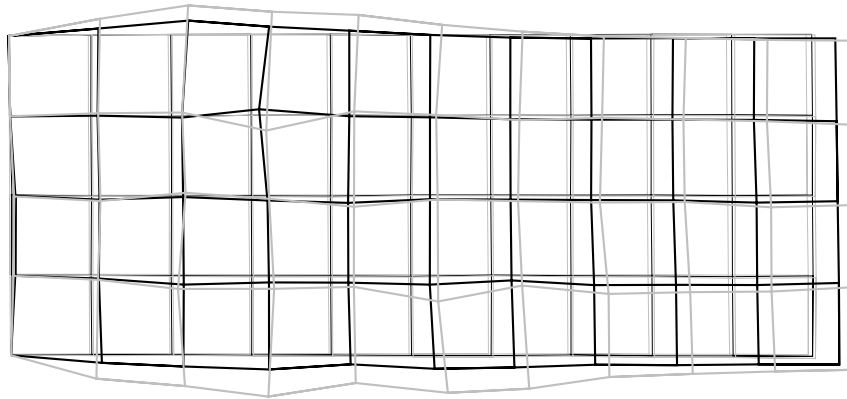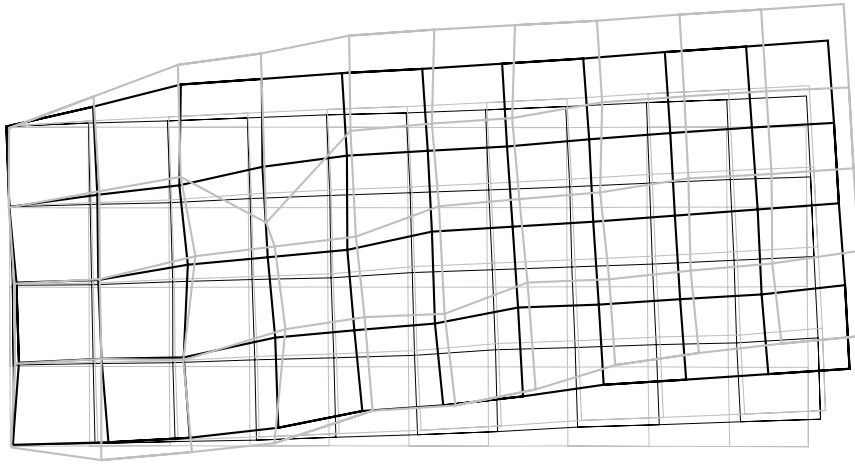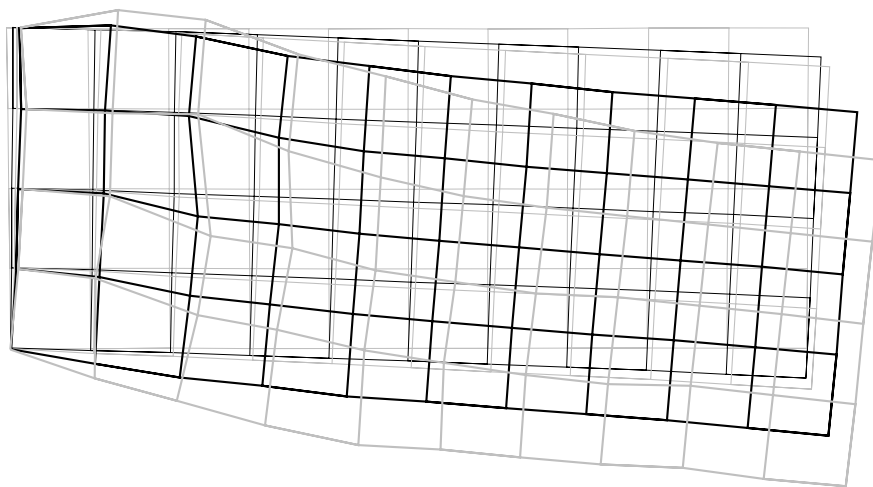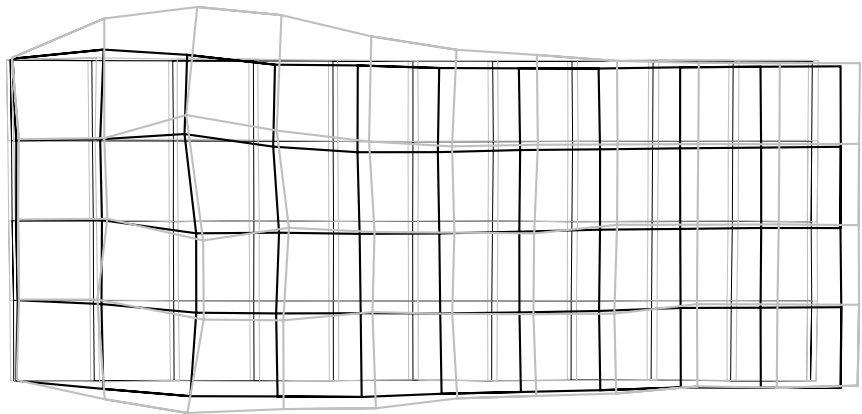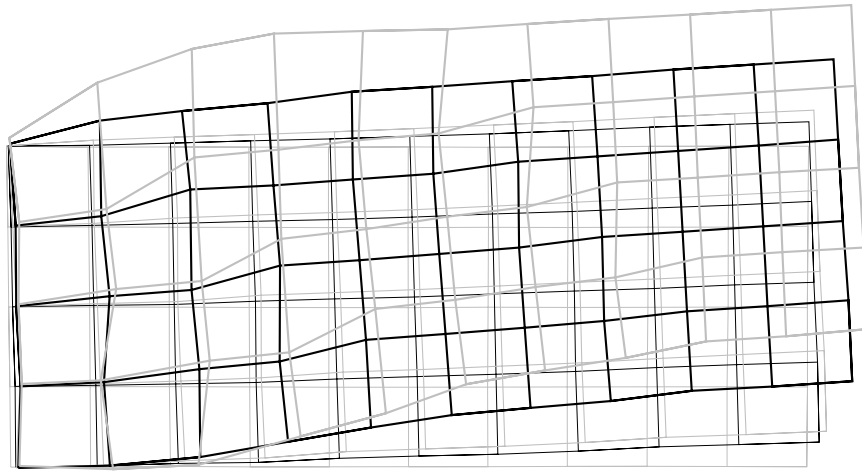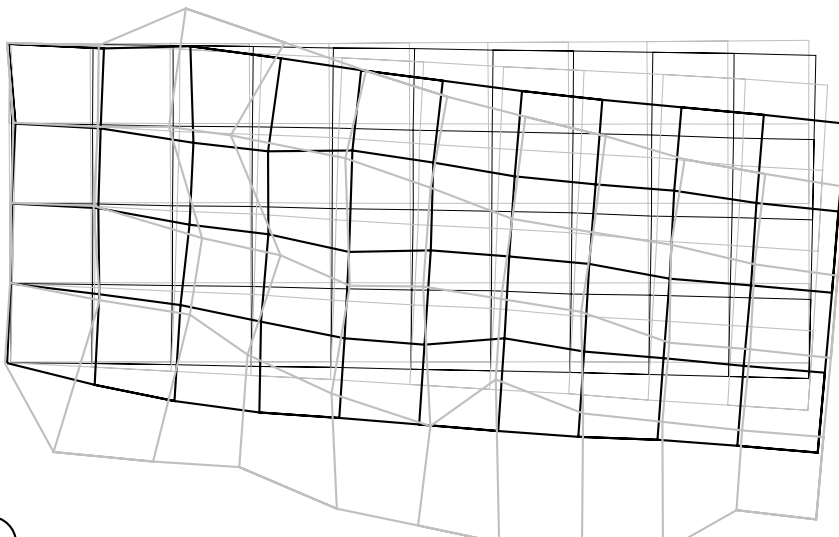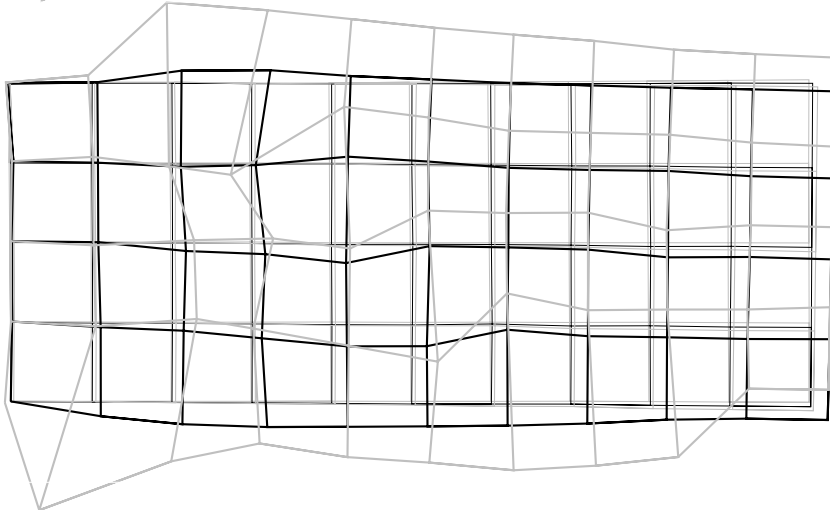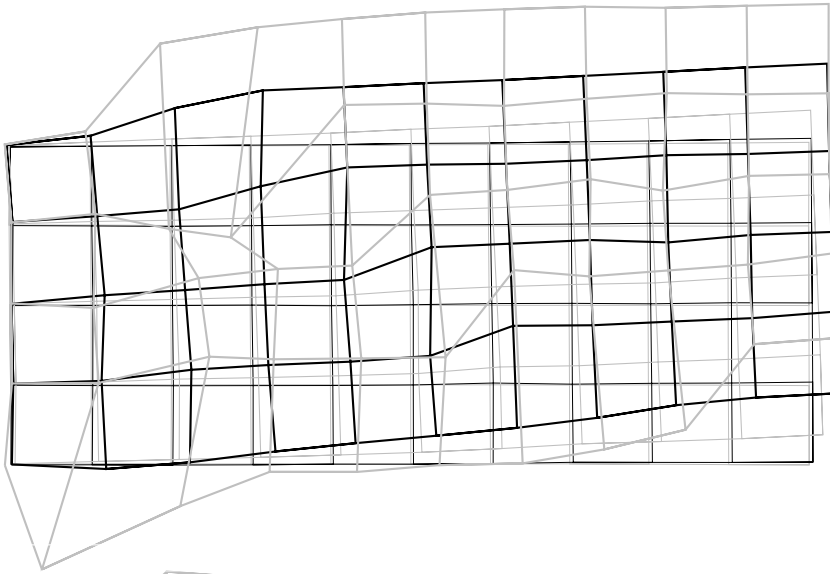
Initial —— 0.75 %^{3} —— 1 %^{3} —— 2 %^{3} —— 3 %^{3}

Figure E.3: Deformation pattern of SB03 at peak and zero states over increasing target drift levels

Figure E.4: Deformation pattern of SB04 at peak and zero states over increasing target drift levels

Figure E.5: Deformation pattern of SB05 at peak and zero states over increasing target drift levels

Figure E.6: Deformation pattern of SB06 at peak and zero states over increasing target drift levels

Figure E.7: Deformation pattern of SB 07 at peak and zero states over increasing target drift levels

Figure E.8: Deformation pattern of SB08 at peak and zero states over increasing target drift levels

Figure E.9: Deformation pattern of SB 09 at peak and zero states over increasing target drift levels

Figure E.10: Deformation pattern of SB10 at peak and zero states over increasing target drift levels

Figure E.11: Deformation pattern of SB11 at peak and zero states over increasing target drift levels

Figure E.12: Deformation pattern of SB 12 at peak and zero states over increasing target drift levels
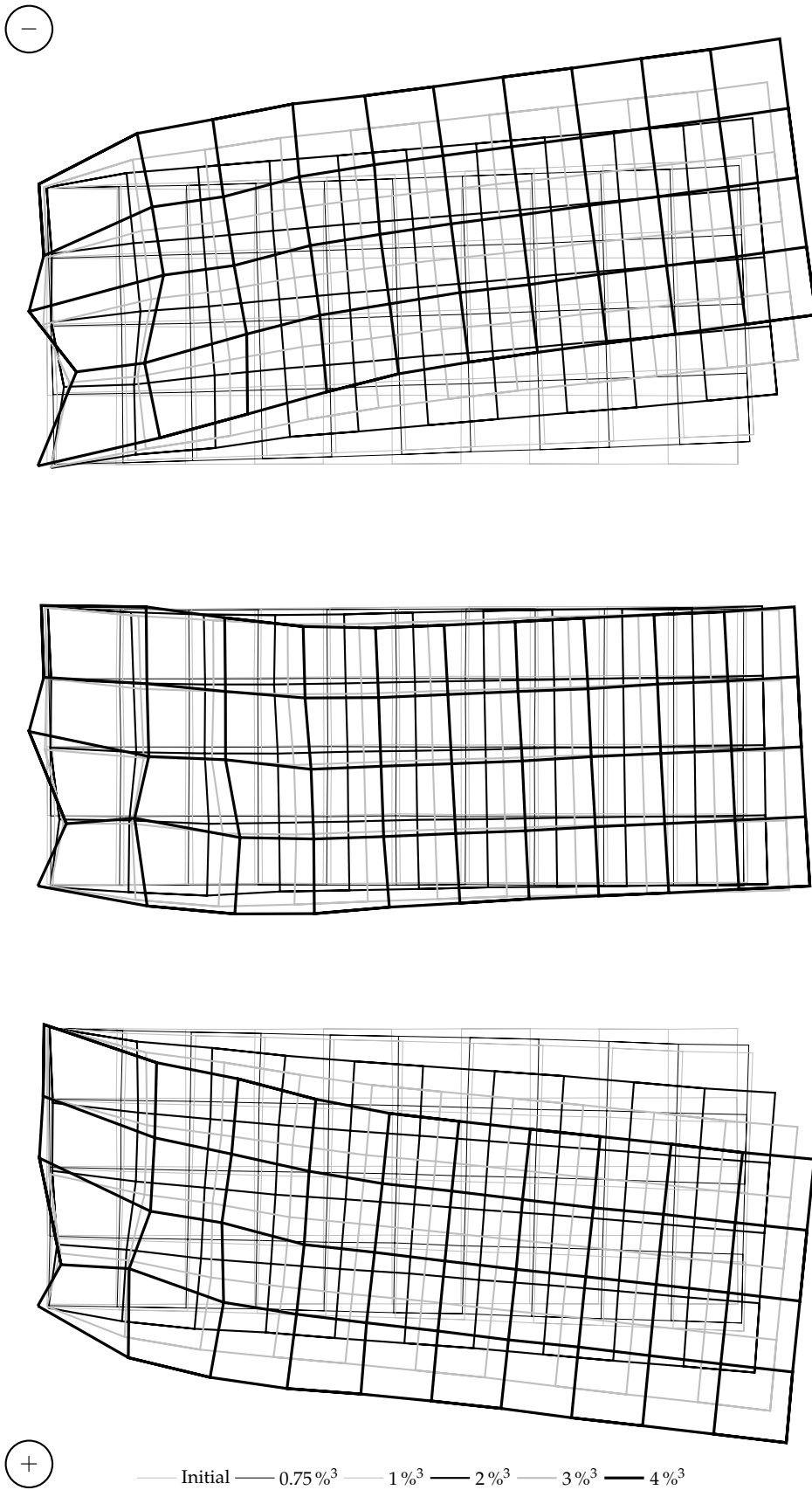
Figure E.13: Deformation pattern of SC1 at peak and zero states over increasing target drift levels
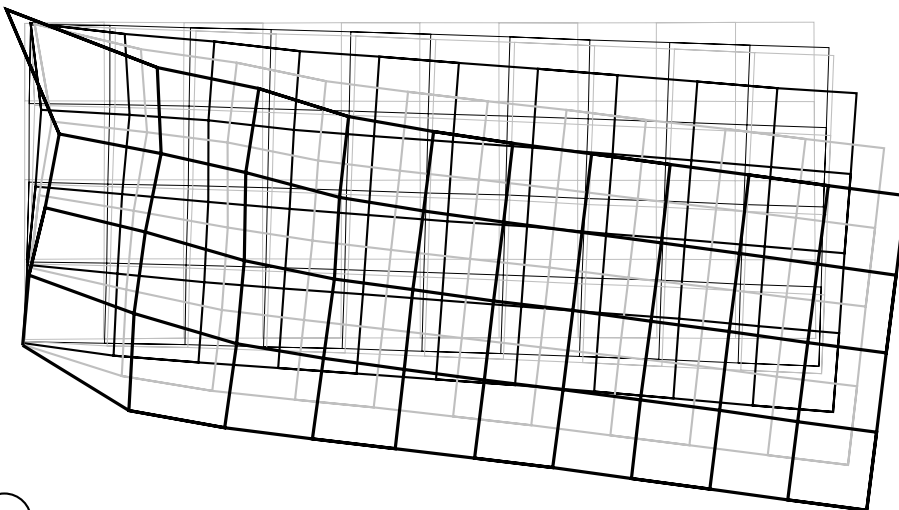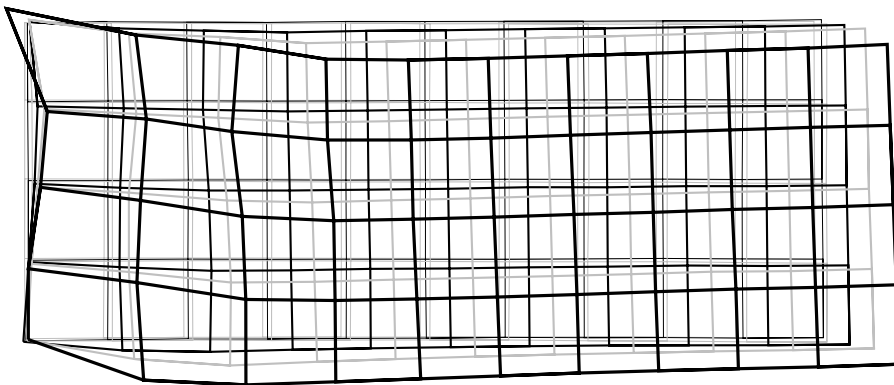
Figure E.14: Deformation pattern of SC 2 at peak and zero states over increasing target drift levels
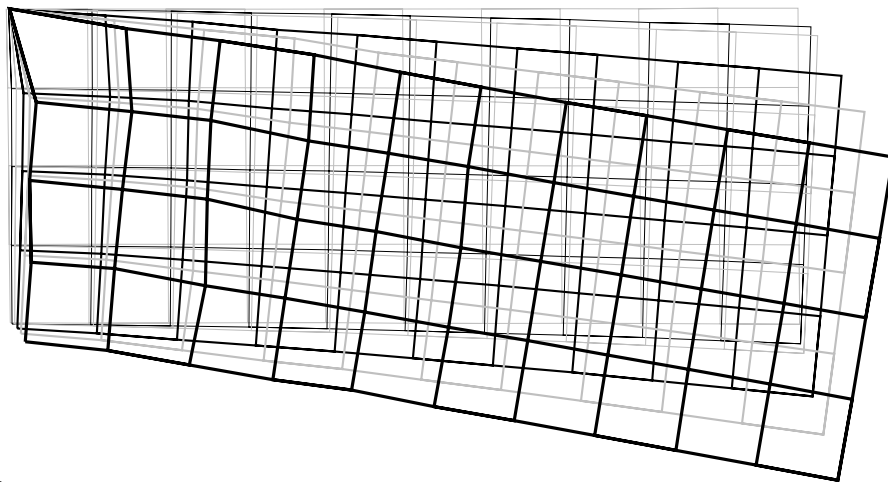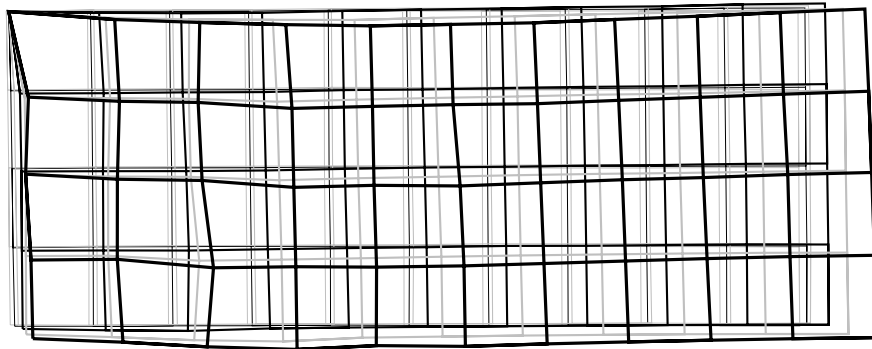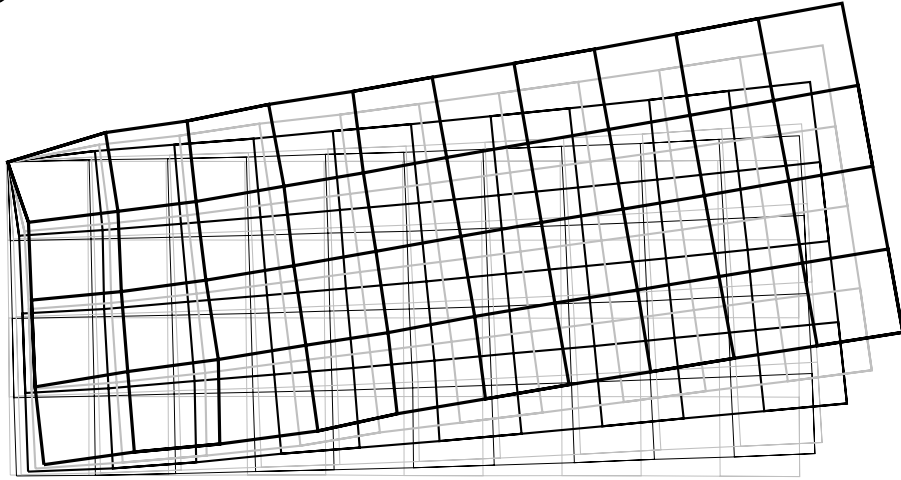
Figure E.15: Deformation pattern of SC 3 at peak and zero states over increasing target drift levels
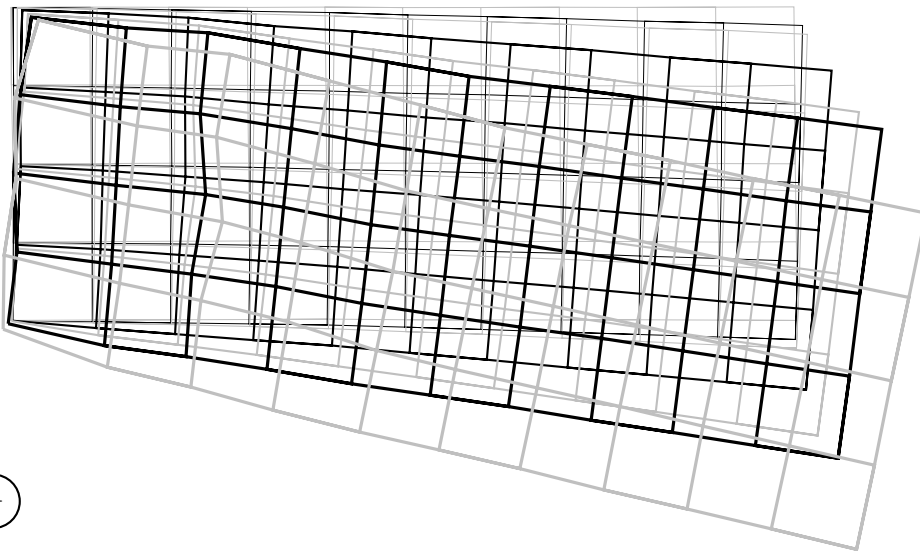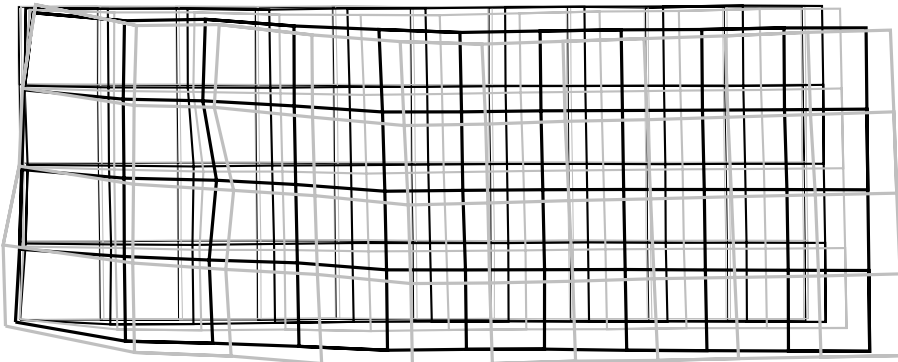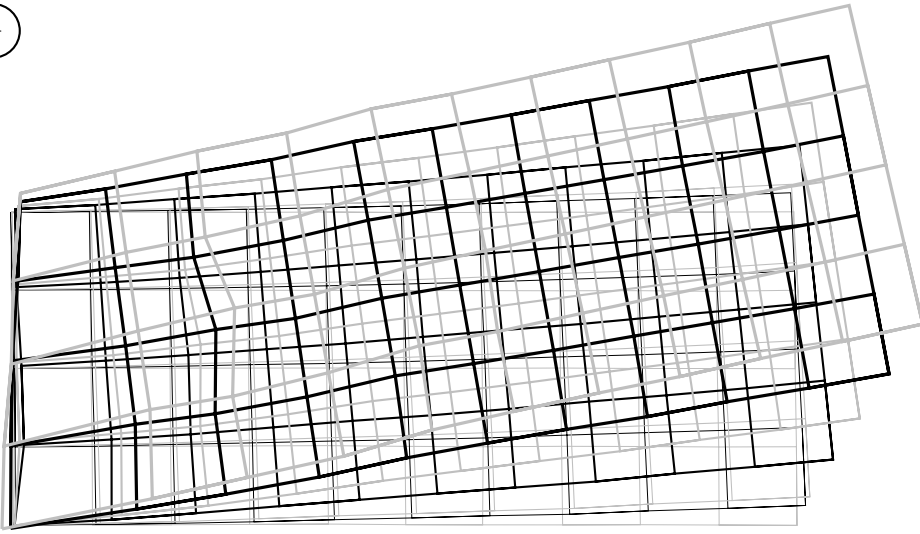
Initial —— 0.75 %^{3} —— 1 %^{3} —— 2 %^{3} —— 3 %^{3} —— 4 %^{3} —— 5 %^{3}

Figure E.16: Deformation pattern of SC 4 at peak and zero states over increasing target drift levels

F
Miscellaneous data

OTHER plots and illustrations resulting from the experiment data that have not been explicitly discussed previously are depicted here for the sake of completion. Extensive commentary on these figures is not provided however.

Tip rotation (θ_{tip}) and moment response for all specimens is expressed in figures F.1 and F.2. The two displacement sensors instrumented at the tip of cantilever for measuring chord rotation angle (Δ) were used to determine tip rotation as:

$$\theta_{tip}(\text{rad}) = \tan^{-1}\left(\frac{\delta_2 - \delta_1}{d_1}\right) \tag{F.1}$$

All the response quantities such as moment (M), drift (Δ), rotation (θ_{hinge}), and axial strain (ϵ_{axial}) measured during the experiment and expressed previously in relation each other are displayed as response history plots in figures F.3 and F.21. Also indicated in each plots are the events corresponding to the occurrences peak resistance and loss of resistance in both positive and negative loading directions.
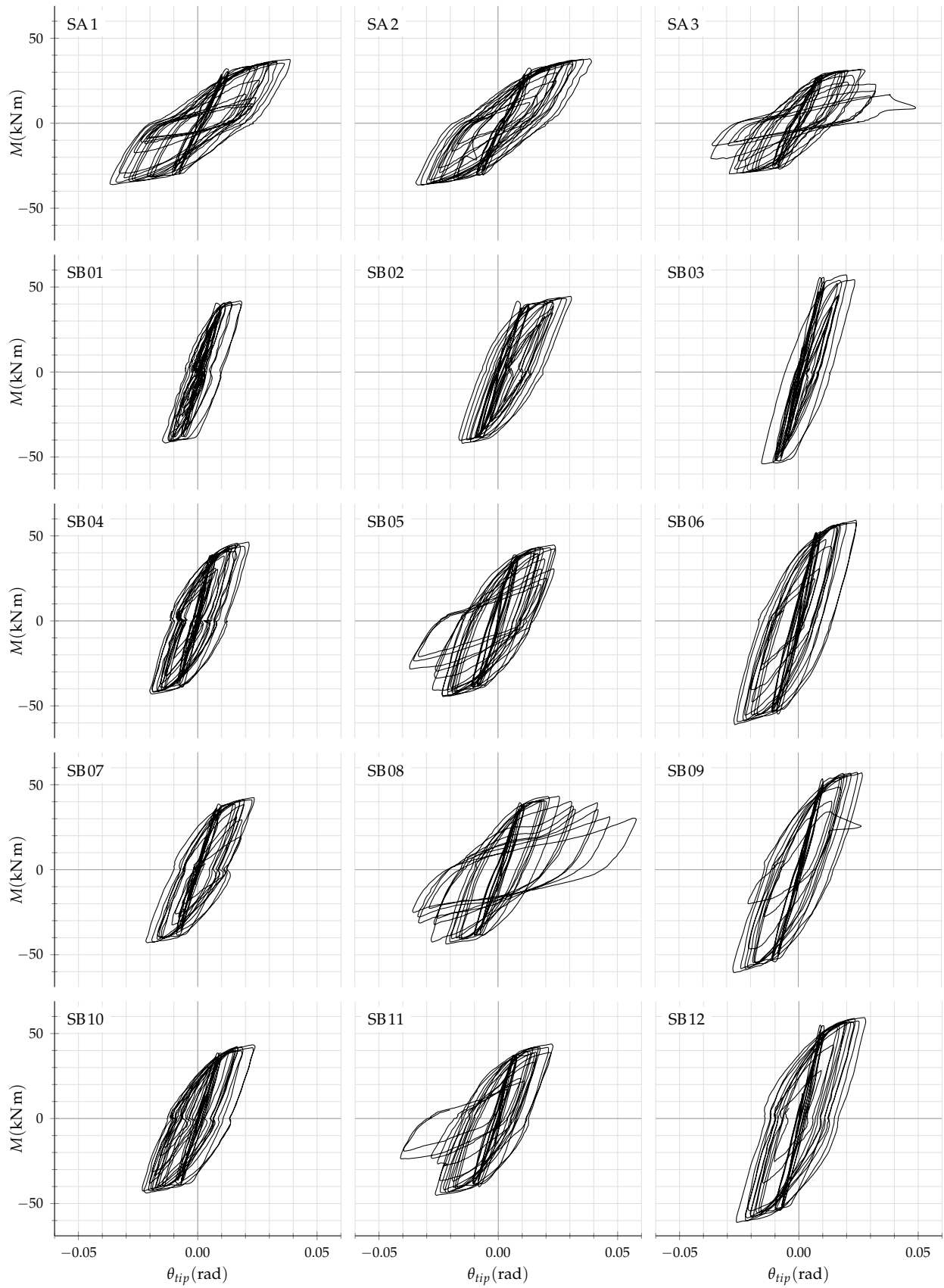
Figure F.1: Moment-tip rotation response (SA and SB series)
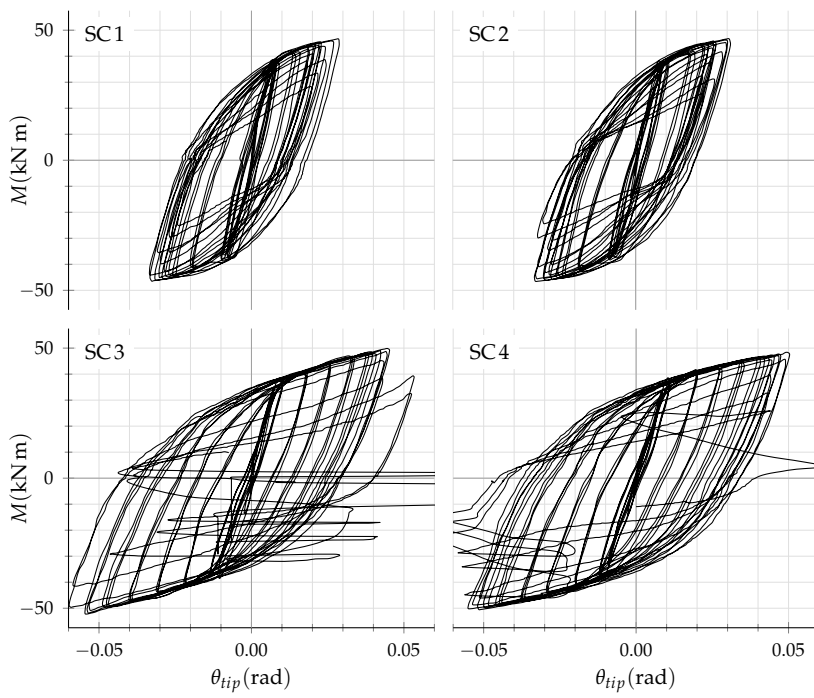
Figure F.2: Moment-tip rotation response (SC series)
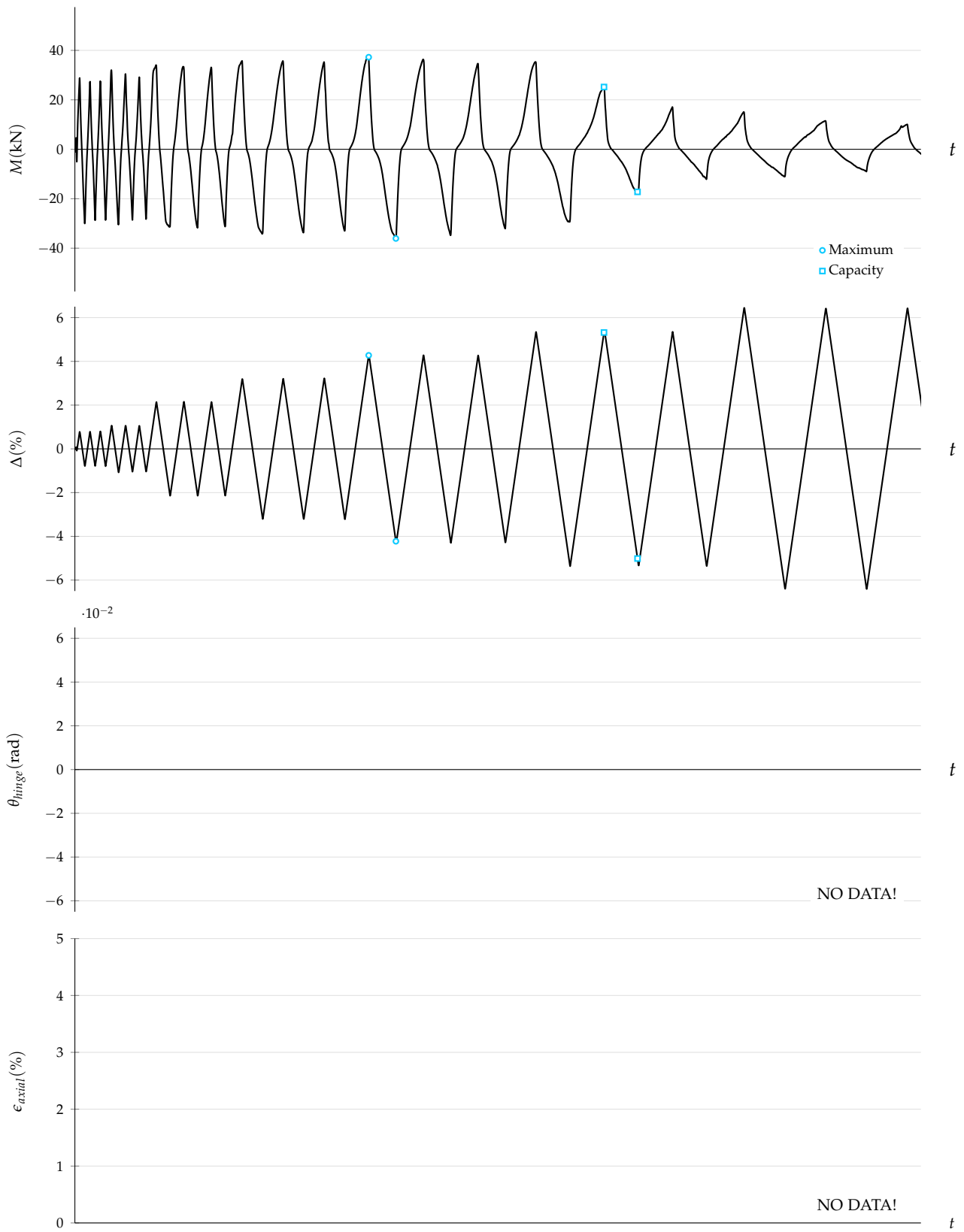
Figure F.3: SA1 response history
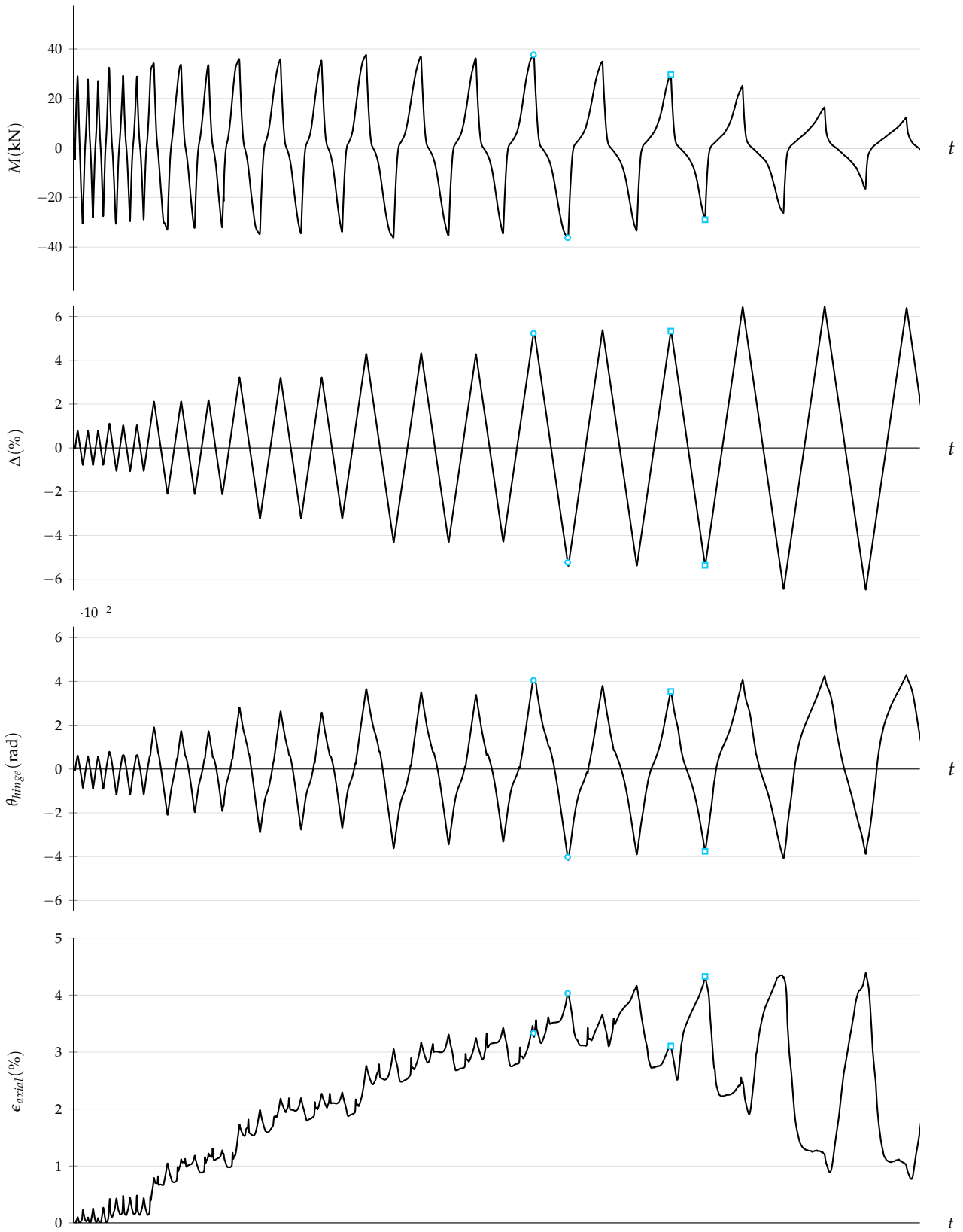
Figure F.4: SA 2 response history
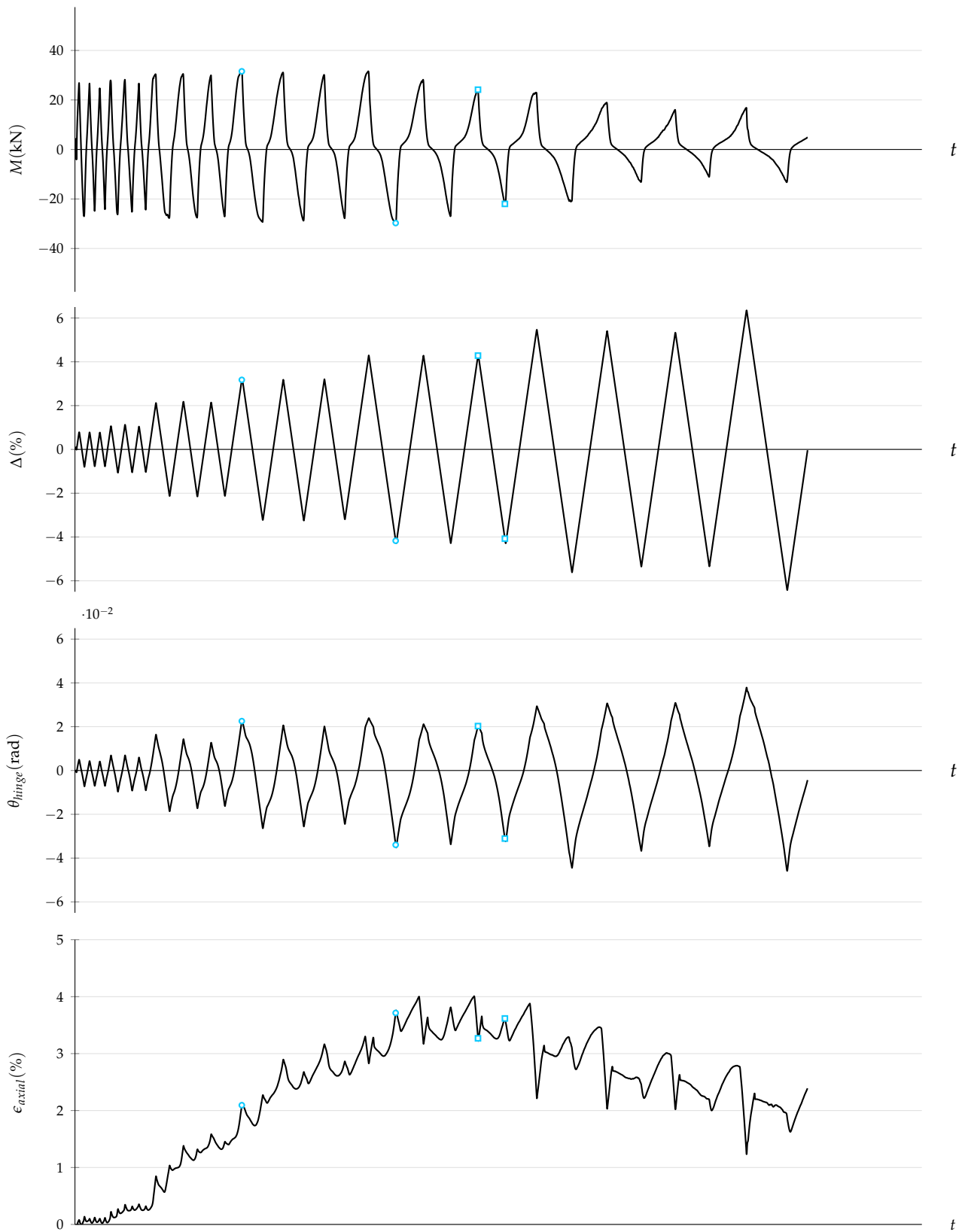
Figure F.5: SA3 response history
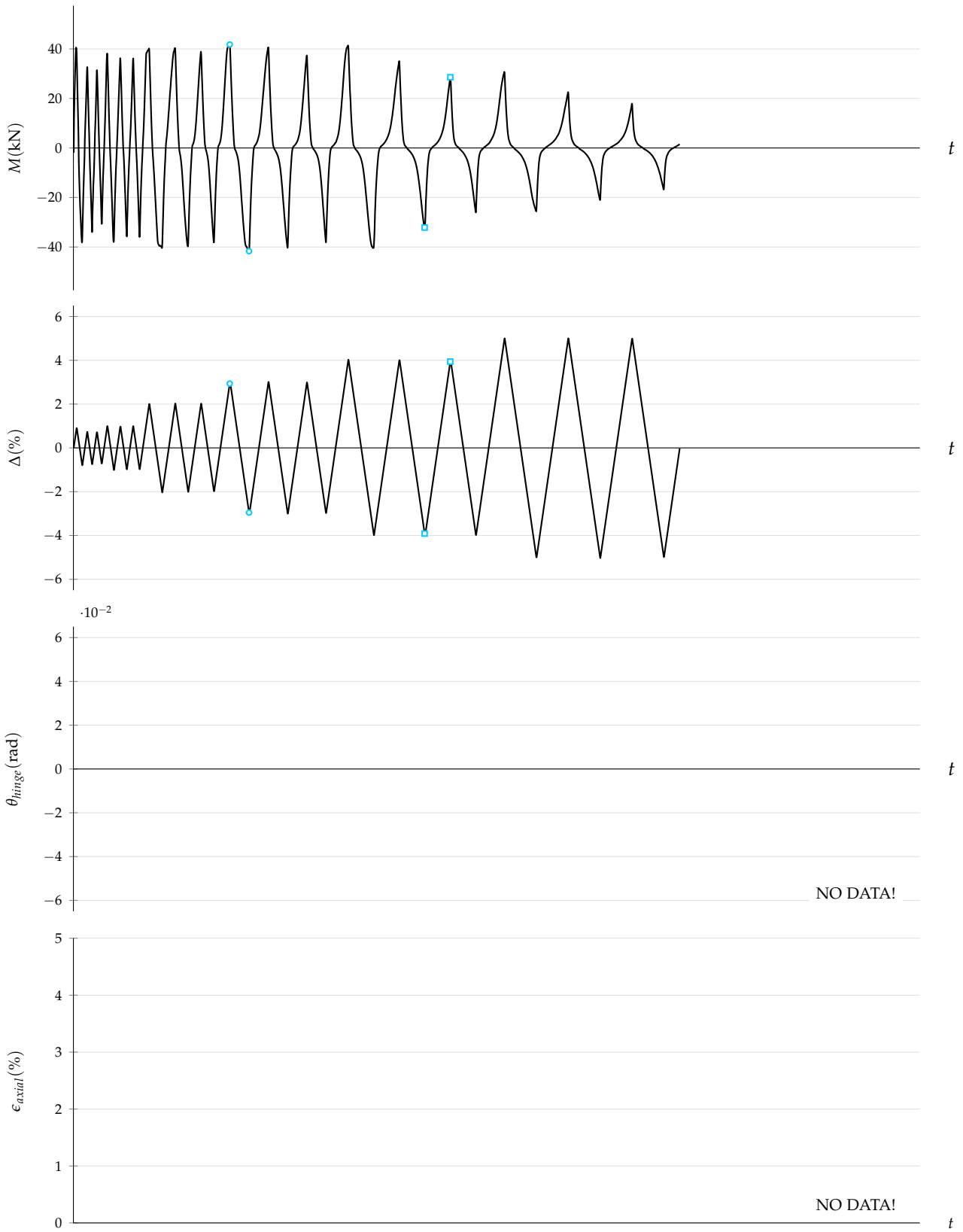
Figure F.6: SB01 response history
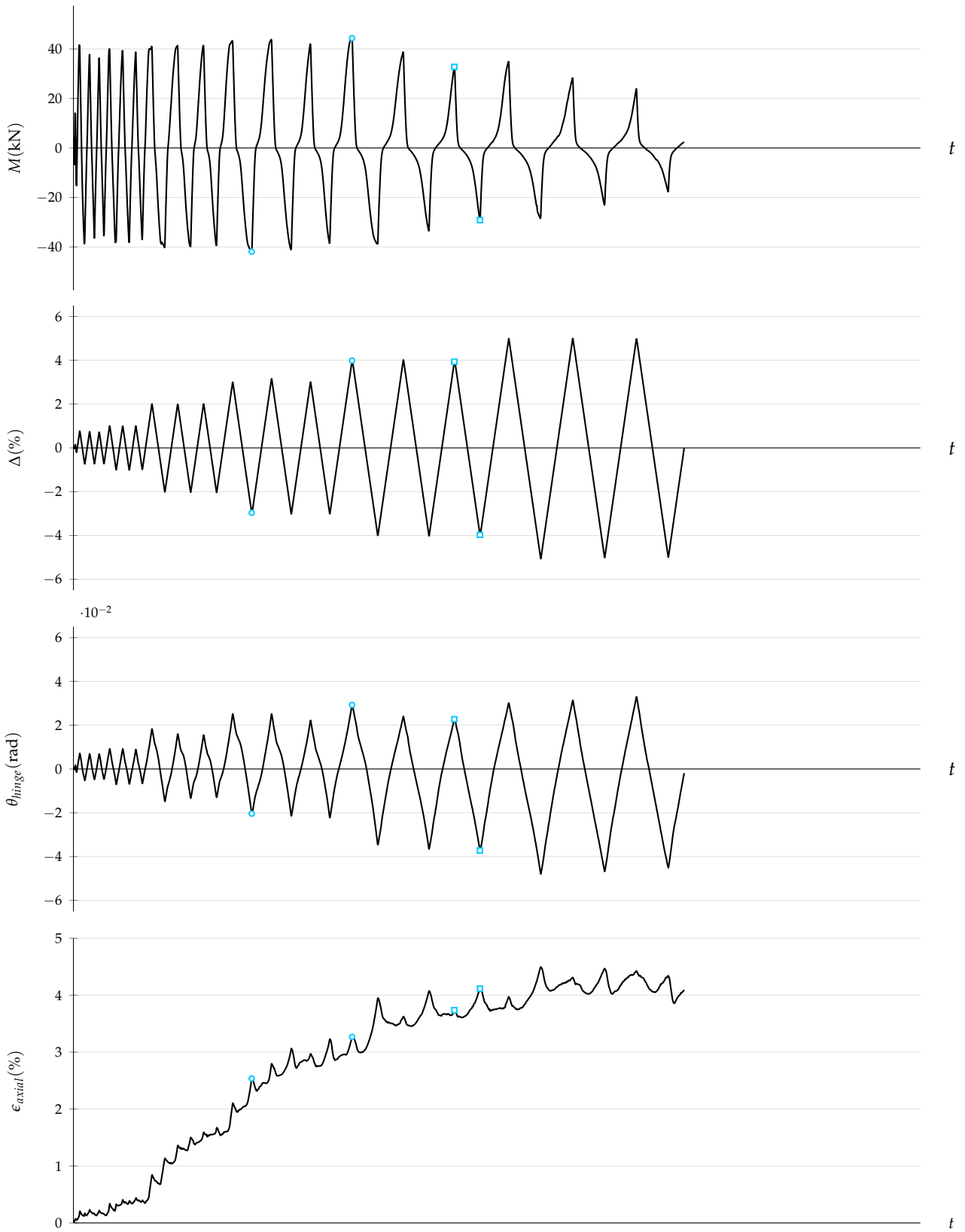
Figure F.7: SB02 response history
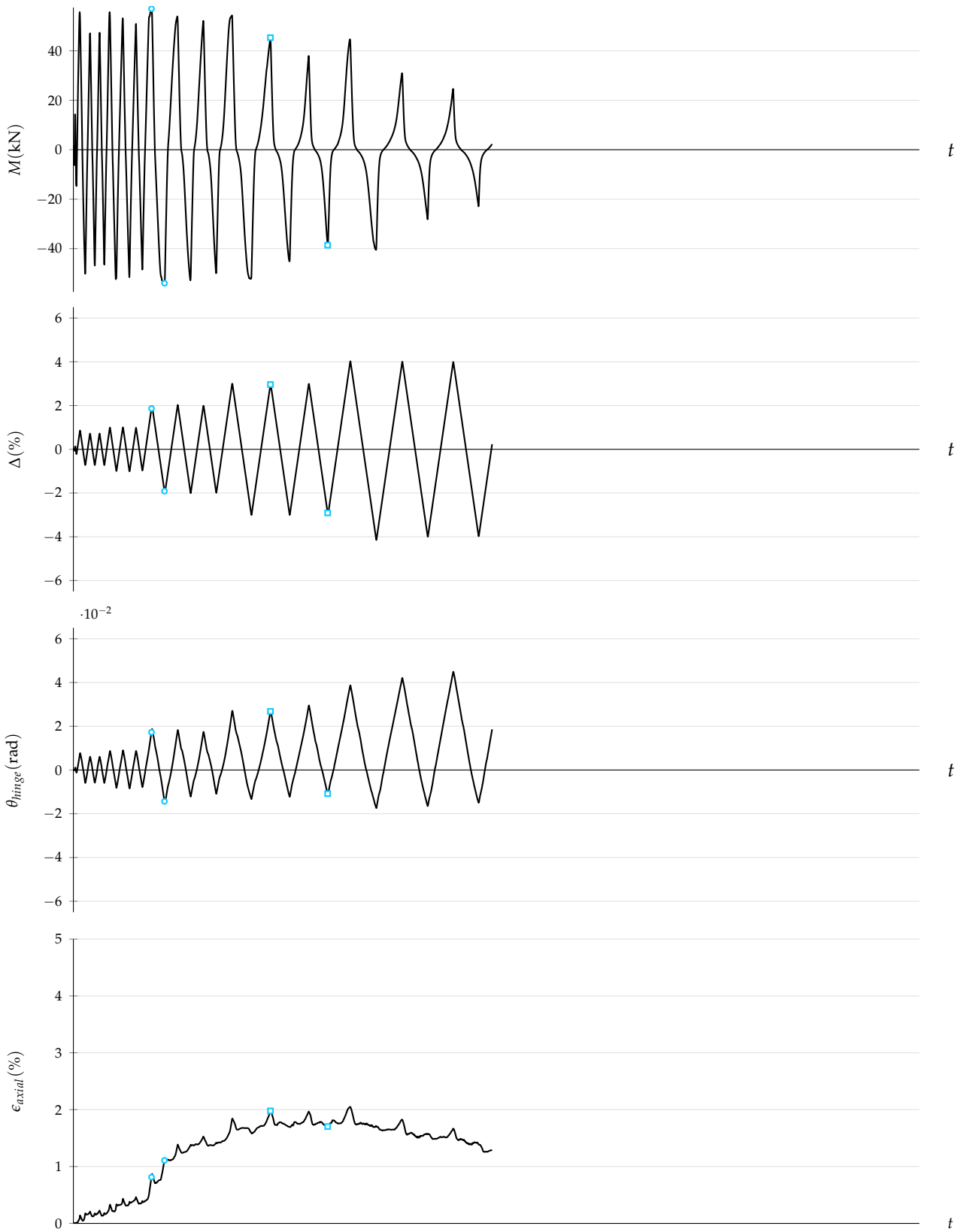
Figure F.8: SB03 response history
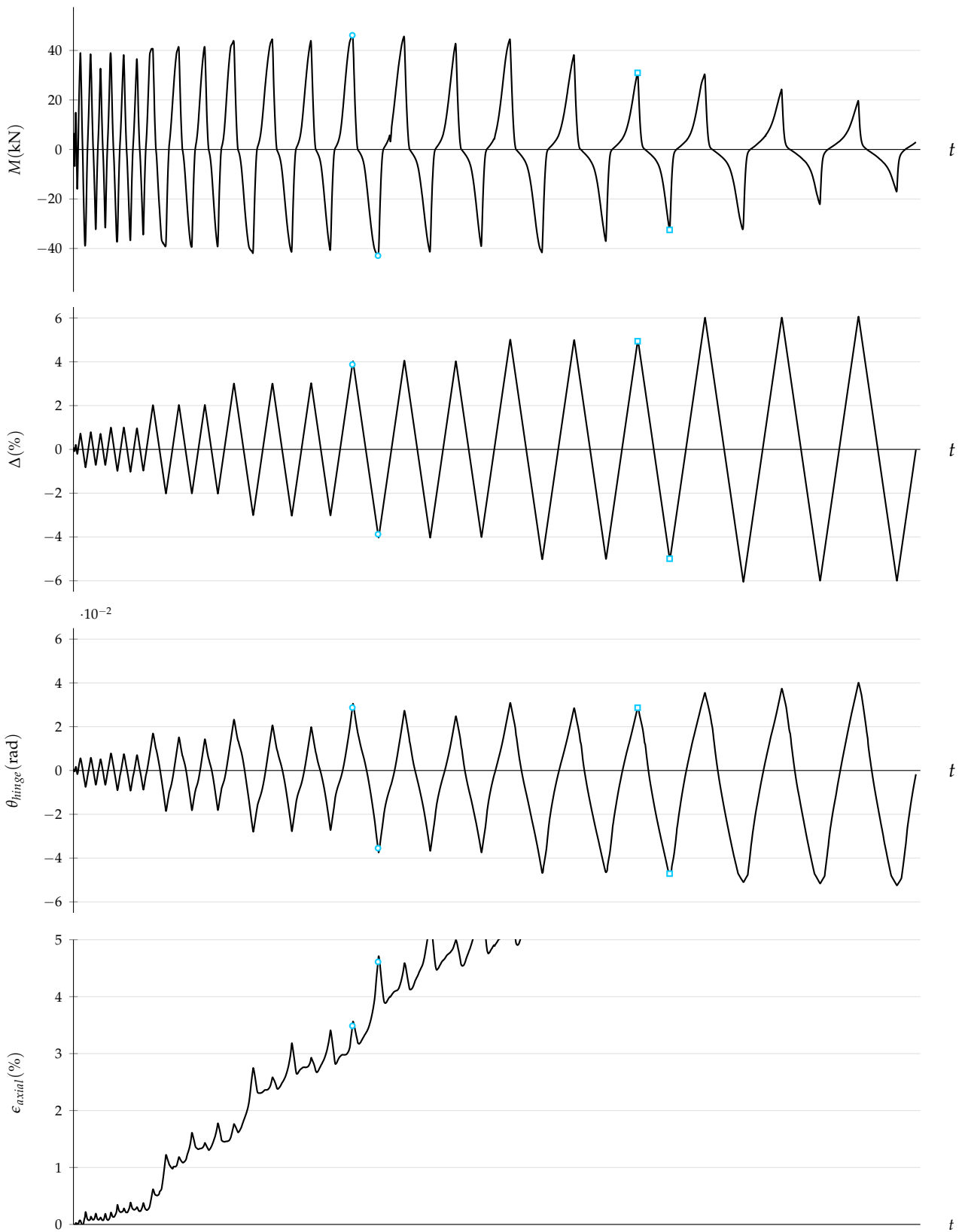
Figure F.9: SB04 response history
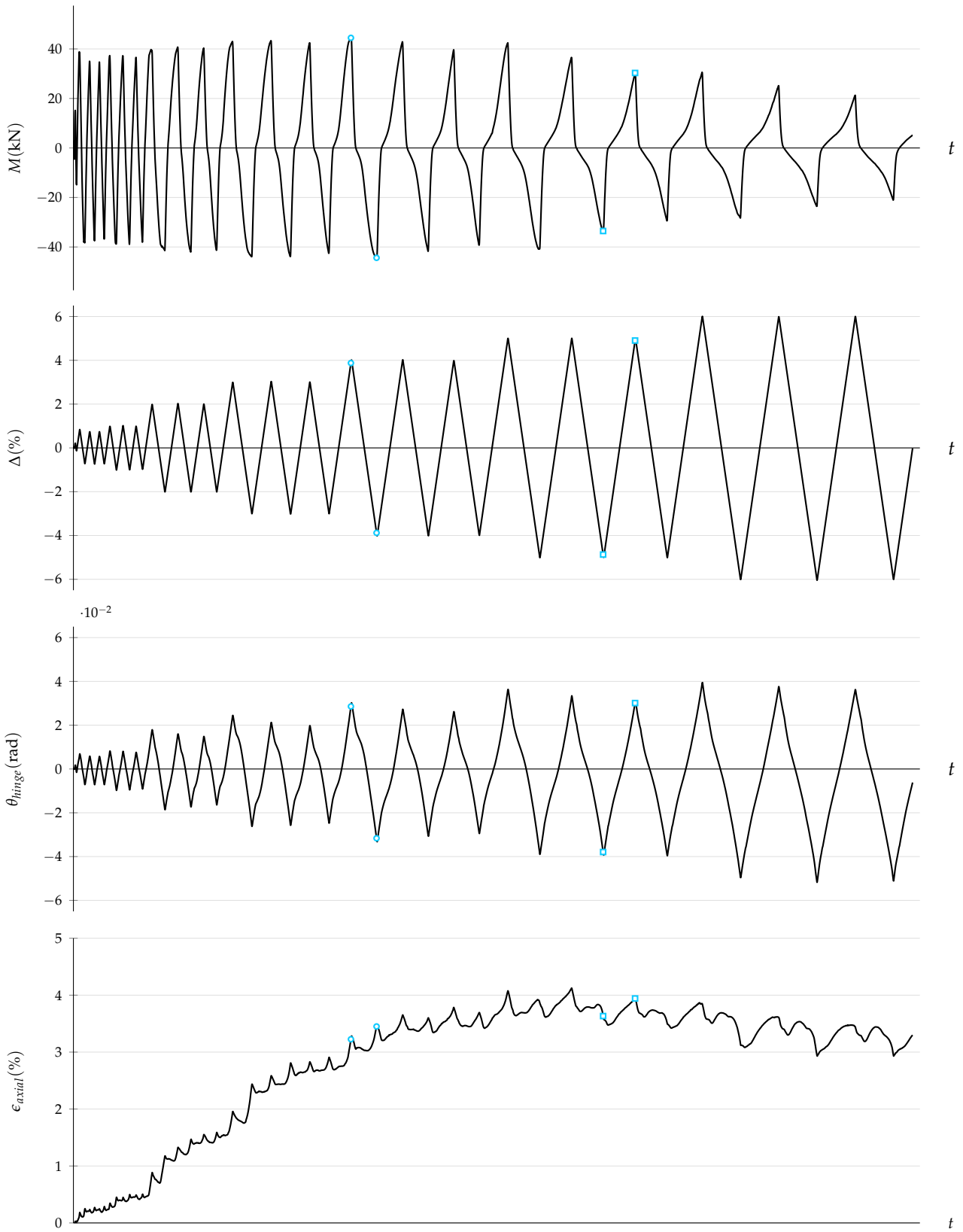
Figure F.10: SB05 response history
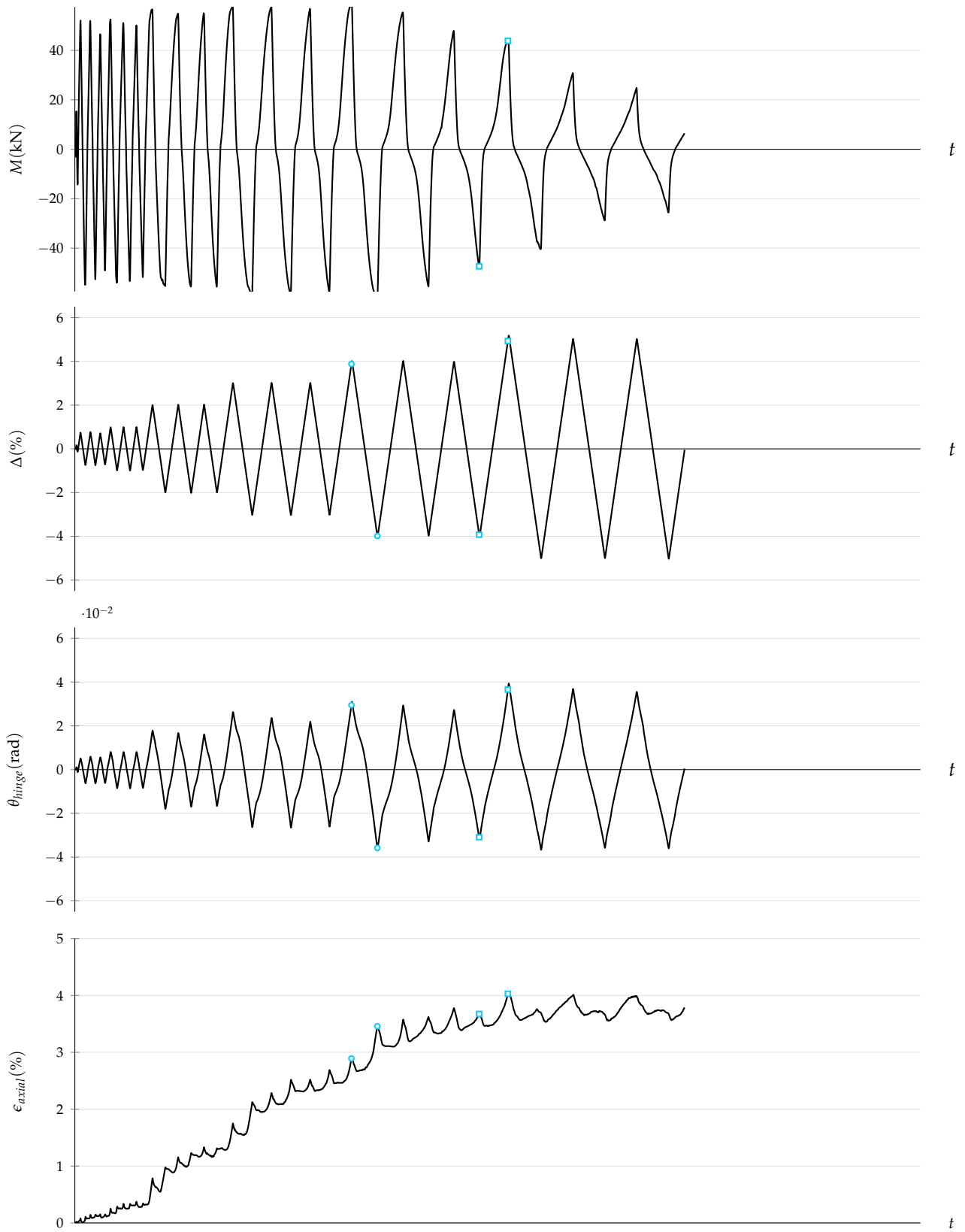
Figure F.11: SB06 response history
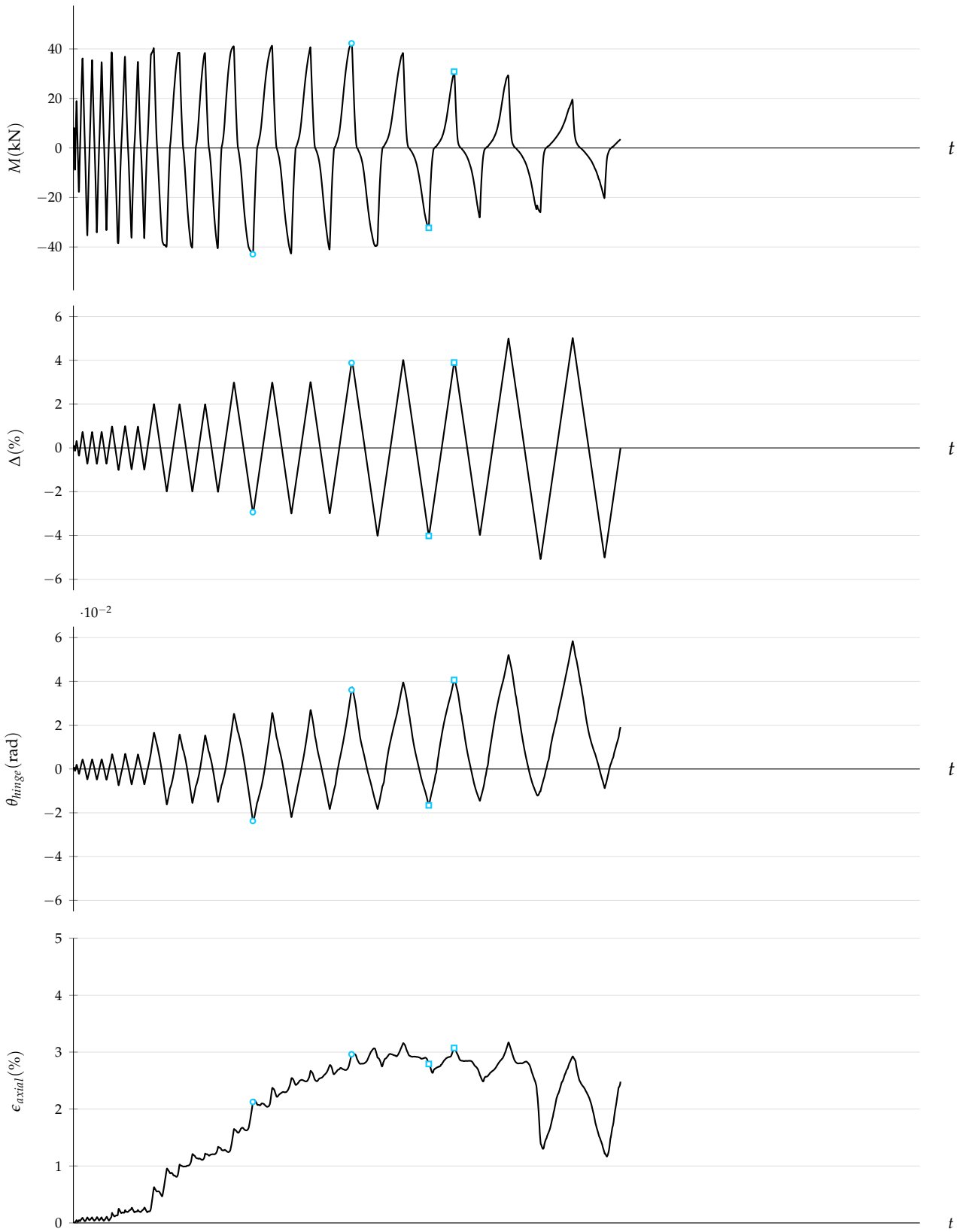
Figure F.12: SB07 response history
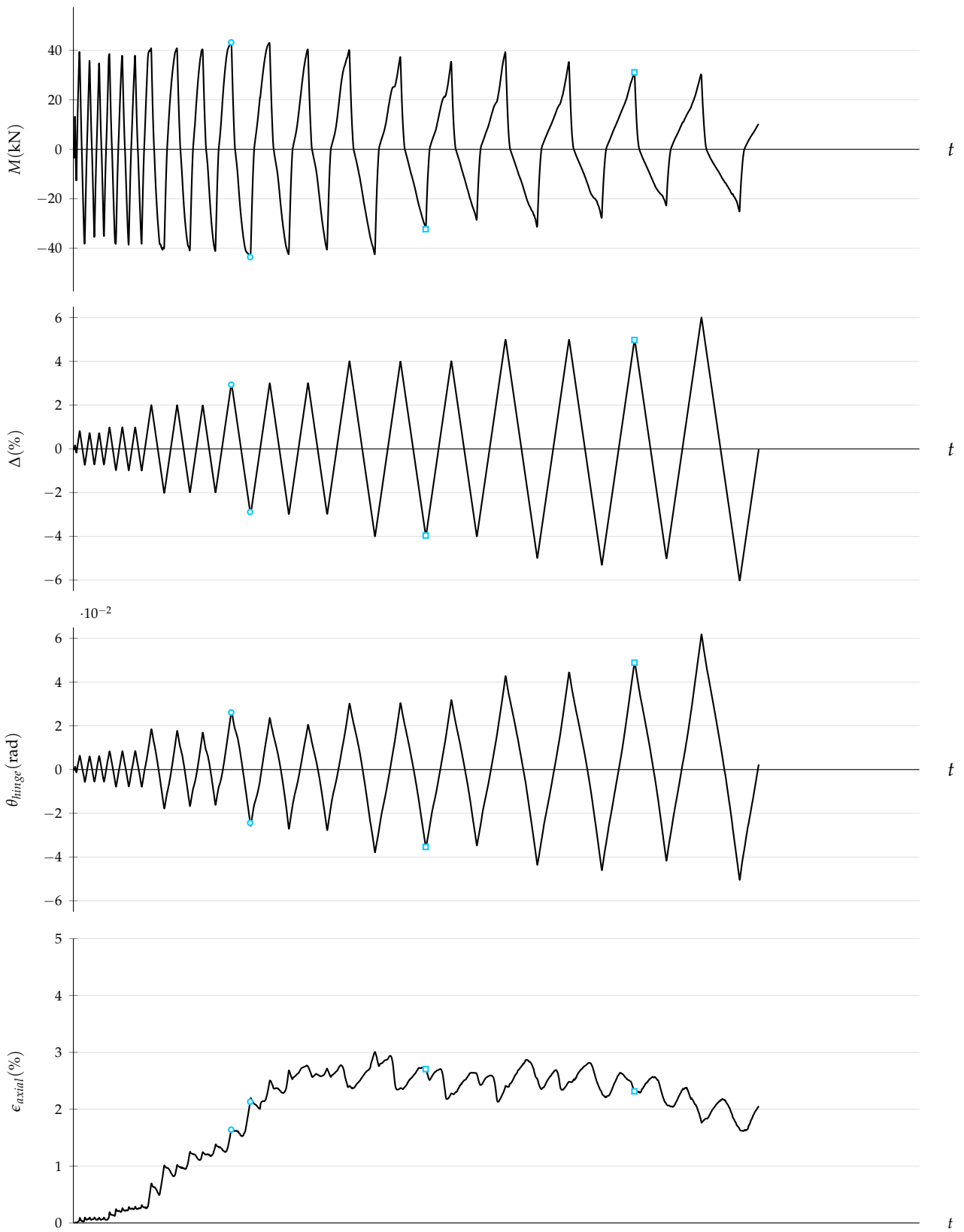
Figure F.13: SB08 response history
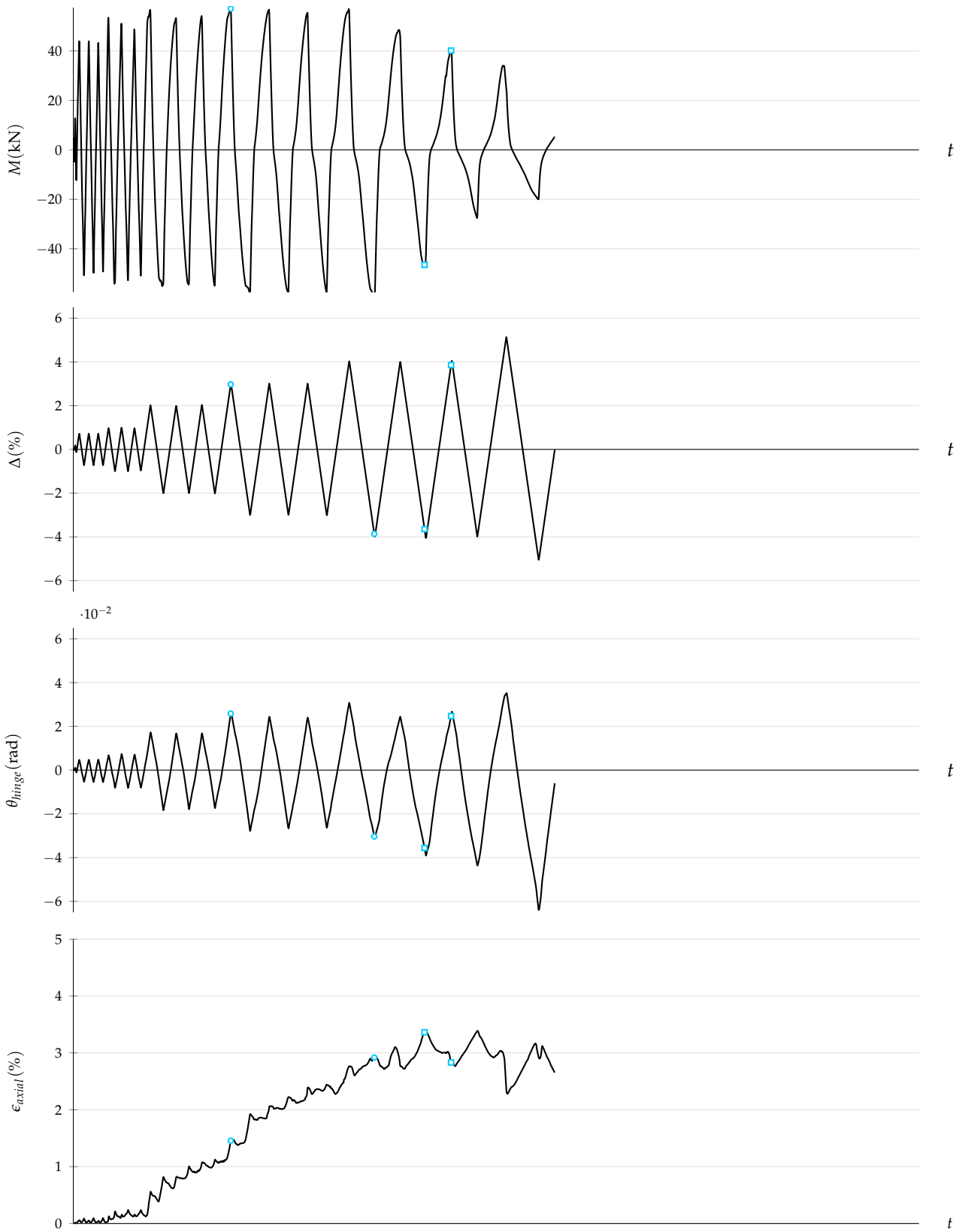
Figure F.14: SB09 response history
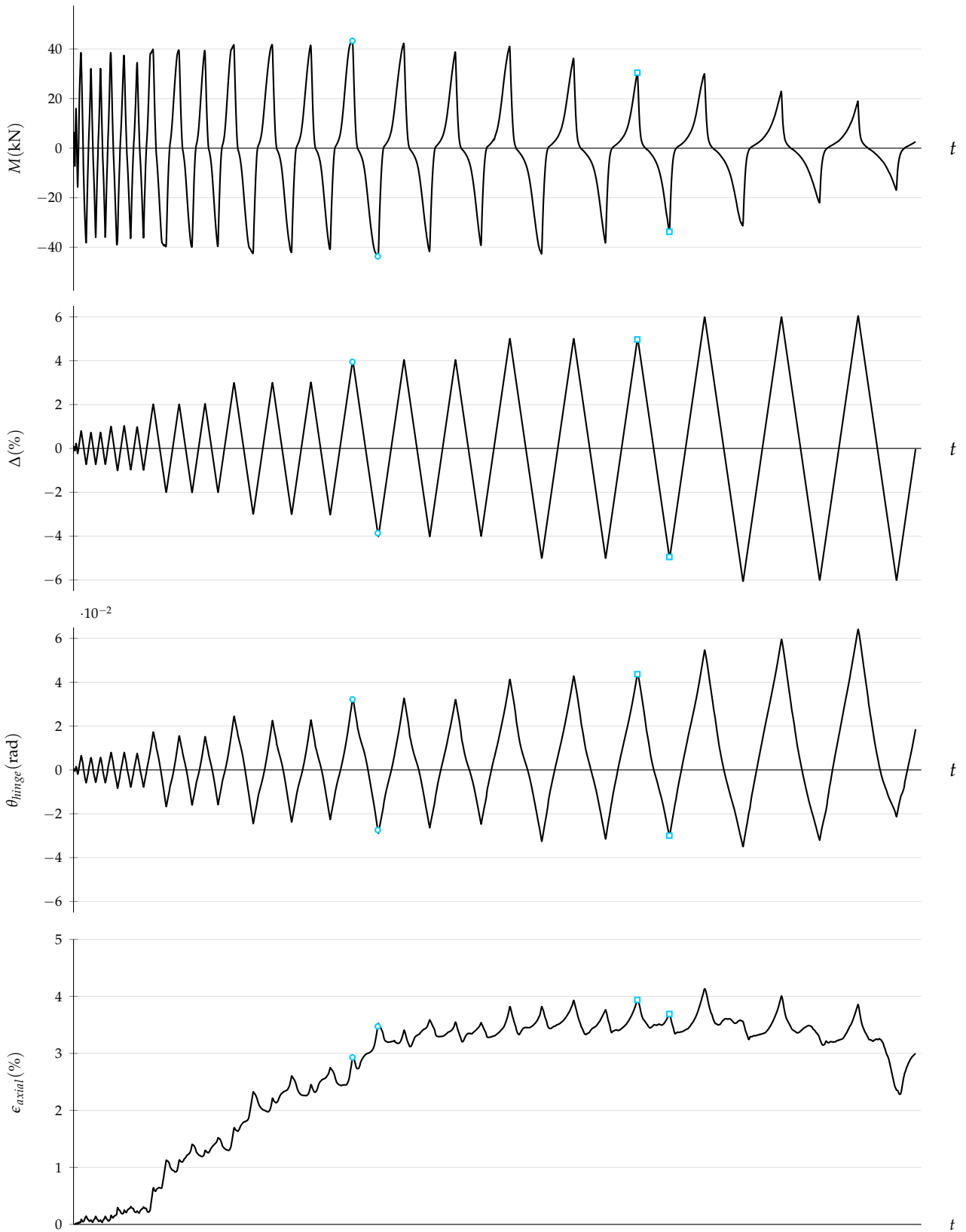
Figure F.15: SB10 response history
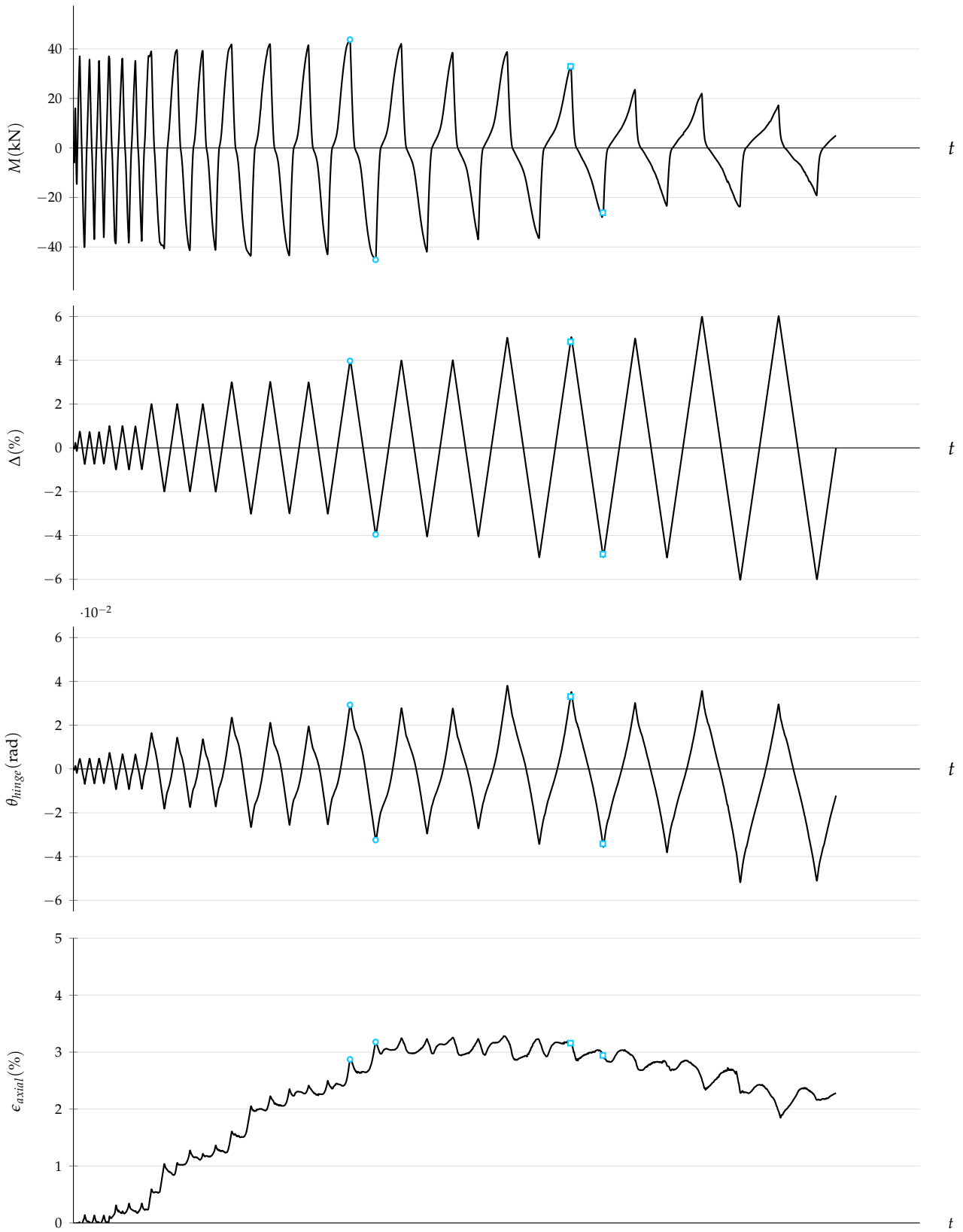
Figure F.16: SB11 response history
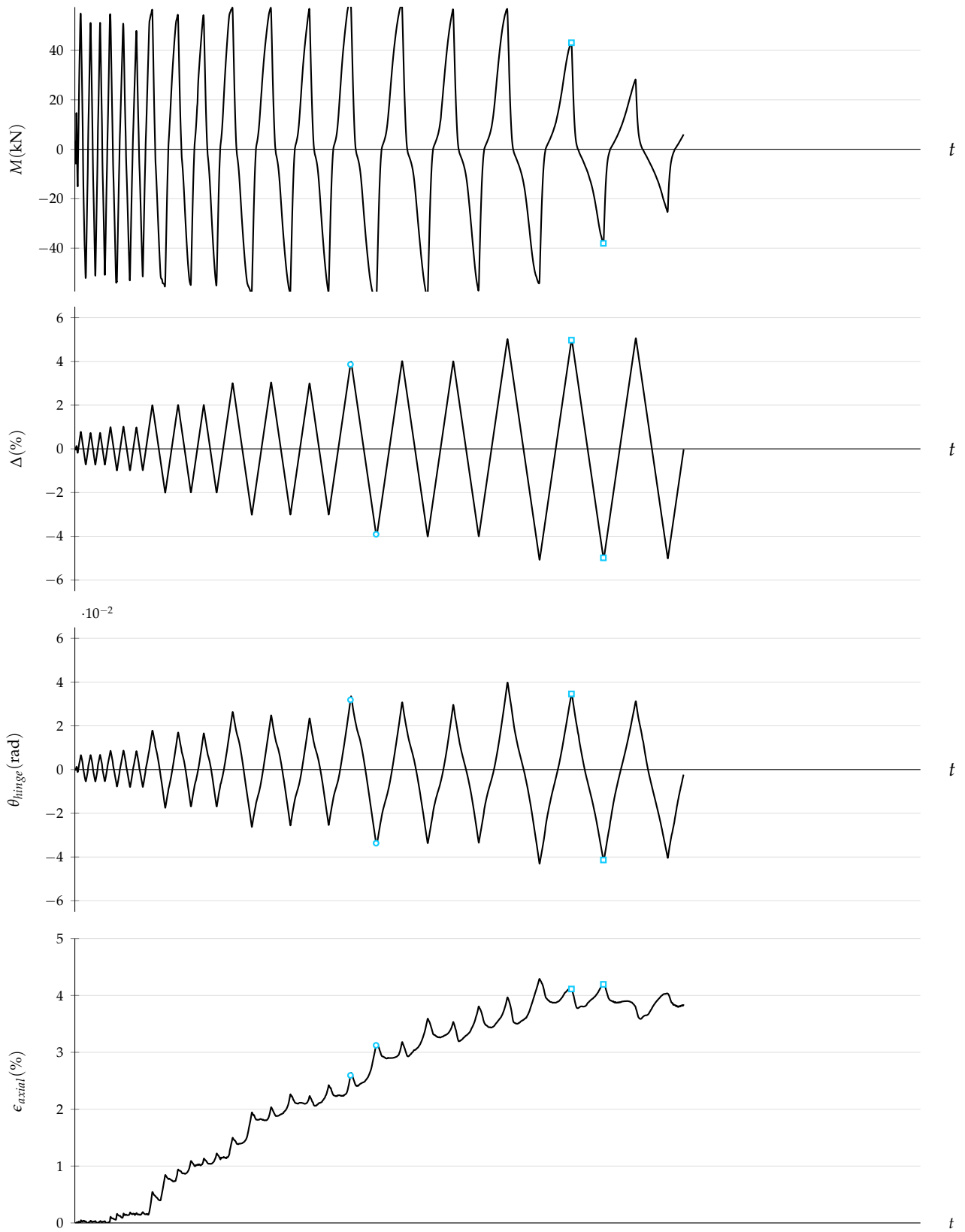
Figure F.17: SB12 response history
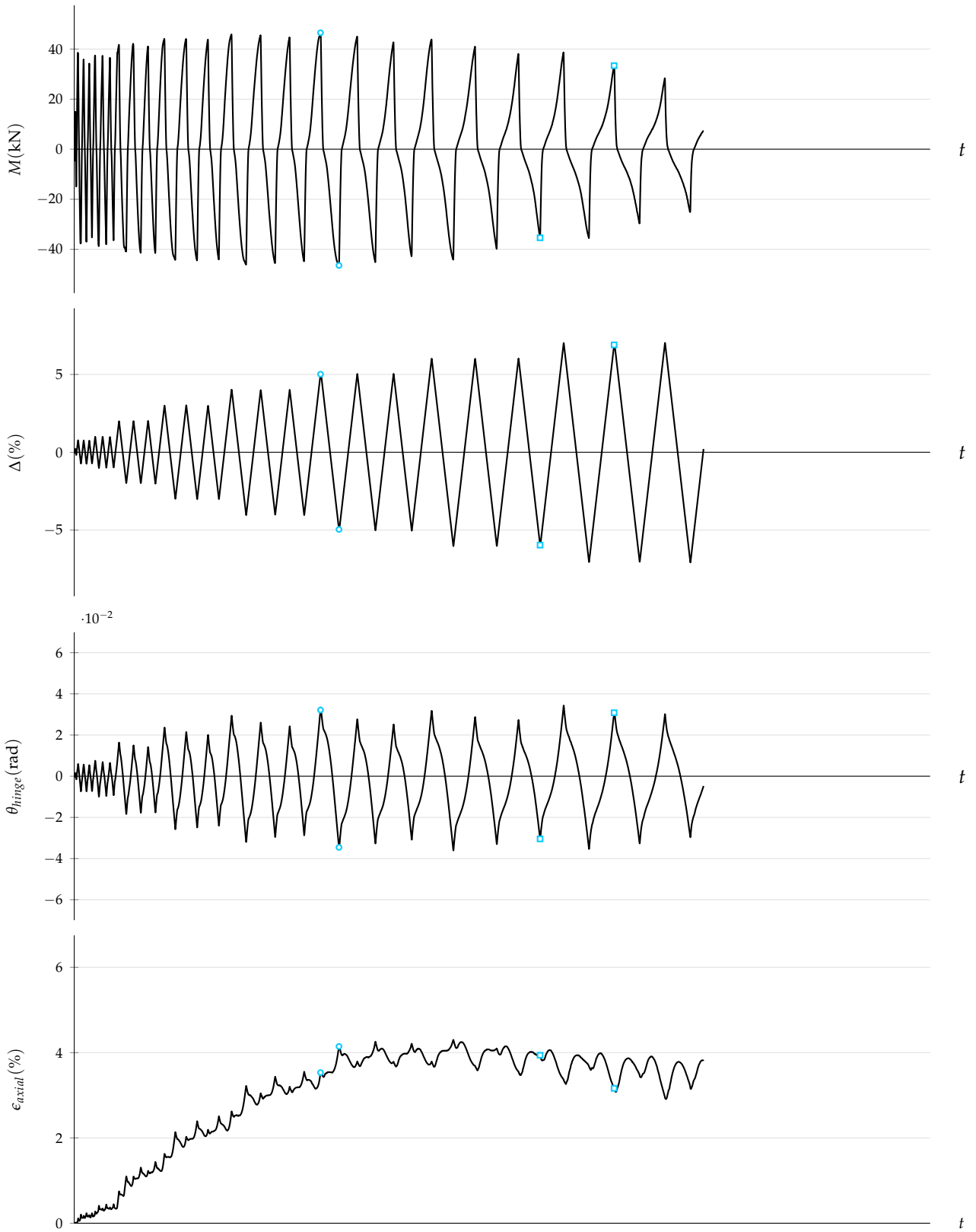
Figure F.18: SC1 response history
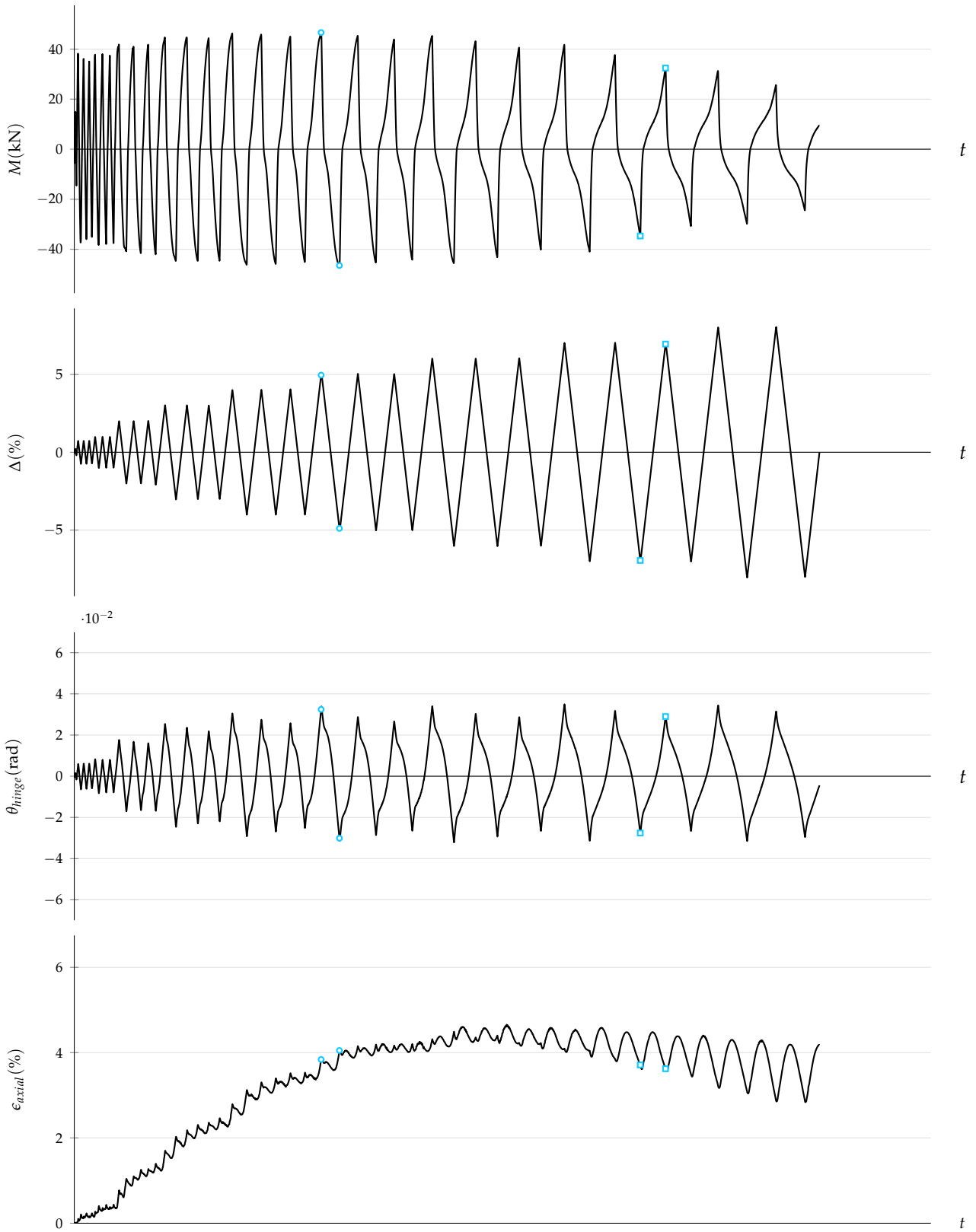
Figure F.19: SC2 response history
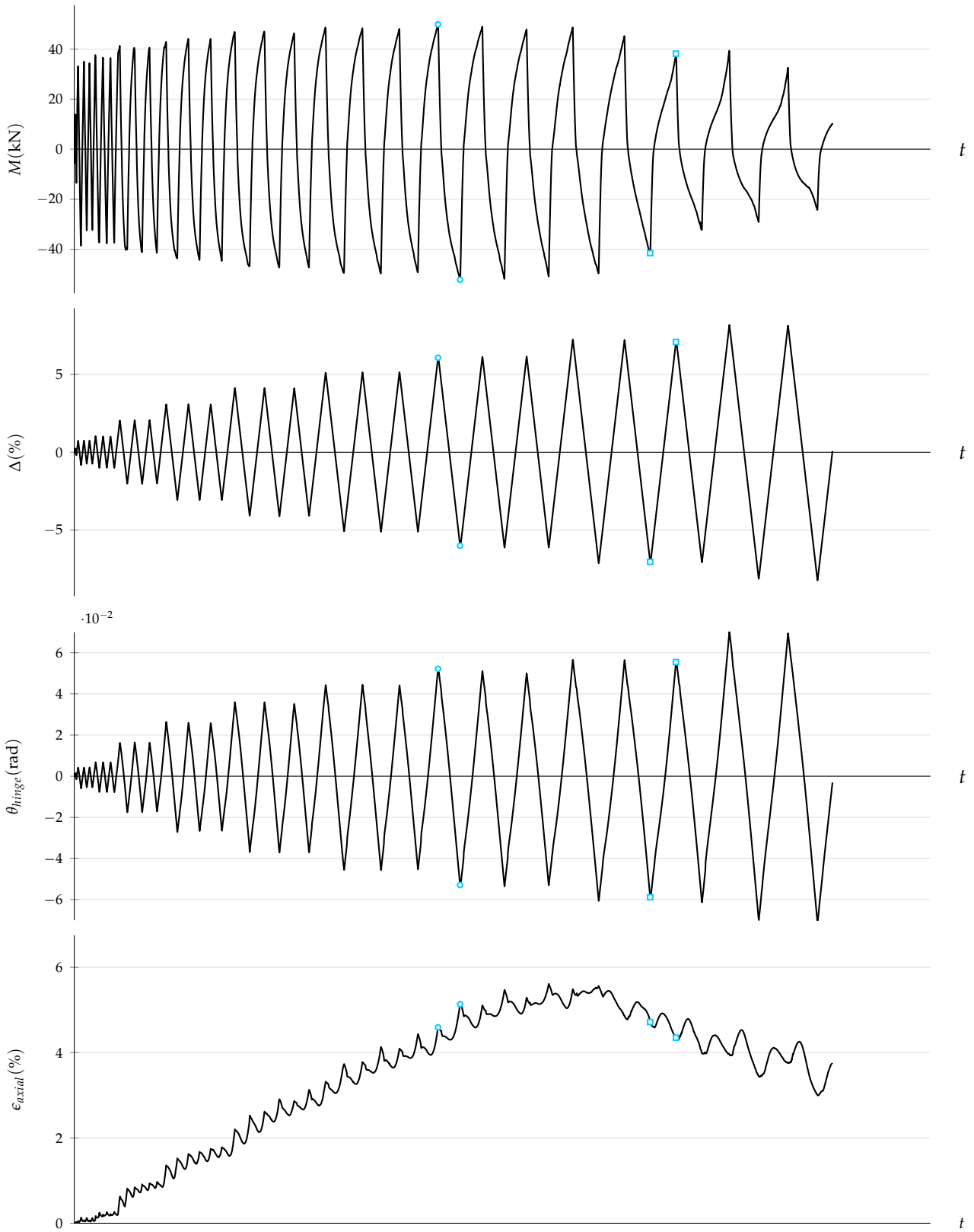
Figure F.20: SC3 response history
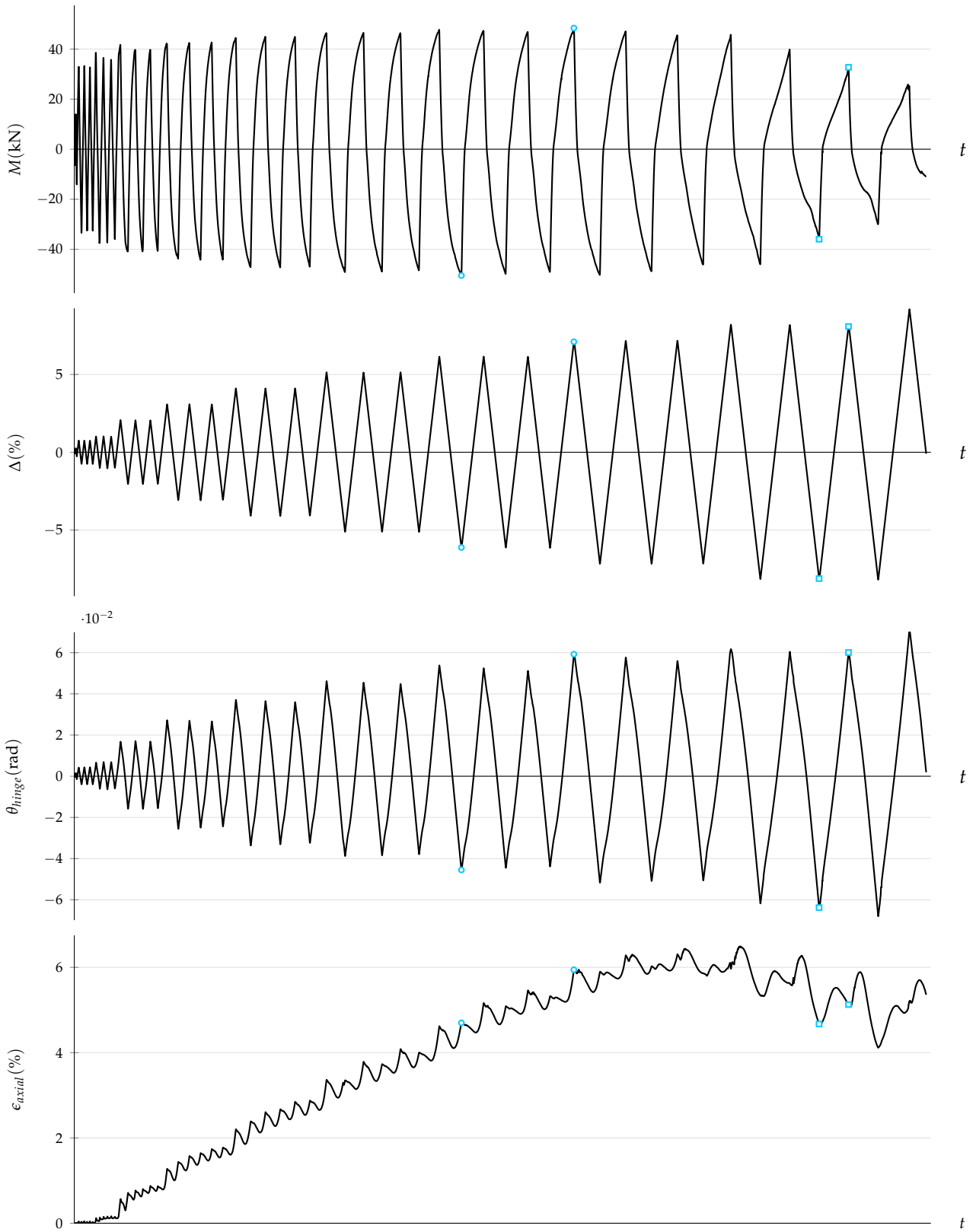
Figure F.21: SC 4 response history

Bibliography

Agrawal, G. L., L. D. Tulin, and K. H. Gerstle. "Response of doubly reinforced concrete beams to cyclic loading". In: *ACI Structural Journal* 62.7 (1965), pp. 823–834. DOI: 10.14359/7726 (cit. on p. 15).

American Concrete Institute. *Building code requirements for structural concrete (ACI 318-14)*. Farmington Hills, MI, 2014. ISBN: 978-1-942727-11-8 (cit. on pp. 31, 91).

American Society of Civil Engineers. *Prestandard and the commentary for the seismic rehabilitation of buildings (FEMA 356)*. Washington, DC: Federal Emergency Management Agency, 2000. ISBN: 978-1-4840-2755-4 (cit. on p. 109).

American Society of Civil Engineers. *Seismic evaluation and retrofit of existing buildings (ASCE/SEI 41-13)*. Reston, VA, 2013. ISBN: 978-0-7844-7791-5 (cit. on pp. 86, 89, 109).

Applied Technology Council. *Seismic design guidelines for highway bridges (ATC-6)*. Berkeley, CA, 1981 (cit. on p. 19).

Architectural Institute of Japan. *Guidelines for performance evaluation of earthquake resistant reinforced concrete buildings (Draft)*. Tokyo, Japan, 2004. ISBN: 978-4-8189-0552-8 (cit. on pp. 86, 109).

Aschheim, M. and J. P. Moehle. *Shear strength and deformability of RC bridge columns subjected to inelastic cyclic displacements*. EERC 92/04. Berkeley, CA: Earthquake Engineering Research Center, University of California, 1992 (cit. on pp. 19, 20).

Bae, S., A. M. Mieses, and O. Bayrak. "Inelastic buckling of reinforcing bars". In: *Journal of Structural Engineering, ASCE* 131.2 (2005), pp. 314–321. DOI: 10.1061/(ASCE)0733-9445(2005)131:2(314) (cit. on p. 22).

Berry, M. P. and M. O. Eberhard. "Practical performance model for bar buckling". In: *Journal of Structural Engineering, ASCE* 131.7 (2005), pp. 1060–1070. DOI: 10.1061/(asce)0733-9445(2005)131:7(1060) (cit. on pp. 21, 86, 88, 96).

Bertero, V. V., E. P. Popov, and T. Y. Wang. *Hysteretic behavior of reinforced concrete flexural members with special web reinforcement*. EERC 74-9. Berkeley, CA: Earthquake Engineering Research Center, University of California, 1974 (cit. on p. 16).

Brachmann, I., J. Browning, and A. Matamoros. "Drift-dependent confinement requirements for reinforced concrete columns under cyclic loading". In: *ACI Structural Journal* 101.5 (2004), pp. 669–677. DOI: 10.14359/13389 (cit. on p. 22).

Bradski, G. "The OpenCV Library". In: *Dr. Dobb's Journal of Software Tools* (2000) (cit. on p. 56).

Brown, D. C. "Close-range camera calibration". In: *Photogrammetric Engineering* 37 (1971), pp. 855–866 (cit. on p. 40).

Brown, R. H. "Reinforced concrete cantilever beams under slow cyclic loadings". PhD thesis. Rice University, 1970 (cit. on p. 15).

Carrasquillo, R. L., A. H. Nilson, and F. O. Slate. "Properties of high strength concrete subject to short-term loads". In: *ACI Structural Journal* 78.3 (1981), pp. 171–178. DOI: 10.14359/6914 (cit. on p. 31).

Celebi, M. and J. Penzien. *Experimental investigation into the seismic behavior of critical regions of reinforced concrete components as influenced by moment and shear*. EERC 73-4. Berkeley, CA: Earthquake Engineering Research Center, University of California, 1973 (cit. on p. 16).

Colajanni, P., A. Recupero, and N. Spinella. "Shear strength degradation due to flexural ductility demand in circular RC columns". In: *Bulletin of Earthquake Engineering* 13.6 (2015), pp. 1795–1807. DOI: 10.1007/s10518-014-9691-0 (cit. on p. 20).

Corley, W. G. "Rotational capacity of reinforced concrete beams". In: *Journal of the Structural Division, ASCE* 92.5 (1966), pp. 121–146 (cit. on p. 18).

Dhakal, R. P. and K. Maekawa. "Path-dependent cyclic stress–strain relationship of reinforcing bar including buckling". In: *Engineering Structures* 24.11 (2002), pp. 1383–1396. DOI: 10.1016/S0141-0296(02)00080-9 (cit. on p. 22).

Elwood, K. J. and J. P. Moehle. "Drift capacity of reinforced concrete columns with light transverse reinforcement". In: *Earthquake Spectra* 21.1 (2005), pp. 71–89. DOI: 10.1193/1.1849774 (cit. on p. 20).

Fang, I.-K., C.-S. Wang, and K.-L. Hong. "Cyclic behavior of high-strength concrete short beams with lower amount of flexural reinforcement". In: *ACI Structural Journal* 91.1 (1994), pp. 10–18. DOI: 10.14359/4477 (cit. on p. 17).

Gosain, N. K. "Effect of cyclic loads on beams with high-strength reinforcement". PhD thesis. Houston, TX: Rice University, 1973 (cit. on p. 16).

Grammatikou, S., D. Biskinis, and M. N. Fardis. "Ultimate strain criteria for RC members in monotonic or cyclic flexure". In: *Journal of Structural Engineering, ASCE* 142.9 (2016). DOI: 10.1061/(ASCE)ST.1943-541X.0001501 (cit. on p. 18).

Haselton, C. B., A. B. Liel, S. T. Lange, and G. G. Deierlein. *Beam-column element model calibrated for predicting flexural response leading to global collapse of RC frame buildings*. PEER 2007/03. Pacific Earthquake Engineering Research Center, 2008 (cit. on pp. 23, 82, 86, 88, 89).

Ibarra, L. F., R. A. Medina, and H. Krawinkler. "Hysteretic models that incorporate strength and stiffness deterioration". In: *Earthquake Engineering & Structural Dynamics* 34.12 (2005), pp. 1489–1511. DOI: 10.1002/eqe.495 (cit. on p. 81).

Ichinose, T. "A shear design equation for ductile RC members". In: *Earthquake Engineering & Structural Dynamics* 21.3 (1992), pp. 197–214. DOI: `10.1002/eqe.4290210302` (cit. on p. 19).

Inai, E. and H. Hiraishi. "Design equations for deformation capacity of reinforced concrete columns failing in flexure". In: *AIJ Journal of Technology and Design* 9.18 (2003), pp. 109–114. DOI: `10.3130/aijt.9.109` (cit. on p. 18).

Ingham, J. M., D. Liddell, and B. J. Davidson. "Influence of loading history on the response of a reinforced concrete beam". In: *Bulletin of the New Zealand Society for Earthquake Engineering* 34.2 (2001), pp. 107–124 (cit. on p. 16).

Japanese Standards Association. *Carbon steels for machine structural use (JIS G 4051:2016)*. Tokyo, Japan, 2016 (cit. on p. 28).

Japanese Standards Association. *Steel bars for concrete reinforcement (JIS G 3112:2010)*. Tokyo, Japan, 2010 (cit. on p. 28).

Lee, J.-Y. and F. Watanabe. "Shear deterioration of reinforced concrete beams subjected to reversed cyclic loading". In: *ACI Structural Journal* 100.4 (2003), pp. 480–489. DOI: `10.14359/12657` (cit. on p. 20).

Mander, J. B., M. J. N. Priestley, and R. Park. "Theoretical stress-strain model for confined concrete". In: *Journal of Structural Engineering, ASCE* 114.8 (1988), pp. 1804–1826. DOI: `10.1061/(ASCE)0733-9445(1988)114:8(1804)` (cit. on p. 91).

Marder, K., C. Motter, K. J. Elwood, and G. C. Clifton. "Testing of seventeen identical ductile reinforced concrete beams with various loading protocols and boundary conditions". In: *Earthquake Spectra* 34.2 (2018). DOI: `10.1193/101717EQS215DP` (cit. on p. 17).

Martín-Pérez, B. and S. J. Pantazopoulou. "Mechanics of concrete participation in cyclic shear resistance of RC". In: *Journal of Structural Engineering, ASCE* 124.6 (1998), pp. 633–641. DOI: `10.1061/(ASCE)0733-9445(1998)124:6(633)` (cit. on p. 19).

Martinez, S., A. H. Nilson, and F. O. Slate. "Spirally reinforced high-strength concrete columns". In: *ACI Structural Journal* 81.5 (1984), pp. 431–442. DOI: `10.14359/10693` (cit. on p. 31).

Mattock, A. H. "Rotational capacity of hinging regions in reinforced concrete beams". In: *Proceedings of the International Symposium on Flexural Mechanics of Reinforced Concrete*. International Symposium on Flexural Mechanics of Reinforced Concrete. Miami, FL: American Society of Civil Engineers, 1965, pp. 143–180 (cit. on pp. 15, 18).

Moyer, M. J. and M. J. Kowalsky. "Influence of tension strain on buckling of reinforcement in concrete columns". In: *ACI Structural Journal* 100.1 (2003), pp. 75–85. DOI: `10.14359/12441` (cit. on p. 21).

Nair, D., R. Rajagopal, and L. Wenzel. "Pattern matching based on a generalized fourier transform". In: *Proceedings of SPIE Vol. 4116*. Advanced Signal Processing Algorithms, Architectures, and Implementations. 2000, pp. 472–480. DOI: `10.1117/12.406527` (cit. on p. 38).

Nmai, C. K. and D. Darwin. *Cyclic behavior of lightly reinforced concrete beams*. SM Report 12. Lawrence, KS: University of Kansas, 1984 (cit. on p. 16).

Pacific Earthquake Engineering Research Center. *Guidelines for performanc-based seismic design of tall buildings*. PEER 2017/06. Berkeley, CA: Pacific Earthquake Engineering Research Center, 2017 (cit. on p. 109).

Panagiotakos, T. B. and M. N. Fardis. "Deformations of reinforced concrete members at yielding and ultimate". In: *ACI Structural Journal* 98.2 (2001), pp. 135–148. DOI: 10.14359/10181 (cit. on pp. 22, 82, 86).

Panagiotou, M., T. Visnjic, G. Antonellis, P. Galanis, and J. P. Moehle. *Effect of hoop reinforcement spacing on the cyclic response of large reinforced concrete special moment frame beams*. PEER 2013/16. Pacific Earthquake Engineering Research Center, 2013 (cit. on p. 17).

Pantazopoulou, S. J. "Detailing for reinforcement stability in RC members". In: *Journal of Structural Engineering, ASCE* 124.6 (1998), pp. 623–632. DOI: 10.1061/(ASCE)0733-9445(1998)124:6(623) (cit. on p. 21).

Papia, M. and G. Russo. "Compressive concrete strain at buckling of longitudinal reinforcement". In: *Journal of Structural Engineering, ASCE* 115.2 (1989), pp. 382–397 (cit. on p. 18).

Park, H.-G., E.-J. Yu, and K.-K. Choi. "Shear-strength degradation model for RC columns subjected to cyclic loading". In: *Engineering Structures* 34 (2012), pp. 187–197. DOI: 10.1016/j.engstruct.2011.08.041 (cit. on p. 20).

Peters, W. H. and W. F. Ranson. "Digital imaging techniques in experimental stress analysis". In: *Optical engineering* 21.3 (1982), pp. 427–431. DOI: 10.1117/12.7972925 (cit. on p. 38).

Popov, E. P., V. V. Bertero, and H. Krawinkler. *Cyclic behavior of three R.C. flexural members with high shear*. EERC 72-5. Berkeley, CA: Earthquake Engineering Research Center, University of California, 1972 (cit. on p. 16).

Priestley, M. J. N., R. Verma, and Y. Xiao. "Sesimic shear strength of reinforced concrete columns". In: *Journal of Structural Engineering, ASCE* 120.8 (1994), pp. 2310–2329 (cit. on p. 19).

Pujol, S., M. A. Sozen, and J. A. Ramirez. "Displacement history effects on drift capacity of reinforced concrete columns". In: *ACI Structural Journal* 103.2 (2006), pp. 253–262. DOI: 10.14359/15183 (cit. on p. 20).

Saito, T. and Y.-G. Zhao. "Optical full field measurement of concrete deformation using digital image correlation method". In: *Proceedings of the JCI Annual Convention*. Takamatsu, Japan: Japan Concrete Institute, 2014 (cit. on p. 38).

Sasani, M. "Life-safety and near-collapse capacity models for seismic shear behavior of reinforced concrete columns". In: *ACI Structural Journal* 104.1 (2007), p. 30. DOI: 10.14359/18430 (cit. on p. 22).

Scribner, C. F. "Reinforcement buckling in reinforced concrete flexural members". In: *ACI Structural Journal* 83.6 (1986), pp. 966–973. DOI: 10.14359/2648 (cit. on p. 21).

Scribner, C. F. and J. K. Wight. *Delaying shear strength decay in reinforced concrete flexural members under large load reversals*. UMEE 78R2. Ann Arbor, MI: University of Michigan, 1978 (cit. on p. 16).

Sezen, H. and J. P. Moehle. "Shear strength model for lightly reinforced concrete columns". In: *Journal of Structural Engineering, ASCE* 130.11 (2004), pp. 1692–1703. DOI: 10.1061/(ASCE)0733-9445(2004)130:11(1692) (cit. on p. 19).

Sinha, B. P., K. H. Gerstle, and L. D. Tulin. "Response of singly reinforced beams to cyclic loading". In: *ACI Structural Journal* 61.8 (1964), pp. 1021–1037. DOI: 10.14359/7819 (cit. on p. 15).

Structural Engineers Association of California. *Performance based seismic engineering of buildings (Vision 2000)*. Sacramento, CA, 1995 (cit. on p. 109).

To, D. V. and J. P. Moehle. "Seismic performace of beams with high-strength reinforcement". In: *Proceedings of the 16th World Conference on Earthquake Engineering*. 16th World Conference on Earthquake Engineering. Santiago, Chile, 2017 (cit. on p. 17).

Wight, J. K. and M. A. Sozen. *Shear strength decay in reinforced concrete columns subjected to large deflection revarsals*. SRS 403. Urbana-Champaign, IL: University of Illinois, 1973 (cit. on p. 16).

Xiao, Y., A. Esmaeily-Ghasemabadi, and H. Wu. "High-strength concrete short beams subjected to cyclic shear". In: *ACI Structural Journal* 96.3 (1999), pp. 392–399. DOI: 10.14359/673 (cit. on p. 17).

Xiao, Y. and R. Ma. "Seismic behavior of high strength concrete beams". In: *The Structural Design of Tall Buildings* 7.1 (1998), pp. 73–90. DOI: 10.1002/(SICI)1099-1794(199803)7:1<73::AID-TAL92>3.0.CO;2-A (cit. on p. 17).

Yang, Y. "Research on post shear failure residual axial strength evaluation of reinforced concrete columns". PhD thesis. Tokyo, Japan: University of Tokyo, 2016 (cit. on p. 102).

Zhang, Z. "A flexible new technique for camera calibration". In: *IEEE Transactions on Pattern Analysis and Machine Intelligence* 22.11 (2000), pp. 1330–1334. DOI: 10.1109/34.888718 (cit. on pp. 41, 56).

List of figures

List of tables

List of algorithms

List of symbols

Δ	Drift at the cantilever tip or chord rotation
ϵ_u	Ultimate strain of steel reinforcement
ϵ_y	Yield strain of steel reinforcement
ϵ_{axial}	Axial strain
$\epsilon_{lateral}$	Lateral strain
ρ	Ratio of longitudinal reinforcement
ρ_s	Ratio of transverse reinforcement
θ_{hinge}	Rotation of the hinge region
b	Section width of specimen
D	Section depth of specimen
d_b	Bar diameter of longitudinal reinforcement
e	Eccentricity of the load transferred to a laterally inclined rebar section
E_c	Modulus of elasticity of concrete
E_s	Modulus of elasticity of steel reinforcement
EI	Flexural stiffness of the concrete section
f_c'	Compressive strength of concrete
f_s	Stress in steel reinforcement at the ultimate state
f_t	Splitting tensile strength of concrete
f_u	Ultimate strength of steel reinforcement
f_y	Yield strength of steel reinforcement
f_{yt}	Yield strength of transverse reinforcement
k_s	Post-yielding stiffness
k_y	Pre-yielding stiffness
l	Loading span length of specimen cantilever
M	Moment at critical section

$M_n m$ Nominal moment strength as per ACI 318-14

M_u Ultimate strength

M_{u_1} Ultimate strength estimated using ϵ_c as 0.45 % and f_s/f_y as 1.15

M_{u_2} Ultimate strength estimated using actual steel stress-strain distribution and Mander's unconfined concrete model

M_{u_3} Ultimate strength estimated using actual steel stress-strain distribution and Mander's confined concrete model

$M_n m$ Nominal moment strength as per ACI 318-14

M_u Ultimate strength

M_{u_1} Ultimate strength estimated using ϵ_c as 0.45 % and f_s/f_y as 1.15